Discrete Element Modeling of Bio-Inspired Soil Penetration Processes for In-Situ Testing Probes

By

YUYAN CHEN
DISSERTATION

Submitted in partial satisfaction of the requirements for the degree of

DOCTOR OF PHILOSOPHY

in

Civil & Environmental Engineering

in the

OFFICE OF GRADUATE STUDIES

of the

UNIVERSITY OF CALIFORNIA

DAVIS

Approved:

Alejandro Martinez, Chair

Jason T. DeJong

Ross W. Boulanger

Committee in Charge

2022

To my parents, teachers and friends.

CONTENTS

List of Figures

List of Tables

Abstract

Discrete Element Modeling of Bio-Inspired Soil Penetration Processes for In-Situ Testing Probes

Soil penetration activities, such as site investigation, pile driving and tunneling, are ubiquitous and fundamentally important in civil engineering. These penetration activities are energy-intensive and responsible for considerable environmental disruption due to the usage of large equipment required to provide reaction force. Bio-inspired geotechnics has received significant attention in recent years due to the growing need for making construction processes more sustainable. This research investigates the anchor-tip strategy inspired by earth and marine worms, razor clams, and caecilians and the circumnutation strategy inspired by plant roots. Throughout this dissertation, it is shown that using the bio-inspired strategies can facilitate soil penetration by reducing the mobilized penetration resistance and generating anchorage reaction forces.

Discrete element modeling (DEM) is used to simulate the bio-inspired soil penetration process of an in-situ testing probe in granular soils. Different soil conditions are examined in the DEM simulations, including soil density and magnitude of overburden stress. Simulations were performed on specimens confined to constant stress levels using servo-controlled algorithms to model deep penetration conditions. Simulations were also performed on unconfined soil specimens under gravity to model shallow soil conditions.

The simulated anchor-tip strategy consists of radially expanding of a probe section or sections (i.e. anchor(s)) and subsequently displacement of the probe tip to deeper locations. The global and meso-scale responses of the probe-soil system are analyzed to shed light on the working mechanisms of this strategy. Specifically, the expanded anchor serves as a integrated anchorage system to provide the reaction force needed for penetration. The anchor expansion leads to reduction in tip resistance by altering stress states around the tip. The effects of a number of aspects of the anchor and tip geometry, as well as of soil depth, are explored. The effects of soil density on the anchor-tip strategy are also highlighted. Due to the complexity of anchor-tip strategy, three simulation strategies are employed to control the probe's motions: displacement-controlled algorithm, velocity controlled algorithm with force limits and force-controlled algorithm. Among these three strategies, the first one is the most simplified one while the last one best approximated the motion used by the model organisms.

The simulated circumnutation inspired motion (CIM) consists of helical movements of the probe tip accompanied by downward penetration of the entire probe. The probe forces, torque, mechanical work and particle contact orientations are analyzed and discussed. The results indicate that CIM leads to a decrease of penetration resistance by altering the contact orientations near the tip from the vertical to the horizontal direction. However, this reduction in penetration resistance comes at a cost of increased torque and in most conditions an increase in rotational work. A comparison of the CIM and rotational penetration (RP) strategies shows that the CIM mobilizes smaller penetration forces and requires less total mechanical work to penetrate the same distance as the RP. The effects of the CIM velocities and probe geometry are also examined.

The understanding of the probe-soil interactions during the bio-inspired penetration processes lays the foundation for the development of innovative soil penetration tools and techniques to increase the efficiency of construction activities. For example, studies on bio-inspired probes can guide the design of future lightweight penetration devices. Such probes could reduce the energy consumption during transport and the challenges associated with limited accessibility in certain sites, such as congested urban areas and outer space bodies. These studies show that by learning from nature, more efficient solutions can be developed for geotechnical engineering applications.

Acknowledgments

First of all, I would like to express my deepest gratitude to my supervisor Prof. Alejandro Martinez for his advice and support, and patience throughout my PhD journey. At many stages of my studies and research, his professional insights on geotechnical engineering and creativity in research inspired me. He also shared important lessons on academia, education, career, collaborations, and positive outlook on life. He serves as a role model for me in many aspects of my life.

I would also like to thank my dissertation committee, Prof. Ross Boulanger and Prof. Jason DeJong, for their guidance and encouragement during my PhD studies. They provided me advice on the research project and helped discern some important matters in my simulations that are related to geotechnical engineering practice. I should also acknowledge the faculty and professors that were not in my committee but also helped and inspired me in the past. Prof. Katerina Ziotopoulou provided me guidance on course learning and teaching. Interacting with Prof. Julian Tao helped me understand the process of bio-inspired design and know more about bio-inspired research.

I want to expand my thanks to the Department of Civil and Environmental Engineering and the Center for Bio-mediated and Bio-inspired Geotechnics for providing diverse resources and opportunities for me to learn and improve myself.

It is also a very nice experience to interact with the research group of Prof. Alejandro Martinez. The group atmosphere is open, friendly, encouraging and enables collaborative learning. Therefore, I would like to thank Dr. Sharif Ahmed, Mandeep Singh Basson, Lin Huang, Kyle O'Hara, Riya Anilkumar, Olivia Hunt, Jasmine Miller, Sam Follett, Damon Nguyen, Matthew Burrall, and Alejandro J. Perez. I also want to thank all the other research colleagues who have helped me with my research project. Particularly I want to express my appreciation to Dr. Ali Khosravi, who guided me to learn the PFC software and codes when I just started my PhD research. I also would like to thank Dr. Kevin Kuei, who generously helped me with data processing in Python.

I would like to thank my mother, Fang Wang, and my father, Mingbao Chen, for their unconditional supports all the way since I was born. Their love and encouragement make me stronger when I encounter difficulties in my life. I also wanted to thank the rest of my big family who supported me. Finally, I would like to thank Dr. Han Yang for being with me, supporting me and bringing me happiness.

Chapter 1

Introduction

1.1 Background and Motivation

In civil engineering, soil penetration activities, such as site exploration, pile driving, pile driving, and tunneling are of paramount importance in the early phases of construction. However, these penetration activities are energy-intensive and usually require the use of large equipment. For examples, drill rigs are needed to provide reaction mass for in-situ Cone Penetration Test (CPT), Pressuremeter Test (PMT), and Dilatometer Test (DMT), hammers and cranes are usually required for pile driving, and tunnel boring machines (TBMs) are needed for underground excavation and tunneling. The need for large equipment can cause challenges in sites with limited accessibility (e.g. Mayne [2007]), such as the toe of a dam, congested urban areas, forested areas, deep water, and extraterrestrial bodies.

The use of large equipment is also responsible for a large portion of the negative environmental impacts and economic costs during site investigation activities [Raymond et al., 2020; Purdy et al., 2020]. Specifically, the energy cost associated with mobilization of equipment accounts for nearly half of the total energy consumed and global warming and acidification potential of site investigation projects for a typical 30 m borehole or sounding. Another challenge in site investigation is refusal at greater soil depths or due to stiff layers (such as CPT testing, Mayne [2007]). Therefore, there is a need to develop innovative and efficient soil penetration solutions for civil engineering applications.

The field of bio-inspired geotechnics has received significant attention in recent years, which focuses on applying biological strategies and principles to develop efficient solutions for engineering problems [Martinez et al., 2021]. Examples of bio-inspired geotechnics research include experimental and numerical studies on the performance of self-penetrating probes and robots in different soil conditions (e.g. Cortes and John [2018]; Khosravi et al. [2018]; Martinez et al. [2020]; Tao et al. [2020]; Huang and Tao [2020]; Chen et al. [2021]; Borela et al. [2021]), laboratory and geotechnical centrifuge investigations on snakeskin-inspired surfaces and piles that develop directional-dependent skin friction (e.g. Martinez et al. [2019]; Martinez and O'Hara [2021]; O'Hara and Martinez [2020]; Stutz and Martinez [2021]), and laboratory and field investigation on tree-root inspired foundations or penetrating robots (e.g. Mallett et al. [2018a]; Meijer et al. [2019]; Burrall et al. [2020]; Del Dottore et al. [2017]).

Biological burrowing strategies can inspire engineers to develop more efficient site exploration devices. A number of animals have developed biological adaptations that allow them to efficiently burrow in different soils, such as caecilians, razor clams, and earthworms. Plants have also evolved strategies of movement for their roots to penetrate soil efficiently.

Many of these burrowing animals use peristalsis locomotion or the 'dual anchor mechanism' as burrowing strategies. The animals that use peristalsis locomotion are soft-bodied and have circular and longitudinal muscles to form alternating waves of elongation and shortening that move along their body to mobilize anchorage forces and push their bodies forward [Gans, 1973; Elder, 1980; Dorgan, 2018]. The main benefit of the peristaltic motions is that the circular expansion of worm body reduces the penetration resistance by inducing soil stress relaxation ahead of the worm head in non-cohesive soils [Dorgan, 2018] and producing cracks and softening in cohesive soils [Trueman, 1968b; Dorgan et al., 2007]. Bivalves, such as razor clams, use a 'dual anchor mechanism' consisting of cycles of expansion-contraction-penetration motions of their back (i.e. shell) and terminal (i.e. pedal or foot) anchors. The shell is initially expanded to form an anchor to provide reaction for the foot to penetrate further into the soil. During retraction, the foot is expanded and the shell is contracted and moved forward. The dual anchor strategy has a similar advantage as the peristalsis strategy leading to a reduction in the penetration resistance due to the expansion of a body part near the animal tip. Since the bivalves usually inhabit near seashore or river banks, the shell and foot expansion could also lead to liquefaction of the saturated (or partially saturated) soils [Trueman, 1968a; Dorgan, 2015].

Plant roots are capable of penetrating different types of soils, from soft clays to dense sands and overconsolidated clays. Many roots use radial tip growth or circumnutative motion as the strategy to penetrate soils. The mechanisms of radial tip growth is similar to the aforementioned animals' strategies. When the soil surrounding the root tip exert a stress in excess of its physiological limit on the plant cells, the axial root elongation is inhibited and the root meristematic region grows radially [Bengough and Mullins, 1990; Jacobsen et al., 2021]. The advantages of this radial growth strategy was examined by Abdalla et al. [1969]; Kirby and Bengough [2002]; Savioli et al. [2014], which showed that the root thickening helps reduce the effective stress ahead of the root tip and enables tip advancement in the weakened zone. The circumnutation strategy consists of a is pattern of helical movement of the root tip during root growth. Previous studies proposed that circumnutation motion facilitates soil penetration by avoiding obstacles [Darwin et al., 1883; Inoue et al., 1999; Taylor et al., 2021], while other studies showed that circumnutation motion helps reduce penetration resistance and improve the energetic efficiency [Del Dottore et al., 2016, 2017].

1.2 Research Scope and Organization

This dissertation investigates the geomechanical processes involved in the soil penetration processes of probes that use two bio-inspired strategies. These bio-inspired soil penetration processes are simulated using discrete element modeling (DEM) method with the software used PFC 3D Version 5.0 (Itasca, Minneapolis, MN). The DEM model consists of a cylindrical virtual calibration chamber, bio-inspired probe and granular soil particles, where the chamber and probe are modeled by rigid walls. The soil particles are simulated as spheres and their interaction is modeled using the linear contact model with rolling resistance [Ai et al., 2011; Wensrich and Katterfeld, 2012].

This dissertation consists of two parts which are organized into seven chapters. The first part of this dissertation investigates the anchor-tip strategy, which includes Chapter 2-5. The second part investigates the circumnutation inspired motion, which is presented in Chapter 6.

Chapter 2 simulates one cycle of the self-penetration process of a bio-inspired probe with single anchor in a medium-dense confined soil specimen. Self-penetration is defined as the ability of a probe to generate enough anchorage forces to overcome the soil penetration resistance and advance the probe tip to greater depths. The probe tip and the anchor are displaced using a velocity-controlled loading algorithm with force limits. The global scale responses, such as probe forces and displacements, are measured and analyzed through the penetration process. The effects of the probe geometry, anchor friction coefficient, and overburden stress on the probe's self-penetration ability are examined.

Chapter 3 investigates the meso-scale responses during the self-penetration process simulated in Chapter 2. Soil stress, strain and particle contact force chains are analyzed to explore the soil responses. The soil stress states and stress paths are investigated to shed light on the interactions between the particles and the probe and between the probe tip and anchor. The effects of anchor length and the distance between the anchor and tip on the penetration process are evaluated.

Chapter 4 explores the improvement of the anchor capacity and probe's penetration ability by using two anchors. The effects of anchor configurations (i.e. anchor spacing, anchor location, and anchor expansion magnitude) on the capacity of both anchors are investigated. In a space that is defined by three anchor configuration parameters, a critical plane that separates the probe configurations that achieved self-penetration from those failed is identified. Both displacement-controlled and force-limited motions are examined.

Chapter 5 simulates multiple cycles of self-penetration processes of a probe with a single anchor in shallow (i.e. unconfined) soil specimens. The anchor and the tip are controlled using a force-controlled loading algorithm. The effects of soil density on the self-penetration process are examined.

Chapter 6 investigates the soil penetration process of a probe that uses a root circumnutation inspired motion in a shallow (i.e. unconfined) soil specimen. The effects of the angular velocity, vertical velocity and probe tip geometry on the generated penetration force, torque, and mechanical work are explored. The performance of probes that use direct-push penetration (CPT penetration), rotational penetration, and circumnutation inspired penetration are compared. Soil particle contact orientations are also analyzed to show the functional mechanism behind the circumnutation inspired motion.

Chapter 7 summarizes the main conclusions of this dissertation and provides recommendations for future work on this topic.

Chapter 2

Modeling the Self-Penetration Process of a Bio-Inspired Probe in Granular Soils

---

This chapter was published in Bioinspiration & Biomimetics under the following citation and is presented here with minor edits.
Chen Y, Khosravi A, Martinez A, DeJong J (2021) Modeling the self–penetration process of a bio–inspired probe in granular soils. Bioinspiration & Biomimetics, 16(4) 046012. DOI link.

2.1 Abstract

Soil penetration is an energy-intensive process that is common in both nature and civil infrastructure applications. Many human construction activities involve soil penetration that is typically accomplished through impact-driving, pushing against a reaction mass, excavating, or vibrating using large equipment. This study presents a numerical investigation on the self-penetration process of a probe that uses an 'anchor–tip' burrowing strategy with the goal of extending the mechanics-based understanding of burrower–soil interactions at the physical dimensions and stress levels relevant for civil infrastructure applications. Self-penetration is defined here as the ability of a probe to generate enough anchorage forces to overcome the soil penetration resistance and advance the probe tip

to greater depths. Discrete element modeling (DEM) simulations are employed to understand the self-penetration process of an idealized probe in non-cohesive soil along with the interactions between the probe's anchor and tip. Results indicate that self-penetration conditions improve with simulated soil depth and favorable probe configurations for self-penetration include shorter anchor–tip distances, anchors with greater length and expansion magnitudes, and anchors with a greater friction coefficient. The results shed light on the scaling of burrowing forces across a range of soil depths relevant to civil infrastructure applications and provide design guidance for future self-penetrating probes.

2.2 Introduction

Many aspects of civil infrastructure rely on soil penetration processes. From characterization of soil engineering properties at project sites required for engineering design to selection of equipment for construction activities such as installation of foundations and tunneling, soil penetration is ubiquitous in the fields of geotechnical and civil engineering. Soil penetration is typically accomplished by impact loading (e.g. pile driving), pseudo-static loading (e.g. pile jacking, CPT penetration), excavation (e.g. tunneling, borehole excavation), or vibration (e.g. sonic excavators). It is an energy-intensive process in all cases, typically requiring large equipment such as cranes, driving hammers, drill rigs, and excavators (Figure 2.1). The use of such equipment is responsible for a significant portion of the environmental impacts of construction activities (e.g. Raymond et al. [2020]; Purdy et al. [2020]).

Challenges associated with soil penetration are also encountered by many animals and plants; they have developed a range of adaptations to burrow in soils of different types (e.g. clays, silts, sands) and in varying environmental conditions (e.g. moisture, depth) [Dorgan, 2015]. Previous research has provided insight into the strategies that marine and earth worms, plant roots, and razor clams use to burrow (Figure 2.1). Animals such as the polychaete Armandia brevis [Dorgan et al., 2013], oligochaete Lumbriculus variegatus [Kudrolli and Ramirez, 2019], sandfish lizard [Maladen et al., 2009], and sand lance [Gidmark et al., 2011] have been observed to burrow using undulatory body motions.

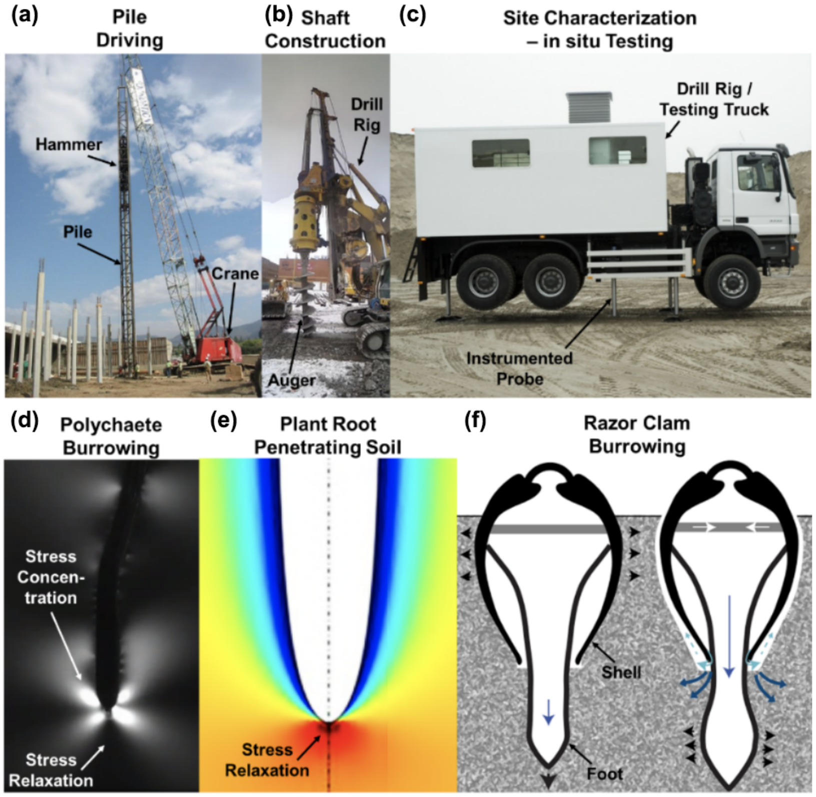

Figure 2.1: Soil penetration in civil engineering applications and living organisms: (a) pile driving uses impact loading applied by a hammer, (b) borehole excavation uses a combination of shear and normal forces, (c) in-situ testing uses the dead mass of a drill rig to overcome the penetration resistance, (d) polychaete in photoelastic gel showing zones with stress concentration and relaxation (after Dorgan et al. [2007]), (e) results of finite element simulation of plant growth showing stress relaxation in warmer colors (after Savioli et al. [2014]), and (f) schematic of 'dual anchor' strategy employed by razor clam (after Trueman [1968a] and Dorgan [2015]).

This mode of locomotion has been associated with burrowing at shallow depths (i.e. less than 10 cm) and in unconsolidated soils. At greater depths, different marine worms and clams employ peristalsis or the 'dual anchor' strategy. These strategies broadly consist of sequences of radial expansion and longitudinal elongation, where the former is used to generate anchorage forces to overcome the penetration resistance at the burrow tip [Trueman, 1968c; Dorgan, 2018]. Radial expansion of a body segment located near the burrow tip has been shown to aid in the burrowing process by altering the state of stresses in the surrounding soil (Figure 2.1). In cohesive soils (i.e. clays), this radial expansion can create fractures and produce deformation-induced softening ahead of the tip [Trueman, 1968d; Abdalla et al., 1969; Greacen and Oh, 1972; Dorgan et al., 2005, 2007], whereas in non-cohesive soils (i.e. sands), it can result in relaxation of the soil effective stresses ahead of the burrow tip [Shin and Santamarina, 2011; Khosravi et al., 2018]. Other strategies for soil penetration have been reported for polychaetes and razor clams, including movement of mouth parts to shear the soil and fluid injection to soften the soil and reduce frictional drag [Trueman, 1968b; Murphy and Dorgan, 2011; Dorgan, 2015].

Researchers have performed experimental and numerical investigations to study bio-inspired burrowing strategies with the aim of extending the findings to engineering applications. Penetration tests of plant root-inspired robots showed that penetrating by developing additive structures near the tip (i.e. tip growth) can reduce the penetration force and energy consumption in comparison to directly pushing the entire robot through the soil [Sadeghi et al., 2014; Naclerio et al., 2018]. Experimental and numerical tests on probes and robots inspired by polychaetes and clams showed that radial body expansion can facilitate penetration into soil by reducing the penetration resistance [Khosravi et al., 2018; Cortes and John, 2018; Ortiz et al., 2019; Ma et al., 2020; Huang and Tao, 2020] while cyclical inflation and deflation of a buried soft robot can facilitate burrowing out of soil [Tao et al., 2020; Huang and Tao, 2020]. These studies, however, have focused on scales relevant to the biological systems being studied (typically, dimensions and depths smaller than 20 cm).

This study presents a numerical investigation on the self-penetration process of an idealized probe that uses an 'anchor–tip' burrowing strategy with the goal of extending the mechanics-based understanding of burrower–soil interactions at the physical dimensions and stress levels relevant for civil infrastructure applications. Self-penetration is defined here as the ability of a probe to generate enough anchorage forces to overcome the soil penetration resistance and advance the probe tip to greater depths. Discrete element modeling (DEM) simulations are used to evaluate the self-penetration ability of the probe in non-cohesive soils (i.e. sands and gravels) subjected to overburden stresses of 5 to 400 kPa (equivalent to depths of 0.5 to 40 m). The anchor–tip strategy consists of radial expansion of a portion of the probe (i.e. anchor) and subsequent displacement of the tip and the anchor in opposite directions using velocity-controlled algorithm with force limits (referred to as force-limited algorithm). This investigation focuses on non-cohesive (i.e. granular) soils as previous research has shown that they present greater challenges for self-penetration than clayey soils [Martinez et al., 2020]. DEM simulations are used to evaluate the effect of the probe geometry (i.e. anchor length L, anchor–tip distance H, anchor expansion magnitude EM, and anchor friction coefficient f_{anchor}) and soil depth on the self-penetration ability of the idealized bio-inspired probe.

2.3 Modeling and Parameters

2.3.1 Model Configuration and Parameters

Discrete element modeling (DEM) simulates the interactions between individual particles within a granular assembly and between particles and other objects, such as boundaries or inclusions [Cundall and Strack, 1979]. These interactions are simulated based on specific contact models (e.g. linear, Hertz, bonded) and the particle kinematics are determined through solution of Newton's second law. Thus, DEM can properly capture many of the behaviors of granular materials, such as shear strength–dilatancy, pressure and density dependency, jamming, and flow, because these behaviors are controlled by individual particle interactions [Santamarina et al., 2001; O'Sullivan, 2011].

The DEM simulations performed in this study used the PFC 5.0 3D software developed by Itasca (Minneapolis, MN). The model consists of a cylindrical virtual calibration chamber with a height ($H_{chamber}$) of 1.2 m and a diameter ($D_{chamber}$) of 0.7 m, shown in Figure 2.2. The chamber has one top, one bottom, and 14 radial ring boundaries. The diameter of the 14 ring boundaries can change independently from each other to maintain a uniform distribution of radial stresses along the chamber height (Figure 2.3a and b). The top and radial boundaries apply constant pressure boundary conditions to the specimen contained within to apply a horizontal to vertical effective stress ratio ($K_0 = \sigma'_r/\sigma'_r$) of 0.5, which is typical of normally-consolidated sandy soils (e.g. of Sciences Engineering et al. [2019]). The size of the particles can be upscaled in DEM modeling to reduce the computational cost, as done previously by other authors [Belheine et al., 2009; Zhao and Evans, 2009]. In this study, the granular assembly is simulated by 210,000 spherical particles with a mean particle size (D_{50}) of 14.4 mm. Figure 2.2b shows the particle size distribution of the simulated soil. All the specimens tested in simulations have an initial density of 1,646.3 kg/m^3, a void ratio of 0.61, and a porosity of 0.38.

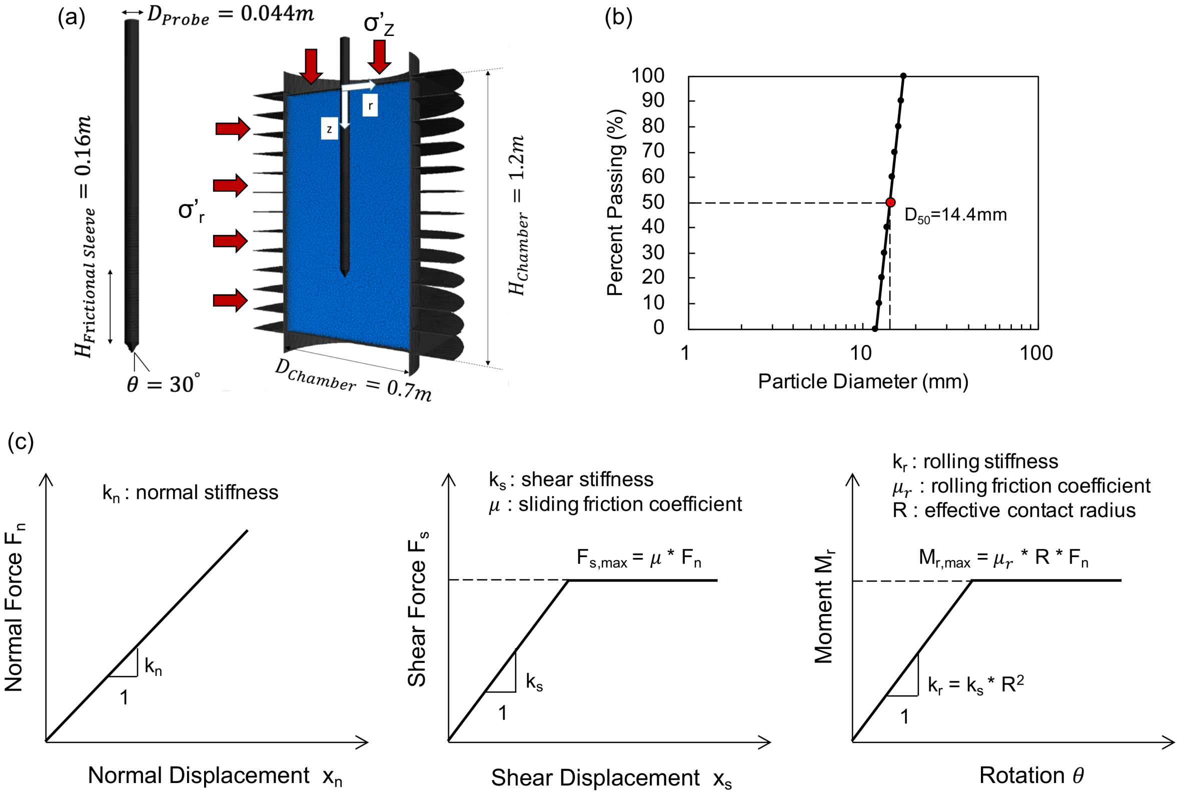

Figure 2.2: DEM Model. (a) Simulated probe and calibration chamber, (b) simulated particle size distribution, and (c) schematics of contact model relationships for normal force, shear force, and moment. R is the particle radius and θ is the half-apex angle.

Spherical particles were used for all the DEM simulations. The interactions between the particles and between the particles and probe were modeled using the linear contact model with rolling resistance, which reproduces the mechanical behavior of assemblies composed of sub-rounded to sub-angular particles [Ai et al., 2011; Wensrich and Katterfeld, 2012]. The linear contact model with rolling resistance simulates the inter-particle normal contact response with a constant-stiffness spring (k_n) and the shear and moment responses with constant stiffness springs (k_s and k_r) and sliders (μ_s and μ_r). Dashpots are

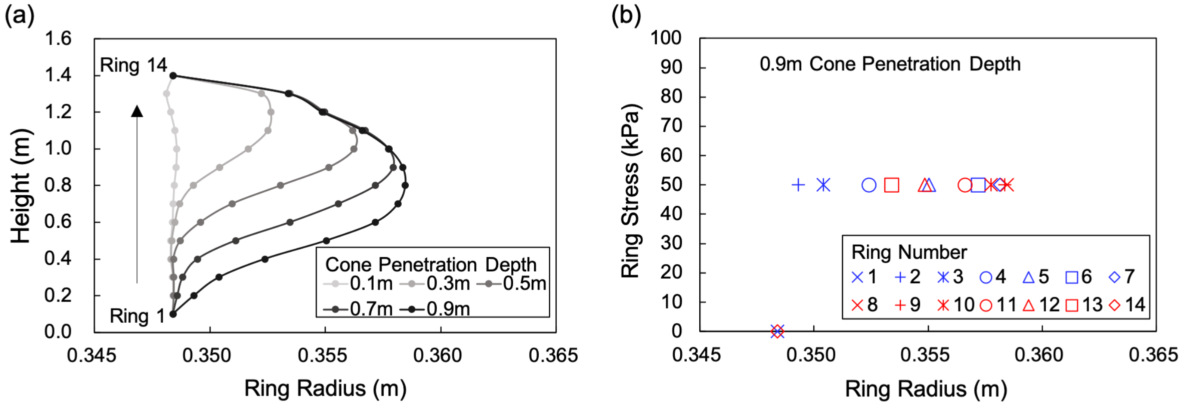

Figure 2.3: Distribution of chamber radius (a) along the chamber height during cone penetration and chamber stresses of (b) at 0.9 m cone penetration depth. Note that Ring 1 and Ring 14 are not activated so they are not shown in (b).

included for viscous energy dissipation [Chen et al., 2020] and local damping is included only during sample preparation. Figure 2.2c provides schematics of selected mechanical components of the contact model. Table 2.1 presents the modeling parameters used in this study, which were calibrated by Kuei et al. [2020] to model the behavior of coarse-grained cohesionless soil under triaxial compression conditions. The simulated probe is

Table 2.1: DEM simulation parameters.

Input Parameter	Symbol	Value
Normal Stiffness to Particle Diameter (N/m^2)	k_n/d	1.0E+08
Normal to Shear Stiffness Ratio	k_n/k_s	1.5
Sliding Friction Coefficient	μ	0.4
Rolling Friction Coefficient	μ_{rr}	0.4
Ball-wall Friction Coefficient	μ'	0.1
Particle Density (kg/m^3)	G_s	2650

modeled with wall elements in PFC. It is composed of a cylindrical shaft with an initial diameter (D_{probe}) of 0.044 m and a tip with an apex angle of 60° (half apex angle, θ, of 30°). This configuration is equivalent to that of Cone Penetration Testing (CPT) probes used to estimate soil engineering properties in the field [Lunne et al., 2002; ASTM, 2012]. The vertical component of the total contact force between the particles and the probe tip are used to calculate the tip penetration resistance (q_c, units of pressure) while the shear forces along the bottom 0.16 m of the shaft are used to calculate the sleeve friction stress (f_s, units of pressure), as follows:

$$q_c = \frac{4\sum_{i=1}^{N} Q_{ztip,i}}{\pi D_{probe}^2} \tag{2.1}$$

$$f_s = \frac{\sum_{i=1}^{N} Q_{zsleeve,i}}{0.16\pi D_{probe}} \tag{2.2}$$

where $Q_{ztip,i}$ is the vertical component of the contact force i acting on the probe tip, $Q_{zsleeve,i}$ is the vertical component of the contact force i acting on the probe shaft, and N is the total number of contacts vertical force acting on the tip or sleeve.

Suitable relative dimensions of the chamber, probe, and particles are important for reproducing field conditions, reducing boundary effects, and maintaining computational efficiency in DEM simulations Khosravi et al. [2020]. In this investigation, the chamber diameter to probe diameter ratio ($D_{chamber}/D_{probe}$) is 15.9 and the probe diameter to particle size ratio (D_{probe}/D_{50}) is 3.1. These dimensions were chosen based on results from Khosravi et al. [2020] who showed that this model configuration provides trends between penetration resistance and parameters such as assembly density, overburden stress, and other calibration parameters that are in agreement with measurements and trends from experimental and field tests. The $D_{chamber}/D_{probe}$ and D_{probe}/D_{50} ratios used in this investigation are in agreement with those used by previous probe penetration studies in 3D DEM simulation, as summarized in Table 2.2. For instance, Ciantia et al. [2016]; Zhang et al. [2019]; Arroyo et al. [2011] used $D_{chamber}/D_{probe}$ ratios of 10.5, 15, and 16.6, respectively, and D_{probe}/D_{50} ratios of 3.3, 3.1, and 2.7, respectively.

2.3.2 Simulation Sequence

The idealized probe employs a simplified 'anchor–tip' strategy for self-penetration. Each simulation consists of the following three stages: cone penetration (CP), anchor expansion (AE), and self-penetration (SP) (Figure 2.4b). During CP, the probe penetrates at a rate of 0.02 m/s to a target depth of 0.9 m within the chamber while the penetration resistance and friction against the shaft behind the tip are measured according to 2.1

Table 2.2: Comparison of relative sizes of probe penetration DEM simulations.

Study	Chamber Diameter, $D_{chamber}$ (mm)	Probe Diameter, D_{probe} (mm)	Mean Particle Size, D_{50} (mm)	$D_{chamber}/D_{probe}$	D_{probe}/D_{50}
Huang and Ma [1994] (2D)	80	5.0	0.8	16.0	6.3
Calvetti and Nova [2005] (2D)	1200	100.0	13.5	12.0	7.4
Arroyo et al. [2011] (3D)	1200	72.1	26.5	16.6	2.7
Lin and Wu [2012] (3D)[1]	20	2.0-0.5	0.167	40-10	3-12
McDowell et al. [2012] (3D)[1,2]	300	18.0	2.0	16.7	9.0
Butlanska et al. [2014] (3D)	1200	72.1	26.5	16.6	2.7
Jiang et al. [2006][3]	5000	160.0	7.6	31.3	21.1
Zhang and Evans [2018] (3D)	12	1.0	0.172	12.0	5.8
Ciantia et al. [2016] (3D)	760	72.1	22.0	10.5	3.3
Zeng and Chen [2016] (3D)	40	2.75	2.0	14.5	1.4
Sadek et al. [2017] (3D)	150	25.0	5.0	6.0	5.0
Zhang et al. [2019] (3D)	760	50.8	16.6	15.0	3.1
Ciantia et al. [2019a] (3D)	432	36.0	8.19	12.0	4.4
This Study (3D)	700	44.0	14.4	15.9	3.1

[1] Used axisymmetry to reduce model size, [2] Employed the particle refinement method, [3] Investigated inclined CPT soundings

and 2.2. Subsequently, during the AE stage, an anchor with a length L positioned at a distance H behind the tip (Figure 2.4a) is expanded radially at a rate of 0.2% per second of initial radius to the target expansion magnitude ($EM = D_{anchor}/D_{probe}-1$) while the radial anchor pressure (P_a) and bearing anchor pressure (P_b) are recorded (Figure 2.4b). During the last simulation stage, SP, the tip is loaded downward and the anchor is loaded upward using a force limited algorithm (Figure 2.5). Throughout the analyses, a convention is adopted such that downward displacement is positive and upward displacement is as negative. A cylindrical wall with a diameter equal to D_{probe} is added between the anchor and the tip to avoid particles from getting inside the probe during this stage. The algorithm for force-limited motion assigns a constant velocity V to the tip or anchor until a target force (F_{target}) is reached. This algorithm is ran independently for the probe sections such that the tip or anchor continue to displace at a rate of V until the force on each section reaches a magnitude equal to F_{target}. Once both the tip and anchor reach F_{target}, the F_{target} value is increased by a constant increment ΔF and the process is repeated. The SP stage is completed once the anchor is displaced upward for 0.04 m or the tip is displaced downward for 0.14m. Force-limited motion is used because it better models the actuation of construction equipment which is often powered by hydraulic pressure. Force-limited motion may also better capture the mechanical constraints of animals and plants, whose motions are limited by muscular capacity and internal pressure limits (e.g. Whiteley et al. [1981]; Bengough and Mullins [1990]; McKenzie and Dexter [1988]; Ruiz et al. [2015]).

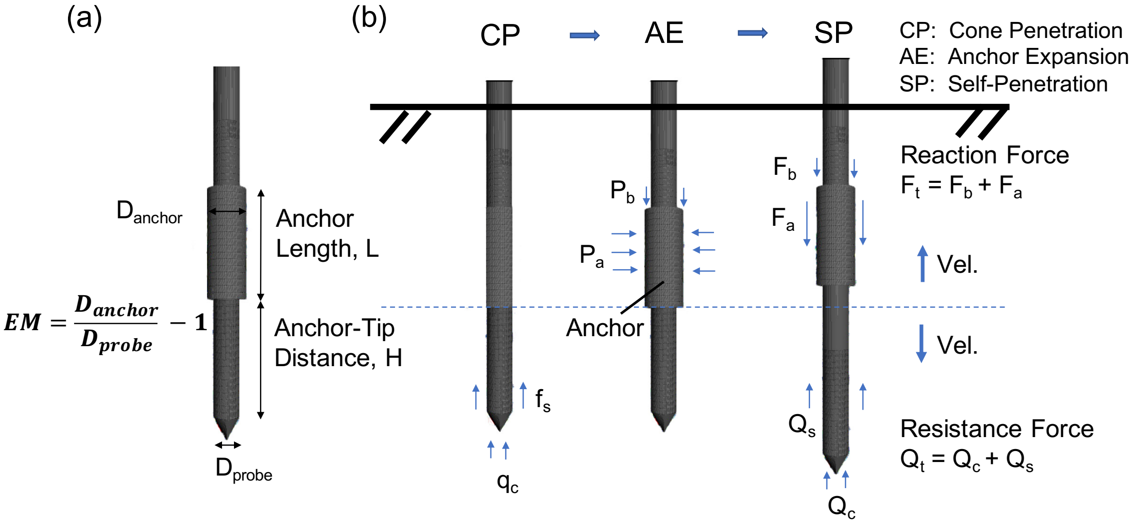

Figure 2.4: (a) Probe geometrical parameters and (b) schematic of simulation stages. The arrows acting against the probe represent soil forces. Note that the motion of the probe's tip and anchor is velocity-controlled.

During the SP process, the component reaction forces (anchor friction force F_a and anchor bearing force F_b, Figure 2.4b) are measured and summed to determine the total reaction force F_t ($F_t = F_a + F_b$). The component reaction forces are related to the anchor pressures as follows:

$$F_a = 2\pi P_a L(1 + EM) D_{probe} f_{anchor} \tag{2.3}$$

$$F_b = \frac{\pi}{4} P_b D_{probe}^2 [(EM + 1)^2 - 1] \tag{2.4}$$

where fanchor is the friction coefficient of the anchor–soil interface and D_{anchor} can be

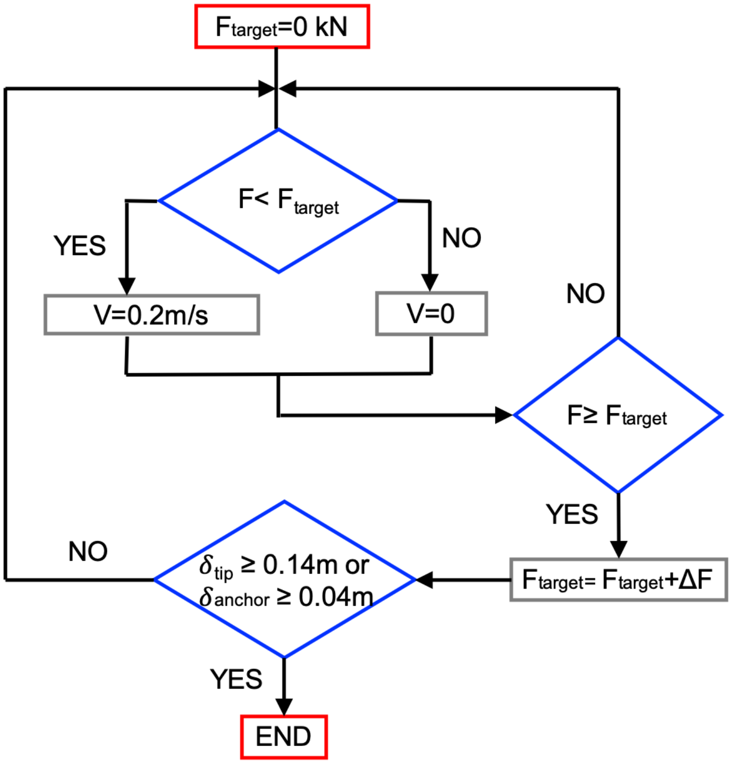

* F represents either of the total force F_t or Q_t.

Figure 2.5: Logic for velocity-controlled algorithm with force limits for the probe's tip and anchor. V is the velocity of the tip and anchor. F represents either of the total forces F_t or Q_t and the value of ΔF was taken as 50 N, which is less than 1% of F_t or Q_t in most simulations.

expressed as $D_{probe}(EM + 1)$. The component resistance forces (penetration resistance force Q_c and sleeve friction force Q_s, Figure 2.4b) are also measured and summed to determine the total resistance force Q_t ($Q_t = Q_c + Q_s$). The component resistance forces are related to the penetration resistances as follows:

$$Q_c = \frac{\pi}{4} q_c D_{probe}^2 \tag{2.5}$$

$$Q_s = \pi f_s D_{probe} \tag{2.6}$$

2.3.3 Model Validation

In this section, the behavior of the simulated soil is examined to confirm through triaxial compression and cone penetration tests to confirm that it successfully reproduces trends characteristic of coarse-grained soils at the representative elementary volume (REV) and field scales (e.g. Lee and Seed [1967]; Holtz et al. [1981]; Jamiolkowski et al. [2003]; Robertson [2016]).

Triaxial compression tests were performed at isotropic confining stresses of 5, 25, 100, and 400 kPa. The cylindrical specimens were prepared to initial void ratios of 0.61. During shearing, the specimens were loaded by increasing the vertical stress (σ'_z) while the radial stress (σ'_r) was kept constant using a servo-control algorithm. This resulted in a uniform increase in the specimen's axial strain (ϵ_z) while the radial (ϵ_r) and volumetric strains (ϵ_v) changed based on the dilatancy behavior of the specimens. The triaxial test imposes stress and strain conditions in the specimens such that the vertical direction is the major principal direction and the horizontal direction is the minor principal direction, i.e. $\sigma'_z = \sigma'_1$, $\sigma'_r = \sigma'_3$, $\epsilon_z = \epsilon_1$, $\epsilon_r = \epsilon_3$. The DEM simulations exhibit the expected trends for a dense sub-rounded granular soil (e.g. Lee and Seed [1967]; Holtz et al. [1981]): (i) the greater confining stress led to a greater deviatoric shear stress $q = \sigma'_1 - \sigma'_3$ (Figure 2.6a); (ii) the lower confining stress led to a greater rate and total amount of soil dilation (i.e. increase in volumetric strain ϵ_v, Figure 2.6b) and to a greater maximum deviatoric stress to mean effective stress ratio q/p' (where p' is the mean effective stress, $p' = (\sigma'_1 + 2\sigma'_3)/3$), Figure 2.6c); (iii) the stress ratio q/p' collapsed to a unique value at large strains but the specimens confined under lower stresses exhibited a stiffer stress ratio response (Figure 2.6c); and (iv) the stress paths converged to a unique critical state line (CSL) at the end of the TXC simulation with a slope of 1.46:1, consistent with a soil friction angle of 36.0° (Figure 2.6d) (note: see Schofield and Wroth [1968] and Wood [1990] for detailed information regarding the CSL for soils).

A second validation exercise was used to evaluate the ability of the DEM model to reproduce trends observed in the field. Cone penetration test data (i.e. penetration resistance q_c and sleeve friction f_s) is typically used to determine the stratigraphy of soil deposits and to estimate their engineering properties (Schmertmann [1978]; Baldi [1986]; Jamiolkowski et al. [2003]). The standard probe used in the field is 0.044 m in diameter, has a conical tip with a 60° apex angle and a sleeve with a length of 0.16 m behind the tip, and is advanced at a rate of 0.02 m/s. DEM simulations of CPT tests with the same

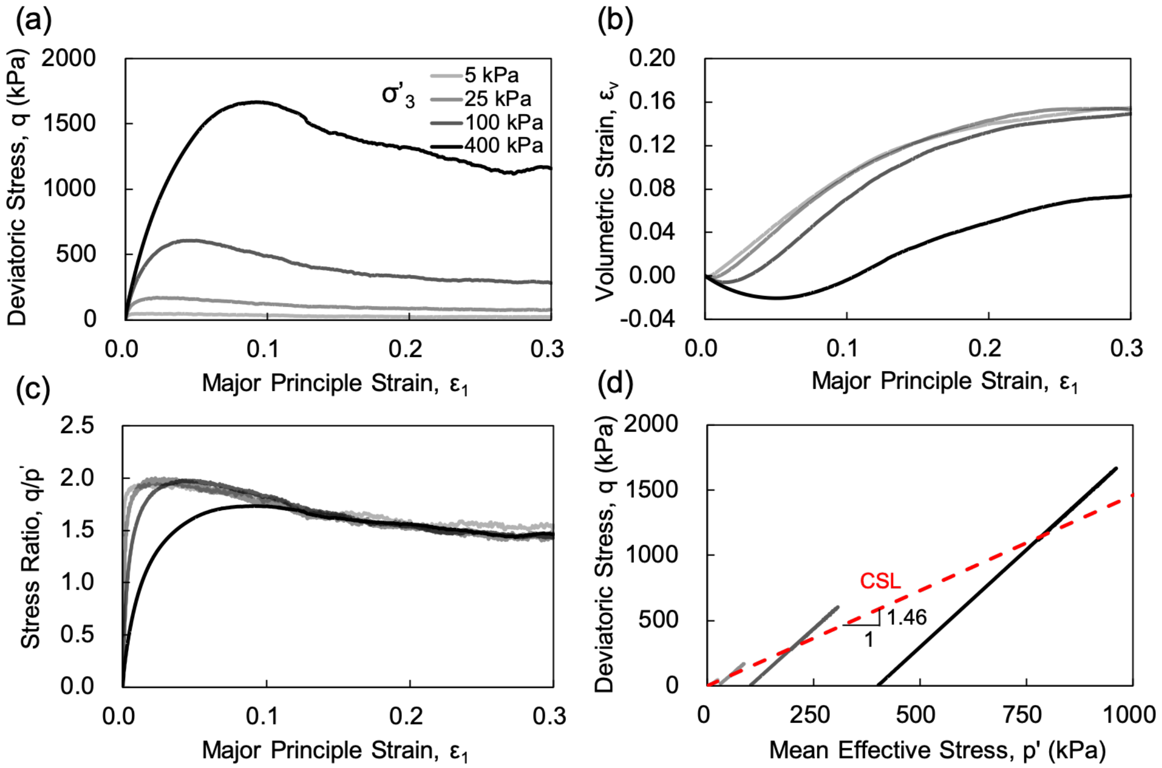

Figure 2.6: Signatures of (a) tip penetration resistance and (b) sleeve friction with depth, and (c) soil behavior type classification based on penetration resistance measurements.

features were performed on four specimens that were prepared to a void ratio of 0.61 and confined at vertical effective stresses σ'_z of 5, 25, 100, and 400 kPa with K_0 of 0.5 to simulate soil depths from 0.5 to 40 m. As expected, greater penetration resistances and friction sleeve values were measured in specimens confined at greater stresses (Figure 2.7a and b). The soil behavior type (SBT) chart is typically employed in geotechnical practice to classify soils based on normalized tip resistance and sleeve friction measurements. In this study, the SBT chart from Robertson [2016] was used to assess the simulation results (Figure 2.7c). The SD and SC classifications represent sands with dilative and contractive behavior, respectively. As expected, all simulated specimens are classified as sands, and the specimens confined under smaller stresses are classified as dilative whereas those confined under greater stresses are classified as contractive. These results indicate that the DEM simulations provide results and trends consistent with those observed in the field.

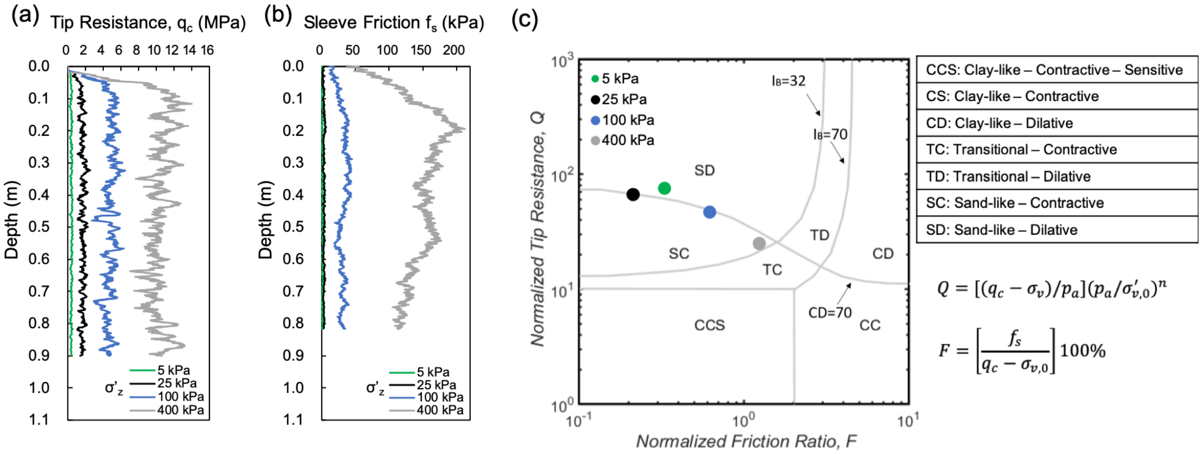

Figure 2.7: Results of triaxial compression tests at isotropic confining pressures of 5, 25, 100, and 400 kPa. Evolution of (a) deviatoric stress ($q = \sigma'_1 - \sigma'_3$), (b) volumetric strain, and (c) stress ratio (q/p') with major principal strain and (d) stress paths in the q-p'' plane. CSL is the critical state line.

2.4 Results

The CP, AE, and SP stages were modeled during a total of 17 simulations to parametrically evaluate the efficacy of the anchor–tip penetration strategy at overburden stress levels relevant for geotechnical applications (Table 2.3). Simulation #1 is the reference case which was used to investigate the evolution of the forces and displacements of the tip and anchor during the simulation sequence for a probe with anchor–tip distance (H) of 0.176 m (4 times D_{probe}), anchor length (L) of 0.176 m (equal to D_{probe}), expansion magnitude (EM) of 50%, anchor friction coefficient (f_{anchor}) of 0.3, and an overburden stress (σ'_z) of 100 kPa. Comparisons of the remaining simulations provide insight into the effects of H (Simulations #2 to #6), L (Simulations #7 to #9), EM (Simulations #10 and #11), f_{anchor} (Simulations #12 and #13), and σ'_z (Simulations #14 to #17) on the interactions between the tip and anchor and the self-penetration ability of the simulated bio-inspired probe.

2.4.1 Reference Simulation

In DEM, physical time is divided into time steps to implement a convergent integration algorithm when calculating time-related variables such as acceleration, velocity, and displacement. In order to present the evolution of simulation measurements, a normalized

Table 2.3: DEM simulation matrix.

#	Anchor Length, L	Anchor–Tip Distance, H	Expansion Magnitude, EM	Vertical Stress, σ'_z (kPa)	Anchor Friction Coefficient, f_{anchor}
1*	4 D_{probe}	4 D_{probe}	0.5	100	0.3
2	4 D_{probe}	1 D_{probe}	0.5	100	0.3
3		2 D_{probe}			
4		3 D_{probe}			
5		6 D_{probe}			
6		8 D_{probe}			
7	2 D_{probe}	4 D_{probe}	0.50	100	0.3
8	6 D_{probe}				
9	8 D_{probe}				
10	4 D_{probe}	4 D_{probe}	0.25	100	0.3
11			1.00		
12	4 D_{probe}	4 D_{probe}	0.50	100	0.1
13					0.5
14	4 D_{probe}	4 D_{probe}	0.50	5	0.3
15				25	
16				250	
17				400	

*reference simulation, D_{probe}=0.044m

timestep ($\overline{N}$) is defined as follows:

$$\overline{N} = \begin{cases} \dfrac{n}{n_1} & (n \leq n_1) \\ 1 + \dfrac{n - n_1}{n_2 - n_1} & (n_1 < n \leq n_2) \\ 2 + \dfrac{n - n_2}{n_3 - n_2} & (n_2 < n \leq n_3) \end{cases} \tag{2.7}$$

where n is the time step and n_1, n_2, and n_3 are the time steps at the end of CP, AE, and SP stages, respectively. The definition of $\overline{N}$ is such that values smaller than 1 correspond to the CP stage, values between 1 and 2 correspond to the AE stage, and values greater than 2 correspond to the SP stage. The $\overline{N}$ parameter is employed here to allow for visualization of the CP, AE, and SP stages in one single plot. While a time history of the measurements would convey similar information, the comparison of results across stages is challenged by the fact that the timestep differs between simulation stages (i.e. it is a function of the minimum eigen-period of the total system and of the particle mass and contact stiffness matrix, Cundall and Strack [1979]; Potyondy [2009]). In addition, the time duration of the CP process is significantly greater than that for the AE and SP processes due to the greater penetration distance during CP.

The tip resistances and anchor pressures from Simulation 1 as a function of $\overline{N}$ are presented in Figure 2.8a. As the probe is penetrated in the chamber during CP ($\overline{N} \in [0, 1]$), the penetration resistance increases to values that average 4.8 MPa (with variations between 3 and 6 MPa), which represents the penetration resistance exhibited by the specimen (Figure 2.8a). The tip vertical displacement increased linearly with time since probe penetration occurs at a constant rate. During AE ($\overline{N} \in [1, 2]$), the anchor is radially expanded leading to an increase in the anchor radial and end bearing pressures (P_a and P_b, respectively). The value of P_a approaches an asymptotic limiting pressure of about 780 kPa, which is referred to as the limit pressure (P_L) and is consistent with simulations using cavity expansion theory from Yu and Houlsby [1991], Salgado and Prezzi [2007], and Martinez et al. [2020] which predict limit pressure values between 600 and 1000 kPa for mildly dilatant sands with a friction angles between 30 and 36°. The penetration resistance decreases from its value of 4.8 MPa at the end of CP to a value of about 3.4 MPa at an $\overline{N}$ of 2, showing that the anchor expansion process influences the penetration resistance and suggests a change in the stresses around the probe tip, consistent with previous related experimental and numerical studies [Dorgan et al., 2007; Shin and Santamarina, 2011; Khosravi et al., 2020; Huang and Tao, 2020; Ma et al., 2020; Chen et al., 2020].

During SP ($\overline{N} \in [2, 3]$), the displacement of the anchor and tip are controlled using force-limited algorithm (Figure 2.5). The measurements shown in Figure 2.8a are presented in Figure 2.8b in terms of force components (F_a, F_b, Q_s, Q_c), total forces (F_t and Q_t), and displacement of the anchor and tip. At $\overline{N} \leq 2.5$, the anchor remained stationary while the tip moved downward. This is because the total reaction force (F_t) was greater

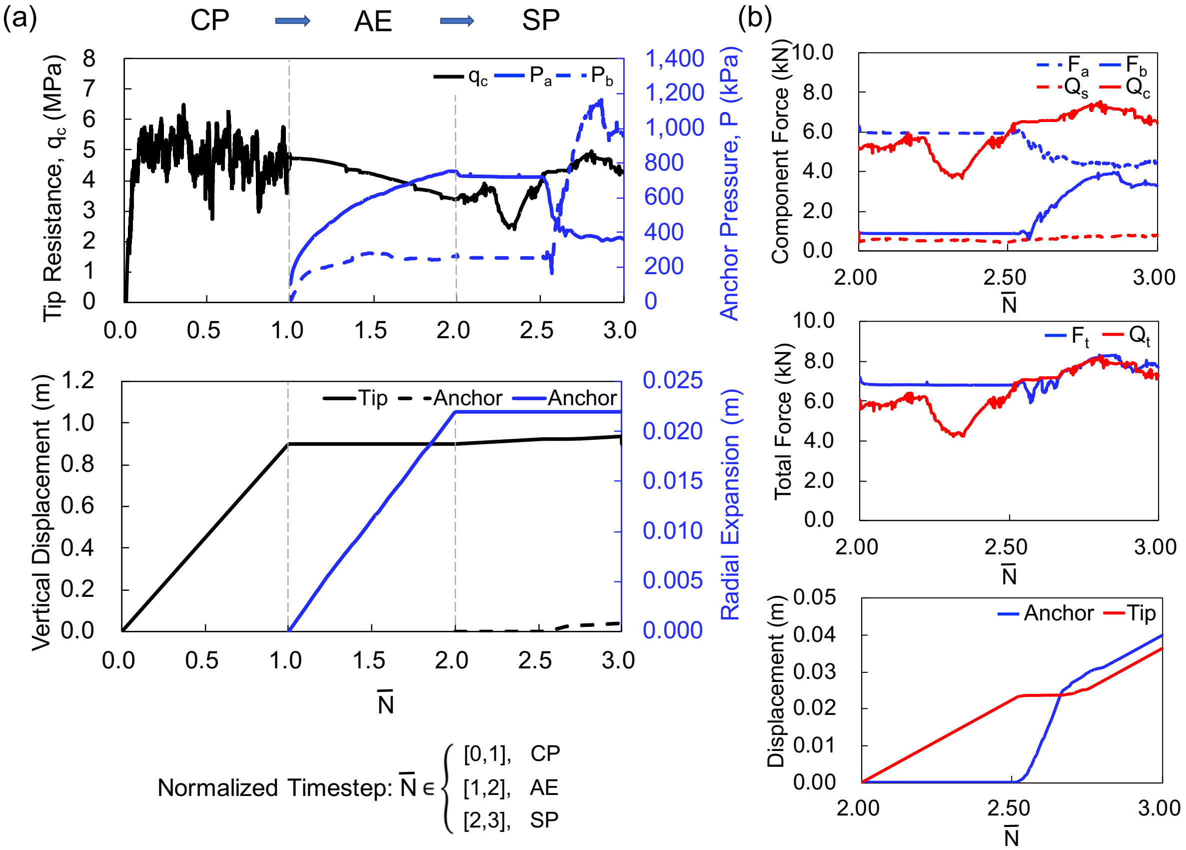

Figure 2.8: Tip and anchor pressures and displacements during CP, AE, and SP stages Simulation #1 (note: $\overline{N}$ is normalized timestep, CP takes place when $\overline{N} \in [0, 1]$, AE takes place when $\overline{N} \in [1, 2]$, SP takes place when $\overline{N} \in [2, 3]$).)

than the target force (F_{target}) while the total resistance force (Q_t) was smaller than F_{target}. Therefore, the anchor friction force component (F_a) and bearing anchor force component (F_b) remained constant. At $\overline{N}$ of about 2.5, both F_t and Q_t achieved values equal F_{target} so the F_{target} was increased by ΔF. At $2.50 < \overline{N} < 2.65$, F_{target} continued to be greater than F_t and smaller than Q_t, so the anchor moved upward while the tip remained stationary. This led to a decrease in F_a and an increase in F_b. At $\overline{N} > 2.65$, F_{target} was greater larger than F_t and Q_t, so both the tip and anchor were displaced to generate the F_{target} requirement. At the end of SP, the penetration resistance (q_c) reached an average value of 4.3 MPa. Figure 2.9 presents time histories of the force components, total forces, and displacements. As shown, the trends are similar to those shown in Figure 2.8b. In addition, the constant slope of the displacement time histories reflect the constant velocity assigned to the anchor and tip when their respective forces are smaller than F_{target}. The DEM simulations produce information regarding the interactions and kinematics of all the particles in the granular assembly. These are shown for the end of the CP, AE, and SP stages along vertical planes through the middle of the Simulation #1 specimen. Figure 2.10a shows force chain maps, where the normal contact forces between the particles and between the particles and the probe greater than 50 N are represented by lines whose thickness and color are proportional the contact force magnitude. Figure 2.10b shows particle displacement vectors where the color of the arrows is proportional to the particle displacement magnitude. During the CP stage, force chains with greater magnitudes occur near the probe tip which generate the penetration resistance. The particle displacement vectors show that the particles directly below the probe are displaced downwards and radially outward due to the compressive and shear stresses induced by the probe penetration while the particles surrounding the probe shaft are displaced downward due to the friction at the probe–particle interface. During the AE stage, large contact forces form around the anchor while the magnitude of the contact forces near the tip decreases, reflecting the decrease in q_c shown in Figure 2.8. The particles around the anchor move radially outward due to the applied compressive stress while the particles near the tip move upward due to the reduction in the compressive stress in that location. During SP, large contact forces develop near the tip as the probe is displaced downward and large contact forces are generated on the upper base of the anchor as it is displaced upward. This upward anchor displacement causes a decrease in the contact forces around it, which produces a decrease in F_a as shown in Figure 2.8b. During AE and SP, the contact forces at locations

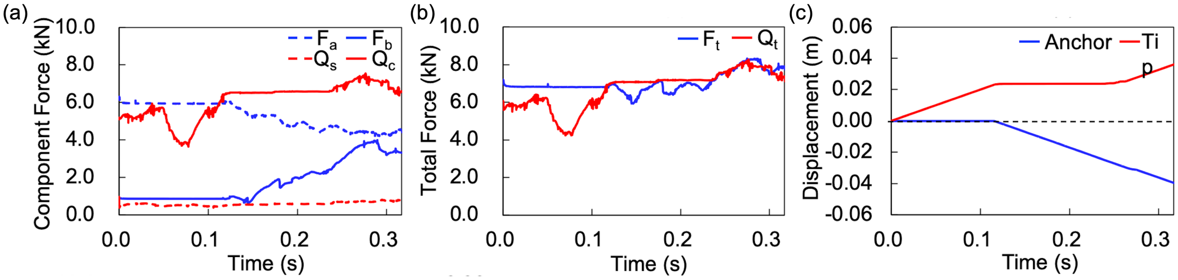

Figure 2.9: Time histories of Simulation #1 using real time recordings component forces, total forces, and displacement of probe tip and anchor during SP stage.

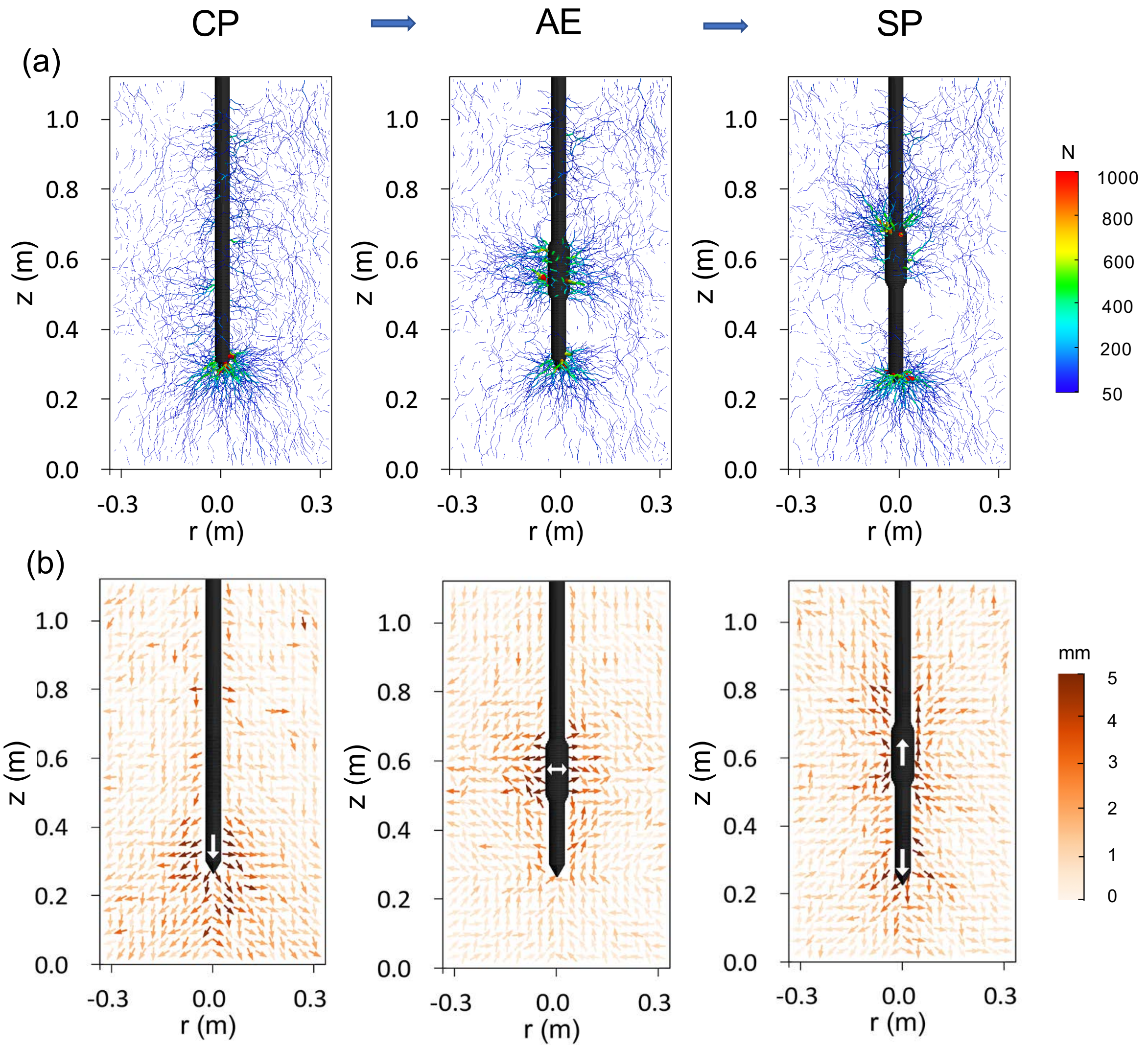

Figure 2.10: (a) Force chain map and (b) cumulative particle displacement vectors of Simulation #1 obtained at the end of CP ($\overline{N} = 1$), AE ($\overline{N} = 2$), and SP ($\overline{N} = 3$) stages. Note that force and displacement measurements taken along cross-section through the center of the specimen; in (a) the thickness and color of lines is proportional to contact force magnitude and only forces greater than 50 N are shown, in (b) the color of the arrows is proportional to the particle displacement magnitude.

between the anchor and the tip significantly decrease, as evident by the absence of force chains with magnitudes greater than 50 N. This is caused by the reduction in compressive stress that is developed as the anchor is expanded and as the anchor and tip are displaced away from each other.

2.4.2 Anchor-Tip Interactions

Changes in probe forces and stresses reveal how the anchor and tip interact with each other during the anchor expansion and self-penetration processes. Figures 2.11a-e show the effects of the anchor–tip distance (H), anchor length (L), expansion magnitude (EM), anchor friction coefficient (f_{anchor}), and overburden stress (σ'_z) on these interactions in terms of the evolution of tip resistance (q_c) and anchor radial pressure (P_a) during the AE stage, while Figures 2.12a-e and 2.13a-e show these effects in terms of the q_c and P_a magnitudes at the end of the CP, AE, and SP stages.

The distance H has an important influence on the interactions between the anchor and tip during AE. A greater decrease in q_c was observed for simulations with smaller H (Figures 2.11a and 2.12a). For instance, q_c decreased from a value of 4.5 MPa at the end of CP to 1.9 MPa at the end of AE when H was equal to D_{probe} (0.044 m). In contrast, q_c only decreased to 4.3 MPa when H was equal to 8 D_{probe} (0.352 m). The decrease in q_c is due to the changes in stresses caused by the anchor expansion process, where the interparticle forces in the soil around the anchor increase but the forces at locations ahead of the probe decrease. This phenomenon, consisting of a reduction of compressive stresses in the soil located ahead of an elongated cavity, is described by Shin and Santamarina [2011]. The authors refer to this phenomenon as an open-mode discontinuity and they show its occurrence during root and ice lens growth. In the context of the DEM simulations, the reduction of stresses that takes place around the probe tip increases as H is decreased, as shown by the changes in the force chains and particle displacement vectors around the probe tip (Figures 2.13a and b). Namely, there are fewer force chains near the tip during Simulation #2 ($H = 1D_{probe}$) than during Simulation #1 ($H = 4D_{probe}$, Figure 2.10a), and the particle displacement vectors have a greater upward magnitude during Simulation #2 (Figures 2.10b and 12a). The results in Figures 2.11a and 2.12a show that H had no significant effect on P_a, indicating that the failure of soil around the anchor is independent of this parameter.

The anchor length L also has an effect on the q_c and P_L values at the end of AE. As L was increased from 2 D_{probe}(0.088 m) to 8 D_{probe}(0.352 m), q_c decreased to lower values and lower P_L magnitudes were generated (Figures 2.11b, 2.12b, and 2.13b). The greater decrease in q_c with increasing L is due to the greater soil volume failed as the longer anchor is expanded (Figures 2.10a, 2.10b, and 2.14b). The smaller P_a values generated by the longer anchors are in agreement with other studies (e.g. Schnaid [1990]; Ajalloeian and Yu [1998]) and are associated with the shape of the soil failure zone. This trend is captured by cavity expansion theory which predicts that expanding a spherical cavity requires between 2.5 and 5.0 times greater pressure than expanding a cylindrical cavity, where the range reflects the effect of the soil strength and stiffness properties [Collins et al., 1992; Yu and Houlsby, 1991]. In this case, the shape of the failed soil zone becomes more spherical for shorter anchors and more cylindrical for longer anchors.

The effect of the remaining parameters can be summarized as follows: (i) greater EM resulted in lower q_c and greater P_a values at the end of AE (Figures 2.11c, 2.12c, and 2.13c), (ii) the f_anchor magnitude had no obvious effect on q_c and P_a (Figures 2.11d, 2.12d, and 2.13d); however, f_anchor does have an influence on the self-penetration ability of the bio-inspired probe because the anchorage friction force (F_a) is directly proportional to f_anchor (Eq.2.3), and (iii) q_c and P_a increased as the overburden stress increased (Figures 2.11e, 2.12e, and 2.13e). The influence of the overburden stress is complex since the different force components scale differently with increasing σ'_z; this is further described in the discussion section.

Figures 2.12a-e and 2.13a-e show q_c and P_a at the end of the SP stage. As shown, the q_c values returned to values close to those measured at the end of CP. This trend was observed across all the H, L, EM, f_{anchor}, and σ'_z values considered in this investigation. The tendency of q_c to be remobilized is likely detrimental for penetration efficiency and energy consumption, as it indicates that the reduction in tip resistance due to anchor expansion is lost once the tip is advanced. However, the remobilization of q_c is beneficial

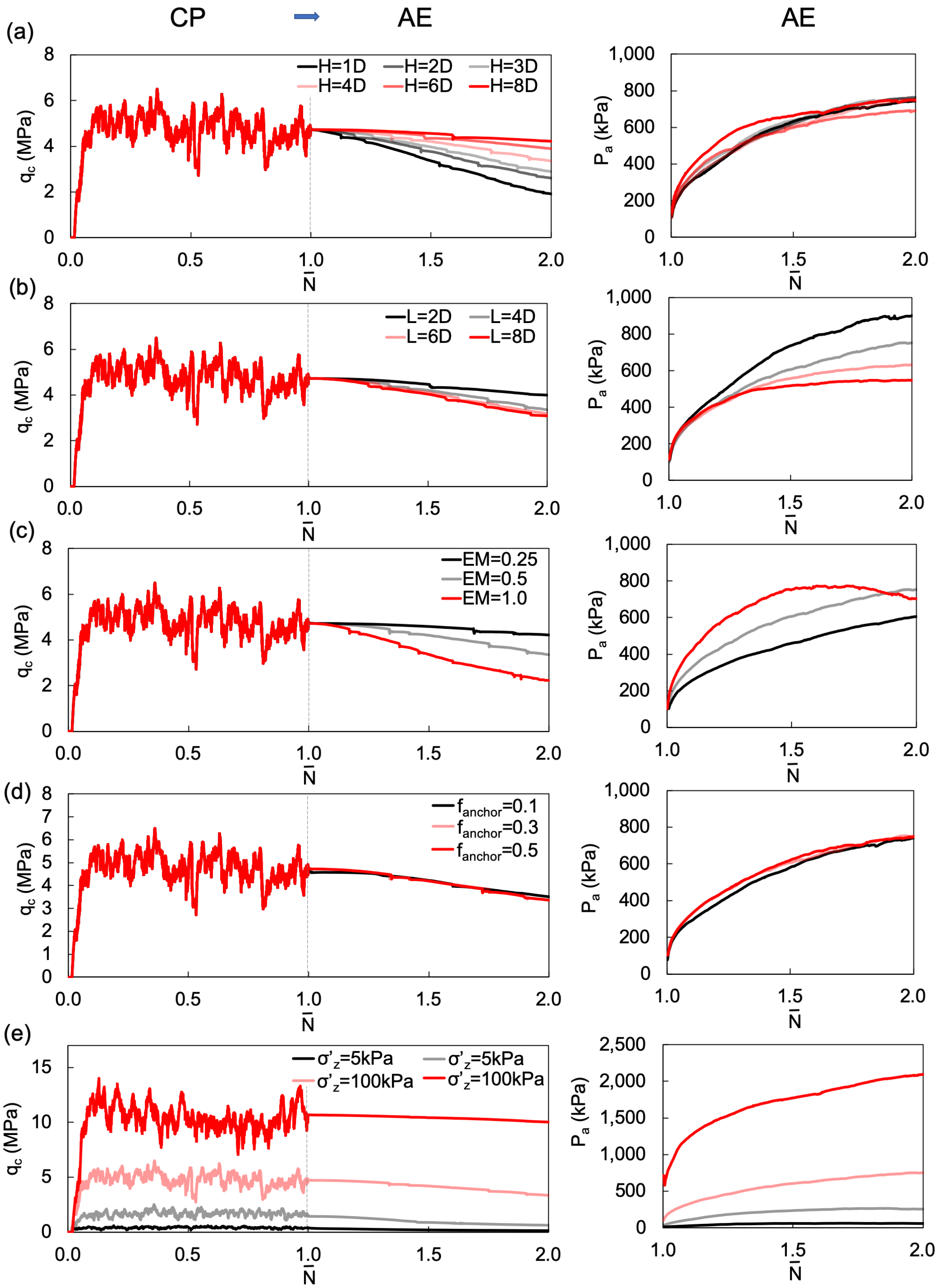

Figure 2.11: Anchor–tip interactions during AE. Effect of (a) anchor–tip distance H (Simulations #1 to 6), (b) anchor length L (Simulations #1 and #7 to 9), (c) expansion magnitude EM (Simulations #1 and #10 and #11), (d) anchor friction coefficient f_{anchor} (Simulations #1 and #12 and 13), and (e) overburden stress σ'_z (Simulations #1 and #14 to 17).

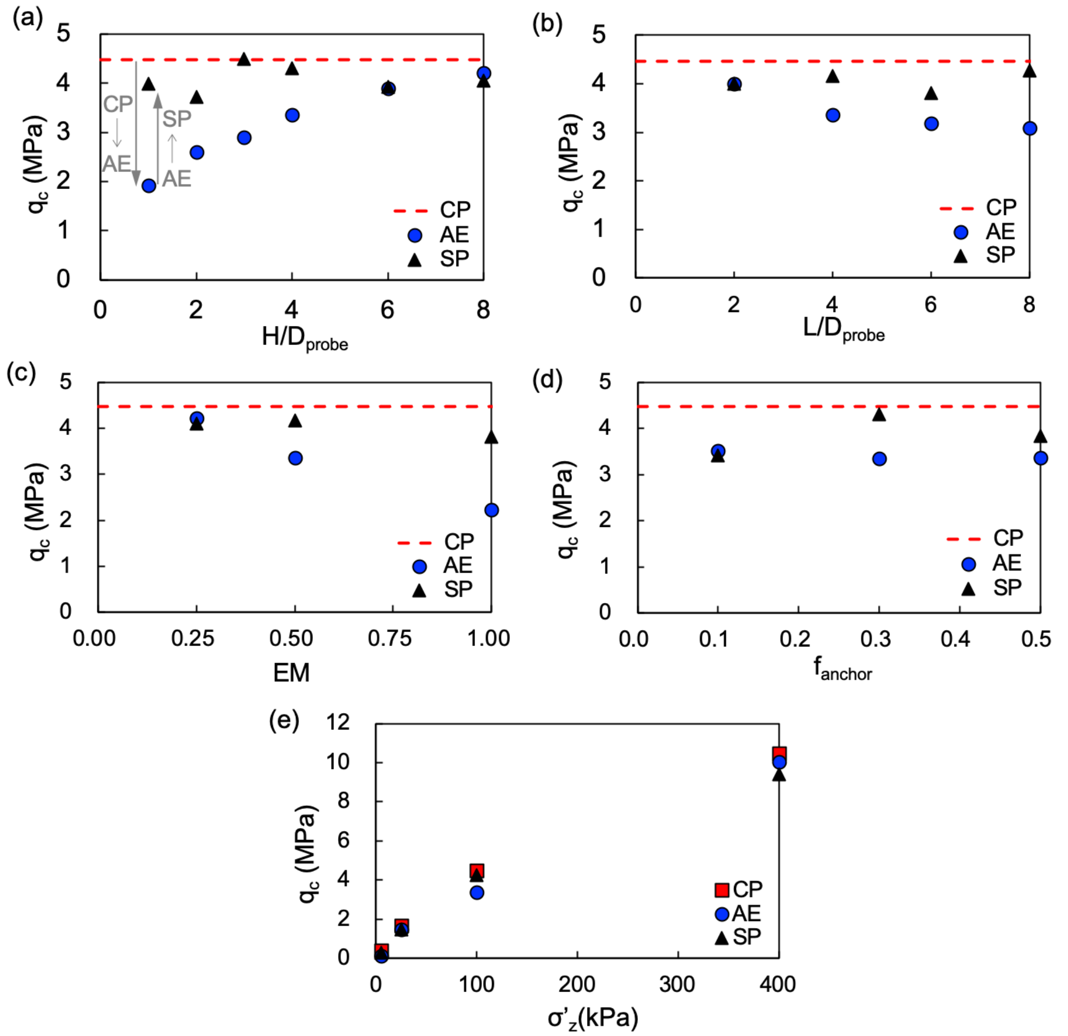

Figure 2.12: Penetration resistance at the end of the simulation stages. Effect of (a) anchor–tip distance H (Simulations #1 to 6), (b) anchor length L (Simulations #1 and #7 to 9), (c) expansion magnitude EM (Simulations #1 and #10 and 11), (d) anchor friction coefficient f_{anchor} (Simulations #1 and #12 and 13), and (e) overburden stress σ'_z (Simulations #1 and #14 to 17) (note: the q_c at the end of CP (red lines) is the average q_c from 0.7 to 0.9 m penetration depth).

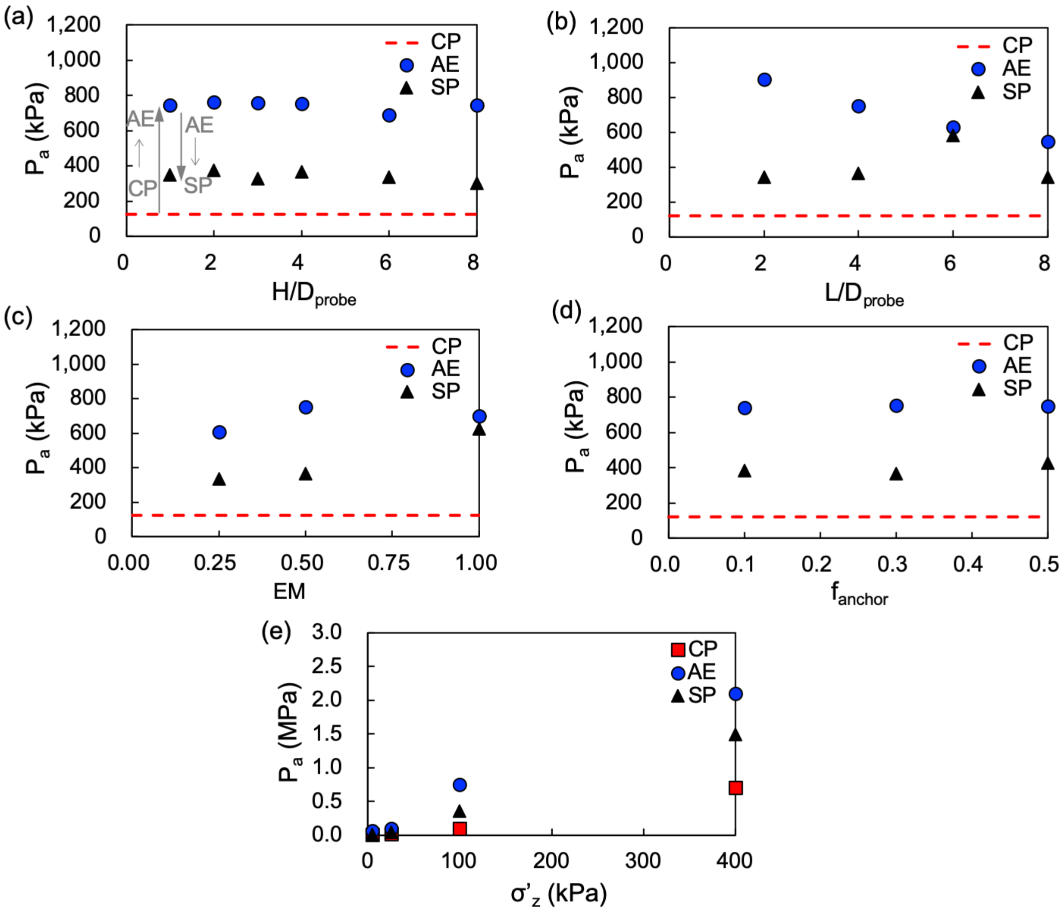

Figure 2.13: Anchor pressure at the end of the simulation stages. Effect of (a) anchor–tip distance H (Simulations #1 to 6), (b) anchor length L (Simulations #1 and #7 to 9), (c) expansion magnitude EM (Simulations #1 and #10 and 11), (d) anchor friction coefficient f_{anchor} (Simulations #1 and #12 and 13), and (e) overburden stress σ'_z (Simulations #1 and #14 to 17).

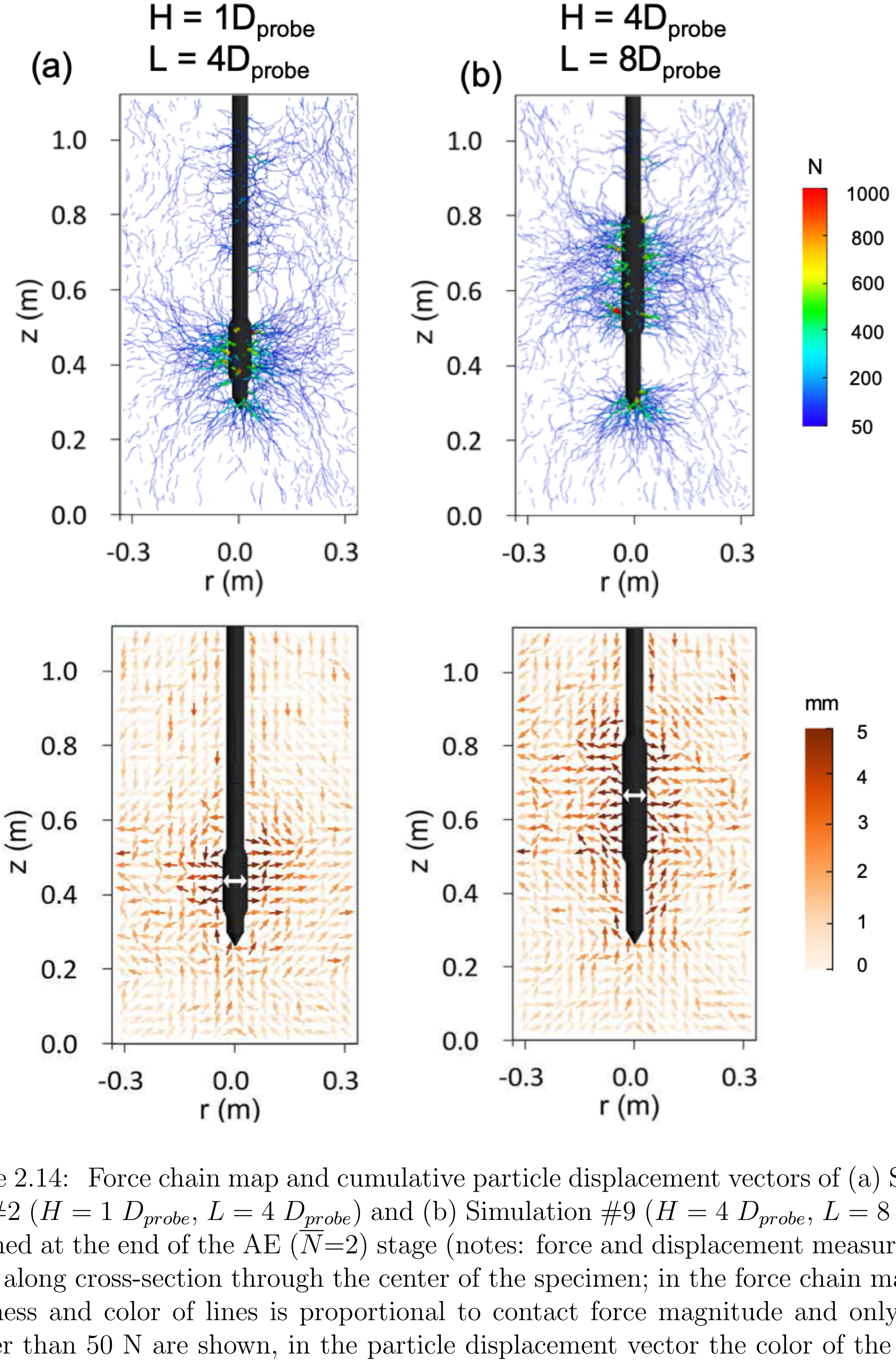

Figure 2.14: Force chain map and cumulative particle displacement vectors of (a) Simulation #2 ($H = 1\ D_{probe}$, $L = 4\ D_{probe}$) and (b) Simulation #9 ($H = 4\ D_{probe}$, $L = 8\ D_{probe}$) obtained at the end of the AE ($\overline{N}$=2) stage (notes: force and displacement measurements taken along cross-section through the center of the specimen; in the force chain maps the thickness and color of lines is proportional to contact force magnitude and only forces greater than 50 N are shown, in the particle displacement vector the color of the arrows is proportional to the particle displacement magnitude).

for geotechnical site characterization, as a fully mobilized q_c measurement during pseudo-static penetration (i.e. CP stage) is one of the most widely-adopted measurements used to estimate soil stratigraphy and engineering properties ([Lunne et al., 2002; of Sciences Engineering et al., 2019]. These results suggest that while expanding an anchor can decrease the penetration resistance, a steady q_c value can still be obtained during self-penetration.

2.4.3 Self-Penetration

The ability of a bio-inspired probe to self-penetrate in soil depends on the magnitude and evolution of the total reaction and penetration resistance forces (F_t and Q_t). During the SP stage, the anchor and the tip are displaced upward and downward, respectively, using the force-limited motion. In this manner, the probe section (i.e. the anchor or the tip) that generates forces smaller than the F_{target} is displaced. The downward tip displacement δ_{tip} is defined as positive and upward anchor displacement δ_{anchor} is defined as negative. The self-penetration displacement is defined as follow:

$$\Delta D = \delta_{tip} + \delta_{anchor} \tag{2.8}$$

The self-penetration displacement was determined to evaluate the probes' self-penetration ability since it reflects the relative magnitudes of F_t and Q_t with respect to F_{target}. A positive ΔD indicates net downward displacement (i.e. self-penetration) whereas a negative ΔD indicates that the anchor is lifted. Figures 2.15a through 2.15e show the measurements of ΔD during SP for probes with varying H, L, EM, and f_{anchor}, and under varying σ'_z levels. The self-penetration displacement ΔD increased as H was decreased (Figure 2.15a). For an L equal to 4 D_{probe} (0.176 m), self-penetration was only achieved when H is smaller than 4 D_{probe} (0.176 m). This is because a sufficient reduction in q_c is required for the reaction forces to prevail. In fact, the P_a magnitude at the end of AE, which determines the anchorage force (F_a), is shown to be independent of H (Figure2.13a); thus, the effect of H is limited to its influence on the penetration resistance during AE. Figures 2.16a and 2.16b highlight these trends, where Q_c for the probe with an H equal to D_{probe} (Simulation #2) has a lower initial value of 3.2 kN and slowly increases during self-penetration while F_a and F_b remain relatively constant. In contrast, Q_c for the

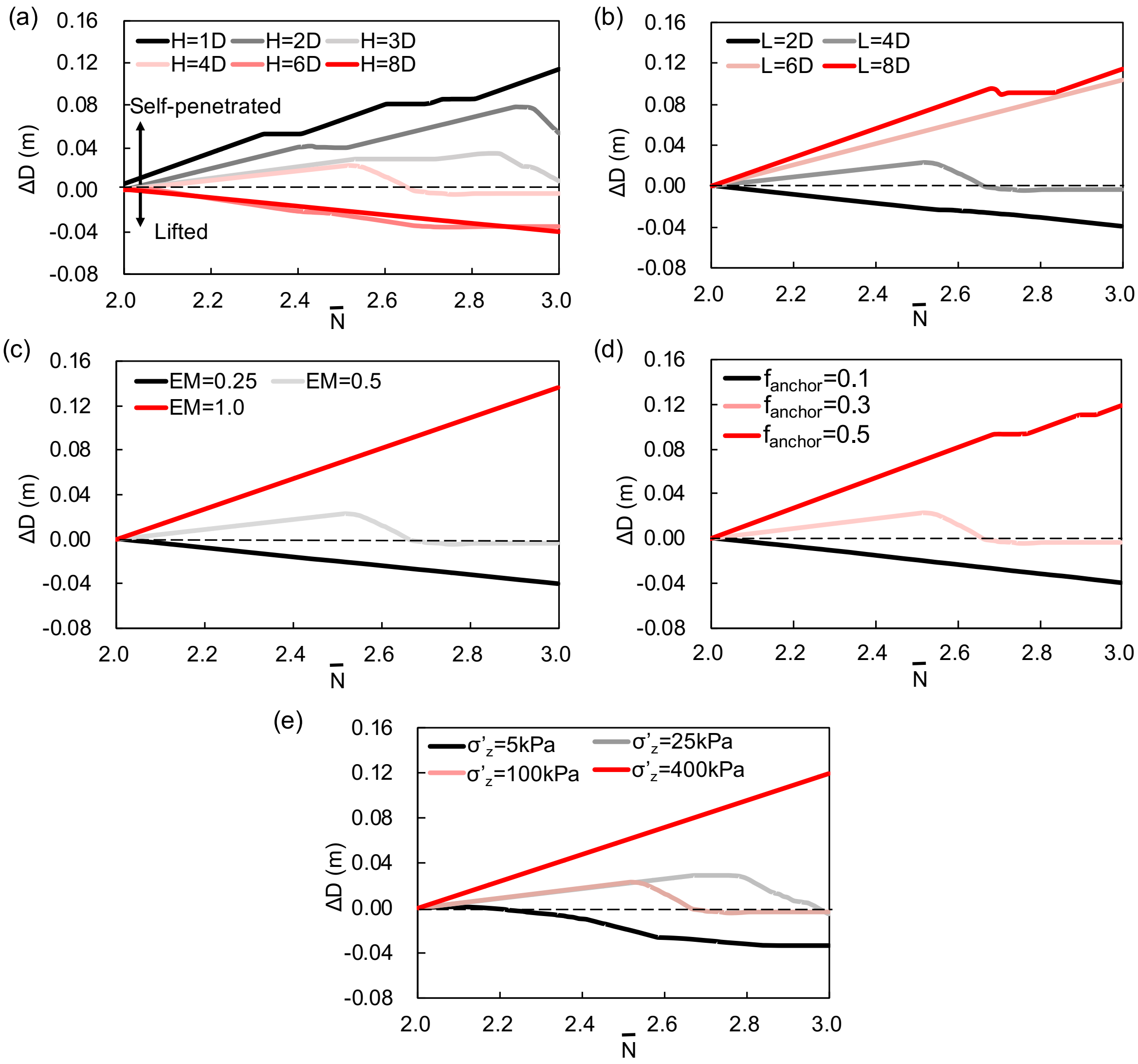

Figure 2.15: Self-penetration displacement ΔD for varying (a) anchor–tip distance H (Simulations #1 to 6), (b) anchor length L (Simulations #1 and #7 to 9), (c) expansion magnitude EM (Simulations #1 and #10 and 11), (d) anchor friction coefficient f_{anchor} (Simulations #1, #12 and, 13), and (e) overburden stress σ'_z (Simulations #14 to 17).

probe with H equal to 8 D_{probe} (Simulation #6) remains constant with a value of about 6.2 kN while F_a and F_b continue to decrease and increase, respectively.

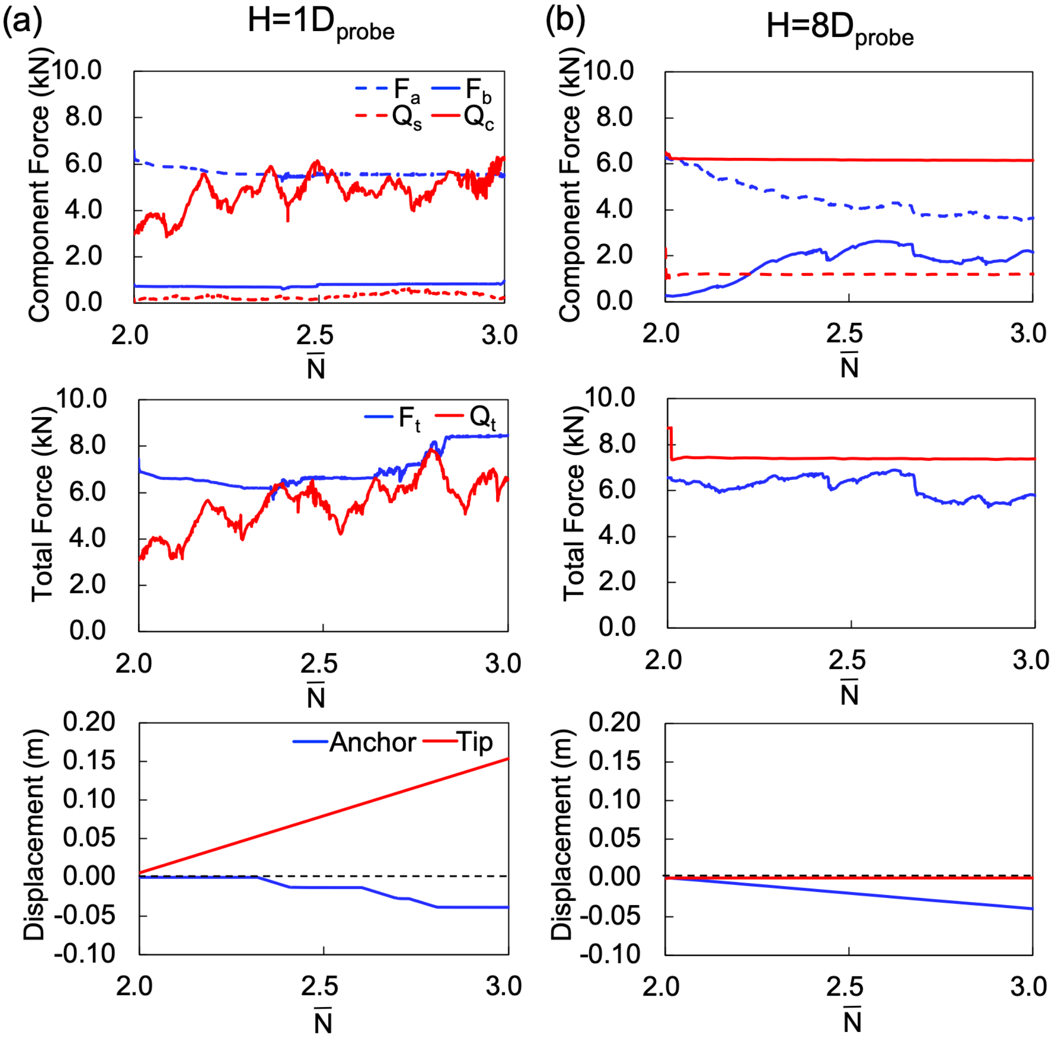

Figure 2.16: Effect of anchor–tip distance H on self-penetration forces, for H values of (a) 1 D_{probe} (Simulation #2) and (b) 8 D_{probe} (Simulation #6).

Figure 2.15b shows the results of varying L and produces a similar finding to Figure 2.15a. In this case, when H is held constant at 4 D_{probe} (0.176m), self-penetration occurs only for anchors with L greater than 4 D_{probe}. An increase in L has two benefits for self-penetration. First, the longer anchors produce a greater reduction in q_c (Figures 9b and 10b). Second, the longer anchors generate greater F_a due to their greater surface area (Eq.2.3). These effects, evident in Figures 2.17a and 2.17b, show the smaller initial

Q_c for the probe with the longer anchor (4.8 kN for Simulation #9 versus 6.0 kN for Simulation #7) and the greater F_a for the probe with the longer anchor (average of 7.5 kN for Simulation #9 versus average of 3.2 kN for Simulation #7). The self-penetration displacement ΔD increased as the anchor expansion magnitude was increased (Figure 2.15c), and the effect of EM on q_c, F_a, and F_b is similar to that of L. Namely, a greater EM led to a greater reduction in q_c and greater F_a and F_b magnitudes (Eqs.2.3and2.4). Because F_a is directly proportional to f_anchor, an increase in f_anchor results in a greater self-penetration displacement (Figure 2.15d). Increases in the overburden stress (σ'_z)

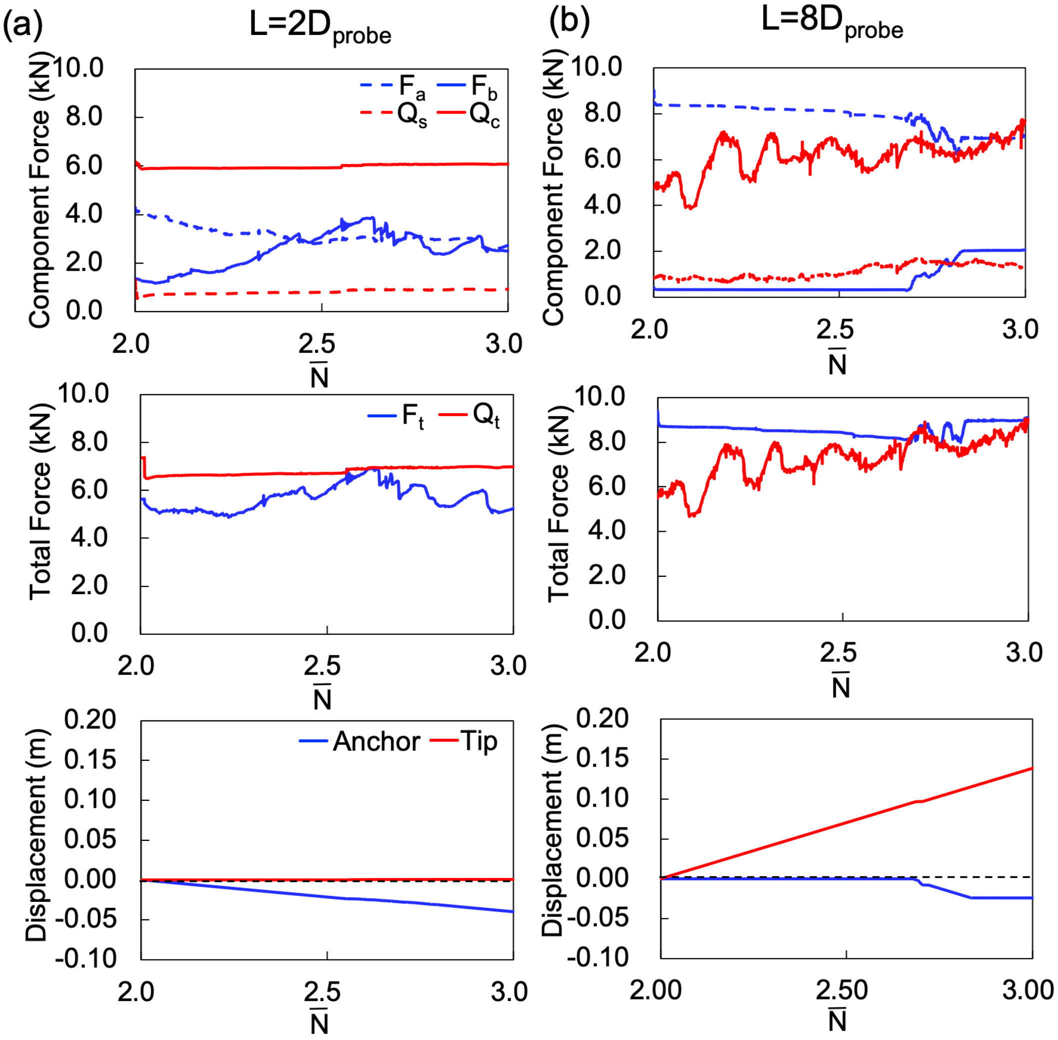

Figure 2.17: Effect of anchor length L on self-penetration forces, for L values of (a) 2 D_{probe} (Simulation #7) and (b) 8 D_{probe} (Simulation #9).

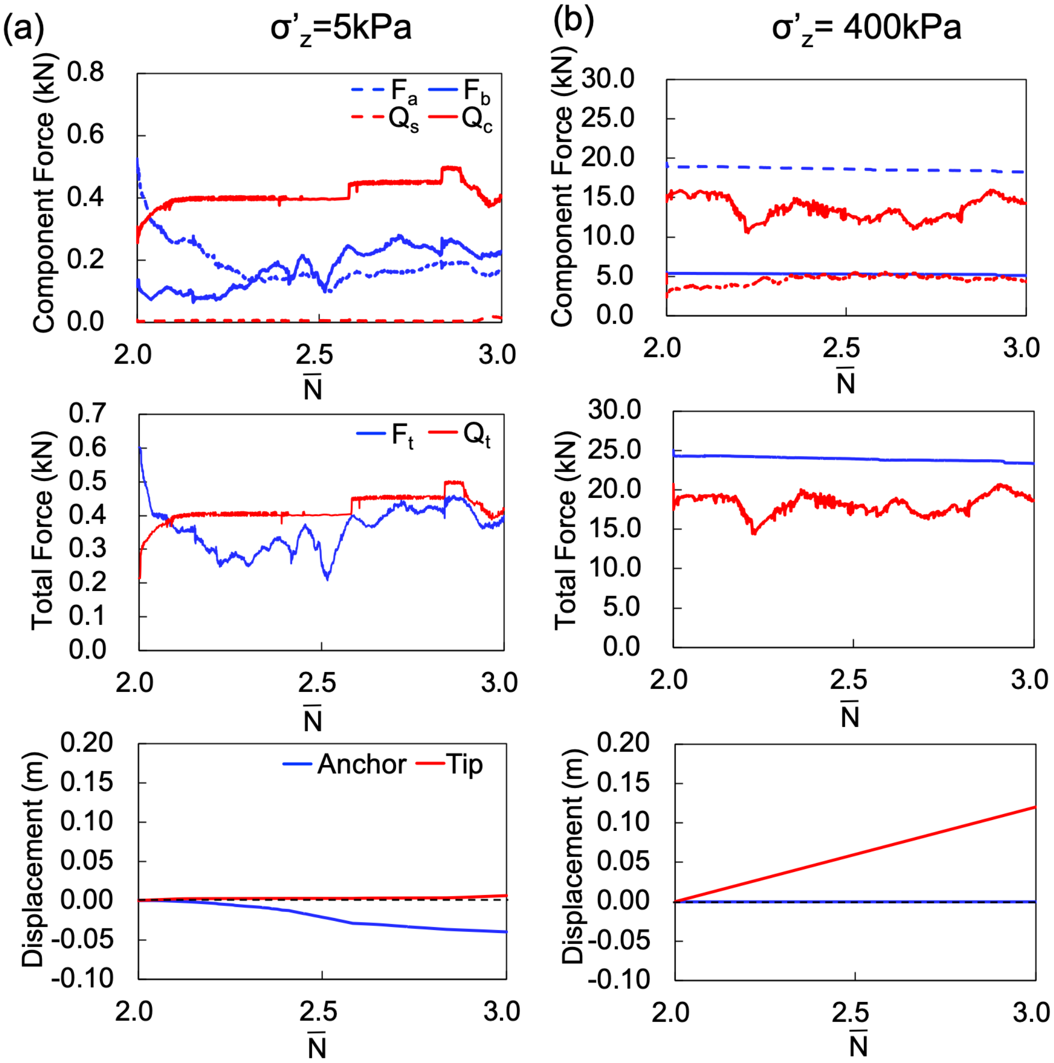

Figure 2.18: Effect of overburden stress σ'_z on self-penetration forces, for σ'_z values of (a) 5 kPa (Simulation #14) and (b) 400 kPa (Simulation #17).

increased the self-penetration ability of the bio-inspired probe (Figures 2.15e, 2.17a, and 2.17b). For the reference probe geometry in Simulation #1 ($L = 4\ D_{probe}$, $H = 4\ D_{probe}$, $EM = 0.50$), the probe was lifted at a σ'_z of 5 kPa, as shown by the negative ΔD values. In contrast, self-penetration was accomplished at greater σ'_z, with the simulation at $\sigma'_z =$ 400 kPa showing a steady self-penetration. This is because the reaction forces increase at a greater rate with increasing overburden stress than the resistance forces. For example, when σ'_z increases from 5 kPa to 400 kPa, the total penetration resistance (Q_t) increases from 0.40 kN to 18 kN (about 45 times) while the total reaction force (F_t) increases from 0.38 kN to 24 kN (about 63 times) (Figure 2.18a and 2.18b).

2.5 Discussion

2.5.1 Scaling Tip and Anchor Forces with Increasing Depth

Analysis of the scaling of the tip and anchor forces with increasing overburden stress is necessary for assessing the applicability of the 'anchor–tip' strategy to civil infrastructure applications. This is necessary because burrowing animals habituate depths that are typically shallower than a couple meter whereas infrastructure applications typically require penetration to depths of tens to hundreds of meters. In addition, from an energetic and physiological point of view, the magnitude of the burrowing forces imposes limits on how deep animals and plants can penetrate due to limits in muscular capacity and internal pressure [Bengough and Mullins, 1990; McKenzie and Dexter, 1988; Ruiz et al., 2015].

Simulations at different σ'_z magnitudes are employed here to investigate the effect of simulated depth ($\sigma'_z = \rho g z$ where z is depth). Analysis of the component and total resistance and reaction forces reveals that they scale in a power-law fashion with increasing overburden stress (Simulations #1 and #14-#17, Figure 2.19a and 2.19b). The exponent of the fitted relationships reflects the sensitivity of a given force to the overburden stress magnitude. As shown, the anchor friction force (F_a) and anchor bearing force (F_b) relationships have exponents of 0.76, while the Q_c relationship has a smaller exponent of 0.70 (Figure 2.19a). The Q_s relationship has a larger exponent of 1.08, but the Q_s magnitudes are much smaller than those of the other three component forces. As a result, the F_t relationship has a greater exponent than the Q_t relationship, with respective values of 0.80 and 0.71 (Figure 2.19b). These results agree qualitatively with experiments on living animals. For instance, Dorgan [2015] presents a summary of burrowing strategies showing that at greater depths where enough anchorage forces can be generated, animals tend to use strategies that rely on anchorage forces such as peristalsis. In contrast, animals tend to use an undulatory motion strategy at shallower depths. Similarly, Kudrolli and Ramirez [2019] provide evidence indicating that *L.* variegatus specimens adapt their locomotion strategy based on the medium, using peristalsis in consolidated sediments and undulatory motion in unconsolidated sediments. Overall, these results suggest that the 'anchor–tip' strategy becomes more efficient at greater depths in the situation where the burrowing capacity is not limited by energetic or physiological limits, as may be the case for construction activities using diesel- and hydraulically-powered equipment.

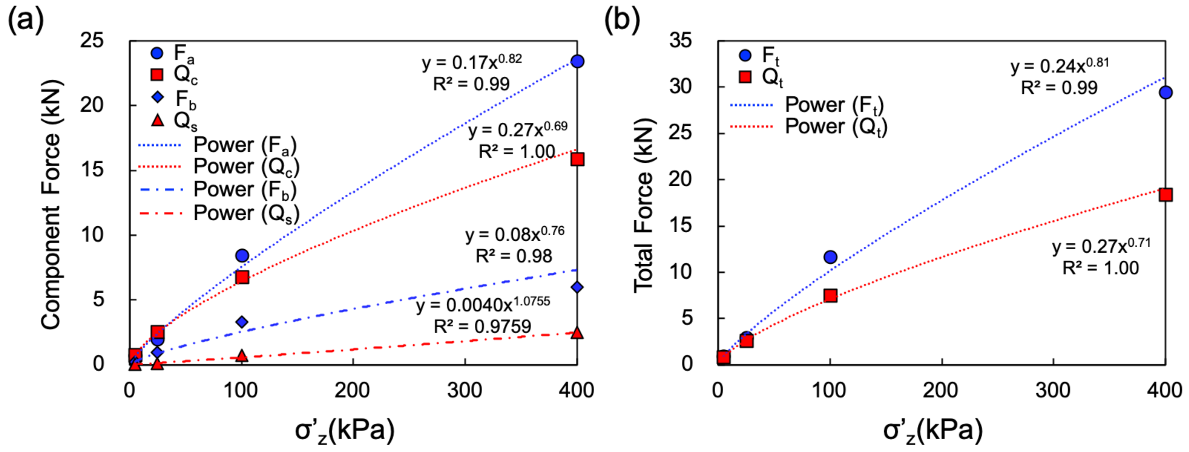

Figure 2.19: Scaling of (a) component and (b) total forces with overburden stress (σ'_z).

2.5.2 Self-Penetrating Probes for Geotechnical Site Characterization

The simulation results can provide guidance for design of future self-penetration technologies for geotechnical and infrastructure engineering. One particular opportunity exists for site characterization, which is one of the first steps in the design of infrastructure systems as it provides the soil properties required for engineering design and helps identify potential challenges and risks (e.g. weak foundation beneath a dam). Generation of a sufficient reaction force to advance probes typically requires the use of large 20-ton truck rigs to provide the reaction by means of dead mass (Figure 2.1c). However, many projects require site characterization in areas with limited access to large equipment, such as at the toe of or beneath existing dams, congested urban areas, forested areas, and even in outer space, or in locations with stiff layers that can lead to “penetration refusal.”

Implementation of the anchor–tip strategy as an alternate means to generate the reaction force necessary for geotechnical site characterization technology may lead to development of lighter or portable equipment that could improve access at difficult sites and reduce environmental impacts. As shown in this study, expansion of an anchor can provide enough reaction force to overcome the penetration resistance and advance a probe. Probe configurations that enable self-penetration include shorter anchor–tip distances, longer anchors, greater anchor expansion, and a greater anchor friction coefficient. In addition, increasing overburden stress (i.e. depth) increases the self-penetration ability of the bio-inspired probe. While the effect of density was not explicitly considered in this study, analytical results have shown that self-penetration can be more challenging to realize in denser coarse-grained soils [Martinez et al., 2020], such as the ones considered in the present study.

2.6 Conclusions

This study presents the results of simulations of the self-penetration process of a bio-inspired probe in granular soils performed with a calibrated 3D discrete element model. The simulations consist of three stages: (1) cone penetration (CP), during which the probe is pseudo-statically pushed into the granular assembly, (2) anchor expansion (AE) during which an anchor is radially expanded (AE), and (3) self-penetration (SP) during which the probe tip and anchor are displaced in opposite directions using a force-limited algorithm.

The simulation results indicate that the self-penetration ability of the bio-inspired probe, defined as its ability to generate enough anchorage forces to overcome the soil penetration resistance and advance the probe tip to greater depths, depends on the probe configuration and the soil conditions. Greater anchorage forces can be generated by longer anchors, anchors with greater expansion magnitudes, and anchors with greater coefficients of friction. In addition, radial expansion of the probe's anchor produces a temporary decrease in the penetration resistance, which was more pronounced when the anchor was positioned closer to the tip and when the anchor was longer or more expanded.

The self-penetration ability of the probe increased as the overburden stress was increased from 5 to 400 kPa (simulated depths of 0.5 to 40 m). The probe forces involved in self-penetration are shown to have a power-law relationship with overburden stress, and the total anchorage force increases at a greater rate with increasing simulated depth than the total penetration force. These results may shed light on the mechanisms involved in the burrowing behavior of animals such as polychaetes and oligochaetes which have been shown to employ strategies such as peristalsis or the so-called double-anchor strategy at greater depths or in more consolidated soils where anchorage forces with enough magnitude can be generated.

Bio-inspired burrowing strategies implemented in construction equipment may facilitate soil penetration in more efficient ways, possibly enabling development of more lightweight and portable equipment that would reduce the challenges of characterizing low-accessibility sites such as areas near dams, congested urban regions, and outer space bodies. While development of such technology requires advances in other areas such as actuation and advanced materials, the results presented herein provide evidence indicating that the 'anchor–tip' strategy could be successfully employed for developing self-penetrating technology capable of penetrating to depths in the order of tens of meters.

2.7 Acknowledgements

This material is based upon work supported by the Engineering Research Center Program of the National Science Foundation under NSF Cooperative Agreement No. EEC-1449501 and the Center for Information Technology Research in the Interest of Society (CITRIS). Any opinions, findings, and conclusions or recommendations expressed in this material are those of the author(s) and do not necessarily reflect those of the National Science

Foundation or CITRIS.

Chapter 3

DEM Study of the Alteration of the Stress State in Granular Media around a Bio-Inspired Probe

---

This chapter was accepted in Canadian Getechnical Journal under the following citation and is presented here with minor edits.

Chen, Y, Martinez A, DeJong J (2022) Alteration of the stress state around a bio–inspired probe enables self–penetration. In publication by Canadian Geotechnical Journal. DOI link.

3.1 Abstract

Soil penetration is a ubiquitous energy-intensive process in geotechnical engineering that is typically accomplished by quasi-static pushing, impact driving, or excavating. In contrast, organisms such as marine and earthworms, razor clams, and plants have developed efficient penetration strategies. Using motion sequences inspired by these organisms, a probe that uses a self-contained anchor to generate the reaction force required to advance its tip to greater depths has been conceptualized. This study explores the interactions between this probe and coarse-grained soil using 3D discrete element modeling. Spatial distributions of soil effective stresses indicate that expansion of the anchor produces arching and rotation of principal effective stresses that facilitate penetration by inducing

stress relaxation around the probe's tip and stress increase around the anchor. Spatial strain maps highlight the volumetric deformations around the probe, while measurements of both stresses and strains shows that the state of the soil around the anchor and tip evolves towards the critical state line. During subsequent tip advancement, the stresses and strains are similar to those during initial insertion, leading to the remobilization of the tip resistance. Longer anchor and shorter anchor-to-tip distance better facilitate tip advancement by producing greater stress relaxation ahead of the tip.

3.2 Introduction

Soil penetration is a ubiquitous process in geotechnical applications, relevant to activities such as site characterization (Figure 3.1a), pile driving (Figure 3.1b), and tunneling, where large equipment (e.g., drill rigs, driving hammers, augers, and cranes) is usually required to provide reaction forces to overcome the penetration resistance. Common accompanying problems in soil penetration processes include inadequate reaction forces (e.g., Mayne [2007]), limited access to specific sites (e.g., the toe of a dam, congested urban area, and vegetated areas), and negative environmental impacts (e.g., Raymond et al. [2020]; Purdy et al. [2020]). These challenges present a need for exploring alternative soil penetration solutions to better achieve engineering functionality and environmental sustainability. Efficient soil penetration processes may be inspired by organisms that have developed different adaptations for soil penetration and burrowing, such as marine worms (Figure 3.1c) and growing plant roots (Figure 3.1d). Many of the adaptations used by these organisms involve concurrent or sequential motions consisting of body expansion/contraction and tip advancement. Polychaetes Alitta virens [Dorgan, 2015], Nereis virens [Dorgan et al., 2007; Che and Dorgan, 2010], and Thoracophelia mucronata [Dorgan, 2018] expand their anterior tips to widen cracks laterally and extend cracks anteriorly to achieve forward movement in marine sediments. Tree roots use tip radial growths to weaken soils ahead of tips and enable further tip advancement [Savioli et al., 2014; Ruiz and Or, 2018]. Earthworms use peristalsis that involves sequential wave-like motions consisting expansion and contraction of their circular muscles; peristalsis allows worms to move within excavated

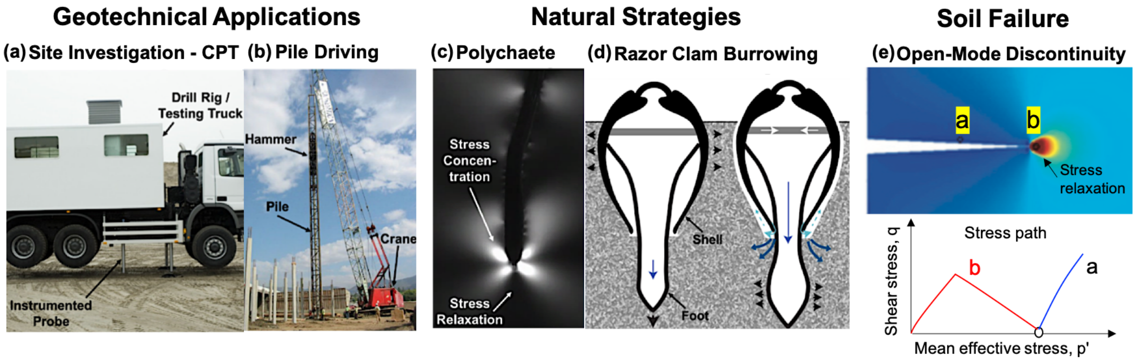

Figure 3.1: Soil penetration in geotechnical applications, polychaete burrowing and plant root growth, and open-mode discontinuity. (a) in-situ cone penetration test uses the weight of drill rigs as reaction for probe penetration, (b) pile driving uses impact loading applied by a hammer, (c) polychaete in photoelastic gel showing zones with stress concentration and relaxation (after Dorgan et al. [2007]), (d) results of finite element simulation of plant growth showing stress relaxation in warmer colors (after Savioli et al. [2014]), and (e) results of numerical study on open-mode discontinuity showing stress relaxation ahead of the invasive immiscible phase (after Shin and Santamarina [2011]).

tunnels as well as to loosens the soil ahead of tip [Sadava et al., 2009; Barnett et al., 2009; Kurth and Kier, 2014]. Razor clams use the 'dual anchor' burrowing strategy, which involves alternating expansion of their foot and shell, to induce stress relaxation ahead of foot and facilitate penetration [Trueman, 1968a,c; Murphy and Dorgan, 2011; Dorgan, 2015]. The soil penetration processes used by these organisms resemble the formation of open-mode discontinuities driven by immiscible invasive phases, where concentration of stresses against the burrow or crack lateral walls induces a relaxation of stresses ahead of burrow or crack tip, as shown in the stress paths in Figure 3.1e from numerical simulations by Shin and Santamarina [2011].

There has been recent interest in bio-inspired design for geotechnical engineering applications [Martinez et al., 2021]. Several investigations focused on the development of new foundations with surfaces that generate direction-dependent friction and soil anchoring elements inspired by tree-roots (e.g.,Mallett et al. [2018a]; Martinez et al. [2019]; O'Hara and Martinez [2020]; Aleali et al. [2020]; Burrall et al. [2020]; Stutz and Martinez [2021]). Other experimental and numerical studies on bio-inspired probes and robots also investigated their performance during soil penetration and burrowing. Probes inspired by earthworms, marine worms, and clams use radial body expansion to facilitate soil penetration by reducing the penetration resistance (e.g.,Cortes and John [2018]; Khosravi et al. [2018]; Ma et al. [2020]; Ortiz et al. [2019]; Tao et al. [2020]; Huang et al. [2020]; Huang and Tao [2020]; Borela et al. [2021]; Chen et al. [2020]). Plant root-inspired robots also showed high soil penetration efficiency by developing additive tip tissues that reduced the mobilized friction against the robot's embedded surface area (e.g.,Sadeghi et al. [2014]; Naclerio et al. [2018]). Chen et al. [2021] presented the results of 3D discrete element modeling (DEM) simulations of an idealized bio-inspired probe which uses an 'anchor-tip' strategy to penetrate soil. The 'anchor-tip' strategy consists of radially expanding an anchor that mobilizes reaction forces, and subsequently advancing the tip if the mobilized reaction forces are greater than the penetration resistance forces. The study showed that the probe was able to self-penetrate a coarse-grained soil specimen, defined as the ability of a probe to penetrate soil only relying on the reaction force generated by its self-contained anchor.

The studies performed to date have proven that burrowing probes and devices can be functional in different soil types and at different scales. However, less attention has been devoted to the soil failure mechanisms and soil-probe interactions involved in the burrowing processes. This understanding is required to further optimize probe performance and provide insight of the geomechanical processes involved in animal and plant burrowing. The DEM study presented herein has the objective of investigating the soil failure mechanisms involved in the expansion of an anchor and subsequent tip advancement of a bio-inspired probe that uses the 'anchor-tip' strategy. The soil failure mechanisms are investigated in terms of spatial distributions of mean, radial, and vertical effective stresses, directions and relative magnitudes of principal stresses, and stress paths at specific locations. DEM simulations of three different probes from Chen et al. [2021] are used to evaluate the effects of probe geometry (e.g., anchor-tip distance H and anchor length L) on the probe responses as well as the state of soil stresses and strains.

3.3 Model Description

DEM simulations are performed using the PFC 3D software (Itasca, Minneapolis, MN). Each simulation model consists of a bio-inspired probe and a cylindrical virtual calibration chamber (VCC) containing about 210,000 soil particles. The simulated bio-inspired probe is composed of a cylindrical shaft with an initial diameter (D_{probe}) of 0.044 m (cross section area of 15 cm^2) and a cone tip with an apex angle of 60° (half apex angle, θ, of 30°), equivalent to the cone penetration testing (CPT) probes routinely used for site characterization [ASTM, 2012]. The cylindrical shaft consists of multiple radial ring segments that are 0.01 m in height, which allow deploying an anchor with a given length and at a given location behind the tip. The probe friction coefficient (μ_p) is taken as 0.3 for all simulations, which is equivalent to an interface friction angle of 16.7° that is typical of that of conventional CPT friction sleeves [Martinez and Frost, 2017; Khosravi et al., 2020].

The cylindrical virtual calibration chamber is 1.2 m in height ($H_{chamber}$), 0.7 m in diameter ($D_{chamber}$), and composed of one top, one bottom, and 14 radial ring walls (Figure 3.2a). Each wall is individually servo-controlled to achieve constant vertical and radial boundary effective stresses (σ'_z and σ'_r, respectively) throughout the simulations, with $\sigma'_z = 100$ kPa and $\sigma'_r = 50$ kPa, for a $K_0 = \sigma'_r/\sigma'_z = 0.5$. Using 14 radial ring walls to simulate radial boundary enables a uniform radial stresses of 50 kPa along the VCC's height to be maintained during the penetration and anchor expansion processes (Figure 3.3) shows the boundary stresses and chamber radii during probe insertion). The constant-stress conditions applied to the chamber boundaries simulate deep penetration conditions [Arroyo et al., 2011; Khosravi et al., 2020]. A friction coefficient between particles and wall is 0.1 to improve the stability of servo-control on boundary walls.

The particles are spherical in shape with a mean particle size (D_{50}) of 0.0144 m. The particle size distribution is characterized by a coefficient of uniformity (C_U) and a coefficient of curvature (C_C) of 1.2 and 0.96 respectively. The particle density is taken as 2650 kg/m^3, and the specimens are consolidated to an initial void ratio of 0.61. The simulations employ the linear contact model with rolling resistance to simulate the response of

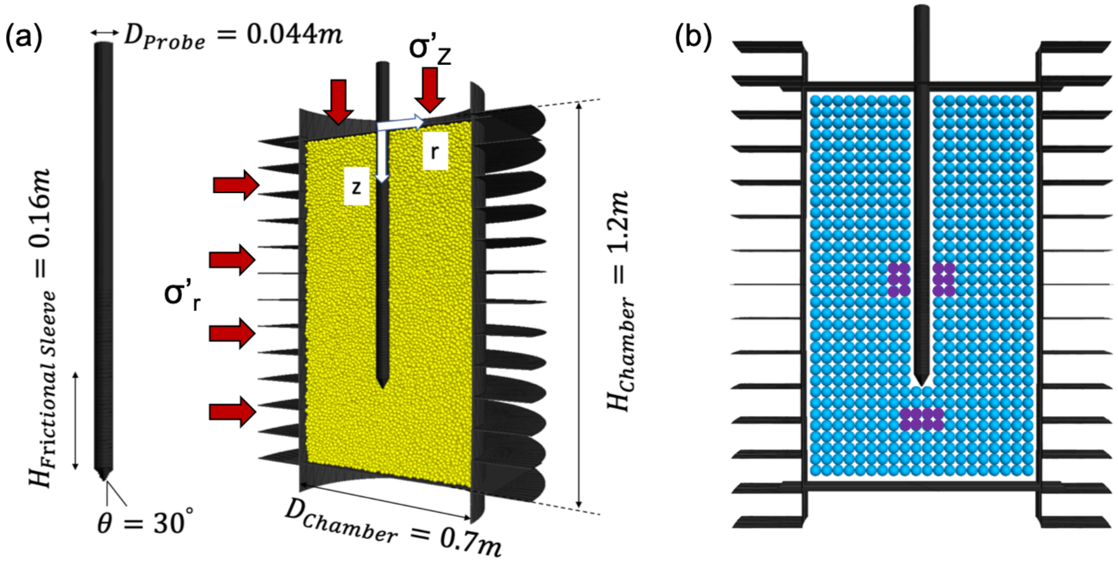

Figure 3.2: DEM simulations model: (a) calibration chamber and simulated probe; (b) configuration of measurement spheres. Note that the purple spheres are used to plot stress paths of soils around the anchor and tip.

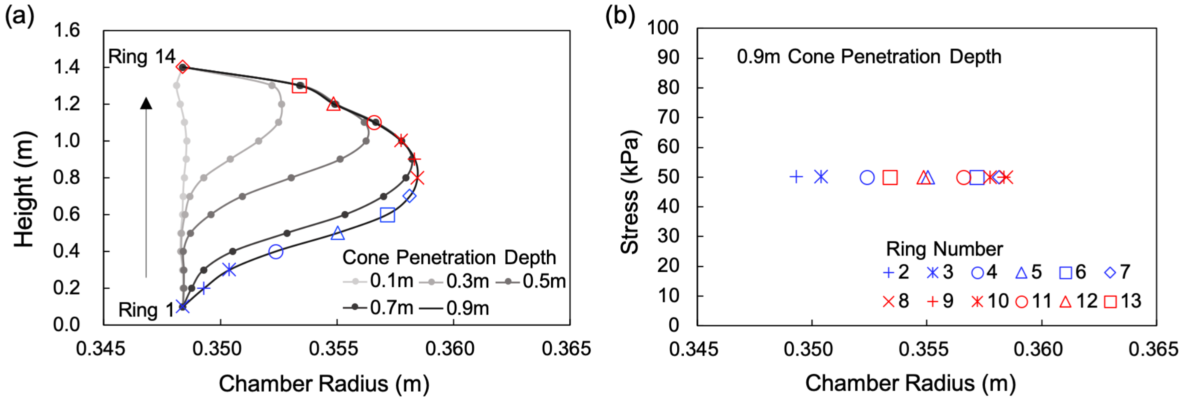

*Note: Ring 1 and 14 are not activated so their stresses are zero.

Figure 3.3: (a) Distribution of ring radius along chamber height during the Cone Penetration stage and (b) ring stresses at the end of the Cone Penetration stage. Note that Ring 1 and Ring 14 are not in contact with particles, therefore they are not shown in (b).

sub-rounded to sub-angular soil [Ai et al., 2011; Wensrich and Katterfeld, 2012; McDowell et al., 2012], where the sliding and rolling friction coefficients (μ_s and μ_r, respectively) are taken as 0.4 (Table 3.1). The particle normal stiffness (k_n) is proportional to its diameter (d) with $k_n/d = 10^8 N/m^2$.

Table 3.1: DEM simulation parameters.

Input Parameter	Symbol	Value
Normal Stiffness to Particle Diameter (N/m^2)	k_n/d	1.0E+08
Normal to Shear Stiffness Ratio	k_n/k_s	1.5
Sliding Friction Coefficient	μ	0.4
Rolling Friction Coefficient	μ_r	0.4
Ball-probe Friction Coefficient	μ_p	0.3
Ball-wall Friction Coefficient	μ'	0.1
Particle Density (kg/m^3)	G_s	2650
Local Damping of Sample Preparation	ξ	0.6
Local Damping during Simulation	ξ'	0.1

As required by most DEM simulations of boundary-value problems, the particle sizes had to be upscaled to maintain reasonable computational costs. The chamber-to-probe diameter ($D_{chamber}/D_{probe}$) and the probe-to-particle diameter (D_{probe}/D_{50}) are 15.9 and 3.1, respectively. These dimensions have been previously shown by Khosravi et al. [2020] and Chen et al. [2021] to reduce potential boundary and particle-scale effects, and are consistent with previous DEM simulations of probe penetration. For example, $D_{chamber}/D_{probe}$ values from 12.0 to 16.6 and D_{probe}/D_{50} values from 2.7 to 3.1 were adopted by Arroyo et al. [2011]; Butlanska et al. [2014]; Zeng and Chen [2016]; Ciantia et al. [2016, 2019a]; Zhang et al. [2019]; Huang and Tao [2020] in their 3D simulations of probe penetration. Although some other studies employed greater values, such as $D_{chamber}/D_{probe}$ from 30 to 40 and D_{probe}/D_{50} of 21.1, they performed 2D simulations or used symmetric models with only partial chambers simulated [Lin and Wu, 2012; Jiang et al., 2006].

The chamber simulated in this study contained 628 measurement spheres (MSs) arranged in the $r - z$ plane (Figure 3.2b) to obtain the soil stresses and strain rates. Each

MS has a diameter of 0.033 m, which leads to an average ratio of the MS volume to particle volume of about 12. The MSs shown in purple in Figure 3.2b are used to obtain stress paths around the anchor and below the tip.

3.3.1 Model Calibration

Kuei et al. [2020] calibrated the contact parameters of the DEM simulations to capture the mechanical response of coarse-grained soils under different overburden stresses. Results of simulations of triaxial compression tests are presented here to examine the element soil responses. Soil specimens were isotropically confined to an initial void ratio (e) of 0.61 under stresses of 5, 25, 100, and 400 kPa, respectively. Then, the soil specimens were compressed in the vertical (i.e. axial) direction while maintaining the radial confining stresses constant. The results show that: (i) shearing the specimens under greater confining pressures led to mobilization of greater peak and residual deviatoric stresses ($q = \sigma_1' - \sigma_3'$) (Figure 3.4a) and smaller volumetric strains indicating a smaller dilatancy (Figure 3.4b) and (ii) the stress paths of the tests at different confining stresses converged to a critical state line (CSL) in the $q - p'$ (Figure 3.4c) and $e - p'$ planes (Figure 3.4d), where p' is the mean effective stress. The slope of CSL in the $q - p'$ plane is 1.46:1, which corresponds to a friction angle of 36.0° and this is consistent with critical state friction angles reported in literature for coarse grained soils (e.g. Simoni and Houlsby [2006]; Xiao et al. [2016]; Luo et al. [2018]. The CSL obtained from the triaxial simulations is used throughout this paper as a reference when plotting the stress paths at select locations within the soil specimen.

To further examine the ability of DEM simulations of modeling the behavior of coarse-grained soils, four CPT simulations using the same model parameters and VCC and probe configurations have been performed at overburden stresses of 5, 25, 100, and 400 kPa. The tip resistance (q_c) values (Figure 3.4e) increase as the vertical stresses increase and are in agreement with those expected for sub-rounded coarse-grained soils (e.g. Mayne [2007]) along with corresponding sleeve friction (f_s) values [Chen et al., 2021]. When plotting the CPT results on the soil behavior type chart by Robertson [2016] using the normalized tip resistance and sleeve friction, the data points indicate a classification between 'sand-like

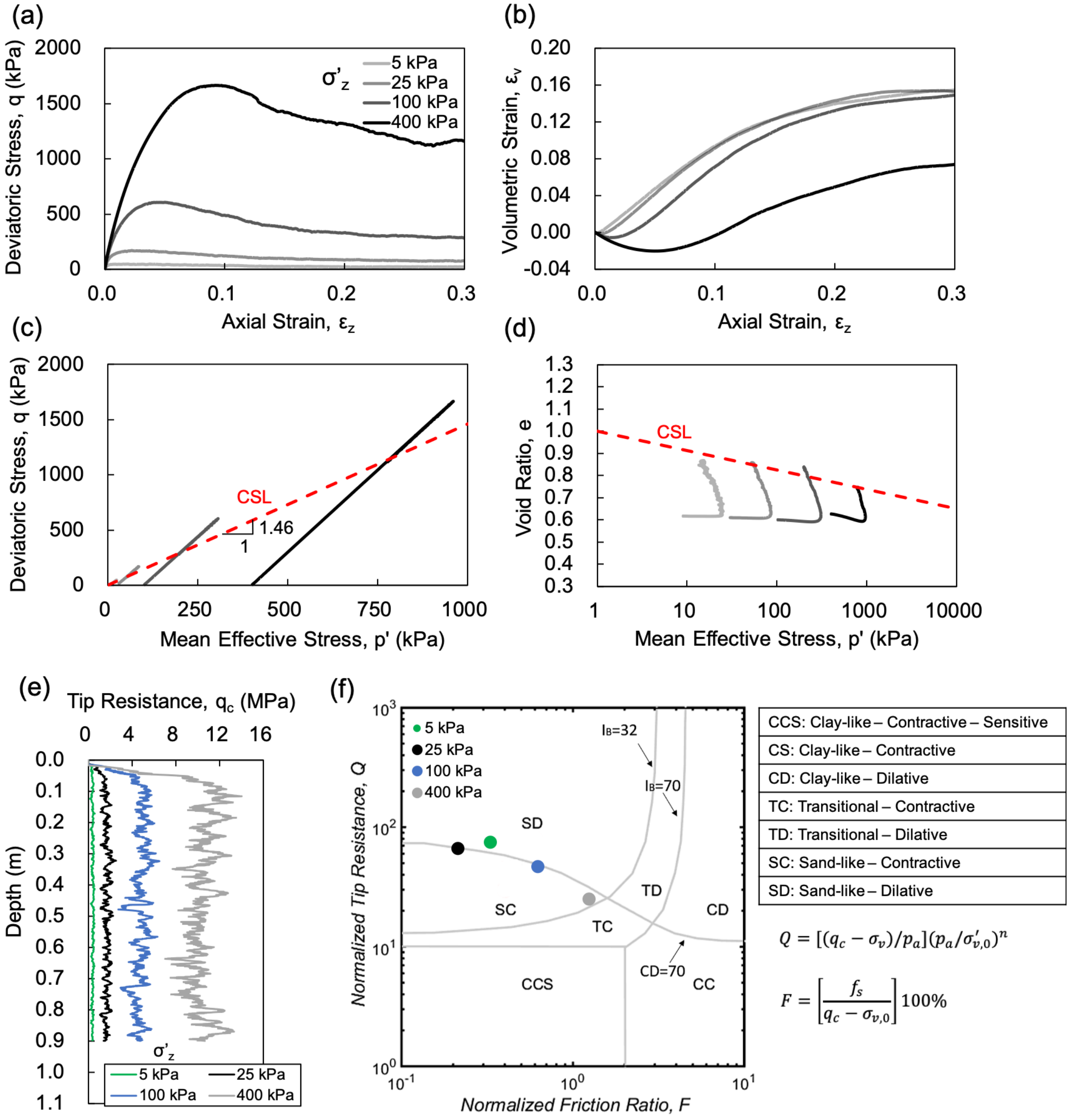

Figure 3.4: Results of triaxial compression tests and cone penetration tests at confining pressures of 5, 25, 100, and 400 kPa. Evolution with axial strain of (a) deviatoric stress and (b) volumetric strain and stress paths in (c) $q - p'$ plane and (d) $e - p'$ plane; signatures of (e) tip penetration resistance and (f) soil behavior type classification based on penetration resistance measurements.

contractive' and 'sand-like dilative' (Figure 3.4f). The results of CPT simulations provide confidence in the ability of the DEM model to reproduce a penetration response that is representative of coarse-grained soils.

3.3.2 Bio-Inspired Probe and Simulation Sequence

The simulated bio-inspired probe consists of an anchor that can expand radially and a tip that is advanced vertically down (Figure 3.5a). The two important probe configuration parameters discussed in this paper are the anchor length (L) and the anchor-tip distance (H). The simulations include three stages (Figure 3.5b) which use a simplified sequence of motions to approximate those of a physical probe. First, during the cone penetration (CP) stage the probe is inserted into soil at a constant rate of 0.2 m/s to a target depth of 0.9 m while the q_c (Eq. 2.1) and fs (Eq. 2.2) are recorded. This motion is similar to that employed during CPT testing [ASTM, 2012]. During the anchor expansion (AE) stage, the probe is stopped and the diameter of the anchor is uniformly expanded at a rate of 0.2% per second of its initial diameter ($D_{probe} = 0.44$ mm) until a target diameter (D_{anchor}) of 0.066 mm is achieved while the radial anchor pressure (P_a) and end bearing anchor pressure (P_b) are measured. This motion is similar to that employed during inflation of a pressuremeter probe in the field [Mair and Wood, 2013]. During the tip advancement (TA) stage, the anchor is displaced upward while the tip is displaced downward using a velocity-controlled algorithm with force limits (referred to as force-limited algorithm, Figure 3.6). This algorithm is analogous to the force loading control mechanisms used in standard laboratory testing, such as cyclic triaxial and cyclic simple shear testing, which applies a constant velocity until a target force is generated. It is noted that this type of control algorithm does not require for the reaction and resistance forces to be in equilibrium. In the DEM simulations, the motions of a probe section (i.e. the anchor or the tip) are updated at each timestep by comparing the forces acting on them (i.e. total reaction or resistance force, F_t or Q_t, respectively) against the target force (F_{target}). When a probe section mobilizes a force that is smaller than F_{target}, it will be displaced at a velocity of 0.2 m/s (downward for the tip and upward for the anchor). The initial value of F_{target} is zero, and it is increased by a small constant increment of 50 N subsequently

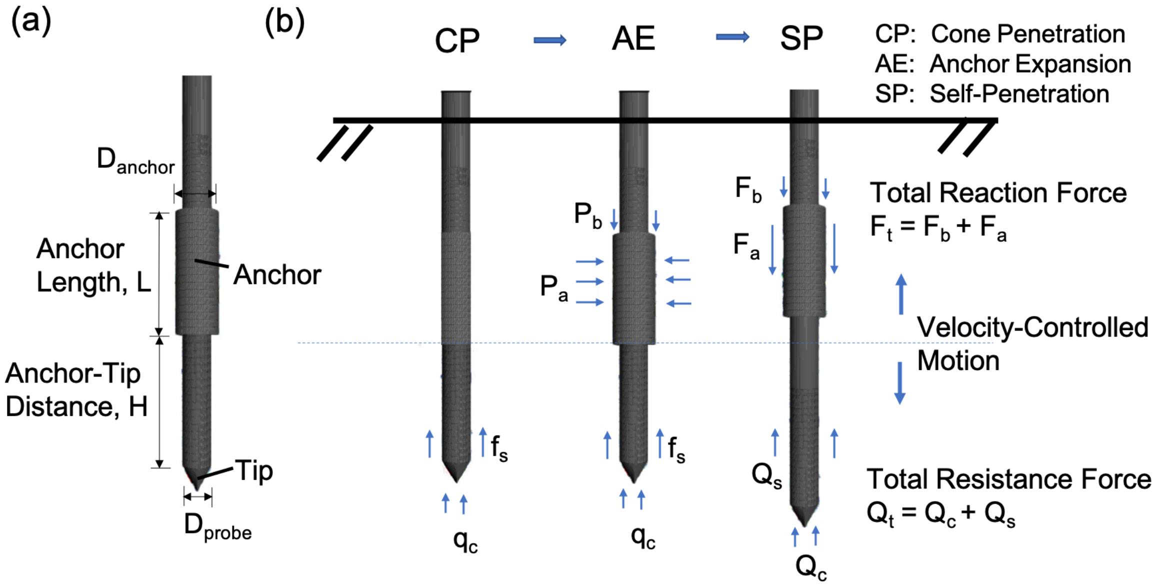

Figure 3.5: (a) Probe configuration parameters and (b) schematic of the three simulation stages. The arrows acting against the probe represent soil stresses or forces acting on it. Notes that each simulation includes the three stages (CP, AE, TA), the motion of the tip and anchor during TA is controlled using the algorithm described in Figure 3.6, and during TA the shaft located above the anchor remains stationary.

(i.e. $F_{target,1} = 50N$, $F_{target,2} = 100N$, etc.). The F_{target} increment was chosen based on iterative calibration that showed that a increments smaller than or equal 50 N have no influence on the results. The tip advancement simulation is terminated when the upward anchor displacement is greater than 0.04 m (about 1 D_{probe}), indicating failure to mobilize enough anchorage, or when the downward tip displacement is greater than 0.14 m, which is considered as successful tip advancement.

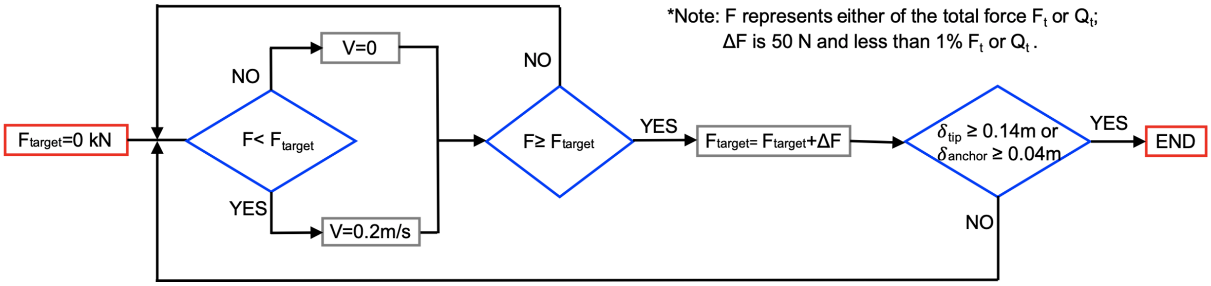

Figure 3.6: Logic for velocity-controlled algorithm with force limits for the tip and the anchor during Tip Advancement (TA) stage. Note that F represents either of the total force F_t or Q_t; ΔF is 50 N and less than 1% F_t or Q_t.

The forces acting on the probe during the TA stage are the total reaction force (F_t), defined as the sum of anchor friction force (F_a, Eq. 3.1) and end bearing force (F_b, Eq. 3.2), and the total resistance force (Q_t), defined as the sum of the tip resistance force (Q_c, Eq. 3.3) and the shaft resistance force (Q_s, Eq. 3.4). Using the force-limited algorithm , the anchor and tip are controlled separately, as previously described (i.e. Figure 3.6).

$$F_a = 2\pi P_a L(1 + EM) D_{probe} \mu_p \tag{3.1}$$

$$F_b = \frac{\pi}{4} P_b (D_{anchor}^2 - D_{probe}^2) \tag{3.2}$$

$$Q_c = \frac{\pi}{4} q_c D_{probe}^2 \tag{3.3}$$

$$Q_s = \pi f_s D_{probe} \tag{3.4}$$

Where $Q_{ztip,i}$ is the vertical component of the contact force i acting on the probe tip, $Q_{zsleeve,i}$ is the vertical component of the contact force i acting on the bottom 0.16 m of probe shaft, $f_s t$ is the average shear stress along the entire probe shaft, and N is the total number of vertical contact forces acting on the tip or sleeve.

Five simulations are performed in this study to examine the influence of the probe configuration on the probe-soil interactions (Table 3.2). Simulation #1 is used as the reference case throughout this paper, which is for the probe with the anchor-tip distance $H = 4D_{probe}$ and the anchor length L = 4 D_{probe}. Simulations #2 and #3 use the same soil specimen as the reference simulation but have different probe configurations. For the ease of comparison, Simulations #1, #2 and #3 are given names with the format HXLY to reflect the probe configuration, where X represents the value of H in D_{probe} equivalents and Y represents the value of L in D_{probe} equivalents. For example, simulation "H1L4" represents the simulation for the probe with anchor-tip distance $H = 1D_{probe}$ and anchor length $L = 4D_{probe}$. Two additional simulations (#4 and #5) were performed with probes on independently generated specimens with the H4L4 configuration. These simulations were performed to assess the variability in the simulation resulting from using different specimens; these simulations are identified with the suffixes 'R1' and 'R2'.

According to contact dynamics, the inertial number (I), which quantifies the inertial forces on grains relative to the skeleton forces, should be smaller than 10^{-3}-10^{-2}

Table 3.2: DEM Simulation matrix.

#	Parameter	Name	Anchor Length, L	Anchor-Tip Distance, H
1	Reference	H4L4	$4D_{probe}$	$4D_{probe}$
2	H	H1L4	$4D_{probe}$	$1D_{probe}$
3	L	H4L8	$8D_{probe}$	$4D_{probe}$
4	Repeatability	H4L4-R1	$4D_{probe}$	$4D_{probe}$
5		H4L4-R2		

to maintain quasi-static conditions [Combe and Roux, 2009; Radjai and Richefeu, 2009; O'Sullivan, 2011]. The inertial numbers during the three stages in this study were calculated as follows: between 2.1×10^{-5} and 4.4×10^{4} during CP, between 2.1×10^{-5} and 3.6×10^{-4} during AE, between 1.1×10^{-6} and 7.2×10^{-4} during TA. The overlap between particles and between particles and walls was also measured throughout the simulations. During all three stages, the overlap of 99% of the simulated particles remained smaller than 1% of the particle radius.

3.4 Global-Scale Results

The results of the simulations from a global perspective are first described, where the evolution of forces and pressures acting on the probe during the entire three simulation stages are summarized to show their evolution during the different simulation stages. Then, the proceeding three sections examine in detail the meso-scale results (i.e. states of stress and strain) during the CP, AE, and TA simulation stages to characterize the soil failure mechanisms and provide further insight into the evolution of the resistance and reaction forces acting against the probe.

The CP stage has a significantly greater time duration than the AE and TA stages due the target penetration depth of 0.9 m. For visualization purposes, the results in this section are presented in terms of a normalized timestep ($\overline{N}$) to highlight the evolution history of probe measurements and displacements throughout the entire simulations. $\overline{N}$ is defined by Eq. 3.5 such that values from 0 to 1 represent the CP stage, 1 to 2 represent the AE stage, and 2 to 3 represent the TA stage:

$$N = \begin{cases} \dfrac{n}{n_1} & (n \le n_1) \\ 1 + \dfrac{n - n_1}{n_2 - n_1} & (n_1 < n \le n_2) \\ 2 + \dfrac{n - n_2}{n_3 - n_2} & (n_2 < n \le n_3) \end{cases} \tag{3.5}$$

where n is the time step and n_1, n_2, and n_3 are the time steps at the end of CP, AE, and TA stages, respectively. Note that $\overline{N}$ is not the computational timestep in DEM, which differs among different simulation stages and is determined by the minimum eigen-period of the total system and of the particle mass and contact stiffness matrix [Cundall and Strack, 1979; Potyondy, 2009].

3.4.1 Cone Penetration (CP), Anchor Expansion (AE), and Tip Advancement (TA)

Figures 3.7a, 3.7d, and 3.7e show the probe pressures and displacements for the three simulations with different anchor configurations. As the probe is inserted into the VCC during CP (i.e. increase in tip vertical displacement) ($\overline{N} \in [0, 1]$) the penetration resistance (q_c) increases to an average value of 4.8 MPa (with variations between 3 and 6 MPa, Figure 3.7). During this stage, the measurements are the same for all three simulated probes because their tips are identical. During AE (i.e. increase in anchor radial expansion) ($\overline{N} \in [1, 2]$), the anchor radial pressure (P_a) and end bearing pressure (P_b) increase as the anchor is radially expanded. The value of P_a approaches an asymptotic limiting pressure (P_L) at the end of AE ($\overline{N} = 2$), which is observed to be independent of the anchor-tip distance (H) but decreases as the anchor length (L) is increased. For example, a P_L value of 753 kPa is developed during simulation H4L4 (Figure 3.7a) and 780 kPa in simulation H1L4 (Figure 3.7b), whereas the P_L value for simulation H4L8 is around 550 kPa (Figure 3.7c). The P_L values in this study are consistent with previous simulations using cavity expansion that predict P_L values between 600 and 1000 kPa for mildly dilatant sands with friction angles between 30 and 36° [Yu and Houlsby, 1991; Salgado and Prezzi, 2007; Martinez et al., 2020]. Expansion of the anchor results in a decrease of q_c. Greater decreases in q_c are observed for the simulations with smaller H

and greater L. For instance, in simulation H4L4 the q_c decreased from a value of 4.8 MPa at the end of CP ($\overline{N} = 1$) to a value of 3.4 MPa at the end of AE ($\overline{N} = 2$) (Figure 3.7a), while q_c decreased from a value of 4.8 MPa at the end of CP to values of 2.0 MPa and 3.2 MPa during simulations H1L4 (Figure 3.7b) and H4L8 (Figure 3.7c), respectively. The reduction in q_c is in agreement with the 3D DEM results presented by Huang and Tao (2020), who reported a reductions between 10% and 40% during expansion of a cylindrical anchor located immediately behind the tip of a bio-inspired probe.

During TA ($\overline{N} \in [2, 3]$) the anchor is displaced upward (i.e. decrease in vertical displacement) and the tip is displaced downward (i.e. increase in vertical displacement) using the force-limited algorithm. At the early stages of TA (e.g., at $\overline{N} < 2.55$, 2.3, and 2.7 which are marked with red arrows in Figures 3.7a-3.7c and 3.8a–3.8c, respectively), the anchor remained stationary while the tip was displaced downward because the total reaction force (F_t) was greater than the total resistance force (Q_t). During this period, there is slight decrease in both anchor radial pressure (P_a) and end bearing pressure (P_b), which is due to the tip penetration. As the TA stage continued, the anchor was displaced upward because the target force (F_{target}) exceeded F_t. This upward displacement of the anchor led to a decrease in P_a and an increase in P_b. At the end of TA ($\overline{N} = 3$), q_c reached a slightly smaller value than the q_c at the end of CP ($\overline{N} = 1$) for all the simulations. Specifically, q_c at the end of TA was 4.5 MPa, 4.0 MPa, and 4.7 MPa for simulations H4L4, H1L4, and H4L8, respectively, compared to a q_c value of 4.8 MPa at the end of CP. The DEM simulation results from Huang and Tao [2020] also show a remobilization of q_c to values that are slightly smaller than those measured before anchor expansion. During the TA stage of simulations H4L4, H1L4, and H4L8, the tip penetrated to depths of 0.936 m, 1.05 m, and 1.04 m, respectively, indicating that both a shorter anchor-tip distance (H) and a longer anchor length (L) enable greater tip penetration displacements.

To assess the possible effects of using the same specimen for all the simulations, two additional reference simulations were performed on independently-generated specimens with the reference probe (i.e. H4L4). A summary of the pressures generated at the end of the three simulation stages are provided in Table 3.3. The results indicate a small

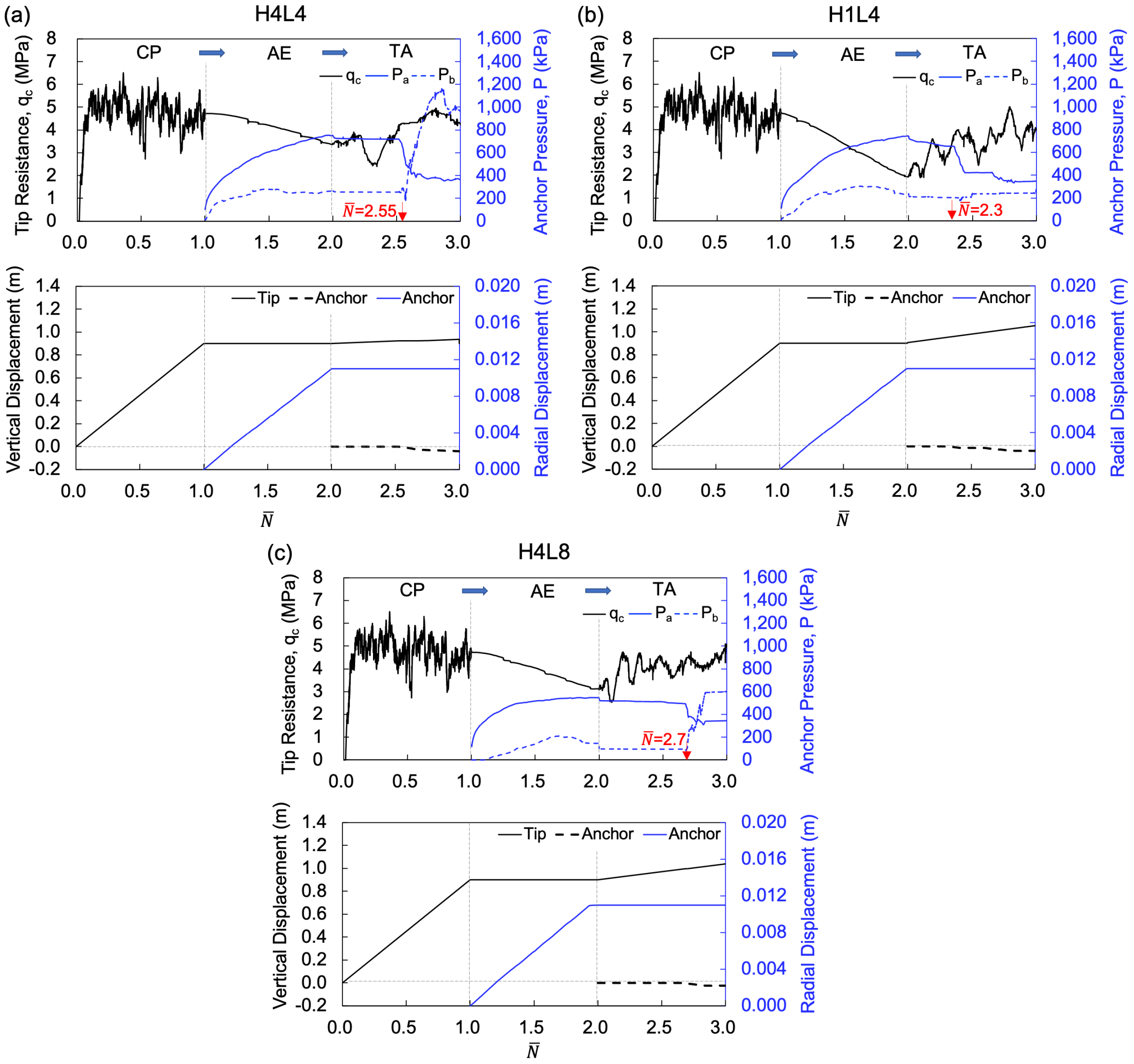

Figure 3.7: Time histories of DEM simulation. Stresses and displacements of the probes with (a) $H = 4D_{probe}$, $L = 4D_{probe}$ (H4L4), (b) $H = 1D_{probe}$, $L = 4D_{probe}$ (H1L4), and (c) $H = 4D_{probe}$, $L = 8D_{probe}$ (H4L8). Note that N is normalized timestep, CP occurs when $N \in [0, 1]$, AE occurs when $N \in [1, 2]$, TA occurs when $N \in [2, 3]$.

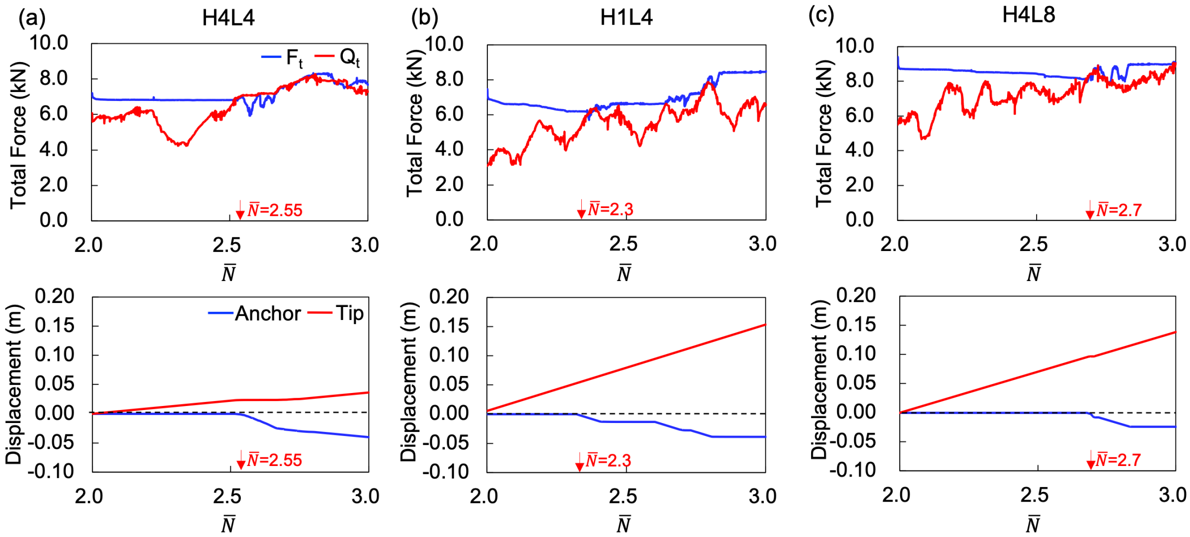

Figure 3.8: Time histories of total reaction and resistance forces and displacements of the probes with (a) $H = 4D_{probe}$, $L = 4D_{probe}$ (H4L4), (b) $H = 1D_{probe}$, $L = 4D_{probe}$ (H1L4), and (c) $H = 4D_{probe}$, $L = 8D_{probe}$ (H4L8). Note that N is normalized timestep, CP occurs when $N \in [0, 1]$, AE occurs when $N \in [1, 2]$, TA occurs when $N \in [2, 3]$.

variabilities in q_c during the CP, AE, and TA stages (coefficients of variation (COV) of 0.6%, 6.8%, and 3.9%, respectively). The P_a values during the AE and TA stages also showed relatively small variabilities (COV of 4.9% and 7.5%), while the Pb values during the TA stage show a somewhat greater variability (COV of 17.6%). Nonetheless, the three simulations show similar trends, with a decrease in q_c and an increase in Pa during the AE stage and an increase in q_c, decrease in P_a, and increase in P_b during the TA stage, indicating that the conclusions drawn from the simulations are dependent on the inherent variability in the simulations.

Table 3.3: Summary of repeated reference simulations.

#	CP stage	AE stage		TA stage		
	q_c (MPa)	q_c (MPa)	P_a (kPa)	q_c (MPa)	P_a (kPa)	P_b (kPa)
H4L4	4.80	3.36	753	4.50	362	957
H4L4-R1	4.74	3.53	704	4.33	312	676
H4L4-R2	4.76	3.84	776	4.16	346	900

3.5 Meso-Scale Results

3.5.1 State of Stresses and Strains during Cone Penetration (CP)

The state of stresses at the end of CP can be visualized by means of force chain maps, which highlight contact forces within the simulated granular assembly, as shown in Figure 3.9a where the normal contact forces between the particles and between the particles and the probe greater than 50 N are represented by lines whose thickness and color represent the contact force magnitude. As expected, Figure 3.9a indicates that force chains with greater magnitudes occur near the probe tip which generate the penetration resistance. While DEM only solves discrete quantities (e.g., contact force, particle displacement), continuum quantities such as stress and strain can be obtained by applying averaging algorithms over an area or volume of interest (e.g., Christoffersen et al. [1981]; Fortin et al. [2003]). The relative difference between the major (σ_1') and minor (σ_3') principal stresses as well as their orientation is visualized in Figure 3.9b using crosses, where the longer line represents the orientation and relative magnitude of the major principal stress and the shorter line represents the orientation and magnitude of the minor principal stress. Due to the K_0 conditions applied to the specimens, σ_1' was initially aligned in the vertical direction. As shown, there is significant rotation of principal stresses near the probe tip. Namely, the direction of σ_1' progresses from horizontally aligned near the cone shoulder to vertically aligned below the cone tip. These results are in agreement with those presented in other studies of CPT and pile penetration (i.e., Jiang et al. [2006]; Ciantia et al. [2019a]). The major principal stresses around the probe shaft are oriented in average at 30° to 70° from horizontal. The intermediate principal stresses (σ_2') are not considered in this 2D cross plot, but they are considered in the stress paths presented in the proceeding sections.

During CP, the soil near the probe tip is subjected to large magnitudes of mean, radial, and vertical effective stresses, as shown in Figures 3.10a–3.10c. The figures show stress maps at the end of the CP stage ($\overline{N} = 1$), where each square represents the average stress in a measurement sphere at that specific location. The effective stresses are concentrated

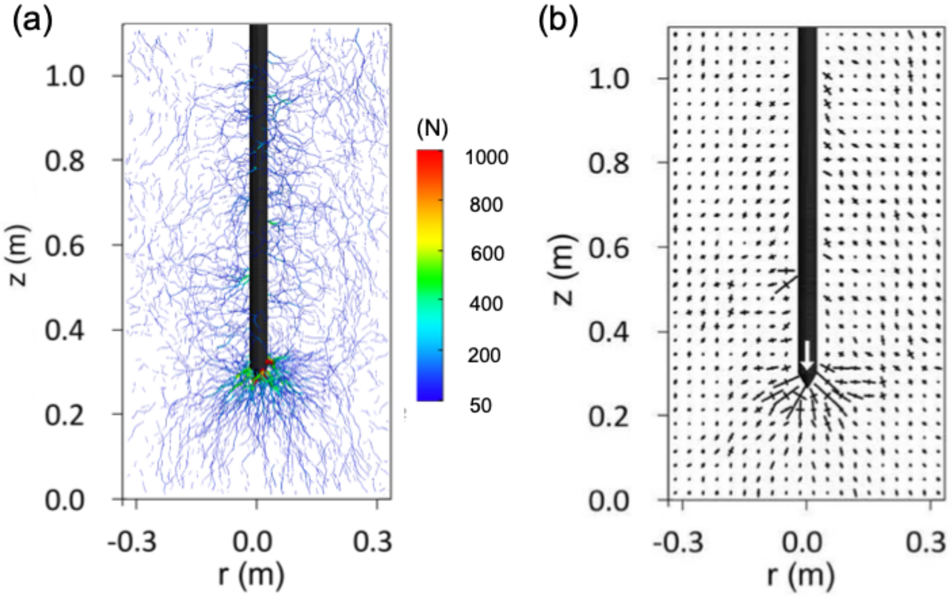

Figure 3.9: (a) Force chain maps and (b) stress state maps at the end of Cone Penetration stage.

in an area around the tip with a radius of 2 to 4 times the probe diameter, in agreement with previous DEM simulations of CPT or pile insertion processes (e.g., Ciantia et al. [2019a]; Zhang and Evans [2018]).

Figures 3.10d–3.10f show the volumetric, radial, and vertical strain maps for the last 0.1 m of penetration during the CP stage, where dilative volumetric strains and compressive strain components are defined as positive. As the tip is displaced downward, soil dilatancy ahead of the tip is observed in the ϵ_v map (Figure 3.10d); the soil radially around the tip experiences compressive ϵ_r while the soil below the tip experiences tensile ϵ_r (Figure 3.10e). In contrast, the soil radially around the tip experiences tensile ϵ_z while the soil below the tip experiences compressive ϵ_z (Figure 3.10f).

Stress paths represent the evolution of the three-dimensional stress state. This analysis presents stress paths obtained from locations around the anchor and ahead of the tip (e.g., purple measurement spheres in Figure 3.2b) for the last 0.1 m of probe penetration. Figures 3.11a and 3.11b show the stress paths in the $q - p'$ and $e - p'$ planes. The critical state lines (CSLs) obtained from triaxial compression simulations (Figures 3.4c and 3.4d)

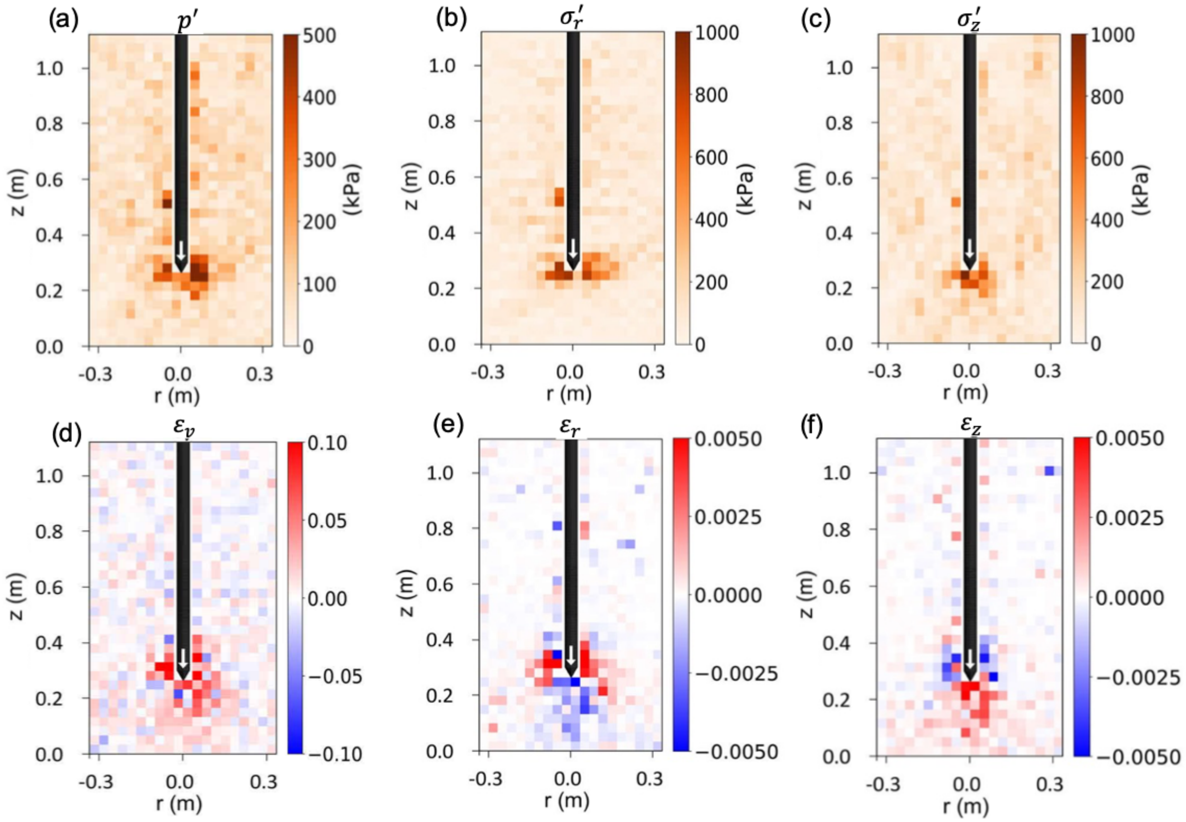

Figure 3.10: Maps of (a) mean (b) radial and (c) vertical effective stresses at the end of the cone penetration (CP) stage ($\overline{N} = 1$) and maps of (d) volumetric, (e) radial and (f) vertical strains for the last 0.1 m of CP. Note that dilatant volumetric strains and compressive strain components are defined as positive.

are included here and used as a reference. In addition, Figure 3.11c shows the influence of the intermediate stress by means of the b value, where b is defined as

$$b = \frac{\sigma'_2 - \sigma'_3}{\sigma'_1 - \sigma'_3} \tag{3.6}$$

Where $b = 0$ indicates the stress state during conventional triaxial testing (i.e.$\sigma'_2 = \sigma'_3$).

The stress paths are the same for the three different simulations (Figures 3.11a–3.11c) because the CP stage is identical for all simulations. As the probe is advanced into the specimen, the particles ahead of the tip are loaded in compression and the stress paths plot slightly above the triaxial CSL, consistent with previous experimental and numerical investigations on cone penetration and pile installation processes (e.g., Jardine et al. [2013]; Jiang et al. [2006]; Sheng et al. [2005]). This is likely because the soil ahead of tip

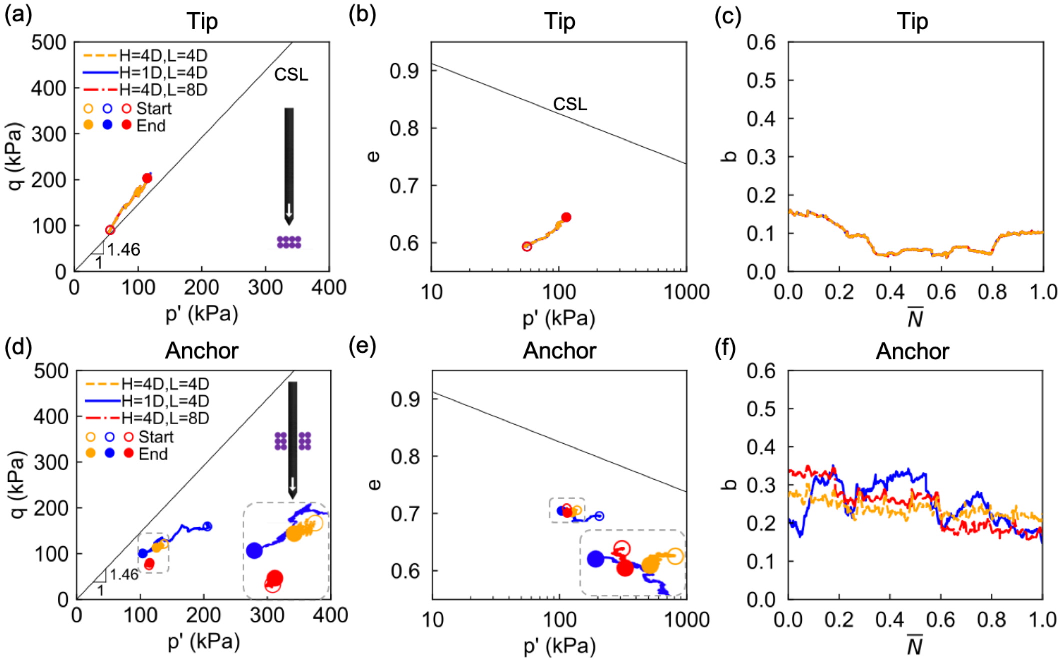

Figure 3.11: Stress paths in $q - p'$ plane and $e - p'$ plane and evolution of b values during the last 0.1 m of the Cone Penetration (CP) stage for soil (a–c) near the tip and (d–f) near the anchors.

has not exhausted its dilatancy potential and has not reached critical state, as shown by the stress paths in the $e - p'$ plane that have not reached the CSL (Figure 3.11b). The stress path near the tip is closer to reaching the CSL in the $q - p'$ plane than in the $e - p'$ plane. While critical state conditions would be expected near the probe tip, it should be considered that the measurement spheres are located 0.1 m below the tip to allow for the subsequent downward movement of the tip during the TA. The b values have magnitudes between 0.05 and 0.15, indicating similar magnitudes of σ'_2 and σ'_3 which closely resemble the stress conditions during conventional triaxial testing.

The stress paths at locations near the anchor indicate that the soil is unloaded as the probe moves downward (Figure 3.11a). The stress path of the soil around the H1L4 anchor shows the greatest decrease in p', while the stress path for the soil around the H4L8 anchor shows the smallest decrease in p', as observed in the Figures 3.11d and 3.11e. In addition, Figure 3.11e shows that the void ratio around the three anchors remains fairly constant during the last 0.1 m of the CP stage because the deformations in these locations are small. The b values near the anchor have magnitudes between 0.33 and 0.18, indicating a greater influence of the intermediate stress.

3.5.2 State of Stresses and Strains during Anchor Expansion (AE)

For all three simulated probes, AE led to an increase in interparticle and particle-probe contact forces at locations around the anchors. Simultaneously, AE led to a decrease in contact forces at locations between the anchors and tips and near the probe tips, as shown by the force chain maps at the end of AE ($\overline{N} = 2$) (Figures 3.12a–3.12c). The cross plots indicate that σ_1' is oriented horizontally around the probes (Figures 3.12d–3.12f), perpendicular to the surface of the expanded anchors. This constitutes a rotation 90° of the principal stresses with respect to that at the end of anisotropic consolidation with $K_0 = 0.5$ and a rotation of 60° to 20° with respect to the end of the CP stage. The σ_1' near the tip decreased in magnitude (i.e., shorter cross length) with respect to the end of CP (i.e., Figure 3.9b), but the orientation of the principal stresses remains relatively unchanged. There is an absence of force chains with a magnitude greater than 50 N between the anchor and the tip, particularly for simulations H4L4 and H4L8, showing the reduction in contact forces at those locations due to arching.

The stress maps for the three simulations indicate that the normal stresses around the anchor increased while the stresses at locations ahead of the anchor decreased, particularly close to the tip. This is shown in Figures 3.13a–3.13i in terms of the difference in normal stresses between the end of the AE ($\overline{N} = 2$) and CP ($\overline{N} = 1$) stages. The increase in mean, radial, and vertical stresses around the anchors is accompanied by soil dilatancy (i.e., positive ϵ_v) owing to the initially dense state of the specimen, as well as radial compressive stains ϵ_r (Figures 3.14a–3.14f). At locations near the probe tip, the mean, radial, and vertical decreased as a result of the anchor expansion (Figures 3.13a–3.13i), which are accompanied by vertical tensile strains (Figures 3.14g–3.14i). It is noted that a greater decrease in stresses occurs during simulations with shorter anchor-tip distance (Simulation H1L4 in Figures 3.13b, 3.13e, and 3.13h). In addition, the longer anchor in Simulation H4L8 deforms a greater volume of soil compared to the shorter anchors

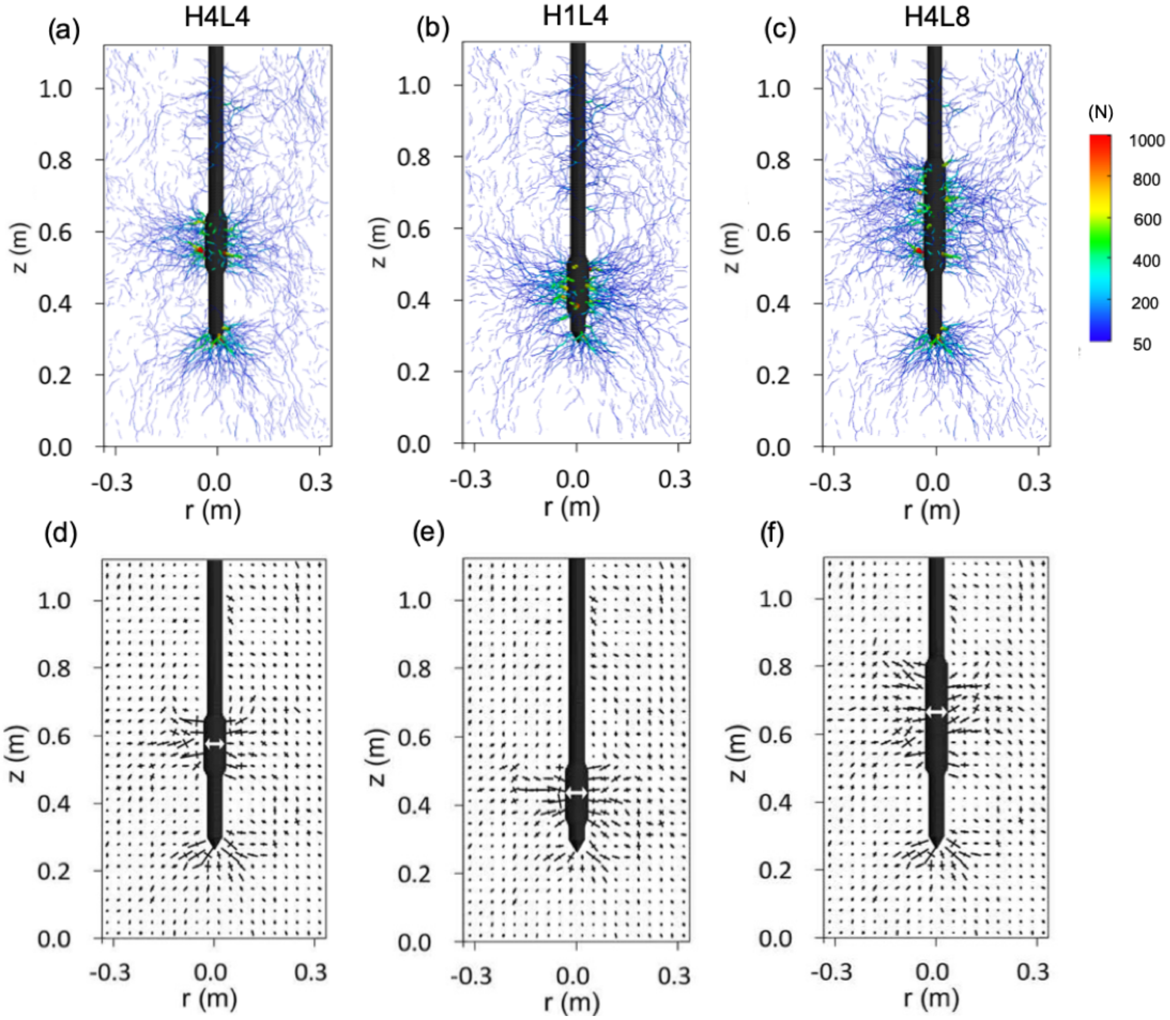

Figure 3.12: (a–c) Soil force chains and (d–f) stress state maps for simulations at the end of Anchor Expansion stage ($\overline{N} = 2$).

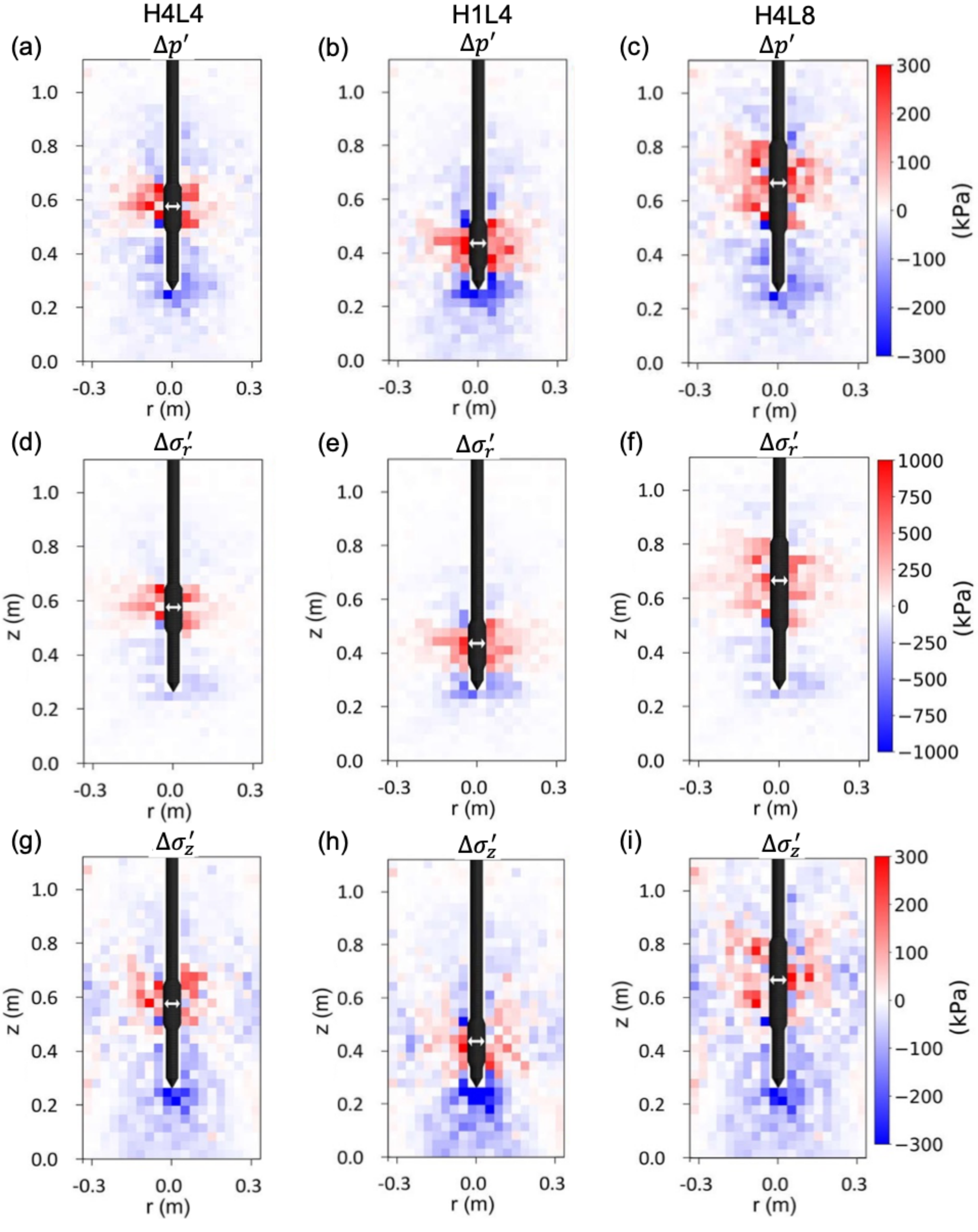

Figure 3.13: Change in (a–c) soil major principal stresses, (d–f) radial stresses, and (g–i) vertical stresses maps at the end of the Anchor Expansion stage ($\overline{N} = 2$).

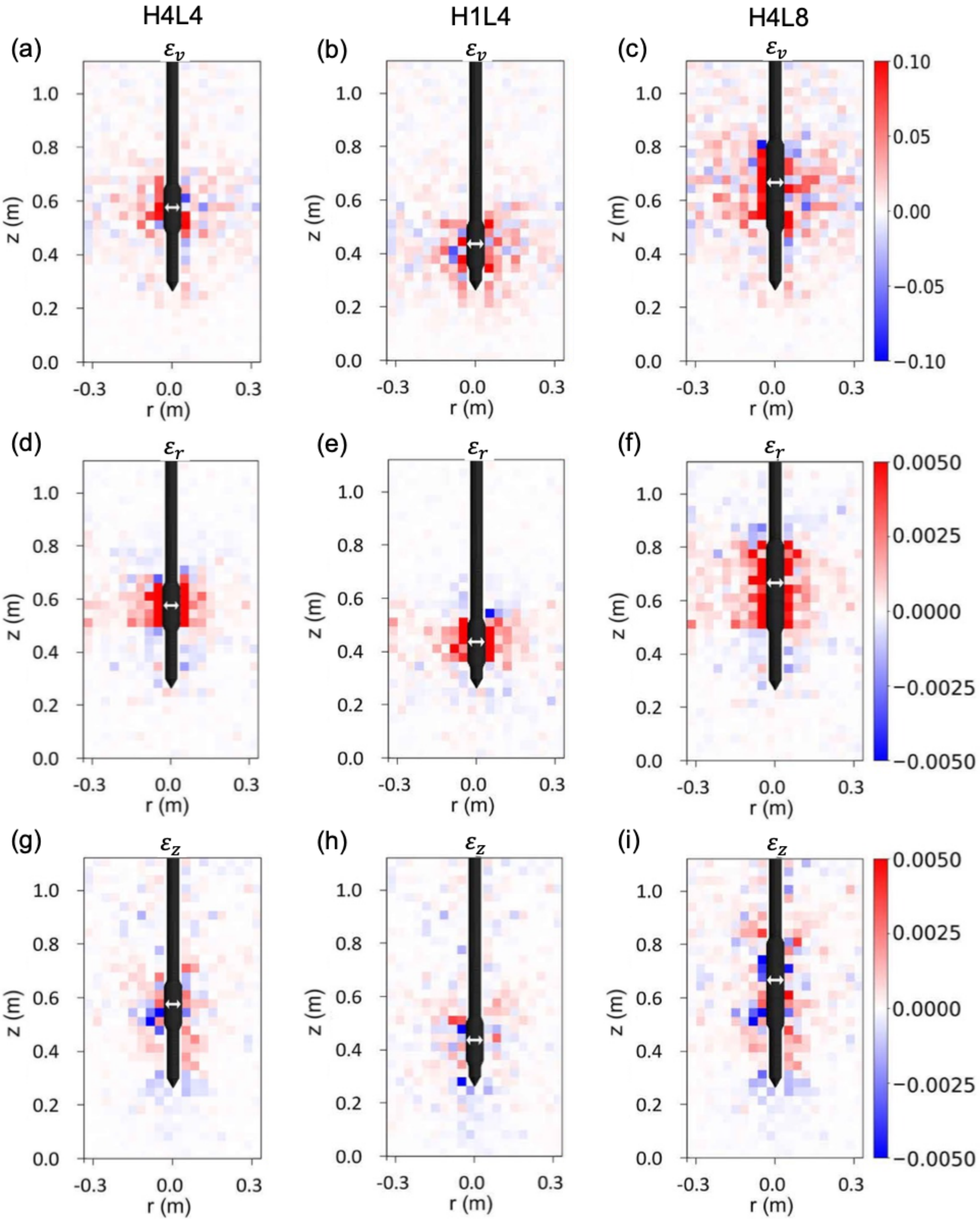

Figure 3.14: (a–c) Soil volumetric, (d–f) radial strain, and (g–i) vertical strain maps for simulations during Anchor Expansion stage. Note that dilatant volumetric strains and compressive strain components are defined as positive.

(Figures 3.14a-3.14i). Altogether, these comparisons highlight the effects of the probe configuration on the alteration of stress states and soil deformations.

The increase in stresses around the expanded anchor are in agreement with the DEM results by Ma et al. [2020] and Huang and Tao [2020]. In addition, the reduction in stresses at locations near the tip have also been reported by Huang and Tao [2020]. The deformations around the cylindrical anchor are in agreement with the shear deformations at the initial stages of inflation around an expanding conforming balloon reported by Ma et al. [2020] (referred to by the authors as the balloon). However, at the latter stages of inflation, the balloon in the Ma et al. [2020] study took a near-circular cross-section which led to compaction and increases in stresses at locations immediately above and below the balloon. In contrast, the state of stresses and deformations of the soil at the ends of the cylindrical anchor modeled in these simulations, as well as that simulated by Huang and Tao [2020], appears to be highly influenced by arching which causes the reported decrease in stresses. This comparison sheds some light on the effects of the anchor shape (i.e. cylindrical versus spherical) on the changes in state of stress and the associated mobilized anchorage forces.

The expansion of the anchor results in a decrease of the soil stresses below the probe the tip, as previously described. These changes in stress produce stress paths that unload along the CSL in the three simulations (Figure 3.15a). Because the volume changes at these locations are small (Figures 3.14a–3.14c), the void ratio only increases slightly while p' decreases (Figure 3.15b). The b-values at locations below the tip increase slightly as the anchor is expanded, likely due to the greatest decrease in vertical effective stresses (Figure 3.13a–3.13i).

The stresses at locations around the anchor increase significantly, as shown by the stress paths that move up and to the right towards the CSL in the $q - p'$ plane (Figure 3.15d). The increase in p' is smallest for the H4L8 simulation owing to the greater length of the anchor, as previously described. The increase in p' is greater for the H1L4 simulation than for the H4L4 simulation. In the $e - p$ plane, the stress paths appear to converge towards the CSL, showing initial contraction (i.e. decrease in e) followed by

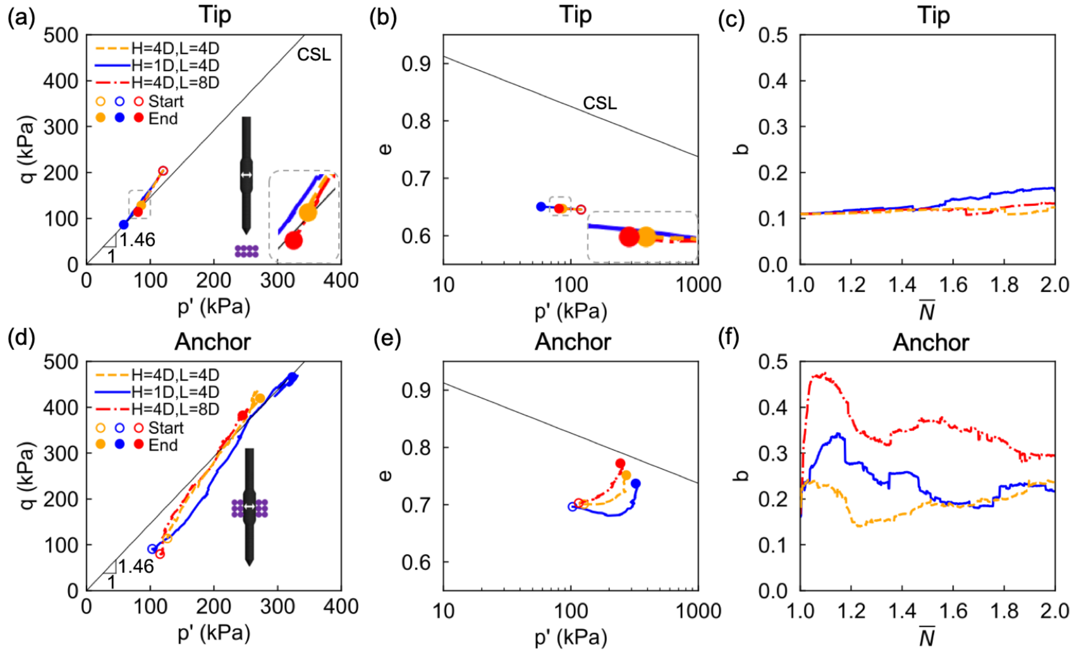

Figure 3.15: Stress paths in $q-p'$ plane and $e-p'$ plane and evolution of b values during the Anchor Expansion (AE) stage for soil (a–c) near the tip and (d–f) near the anchors.

continued dilation (i.e. increase in e) (Figure 3.15e). This increase in void ratio is in agreement with increases in porosity of up to 20% around the balloon anchor reported by Ma et al. [2020]. The b values increase sharply at the initial stages of AE indicating a divergence of the magnitudes of the minor and intermediate principal stresses. At the end of the anchor expansion phase ($\overline{N} = 2$), and b values converge to values between 0.2 and 0.3.

3.5.3 State of Stresses and Strains during Tip Advancement (TA)

This section describes the evolution of the state of stresses and strains during the TA simulation stage. During TA, the tip is displaced downward and the anchor is displaced upward using the force-limited algorithm, such that the tip is displaced downward when Q_t is smaller than F_target and the anchor is displaced upward when F_t is smaller than Ftarget (i.e., Figure 3.6). Figures 3.16a–3.16c present the force chain maps at the end of the TA stage ($\overline{N} = 3$). As shown, force chains with greater magnitude are concentrated near the tip and around the anchor. Stronger force chains around the probe tip occur at the end of TA than at the end of AE (i.e., Figures 3.12a–113.12c), indicating that as the tip was displaced downward the tip resistance was remobilized. Some force chains are oriented horizontally around the expanded anchor. However, strong force chains are also present at the upper base of the anchors, reflecting the mobilization of the P_b resistance as the anchor is displaced upward (i.e., Figures 3.7a, 3.7d and 3.7e). The cross plots shown in Figures 3.16d–3.16f indicate similar trends at locations near the tip and around the anchor as described for the CP and AE stages. The most significant rotation of principal stresses can be observed at the top base of the anchor, with the major principal stress are oriented at angles between 30 and 50° from horizontal.

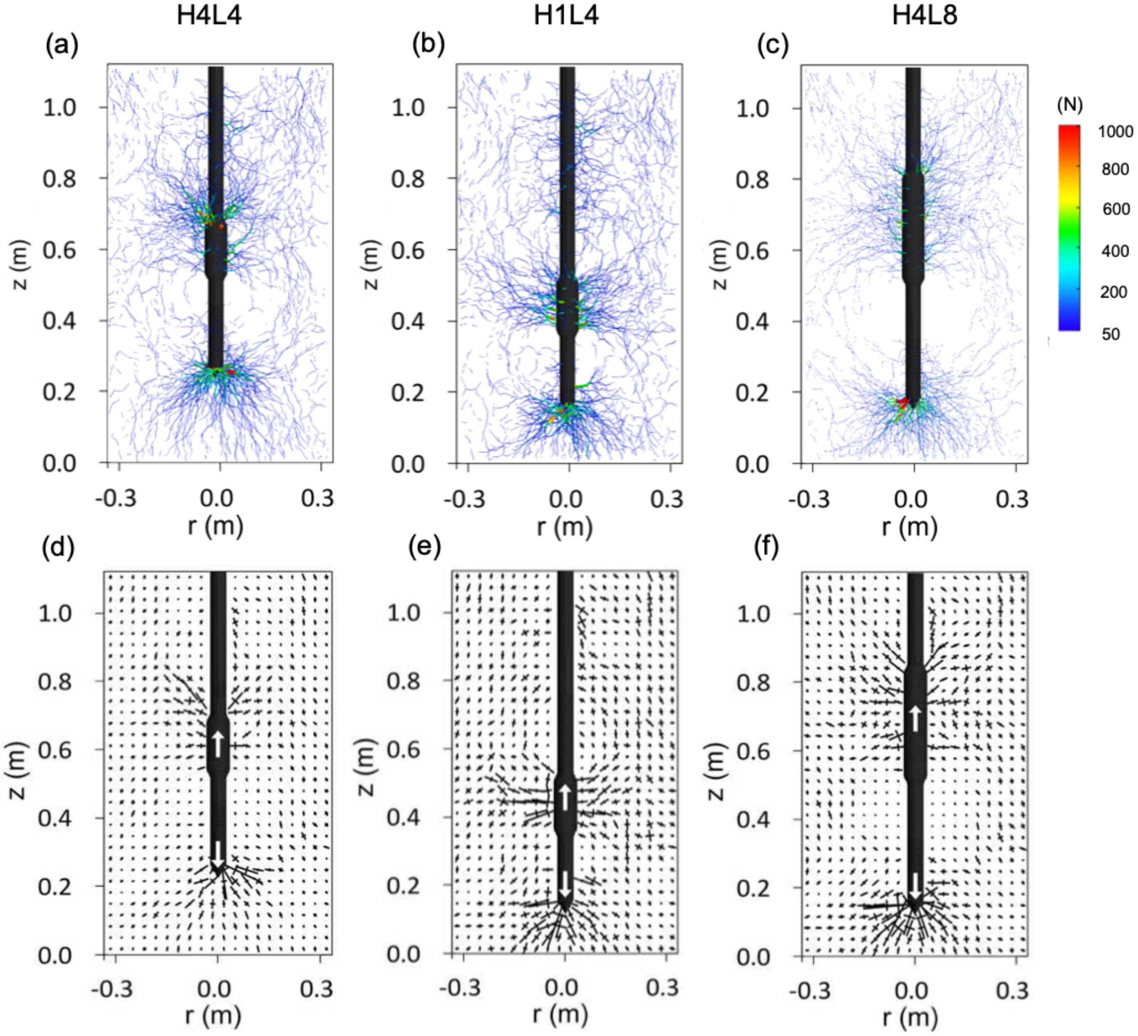

Figure 3.16: (a–c) Soil force chain and (a–c) stress state maps for simulations at the end of the Tip Advancement stage ($\overline{N} = 3$).

The stress maps for the mean, radial, and vertical stresses, expressed in terms of the difference in stress at the end of the TA and AE stages, indicate an increase in stresses at locations below the tip and above the anchor, and decreases in stresses at locations around the anchor and behind the tip (Figures 3.17a–3.17i). A greater increase in stresses near the tip occurs for probes with shorter H (Figures 3.17b, 3.17e, and 3.17h) and longer anchor length L (Figures 3.17c, 3.17f, and 3.17i) because during these simulations the tip was displaced by a greater distance, as shown in Figures 3.8b–3.8c. The probe with shorter H achieves this by decreasing q_c to a smaller magnitude after AE, whereas the probe with longer L mobilizes a greater reaction force due to its greater contact area with the surrounding particles. The strain maps presented in Figures 3.18a–3.18i show similar trends near the probe tip as those observed at the end of the CP stage (i.e., Figures 9d–9f), with positive (dilative) volumetric and vertical (compressive) strains and negative (tensile) radial strains below the tip and positive (compressive) radial strains and negative (tensile) vertical strains around the probe shoulder. The strains around the anchor show small contractive volumetric strains which possibly lead to the decrease in anchor friction force. Additionally, greater strains are shown behind the anchor base due to the anchor's upward movement.

The stress paths during the TA phase at locations below the tip for the first 0.036 m of downward tip displacement are presented, showing similar trends as described for the CP stage. Namely, p' increases and the stress paths follow the CSL in the $q - p'$ plane (Figure 3.19a). In the $e - p'$ plane, the stress paths show slight dilation accompanied with increase in p' (Figure 3.19b). As previously described for the CP stage, the b values are between 0.1 and 0.15 (Figure 3.19c). The stress paths at locations around the anchor indicate a decrease in p' while the stress paths follow the CSL (Figure 3.19d) with minimal changes in void ratio (Figure 3.19e). The p' around the anchor in simulation H4L4 decreased by a greater amount because at this stage of the simulation (0.036 m of tip displacement), the anchor had displaced 0.04 m upward (Figure 3.8a), whereas the anchors in the H1L4 and H4L8 simulations had displaced a smaller amount (Figures 3.8b and 3.8c). The b-values around the anchor stay relatively constant at values between 0.2

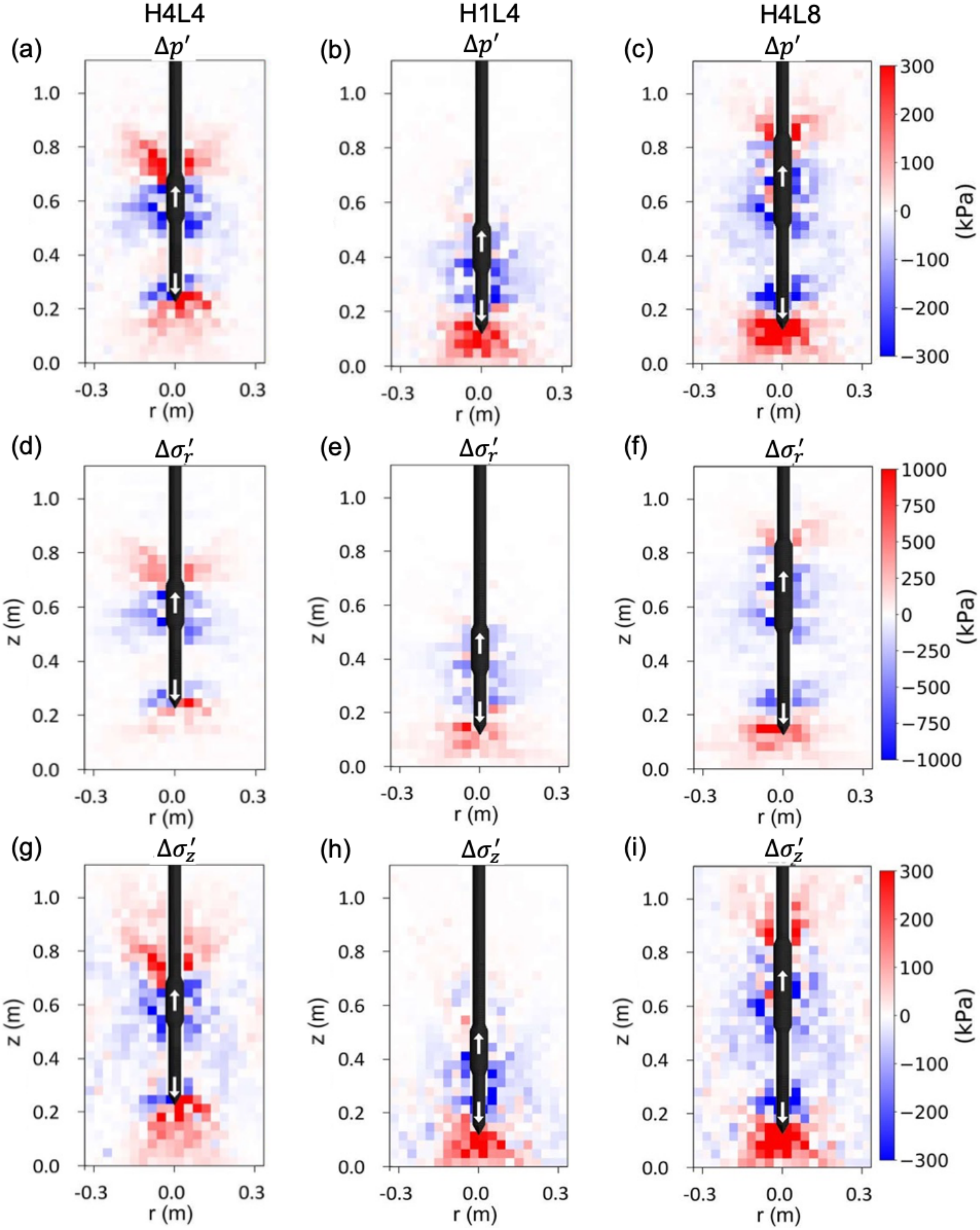

Figure 3.17: Change in (a–c) soil major principal stresses, (d–f) radial stresses, and (g–i) vertical stresses at the end of the Tip Advancement stage ($\overline{N} = 3$).

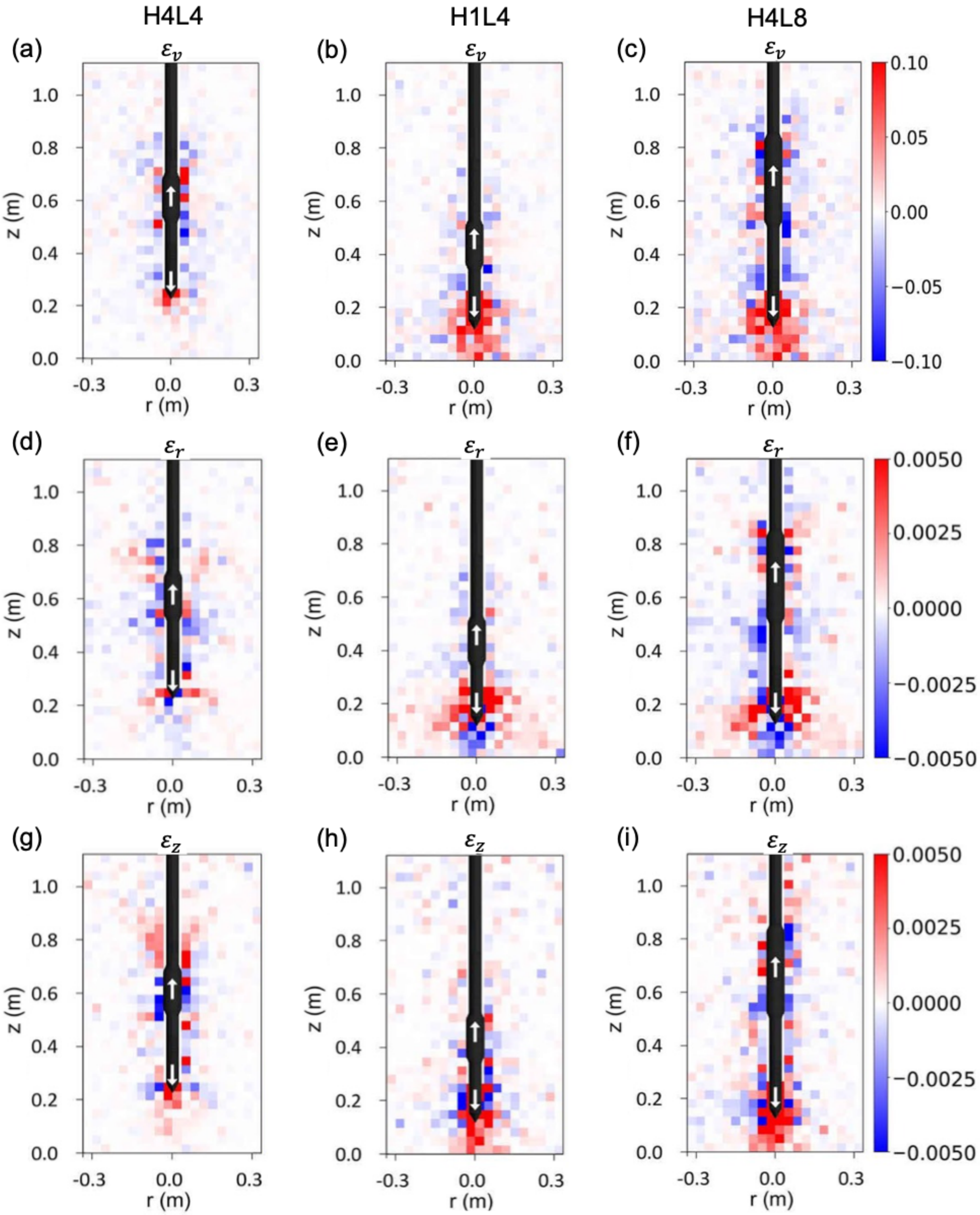

Figure 3.18: (a–c) Soil volumetric strains, (d–f) radial strains, and (g–i) vertical strains strain maps for simulations during the Tip Advancement stage. Note that dilatant volumetric strains and compressive strain components are defined as positive).

and 0.3 (Figure 3.19f), indicating a greater influence of the intermediate major stress as compared to locations below the tip.

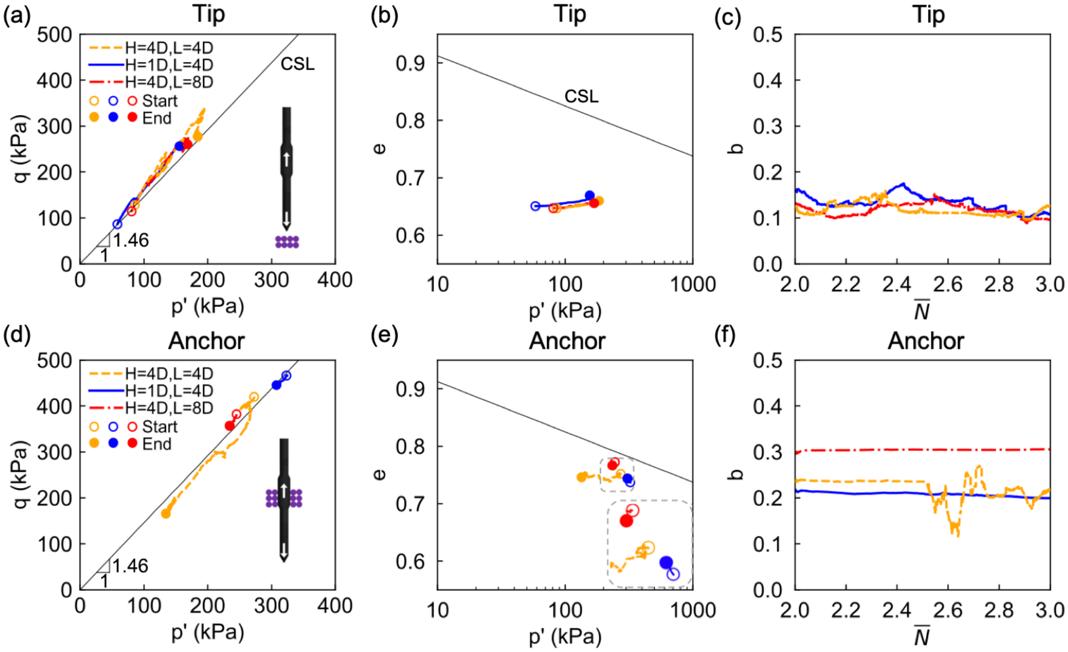

Figure 3.19: Stress paths in $q-p'$ plane and $e-p'$ plane and evolution of b values during the Tip Advancement stage for soil (a–c) near the tip and (d–f) near the anchors.

3.6 Conclusions and Future Needs

This study presents a 3D discrete element modeling analysis of the alteration of the state of soil stresses around a probe that employs a the ‘anchor-tip’ burrowing strategy. The penetration simulations are performed in a virtual calibration chamber that applies constant stress boundary conditions to an medium-dense assembly to model deep penetration simulations. The DEM simulation parameters are calibrated to reproduce realistic coarse-grained soil behavior (i.e. stress-dependent shear strength and dilatancy, convergence to critical state, penetration resistances typical of sands and gravels). Simulations are performed on three different bio-inspired probes to explore the effects of the anchor-tip distance and the anchor length.

During the initial stage the bio-inspired probe penetration simulations, termed Cone Penetration, the probe is advanced into the specimen confined in the VCC in a similar manner as a CPT sounding. The results are in agreement with published trends, with contact forces concentrating near the probe tip which lead to increases in mean, radial, and vertical effective stresses, rotation of principal effective stresses to directions that are close to perpendicular to the surface of the probe's conical tip, and a gradual convergence towards the critical state line in the stress and compression planes of the soil located below the probe tip.

The second stage consists of radially expanding the cylindrical anchor from its initial diameter to a diameter 50% greater. As the anchor is expanded, large contact forces are generated radially around the anchor leading to large increases in mean, radial, and vertical effective stresses and a rotation of 90° the major principal effective stresses. Significant arching is developed at locations above and below the anchor, leading to tensile strains and a decrease in effective stresses at locations near the probe tip. The soil at locations near the probe continues to converge towards the CSL, with the soil around the anchor dilating due to its initially dense state.

In the Tip Advancement stage, a dynamic control algorithm is used to displace the tip and anchor such that only the probe portion (i.e. tip or anchor) that mobilizes a force smaller than the target force is displaced. Strong contact forces develop at the upper base of the anchor due to the mobilization of a bearing anchor pressure which results in increases in stresses and rotation of principal stresses. The stresses within the soil around the anchor decrease due to contractive volumetric strains, leading to the reduction in the anchorage friction force. The soil response around the tip is similar to that during Cone Penetration, leading to the remobilization of the tip resistance.

The results and analysis of this study expand on the current understanding of the soil failure mechanisms involved in the penetration behavior of bio-inspired probes with radially expanding sections which considers the effects of the probe configuration. The use of the force limited algorithm revealed that that longer anchors and smaller anchor-tip distances are more advantageous for the tip advancement process because they lead to greater arching-induced reductions in tip resistance and to mobilization of greater anchorage forces. In the future, a number of advances should be implemented to further understand the behavior of this type of bio-inspired probes and to ultimately lead to their successful deployment in the field: (i) include in the simulation the processes of anchor retraction along with expansion of a second anchoring section near the probe tip in order to model entire self-burrowing cycles, (ii) validate the simulation results with experimental results to assess the possible effects of the upscaled particle sizes and the stress-controlled VCC employed in this study, (iii) investigate the effects of soil parameters such as void ratio, friction angle, and particle size distribution, and (iv) simulate other more complex bio-inspired burrowing strategies in conjunction with anchor expansion, such as tip vibration.

3.7 Acknowledgements

This material is based upon work supported in part by the Engineering Research Center Program of the National Science Foundation under NSF Cooperative Agreement No. EEC-1449501). The first and second authors were supported by the National Science Foundation (NSF) under Award No. 1942369. Any opinions, findings, and conclusions or recommendations expressed in this material are those of the author(s) and do not necessarily reflect those of the National Science Foundation.

Chapter 4

DEM Simulations of a Bio–Inspired Site Characterization Probe with Two Anchors

---

At the time of writing the dissertation, this chapter is under review by Acta Geotechnica and is presented herein with minor edits under the following citation.
Chen Y, Martinez A, DeJong J (2022) DEM simulations of a bio–Inspired site characterization probe with two anchors. In review by Acta Geotechnica.

4.1 Abstract

Insufficient reaction force generated by installation equipment is one of the main challenges in soil penetration processes, which can lead to refusal conditions or pullout failures during in–situ testing, soil sampling, and pile driving. Recent research has focused on developing probes for site characterization that can generate the reaction force required for probe insertion without external equipment. This study presents the results of 3D discrete element modeling (DEM) simulations of probes with single or dual anchors performed in a virtual calibration chamber (VCC) that applies a constant overburden pressure of 100 kPa. Following penetration of the probe to the desired depth, the anchors are expanded and then a single tip advancement stage is simulated using either displacement–controlled or force–limited motion. The simulation results indicate that dual–anchor probes generate

greater capacities than single–anchor probes due to the mobilization of additional bearing forces. However, the capacity per anchor increases with increasing inter–anchor spacing due to the development of an active zone below the leading anchor which produces a decrease in effective stresses around the trailing anchor. During expansion of the anchors, the penetration resistances decrease due to the alteration of stresses around the probe tip. The simulation results are used to define a dimensionless 3D space to determine the combination of probe configurations that enable self–penetration; these configurations include greater inter–anchor spacings, smaller anchor–tip distances, and greater anchor expansion magnitudes.

4.2 Introduction

The process of soil penetration is ubiquitous in geotechnical engineering design and construction, necessary for activities such as soil sampling, drilling, excavation, pile driving, and tunneling. Soil penetration can present a number of challenges in geotechnical problems, including (i) the need to generate sufficient reaction force to overcome the soil penetration resistance in shallow stiff layers (i.e. hardpans, gravels) and at greater depths, (ii) the need to have access routes for the site investigation equipment (i.e. 20-ton CPT truck, drill rig) to reach certain testing location (i.e. toe of a dam, forested, remote, or urban areas), and (iii) the significant environmental impact to civil engineering projects [Raymond et al., 2020; Purdy et al., 2020]. While there are current solutions for penetrating soils with light equipment [Jol, 2008; Navarrete et al., 2021], there is a motivation to develop tools that provide measurements commonly used in geotechnical design practice, such as the Cone Penetration Test (CPT) tip resistance, Pressuremeter (PMT) limit pressure, Dilatometer (PMT) pressures, or shear wave velocity.

Recent research has investigated the burrowing strategies employed by animals and plants in search of solutions to overcome the challenges associated with soil penetration processes. For example, Dorgan [2015] provides a description of the strategies used by different animals to burrow in cohesive and non–cohesive soils from a biological perspective while Martinez and Frost [2017] provides a summary of the geomechanical processes involved in the burrowing of tree root systems, caecilians, razor clams, and earth and marine worms. Additional information regarding the biological aspects of animal and plant burrowing, such as anatomical and energetic constraints, can be found in [Barnett et al., 2009; Kurth and Kier, 2014; Murphy and Dorgan, 2011; Ruiz et al., 2015; Sadava et al., 2009; Trueman, 1968a,c,b,d].

In the field of geotechnical engineering, some studies have explored bioinspired foundation and anchorage systems. For example, O'Hara and Martinez [2020] and Martinez and O'Hara [2021] performed laboratory and centrifuge tests on the snakeskin–inspired surfaces and piles, which exhibited interface friction directionality. Zhong et al. [2021] analyzed the soil deformations and load transfer induced by snakeskin–inspired piles using 2D DEM simulations. Also, Mallett et al. [2018b] investigated the soil deformation patterns and quantified the failure mechanisms around tree root-inspired anchors, Burrall et al. [2020] performed pullout tests on the orchard trees which indicated that root systems are 6 to 10 times more material efficient than conventional pile system, and Anselmucci et al. [2021a,b] used X-ray computed tomography to quantify the deformations around roots growing in sandy soil.

Previous numerical studies have investigated the behavior of bio–inspired probes and probe components with the goal of identifying configurations and strategies that allow a probe to generate the reaction force needed to overcome the soil penetration resistance. This concept is referred to as self–penetration or self–burrowing throughout this chapter, and has been investigated in probes composed of an expandable anchor and a tip (i.e. employing the anchor–tip strategy). For example, Huang and Tao [2020] performed 3D DEM penetration simulations to conclude that that less energy was required for soil penetration subsequent to anchor expansion in comparison to direct penetration. Chen et al. [2021] and Ma et al. [2020] used DEM simulations to show that expansion of an anchor produced a reduction in the penetration resistance, while Chen et al. [2022] explored the geomechanical processes that lead to such reduction in penetration resistance, which include arching and rotation of principal stresses. Martinez et al. [2020] used cavity expansion in combination with data from field tests to conclude that dense sands represent the greatest challenge for self–penetration in probes that employ the anchor–tip strategy.

Researchers have developed laboratory–scale prototypes to evaluate burrowing performance. Cortes and John [2018] performed penetration tests on a miniature cone penetration probe that has a balloon near the cone tip and showed that reduction in penetration resistance takes places when the balloon is inflated. Ortiz et al. [2019] performed horizontal constant–force penetration tests using a soft robot to show that radial body expansion in combination with lateral tip oscillations facilitated a greater distance of penetration. Tao et al. [2020] developed a soft robotic prototype which was able to burrow up to the soil surface by cyclic elongation–contraction motion. Borela et al. [2021] used an X–ray CT scan to show that more robust anchorage and a greater tip advancement are achieved in loose sand than in dense sand. Naclerio et al. [2021] developed a root–like robot that uses tip extension to reduce the friction along the shaft and air fluidization to reduce the soil penetration resistance. The above studies illustrate the challenges associated with generating sufficient anchorage forces to overcome the soil penetration resistance, which has limited the deployment of the experimental prototypes developed to date to shallow soil conditions (i.e. smaller than 50 cm). The majority of these studies have focused on enabling self–penetration by decreasing the penetration resistance [Chen et al., 2021; Cortes and John, 2018; Huang and Tao, 2020; Ma et al., 2020; Ortiz et al., 2019], while less attention has been placed on increasing the magnitude of anchorage that can be generated. Deployment of multiple anchors can be used as a strategy to improve the anchorage capacity; in fact, organisms such as earth and marine worms that employ peristalsis locomotion deploy multiple anchorage points along their body.

The goal of this chapter is to explore the anchorage capacity and tip advancement ability of a bio–inspired probe that deploys two anchors in conditions relevant to geotechnical site characterization. This is done by means of 3D DEM simulations of the penetration process of probes with two anchors arranged in different configurations in a virtual calibration chamber (VCC) that applies K_0 conditions with an overburden pressure of 100 kPa to the granular assembly. Detailed analysis is presented on the interactions between the two anchors, the interactions between the anchors and the tip, and the anchor configurations that best enable self–penetration.

4.3 Model Description

The DEM simulations are performed using the PFC 3D software (Version 5.0, Itasca). The model consists of a virtual calibration chamber, a probe, and particles (Fig. 4.1a). The VCC is simulated by a top wall, a bottom wall, and 12 radial ring walls, which together create a chamber with a diameter ($D_{chamber}$) of 0.7 m and a height ($H_{chamber}$) of 1.2 m. All boundary walls are servo–controlled to apply a constant stress boundary condition with the vertical and radial confining stresses equal to 100 kPa and 50 kPa, respectively (i.e. $K_0 = \sigma'_r/\sigma'_v = 0.5$). The radial ring walls are used to maintain a uniform distribution of radial boundary stress along the chamber height as shown in Fig. 4.2. The probe has a diameter (D_{probe}) of 0.044 m and an apex angle of 60°, which are equivalent to the values in a 15 cm^2 cone penetration test (CPT) probe. The granular assembly contained in the VCC is poorly–graded and consists of about 200,000 spherical particles with a mean diameter (D_{50}) of 0.0144 m, a coefficient of uniformity (C_U) of 1.2, and a coefficient of curvature (C_C) of 0.96. The assemblies are prepared to an initial void ratio of 0.61. More detailed information regarding the grain size distribution of the granular assembly and the specimen creation procedure can be found in Chen et al. [2021, 2022].

The simulated particles were upscaled to reduce the computational cost, as is commonly done in DEM simulations. When upscaling particle sizes, it is important to ensure that the relative dimensions between the chamber, probe, and particles are reasonable to prevent particle size effect. The chamber–to–probe ($D_{chamber}/D_{probe}$) and probe–to–particle (D_{probe}/D_{50}) diameter ratios in this study are 15.9 and 3.1, respectively. Previous studies such as Arroyo et al. [2011]; Butlanska et al. [2014]; Ciantia et al. [2016, 2019a]; Chen et al. [2021]; Khosravi et al. [2020]; Zeng and Chen [2016]; Zhang et al. [2019] have demonstrated that $D_{chamber}/D_{probe}$ and D_{probe}/D_{50} ratios between 10.5 and 16.6 and between 2.7 and 4.4, respectively, allow for minimized particle scale and chamber size effects to properly simulate penetration problems in 3D DEM simulations. Detailed discussion regarding scale effects can be found in Chen et al. [2021, 2022]; Khosravi et al.

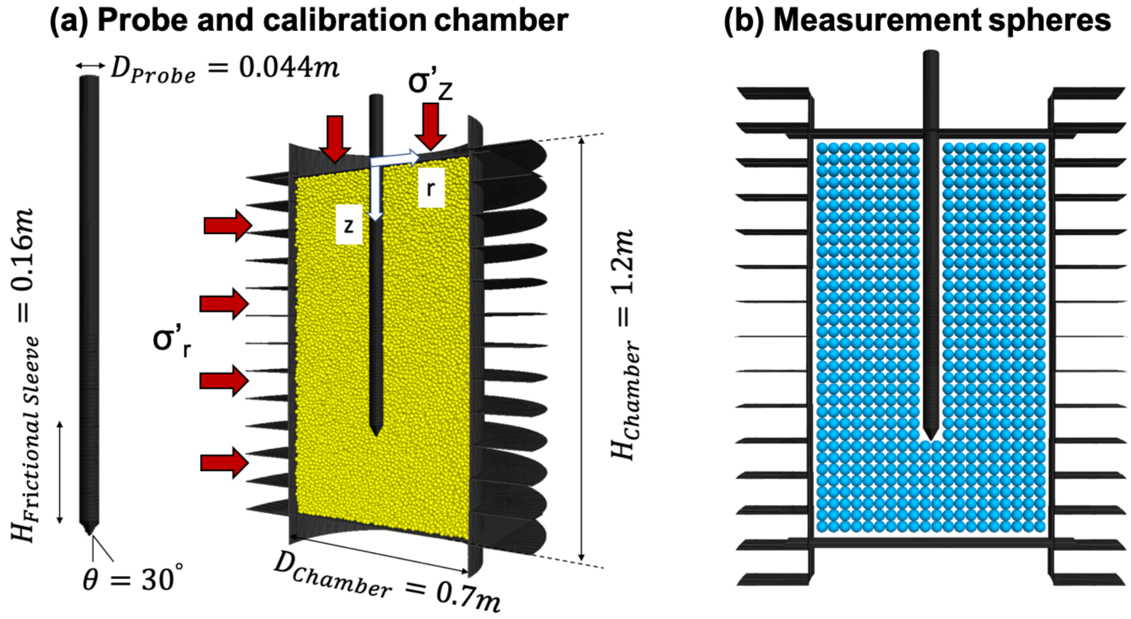

Figure 4.1: DEM simulation model. (a) Simulated probe and virtual calibration chamber, and (b) measurement spheres in the r–z plane.

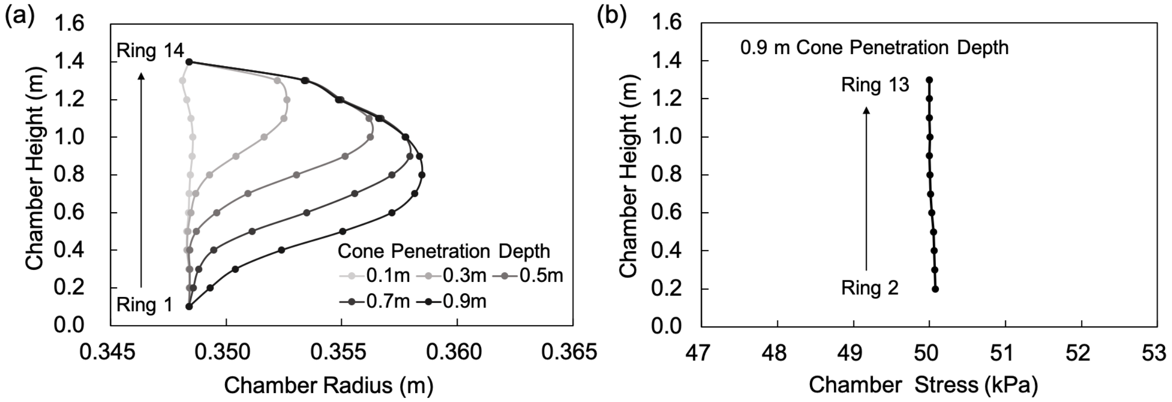

Figure 4.2: Distribution of (a) chamber radius and (b) chamber stress along the chamber height. Note that ring 1 and ring 14 are not in contact with the particles, therefore they are not shown in (b).

[2020]. The simulation parameters were taken from Chen et al. [2021, 2022], which are listed in Table 4.1. Soil particle interactions are modeled using a linear contact model with rolling resistance, where the particle normal stiffness is proportional to its diameter ($k_n/d = 10^8 N/m^2$) and the normal–to–shear stiffness ratio (k_n/k_s) is 1.5. The sliding and rolling friction coefficients (μ and μ_{rr}) are 0.4, where the μ_{rr} provides a resistance to particle rotations which simulates the interlocking effect of particle angularity [Ai et al., 2011; Wensrich and Katterfeld, 2012]. The particle–anchor friction coefficient (μ_p) is 0.3, which is similar to that measured experimentally for conventional CPT friction sleeves [Martinez and Frost, 2017]. The particle and boundary wall friction coefficient (μ') is set to be 0.1 to ensure numerical stability in the simulation. In a vertical r–z plane (Fig. 4.1b), 628 measurement spheres with a diameter (D_{MS}) of 0.033 m are uniformly distributed to measure soil stresses. The measurement sphere–to–mean particle volume ratio is about 12.0.

Table 4.1: DEM simulation parameters.

Input Parameter	Symbol	Value
Normal Stiffness to Particle Diameter (N/m^2)	k_n/d	1.00E+08
Normal to Shear Stiffness Ratio for Particles	k_n/k_s	1.5
Normal Stiffness of Probe (N/m)	k_{np}	1.42E+07
Shear Stiffness of Probe (N/m)	k_{np}/k_{sp}	9.47E+06
Sliding Friction Coefficient	μ	0.4
Rolling Friction Coefficient	μ_{rr}	0.4
Ball–anchor Friction Coefficient	μ_p	0.3
Ball–wall Friction Coefficient	μ'	0.1
Particle Density (kg/m^3)	G_s	2650

The modeling parameters were chosen such that the simulated particle assembly exhibits a behavior typical of coarse–grained soils. While a detailed discussion regarding the selection of the simulation parameters can be found in Chen et al. [2021, 2022]; Kuei et al. [2020], select results of triaxial compression simulations under four different confining stresses are plotted in Fig. 4.3a–c to highlight the response of the assemblies. The triaxial result show expected sand–like soil behaviors: greater peak and residual deviatoric stresses (q), smaller peak stress ratios (q/p'), and smaller dilatancy are mobilized for specimens confined under higher vertical stress. In addition, the stress ratios at large axial strains reach a unique, critical state value. In addition, penetration resistance (q_c) friction sleeve (f_s) measurements, as well as Soil Behavior Type (SBT) classification [Robertson, 2010], at varying overburden stresses show that the simulated granular assembly exhibits a penetration behavior characteristic of medium dense coarse–grained soils. This data is not included here for the sake of brevity; a detailed description of the results and trends can be found in Chen et al. [2021].

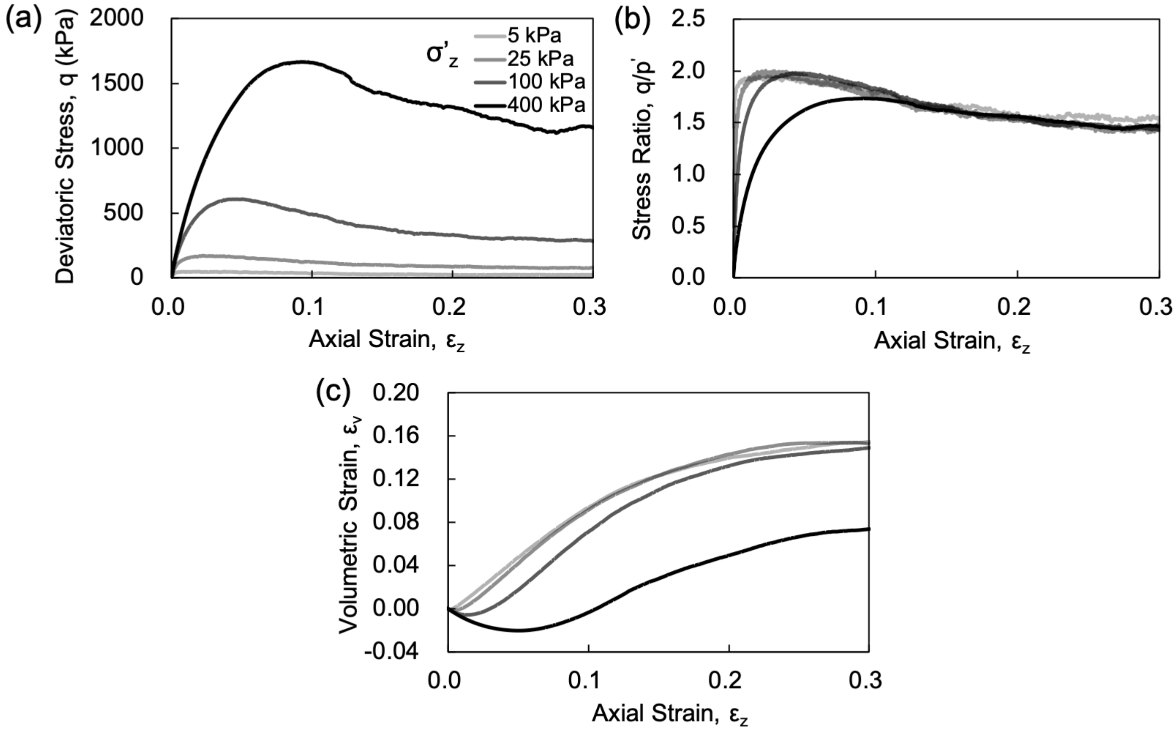

Figure 4.3: Results of triaxial compression simulations. Evolution of (a) deviatoric stress, (b) stress ratio, and (c) volumetric strain with axial strain.

Fig. 4.4a depicts the simulated probe, which can be configured with one or two anchors. The probe configuration is characterized by anchor length (L), inter–anchor spacing (S), anchor–tip distance (H), and anchor expansion magnitude (EM). Each complete simulation models three stages: initial direct pushing stage termed cone penetration (CP), followed by expansion of the anchor(s) (AE), and then by tip advancement (TA), as shown in Fig. 4.4b. During CP stage the probe is displaced downward into the soil at a constant speed of 0.2 m/s to a depth of 0.9 m, during which the mobilized tip resistance (q_c) and sleeve friction (f_s) are calculated as follows:

$$q_c = \frac{4 \sum_{i=1}^{N} Q_{ztip,i}}{\pi D_{probe}^2} \tag{4.1}$$

$$f_s = \frac{\sum_{i=1}^{N} Q_{zsleeve,i}}{L_{sleeve} \pi D_{probe}} \tag{4.2}$$

where $Q_{ztip,i}$ is the vertical component of the contact force i acting on the probe tip, $Q_{zsleeve,i}$ is the vertical component of the contact force i acting on the friction sleeve whose length (L_{sleeve}) of 0.16 m is equal to that of a CPT friction sleeve, and N is the total number of vertical contact forces acting on the tip or sleeve. All simulations begin with the same CP stage to ensure the same initial conditions for the AE and TA stages for all simulations. During the AE stage, the anchor(s) are radially expanded at a rate of 0.2% per second of the probe's initial diameter ($D = 0.044m$) until the target EM is achieved, where EM is defined as:

$$EM = \frac{D_{anchor}}{D_{probe}} - 1 \tag{4.3}$$

During this stage, the radial and bearing anchor pressures (P_a and P_b) are measured (Fig. 4.4b) and the radial and bearing anchor forces (F_n and F_b) are calculated as follows:

$$F_{n(j)} = 2\pi P_{a(j)} L D_{anchor} \tag{4.4}$$

$$F_{b(j)} = \frac{\pi}{4} P_{b(j)} (D_{anchor}^2 - D_{probe}^2) \tag{4.5}$$

where D_{anchor} is the anchor diameter after expansion and the subscript j only exists for dual anchor probes with $j = 1$ representing the top anchor and $j = 2$ representing the bottom anchor. The distance between the anchor and tip was varied between $0.5D_{probe}$ and $6D_{probe}$ equivalents, based on the results from Chen et al. [2021] that indicated that an H of $4D_{probe}$ equivalents is the maximum distance that allows for self-penetration. The close proximity between the anchor and the tip will have an important effect on the CPT f_s measurement; therefore, the f_s measurement was not recorded during the AE and TA stages.

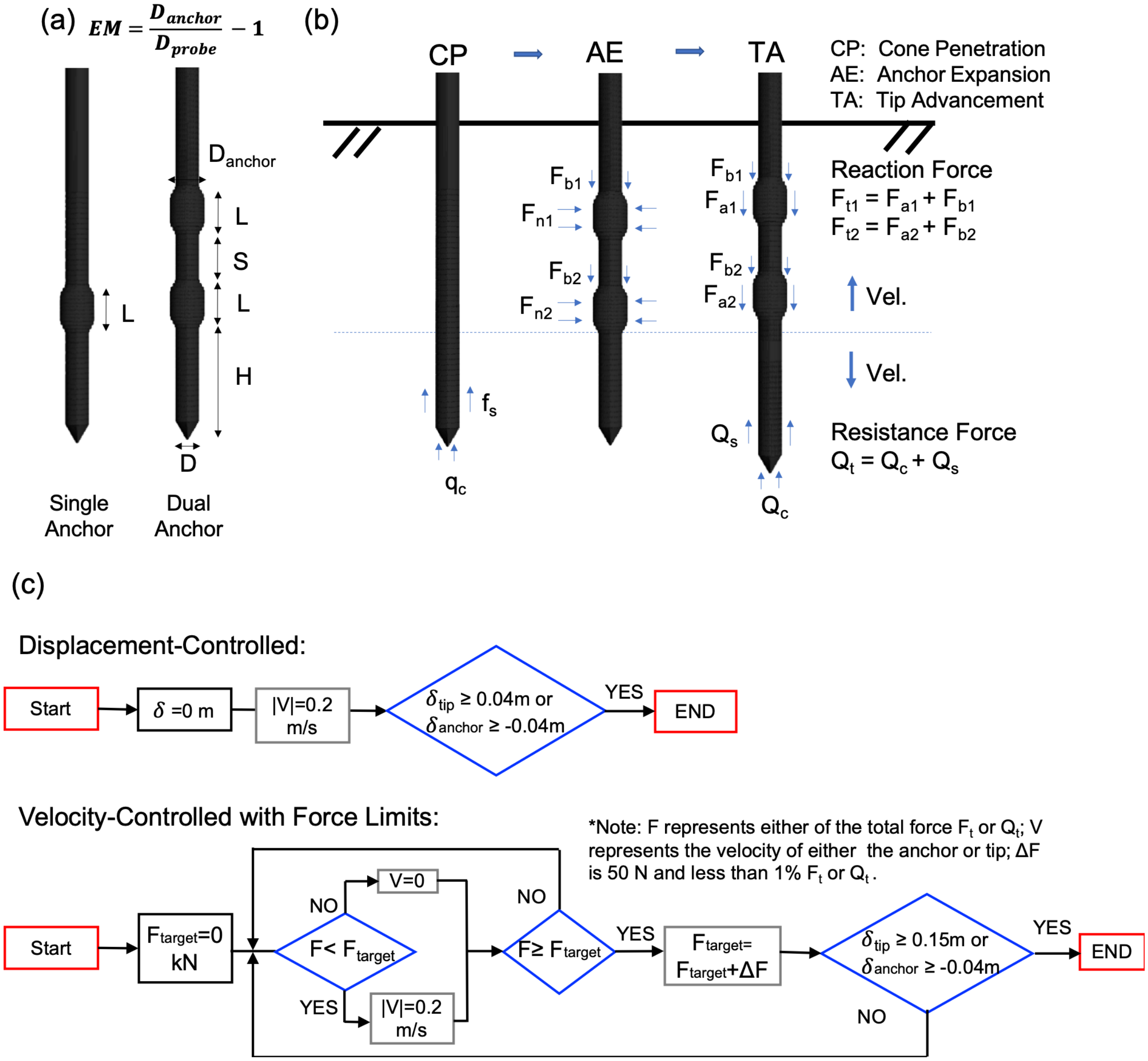

Figure 4.4: Results of triaxial compression simulations. Evolution of (a) deviatoric stress, (b) stress ratio, and (c) volumetric strain with axial strain.

In the TA stage, the anchors are displaced upward and the tip is displaced downward using a displacement–controlled algorithm or a velocity–controlled algorithm with force limits (referred to as force-limited algorithm) (Fig. 4.4c). During the displacement–controlled simulations, the probe anchor(s) and tip are displaced upward and downward, respectively, at a constant velocity of 0.2 m/s. During the force-limited simulations, a target force (F_{target}) is used to decide which of the probe sections is displaced at a constant velocity of 0.2 m/s. When either probe section (i.e. tip or anchor) mobilizes the F_{target} magnitude, it is assigned a velocity of zero. Once both probe sections mobilize F_{target}, the F_{target} is increased by $50N$ (i.e. $\Delta F = 50N$). The F_{target} has an initial value of $50N$ and the ΔF magnitude was determined based on a calibration exercise showing that the simulation results are insensitive to ΔF as long as it is smaller than 100 N. It is noted that the anchor force and the tip resistance force are not always equal during the TA stage but they reach equal values at the end of each loading increment. In either displacement-controlled or force-limited simulations, the TA stage is stopped once a tip displacement of 4 cm or an anchor displacement of 15 cm are reached. This tip displacement limit was chosen based on previous simulations on single anchor probes [Chen et al., 2021] showing that tip resistance is fully or nearly remobilized during the TA stage at displacements smaller or equal to 4 cm. During the TA stage, the overall length of the probe increases due to the movement in opposite directions of the tip and anchor. This is accommodated by an inner wall located between the anchor and tip which avoids particles from moving inside the probe. The properties assigned to this wall are the same as for the remaining of the probe.

During the TA stage, the bearing anchor force (F_b), friction anchor force (F_a), tip resistance force (Q_c), and sleeve friction force (Q_s) are calculated using Eqs. 4.5-4.8.

$$F_{a(j)} = 2\pi P_{a(j)} L D_{anchor} \mu_p \tag{4.6}$$

$$Q_c = \frac{\pi}{4} q_c D_{probe}^2 \tag{4.7}$$

$$Q_s = \pi f_{st} D_{probe} \tag{4.8}$$

where f_{st} is the average shear stress along the probe shaft. The total reaction force (F_t)

and total resistance force (Q_t) are then calculated as follows:

$$F_t = \sum_{j=1}^{N_a} [F_{a(j)} + F_{b(j)}] \tag{4.9}$$

$$Q_t = Q_c + Q_s \tag{4.10}$$

where N_a is the number of anchors. The simulations remain in a quasi–static condition throughout the CP, AE, and TA stages, as evidenced by the inertial numbers (I) which are between 2.1×10^{-5} and 7.2×10^{-4}. These values satisfy the criteria ($I \leq 10^{-3}$) for maintaining quasi–static conditions [Combe and Roux, 2009; O'Sullivan, 2011; Radjai and Richefeu, 2009]. In addition, the stiffness used for the simulations ensure that inter–particle overlaps of 99% of the particles are smaller than 1% of the particle radii.

This study simulated the self–penetration processes of 49 bio–inspired probes to explore the effects of the number of anchors, S, H, EM, and the control algorithm on the anchor capacity and self–penetration ability. As listed in Table 4.2-4.3, each simulation is named by the anchor configuration and control algorithm. For example, the designation 'H4S1EM0.5_D' refers to a probe with an anchor–tip distance H equivalent to 4 D_{probe} (i.e. $H = 4D_{probe} = 0.176m$), inter–anchor spacing S equivalent to 1 D_{probe}, anchor expansion magnitude of 0.5, and which uses displacement–controlled motion. It is noted that to accommodate S values between 1 and 6 D_{probe} within the VCC, L had to be limited to 2 D_{probe} for the probes with two anchors. The two reference simulations performed with one anchor have an L of 2 D_{probe} and 4 D_{probe} and are named H4L2EM0.5_D and H4L4EM0.5_D, with L designated in place of S as compared to the name of simulations with two anchors.

4.4 Results

Results obtained during the CP, AE, and TA stages are presented in this section. The CP stage provides results similar to those obtained during CPT soundings, consisting of q_c and f_s readings. The anchor capacities and the interactions between the anchors and the probe tip during the AE and TA stages are analyzed in terms of the forces acting on the probe sections as well as in terms of soil stresses and particle displacements around

Table 4.2: DEM simulation matrix.

Parameter	#	Name	L/D_{probe}	S/D_{probe}	H/D_{probe}	EM	Number of Anchors	Control Algorithm
Single Anchor	1	H4L2EM0.5_D	2	0	4	0.5	1	DC
	2	H4L4EM0.5_D	4	0	4	0.5	1	DC
Spacing for $H = 4D_{probe}$	3	H4S0.5EM0.5_D	2	0.5	4	0.5	2	DC
	4	H4S1EM0.5_D		1				
	5	H4S2EM0.5_D		2				
	6	H4S3EM0.5_D		3				
	7	H4S4EM0.5_D		4				
	8	H4S5EM0.5_D		5				
	9	H4S6EM0.5_D		6				
Spacing for $H = 1D_{probe}$	10	H1S1EM0.5_D	2	1	1	0.5	2	DC
	11	H1S2EM0.5_D		2				
	12	H1S4EM0.5_D		4				
	13	H1S6EM0.5_D		6				
Spacing for $EM = 0.3$	14	H4S1EM0.3_D	2	1	4	0.3	2	DC
	15	H4S2EM0.3_D		2				
	16	H4S4EM0.3_D		4				
	17	H4S6EM0.3_D		6				
Spacing for $EM = 0.7$	18	H4S1EM0.7_D	2	1	4	0.7	2	DC
	19	H4S2EM0.7_D		2				
	20	H4S4EM0.7_D		4				
	21	H4S6EM0.7_D		6				
Force–limited motion for $S = 1D_{probe}$	22	H4S1EM0.5_F	2	1	4	0.5	2	VC
	23	H1S1EM0.5_F			1	0.5		
	24	H4S1EM0.3_F			4	0.3		
	25	H4S1EM0.7_F			4	0.7		
	26	H2.5S1EM0.5_F			2.5	0.5		

Table 4.3: DEM simulation matrix. (Continued)

Parameter	#	Name	L/D_{probe}	S/D_{probe}	H/D_{probe}	EM	Number of Anchors	Control Algorithm
Force–limited motion for $S = 4D_{probe}$	27	H4S4EM0.5_F	2	4	4	0.5	2	VC
	28	H1S4EM0.5_F			1	0.5		
	29	H4S4EM0.3_F			4	0.3		
	30	H4S4EM0.7_F			4	0.7		
	31	H2.5S4EM0.5_F			2.5	0.5		
Additional force-limited motion for characterizing critical plane (Figure 16)	32	H1L4EM0.5_F	4	0	1	0.5	1	VC
	33	H2L4EM0.5_F			2			
	34	H3L4EM0.5_F			3			
	35	H4L4EM0.5_F			4			
	36	H4S6EM0.5_F	2	6	4	0.5	2	
	37	H2.5S2EM0.5_F		2	2.5			
	38	H1S1EM0.3_F	2	1	1	0.3	2	
	39	H1S4EM0.3_F		4	1			
	40	H2.5S1EM0.3_F		1	2.5			
	41	H2.5S4EM0.3_F		4	2.5			
Additional displacement–controlled motion for characterizing critical plane (Figure 16)	42	H1S1EM0.3_D	2	1	1	0.3	2	DC
	43	H1S4EM0.3_D		4	1			
	44	H2.5S1EM0.3_D		1	2.5			
	45	H2.5S4EM0.3_D		4	2.5			
	46	H2.5S1EM0.5_D	2	1	2.5	0.5	2	
	47	H2.5S2EM0.5_D		2				
	48	H2.5S4EM0.5_D		4				
	49	H2.5S6EM0.5_D		6				
Particle Size	50	H4L2EM0.5_D-R	2	0	4	0.5	1	DC

*Note: L is anchor length, S is spacing between the two anchors, H is the distance between the anchor and the tip, EM is the anchor expansion magnitude, and D is the probe diameter; D and F represent displacement–controlled and force-limited motion, respectively.

the probes. Lastly, the forces acting on the probe are used to map the effects of S, H, and EM on its self–penetration ability. The three stages simulated in this study are used to investigate the soil response and the feasibility of using one or two anchors to generate sufficient reaction forces to overcome the penetration resistance at an overburden pressure of 100 kPa.

4.4.1 Cone Penetration Stage

During the cone penetration stage, the probe is displaced downward into the VCC to a depth of 0.9 m. The profiles of measured q_c and f_s are plotted in Figure 4.5a and b. The depth for the q_c profile corresponds to the tip location, while the depth for the f_s profile corresponds to the mid–point of the sleeve. As the probe is advanced into the specimen, the q_c and f_s increase gradually to relatively constant values with averages of 4.8 MPa and 30 kPa, respectively. The q_c and f_s values are used to calculate normalized tip resistance (Q_{tn}) and friction ratio (F_r) values of 47.3 and 0.62%, respectively. When plotted in the SBT chart by Robertson [2010] (Figure 4.5c), the CPT response are consistent with that of medium–dense sands. Chen et al. [2021] provides more detailed results indicating that the DEM model simulates the penetration behavior of medium–dense sands across a range of overburden stresses between 25 and 400 kPa.

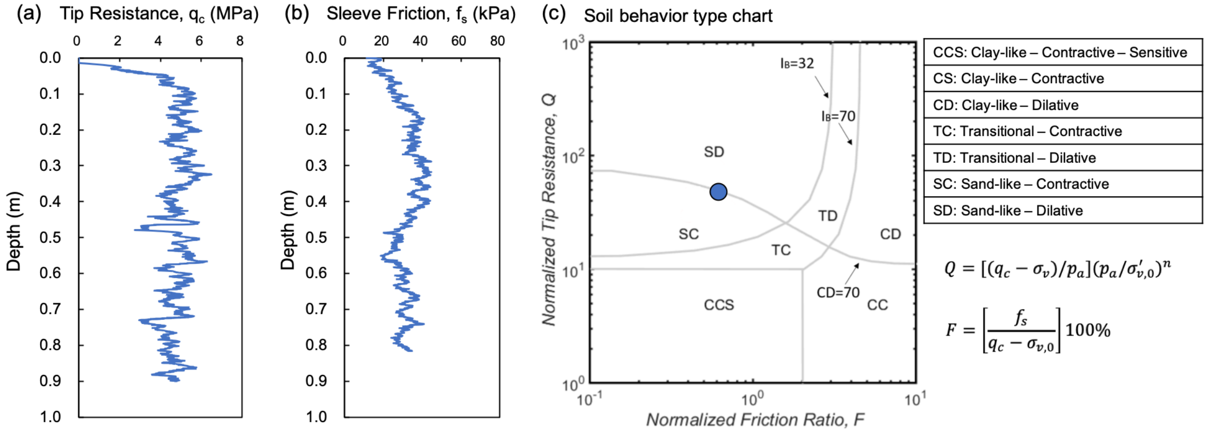

Figure 4.5: Profiles of (a) tip resistance and (b) sleeve friction and (c) soil behavior type classification based on measurements during the cone penetration (CP) stage.

4.4.2 Anchor Expansion Stage

In this section, the results of simulations on two probes with a single anchor (simulations #1–2) and on seven probes with two anchors (simulations #3–9) are presented to investigate the effects of inter–anchor spacing on the anchor capacity on probes with an H of $4D_{probe}$, EM of 0.5 and L of $2D_{probe}$.

During the AE stage, the anchors are radially expanded at a constant rate. The evolution of the normal radial anchor force and tip resistance force of the two single–anchor probes and two dual–anchor probes are shown in Figure 4.6a and 4.6b. The single anchor in the simulation H4L2EM0.5_D has the same length ($L = 2D_{probe}$) as those in the simulations with two anchors, while the single anchor in the simulation H4L4EM0.5_D has twice the anchor length. The S in the dual–anchor simulations is varied between $1D_{probe}$ and $6D_{probe}$. The evolution of corresponding radial anchor forces Fn are shown in Figure 4.6a–d. The single–anchor probes with L of $4D_{probe}$ and $2D_{probe}$ mobilize F_n values of 27.5 and 16.5 kN, respectively, corresponding to anchor pressures of 753 and 904 kPa. The anchor with a greater length mobilizes a smaller P_a likely because as the anchor length is increased the failure mechanism becomes more cylindrical in shape, and expanding a cylindrical cavity requires a smaller pressure than expanding a spherical cavity [Ajalloeian and Yu, 1998; Schnaid, 1990; Yu et al., 1996]. The two anchors of a given probe generate similar F_n values; however, the anchor spacing has an influence on F_n. Namely, the smallest and largest anchor spacings (S of $1D_{probe}$ and $6D_{probe}$) mobilize average F_n values of 12.5 kN and 15 kN, respectively, corresponding to P_a of 685 kPa and 822 kPa.

The magnitude of Q_c decreases as the anchors are expanded. As shown in Figure 4.6e–h, Q_c decreases from an initial value of 7.2 kN to values of 6.05 kN and 5.07 kN for the probes with single anchors with L of $2D_{probe}$ and $4D_{probe}$, respectively, and to values of 5.4 kN and 6.0 kN for probes with two anchors with S of $1D_{probe}$ and $6D_{probe}$. Similar effects on the penetration resistance have been reported by previous studies. For example, Huang and Tao [2020] showed an average reduction in tip resistance of 11.9%, Ma et al. [2020] reported an initial increase in tip resistance due to soil compaction when

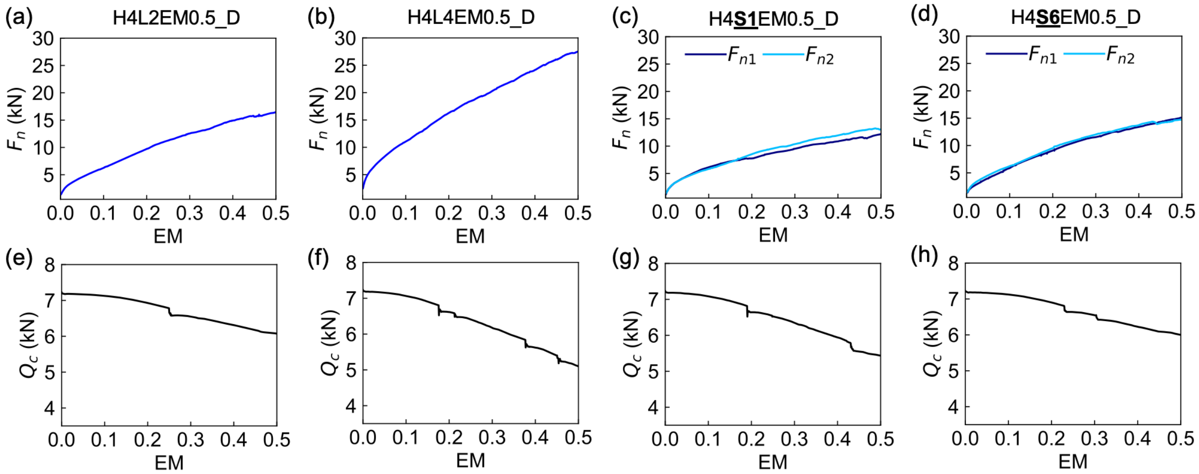

Figure 4.6: Evolution of (a–d) radial anchor forces and (e–h) tip resistances for two single–anchor probes with anchor lengths of 2 D_{probe} and 4 D_{probe} (simulations #1 and #2) and for two dual–anchor probes with spacings of 1 D_{probe} and 6 D_{probe} (simulations #4 and #9) during the anchor expansion (AE) stage.

inflating a balloon–shaped anchor which was followed by a subsequent decrease in tip resistance during anchor deflation, and Chen et al. [2021, 2022] illustrated that the reduction in Q_c is due to an increase in void ratio and tensile vertical strains induced near the cone tip due to anchor expansion.

The results described above indicate that the dual anchor probe with an S of $1D_{probe}$ mobilizes a similar P_L magnitude and a similar Q_c reduction as the single anchor simulation with L of $4D_{probe}$, implying that the proximity of the two anchors in the former results in a behavior similar to that of a single, longer anchor. On the other hand, the simulation with two anchors with S of $6D_{probe}$ mobilizes similar P_L and Q_c as the single anchor probe with L of $2D_{probe}$, suggesting that each anchor in the widely–spaced dual–anchor ($S = 6D_{probe}$) simulation behaves in a near–isolated manner.

The trends of the anchor capacities can be further explored using particle– and meso–level quantities obtained from the DEM simulations, such as particle displacements and soil stresses. Spatial maps of particle displacements and soil stresses during the AE stage are presented in Figs. 4.7 and 4.10, respectively.

In the particle displacement maps, each particle's color is proportional to the magnitude of its displacement. The figures present results for the two single–anchor probes and four dual–anchor probes with varying S while H and EM are fixed at $4D_{probe}$ and 0.5, respectively. For the single–anchor simulations, the probe with the shorter anchor exhibits a more spherical–shaped failure zone (Figure 4.7a) whereas the probe with the longer anchor exhibits a more cylindrical–shaped failure zone (Figure 4.7b). These results are in qualitative agreement with the fact that the shorter anchor mobilized a greater anchor pressure. For the dual–anchor simulations, as the anchor spacing is increased from $1D_{probe}$ to $6D_{probe}$, the soil particle displacements between the two anchors decrease and the failure mode changes from one that encompasses a single zone around both anchors for the simulation with S of $1D_{probe}$ to two individual failure zones for the simulation with S of $6D_{probe}$ (Figure 4.7c–f).

Spatial maps of stress magnitudes and changes in stresses as a result of AE were generated. The soil stresses are obtained from the measurement spheres shown in Figure 3.3b. The σ'_r and σ'_v maps at the end of the CP stage are included in Figure 4.8 for reference. Only radial stress maps for the end of the AE stage are provided for select probes in Figs. 4.93. To better visualize the effects of each stage, changes in radial ($\Delta\sigma'_r$) and vertical ($\Delta\sigma'_z$) stresses are calculated at each measurement sphere. For the AE stage, $\Delta\sigma'_k = \sigma'_{k,AE} - \sigma'_{k,CP}$, and for the TA stage, $\Delta\sigma'_k = \sigma'_{k,TA} - \sigma'_{k,AE}$, where $\sigma'_{k,CP}$,$\sigma'_{k,AE}$, and $\sigma'_{k,TA}$ are the stresses component at the end of the CP, AE, and TA stages, respectively, and k is either the vertical (z) or radial (r) direction.

During the AE stage, the stresses around the anchor increase while the stresses above and below the anchor and around the tip decrease, as shown in the stress change maps for the single–anchor probe (Figure 4.10a and e). These stress maps reflect the mobilization of the radial anchor force and the reduction of tip resistance force, as previously shown in Figure 4.6a and e and as described in detail in Chen et al. [2021]. For dual–anchor probes, the stresses surrounding the anchors of the dual–anchor probes with S of $1D_{probe}$, $4D_{probe}$, and $6D_{probe}$ increase while the stresses around the probes' tip decrease (Figure 4.10b–d, f–h). Clear interactions between the anchors take place during AE for the probe with $S = 1D_{probe}$ at locations between the anchors (Figure 4.10b, f). In fact, the stress change maps for this simulation are similar to that of the single anchor with an L of $4D_{probe}$

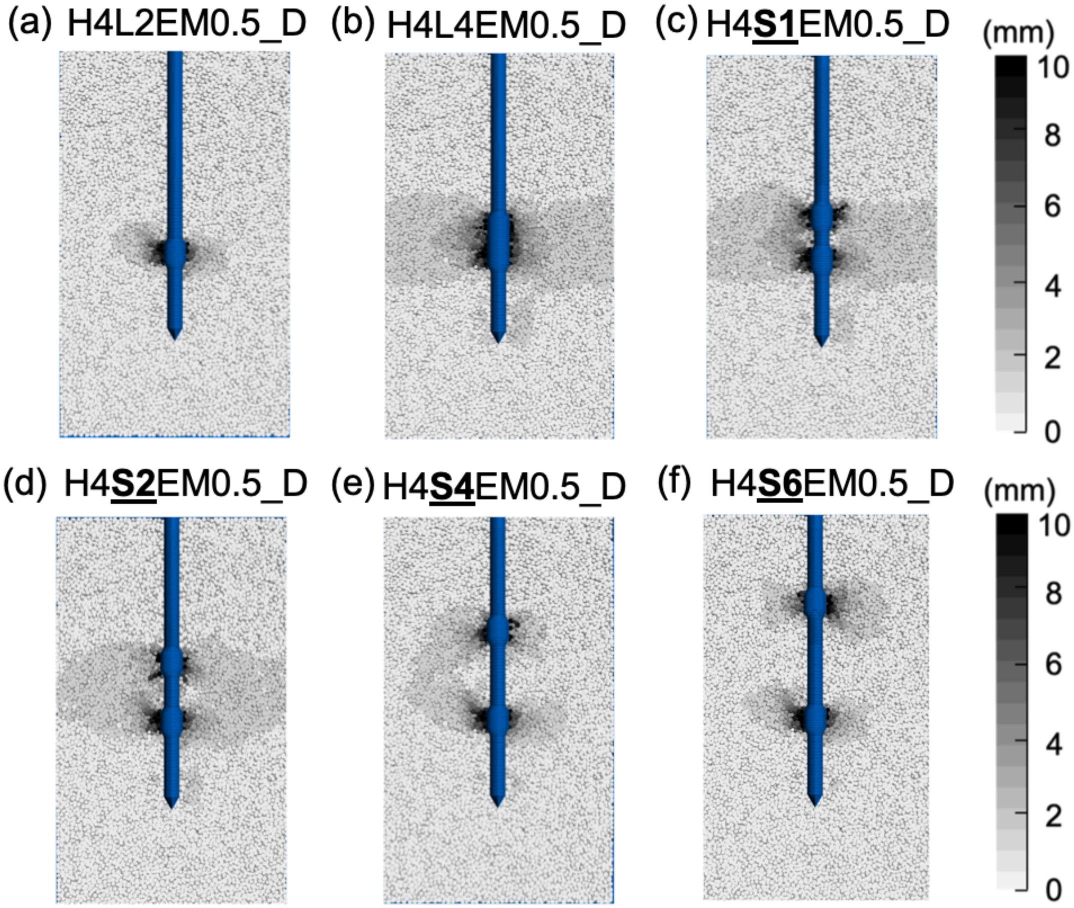

Figure 4.7: Particle displacement maps at the end of anchor expansion (AE) stage for (a–b) two single–anchor probes with lengths of 2 D_{probe} and 4 D_{probe} (simulations #1 and #2) and (c–f) four dual–anchor probes with spacings varying from 1 D_{probe} to 6 D_{probe} (simulations #4, #5, #7, #9).

(Figure 4.10a, e), consistent with the corresponding particle displacement maps. As S is increased, the interactions between the anchors diminish. This is shown by the soil between the anchors which experiences a decrease in stress for the probes with S of $4D_{probe}$ and $6D_{probe}$ (Figure 4.10c, d, g, h). The figures also show a greater decrease in stresses around the probe tip when S is $1D_{probe}$ (Figure 4.10b, f compared to Figure 4.10d, h), which explain the greater decrease in Q_c for smaller S shown in Figure 4.6g, h.

The results of 19 simulations on probes with two anchors (simulations #3–#21) are used to further investigate the effects of the S, H, and EM on the anchor normal forces and penetration resistances during the AE stage. The S values are varied between $1D_{probe}$

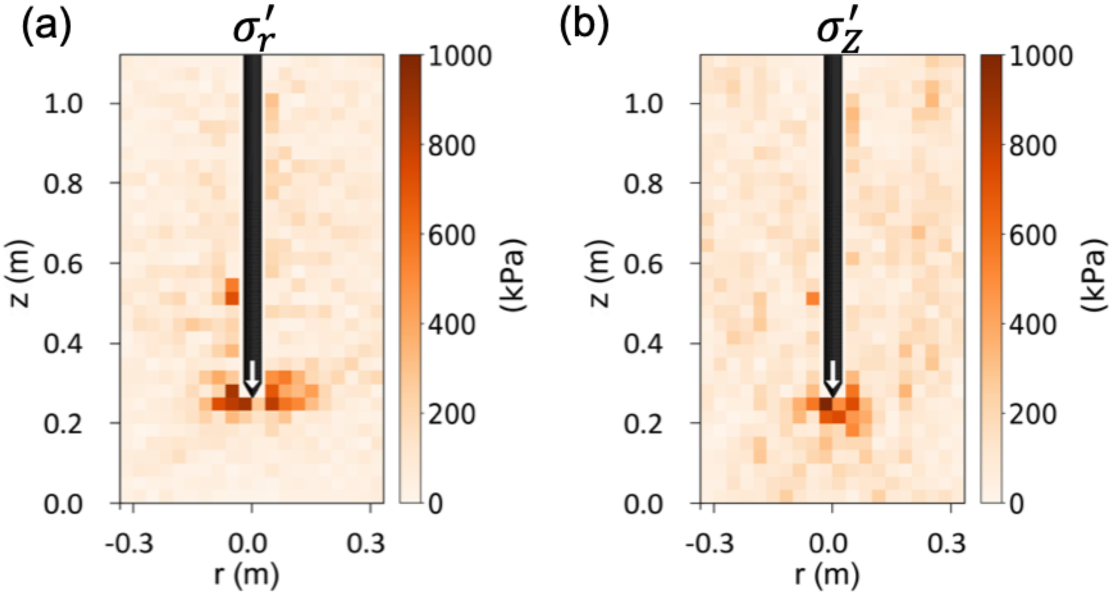

Figure 4.8: Stresses at the end of cone penetration (CP) stage: (a) radial and (b) vertical soil stresses.

and $6D_{probe}$, the H values are either $1D_{probe}$ or $4D_{probe}$, and the EM values are 0.3, 0.5, and 0.7.

Figure 4.11a-f presents the change in F_n on the top and bottom anchors (F_{n1} and F_{n2}, respectively) and Q_c with increasing S/D_{probe} at the end of the AE stage for probes with varying H and EM. The dashed lines represent the values for the single–anchor simulations with L of $2D_{probe}$ and $4D_{probe}$ for comparison. Both F_{n1} and F_{n2} increase with increasing S/D_{probe} (Figure 4.11a–d), indicating a decrease in the interaction between the anchors as S/D_{probe} is increased. At the same S/D_{probe}, F_{n1} and F_{n2} are largely independent of H (Figure 4.11a, c). Conversely, the probes with greater EM mobilize greater F_{n1} and F_{n2} (Figure 4.11b, d) due to the increase in anchor surface area with EM. The Q_c values at the end of AE increase as S is increased (Figure 4.11e, f), indicating that both anchors interact with the tip for both $H = 1D_{probe}$ and $H = 4D_{probe}$ cases. In addition, greater reductions in Q_c occur for simulations with smaller H (Figure 4.11e) and with greater EM (Figure 4.11f).

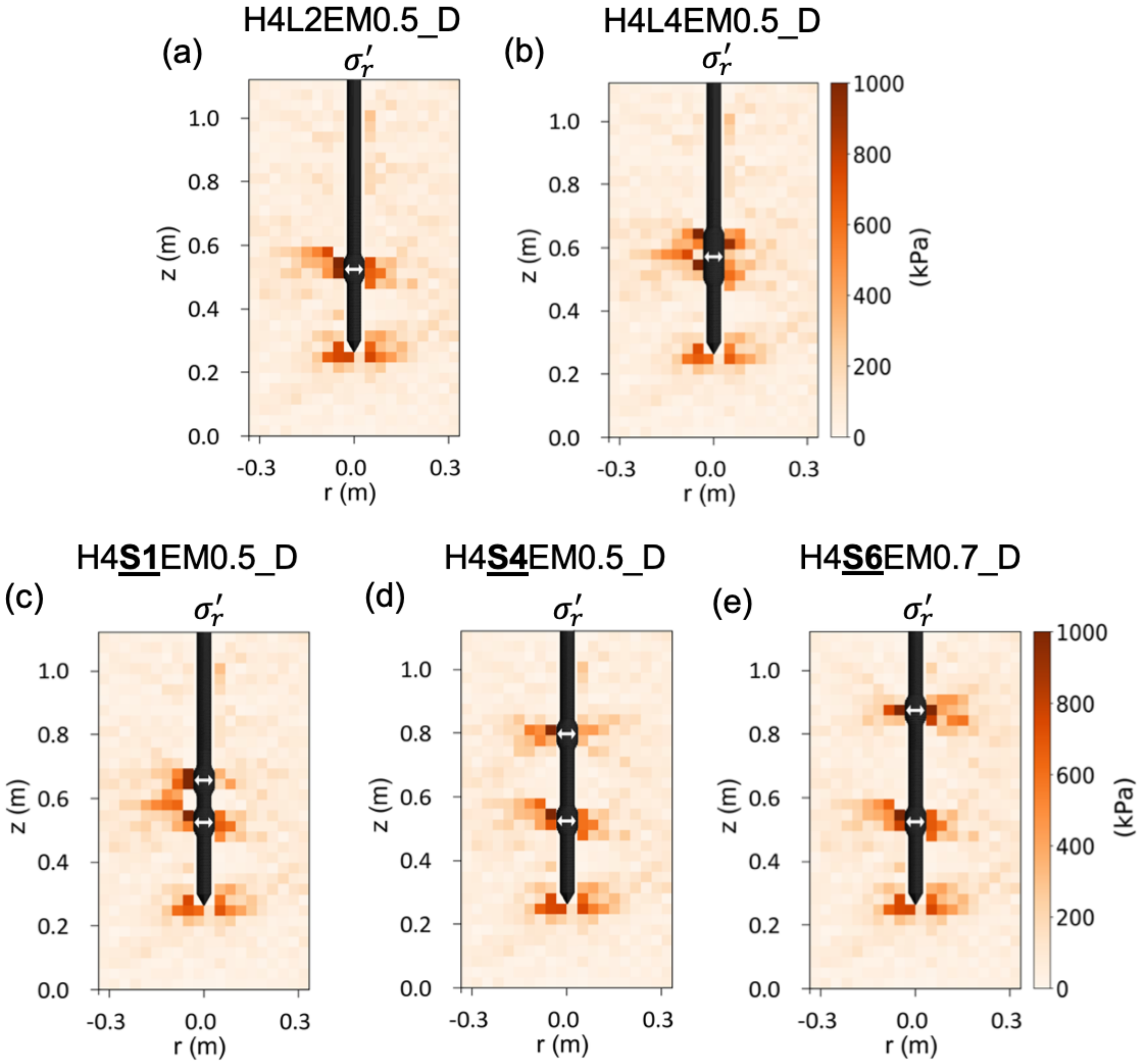

Figure 4.9: Radial stresses at the end of anchor expansion (AE) stage for probes (a) H4L2EM0.5_D (simulation #1), (b) H4L4EM0.5_D (simulation #2), (c) H4S1EM0.5_D (simulation #4), (d) H4S4EM0.5_D (simulation #7), and (e) H4S6EM0.5_D (simulation #9).

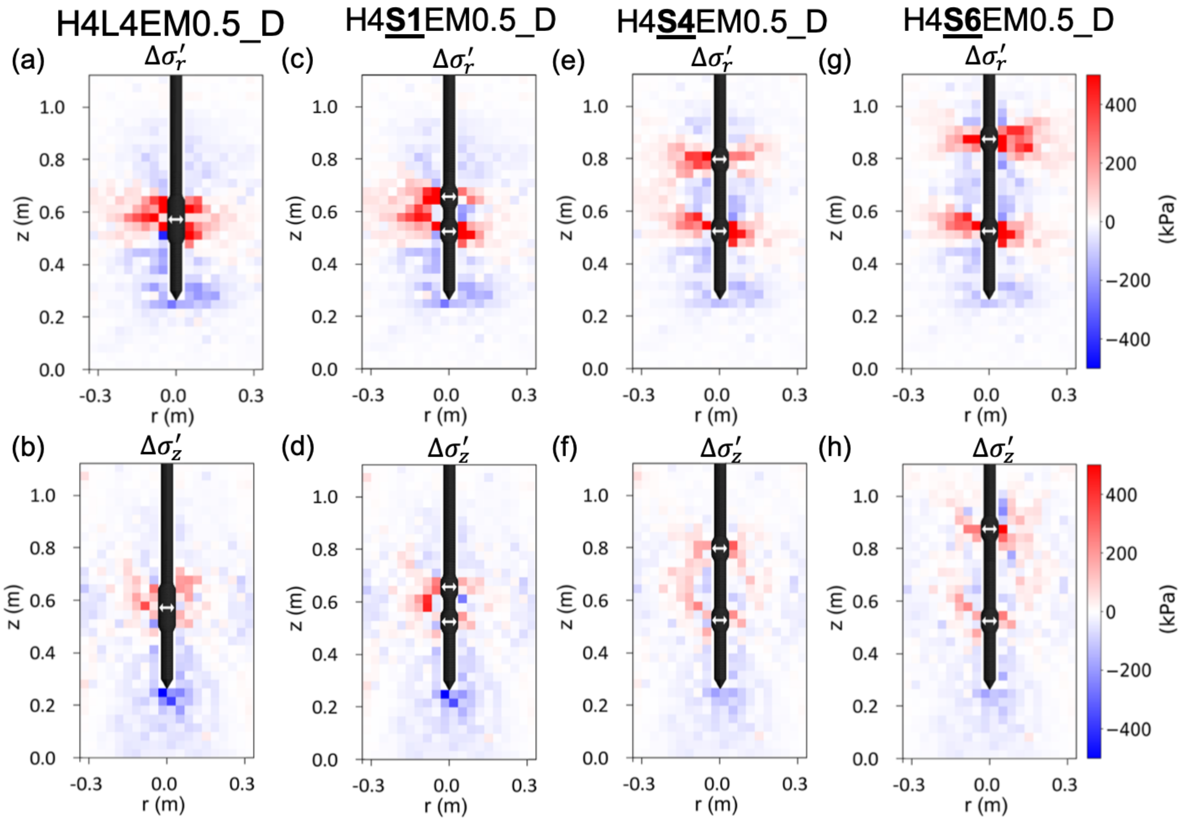

Figure 4.10: Change in soil stresses at the end of the anchor expansion (AE) stage. (a–d) Radial stresses, and (e–h) vertical stresses for single–anchor probe H4L4EM0.5_D (simulation #2) and dual–anchor probes H4S1EM0.5_D (simulation #4), H4S4EM0.5_D (simulation #7), and H4S6EM0.5_D (simulation #9).

4.4.3 Tip Advancement Stage

The evolution of total forces F_t and Q_t (Eqs. 4.9 and 4.10) and the corresponding component forces F_a, F_b, Q_c, and Q_s (Eqs. 4.5–4.8) during the displacement-controlled TA stage for the two single–anchor probes and two dual–anchor probes with S of $1D_{probe}$ and $6D_{probe}$ are plotted in Figure 4.12a–h as a function of vertical displacement. The single anchor probes with L of $2D_{probe}$ and $4D_{probe}$ mobilize F_t forces (Figure 4.12a, b) averaging 5.5 kN and 7.4 kN, respectively; the greater force mobilized by the latter is due to its larger surface area. At the end of the TA stage, the H4L4EM0.5_D probe generates an F_a of 4.0 kN while the H4L2EM0.5_D probe generates a F_a of 2.1 kN (Figure 4.12e and f). Both probes mobilize a similar F_b with a magnitude around 3.4 kN as well as mobilize similar Q_t forces, averaging about 7.8 kN, over the last 0.01 m of displacement

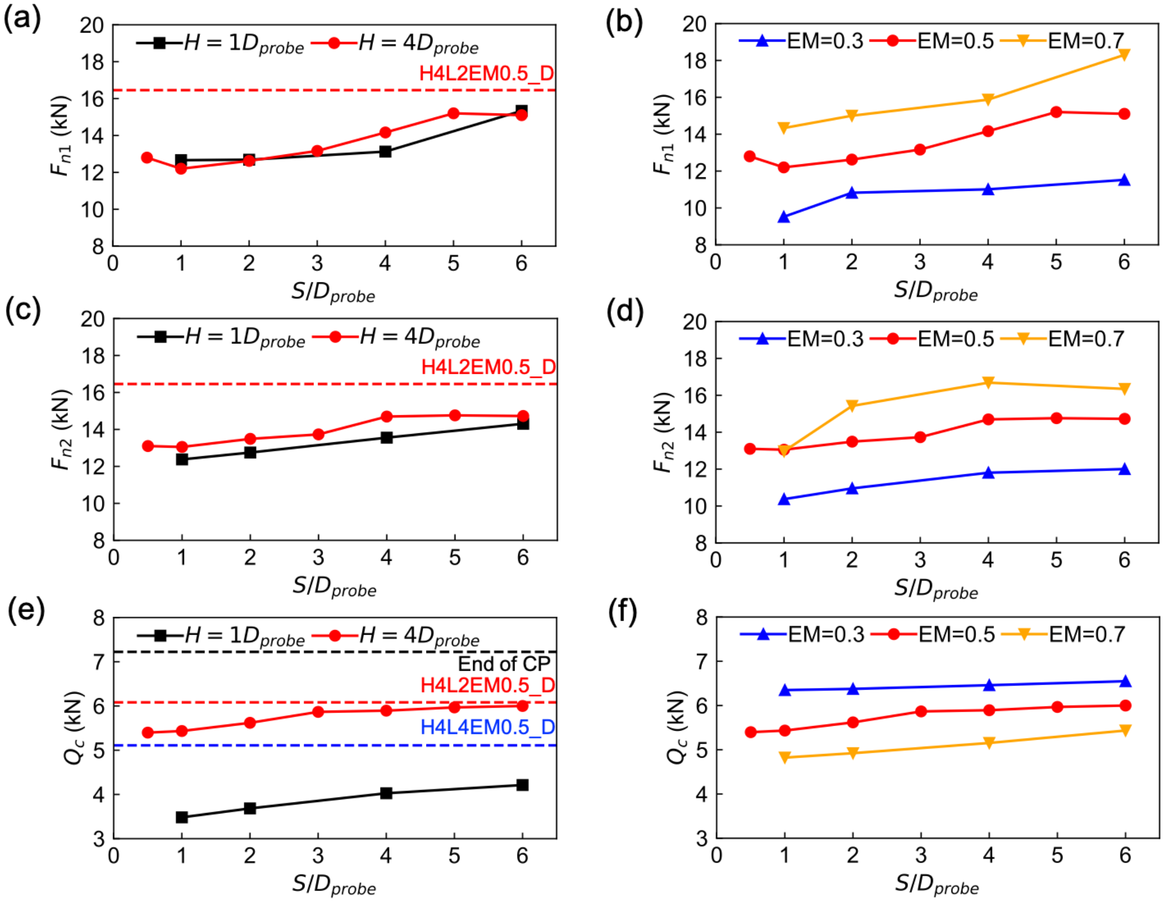

Figure 4.11: Change in forces at the end of the anchor expansion (AE) stage: (a–b) radial forces on the top anchor, (c–d) radial forces on the bottom anchor, and (e–f) tip resistance with increasing spacing for probes with different anchor–tip distance and expansion magnitude (simulations #3–#21).

(Figure 4.12a–d).

The dual–anchor probes mobilize greater F_t than the single–anchor probes due to the generation of bearing forces by the two anchors. The F_{a2} and F_{b2} components of the bottom anchor on the probe with an S of $6D_{probe}$ are greater than those for the probe with an S of $1D_{probe}$ by 70% and 66%, respectively. This highlights the effect of S on the mobilization of anchorage force. Both of these probes mobilize Q_t forces similar to those mobilized by the single–anchor probes. These Q_t values correspond to q_c values close to 4.8 MPa, which is in agreement with results from Chen et al. [2021] indicating that the q_c magnitude remobilized to values close to those at the end of the CP stage. This suggests that the q_c measured at the end of the TA stage could be used to estimate soil engineering

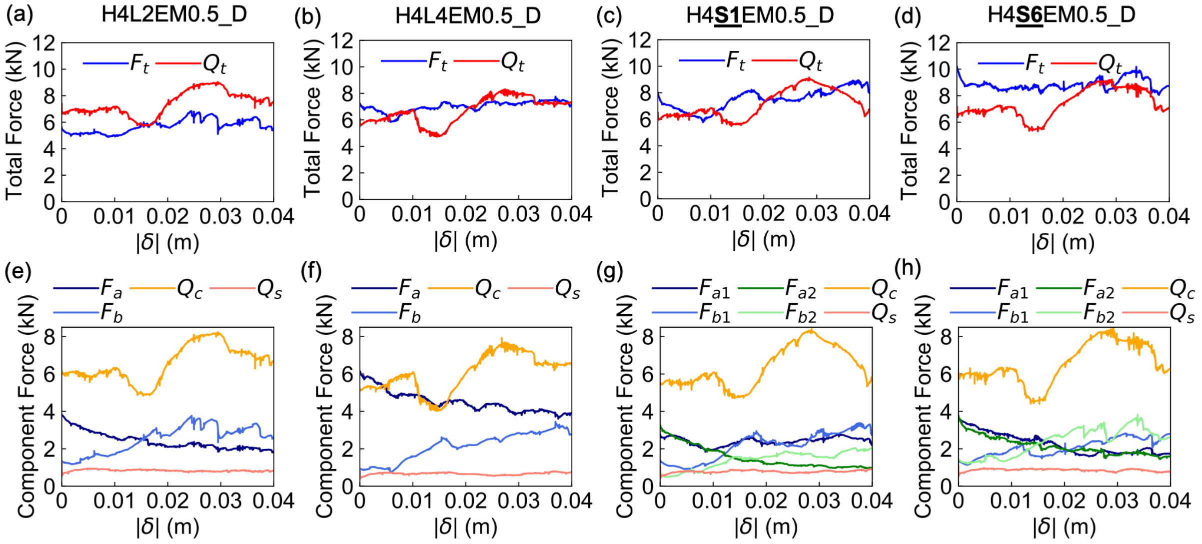

Figure 4.12: Evolution of (a–d) total reaction and resistance forces and (e–h) component reaction and resistance forces during the tip advancement (TA) stage for single–anchor and dual–anchor probes. Note that simulations are displacement–controlled).

properties using established CPT procedures. The results presented in Figure 4.12 (e-h) together with those in Chen et al. [2021] indicate that q_c tends to remobilize irrespectively of S.

The influence of S on the capacity of dual–anchor probes is further illustrated in Figure 4.13a–c, which show the relationship between average F_a, F_b, and F_t obtained during the last 0.01 m of displacement with normalized spacing (S/D_{probe}). The dashed lines represent the values for the single–anchor simulations with L of $2D_{probe}$ and $4D_{probe}$ for comparison. The results indicate that the F_{a1} and F_{b1} (forces on the top anchor) are largely independent of S/D_{probe}, while the F_{a2} and F_{b2} (forces on the bottom anchor) increase with increasing S/D_{probe} (Figure 4.13a, b). As shown in Figure 4.13c, the total reaction force mobilized by the probes with two anchors (F_t= F_{t1}+ F_{t2}) increases as S/D_{probe} is increased due to the increase in F_{t2}. In all instances, the F_t values for the dual–anchor probes are greater than those for the single–anchor probes. However, the F_t values for the two–anchor probes are smaller than twice the F_t value for the single–anchor probe with an L of $2D_{probe}$, indicating that while the capacity of two anchors is greater than the capacity of one, the efficiency of the former in terms of total capacity per anchor number is decreased. These results are consistent with those in previous numerical and experimental studies on helical anchors, which demonstrate the reduction in efficiency when the inter–helix spacing was smaller than 1.5 to 3 base diameter equivalents [Hao et al., 2019; Misir, 2018; Nally and Hambleton, 2019].

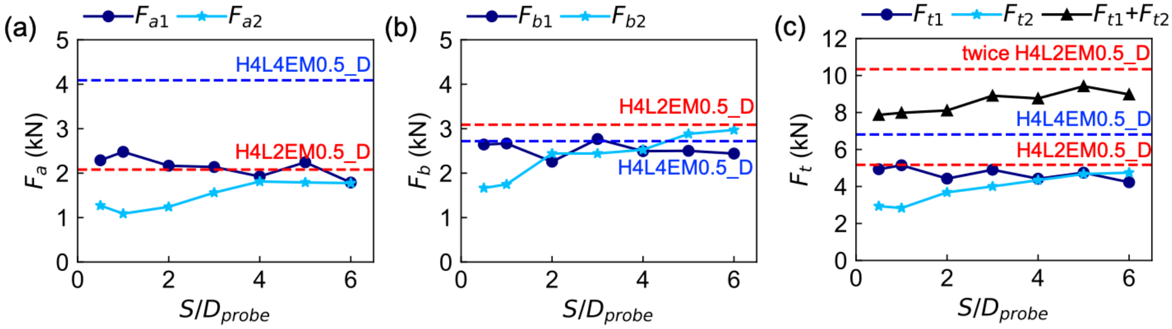

Figure 4.13: Component (a and b) and total reaction forces (c) mobilized at the end of the tip advancement (TA) stage by probes with dual anchors with varying inter–anchor spacing (simulations #3–#9). Note that dashed lines provide values for probes with one anchor (simulations #1 and #2).

The spatial maps of particle displacements and soil stresses for single–anchor and double–anchor probes are presented to investigate the interaction effects during the TA stage. The particle displacement maps for the TA stage show that as the tip is displaced downward, significant particle displacements occur around and below the tip in a similar manner for all simulations (Figure 4.14a–f). As the anchors are displaced upward, a 'butterfly–shaped' zone is formed around the anchors with the particles undergo large displacements. When the S is $1D_{probe}$, particle displacements greater than 10 mm are observed between the two anchors, indicating significant interactions between them (Figure 4.14c, d). The shape of the disturbed zone between the single–anchor simulation with an L of $4D_{probe}$ and dual–anchor simulation with an S of $1D_{probe}$ is remarkably similar (Figure 4.14b, c). In contrast, much smaller displacements (1 to 4 mm) between the two anchors are observed for the probe with an S of $6D_{probe}$ (Figure 4.14f). This difference in failure mode for small and large spacings has also been analyzed in previous multi–plate anchors related topic. For example, Wang et al. [2013] showed that a global 'cylindrical failure' in the incremental displacement fields occurred during the uplifting of two–plate anchors when spacing is smaller than 3 base diameter equivalents, while individual bearing failure mechanisms occurred when the spacing is greater than 5 base diameter equivalent. Additionally, Nally and Hambleton [2019] showed that increasing the number of plate anchors gradually changed the soil failure mode from a 'passive' failure zone, which extend from bottom anchor to soil surface, to a uniform 'single–column' failure zone passing through all anchors. The smaller interactions in the DEM simulations between the anchors at larger S can help explain the previously discussed trends, including the convergence of F_{n1} and F_{n2} to the single–anchor case during AE and the convergence of F_{a1}, F_{a2}, F_{b1}, F_{b2}, F_{t1}, and F_{t2} to the single–anchor case during TA as S approaches $6D_{probe}$ (Figs. 4.11, 4.13).

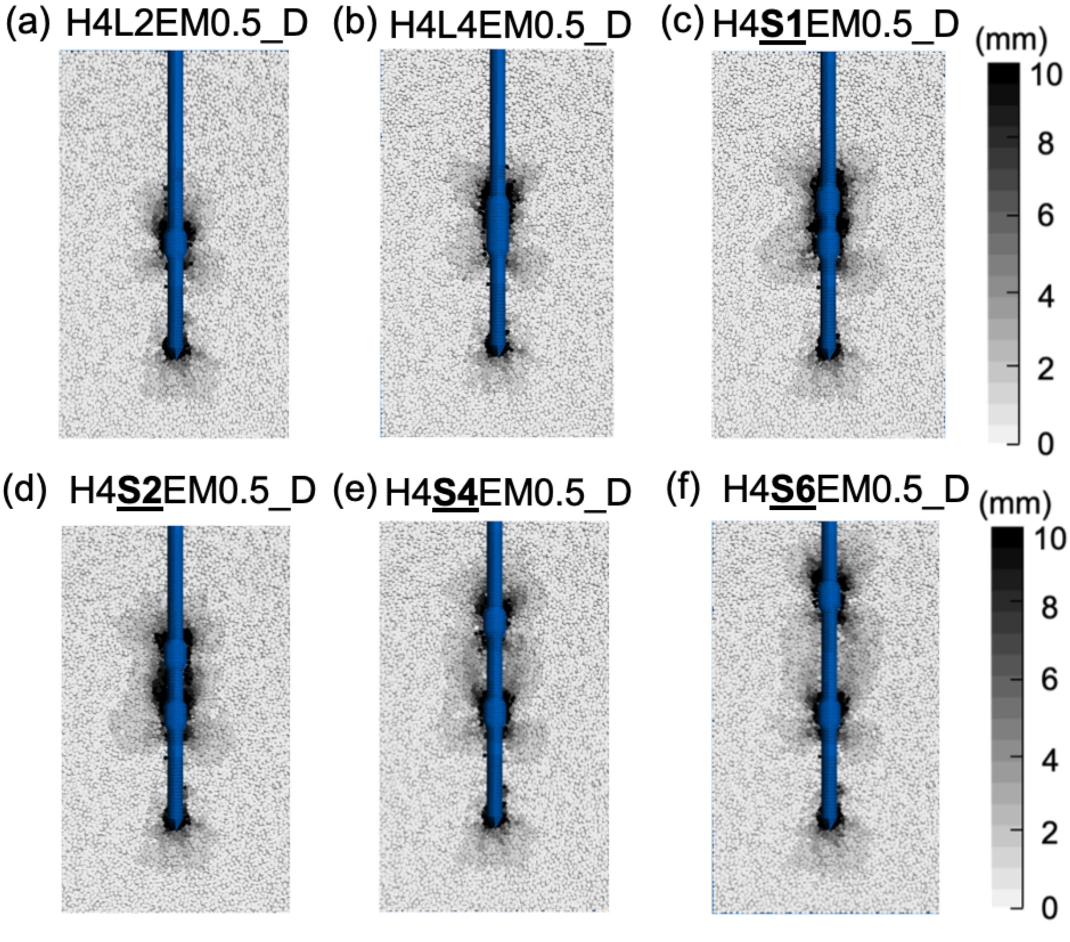

Figure 4.14: Particle displacements at the end of tip advancement (TA) stage for (a–b) two single–anchor probes with anchor lengths of $2D_{probe}$ and $4D_{probe}$ (simulations #2 and #1) and (c–f) four dual–anchor probes with spacings varying from $1D_{probe}$ to $6D_{probe}$ (simulations #4, #5, #7, #9).

The spatial stress difference maps at the end of the TA stage are shown in Figure 4.15. The radial stresses at the end of the TA stage can be found in Figure 4.16. During the TA stage, strong interactions occur between the anchors for the probe with an S of $1D_{probe}$. Namely, the stresses at locations immediately below the top anchor decrease while those at locations immediately above the bottom anchor increase, indicating development of active and passive zones within the particles (Figure 4.15b, f). The active zone developed below the top anchor results in smaller stresses being mobilized around the bottom anchor in comparison with the simulations with an S of $4D_{probe}$ and $6D_{probe}$ (Figure 4.15c, d, g, h), which is responsible for the smaller bearing and friction forces being mobilized by the bottom anchor, as shown in Figure 4.13a–c. The stresses below the probe tip are comparable in all three simulations, indicating limited effects of spacing on the Q_c force.

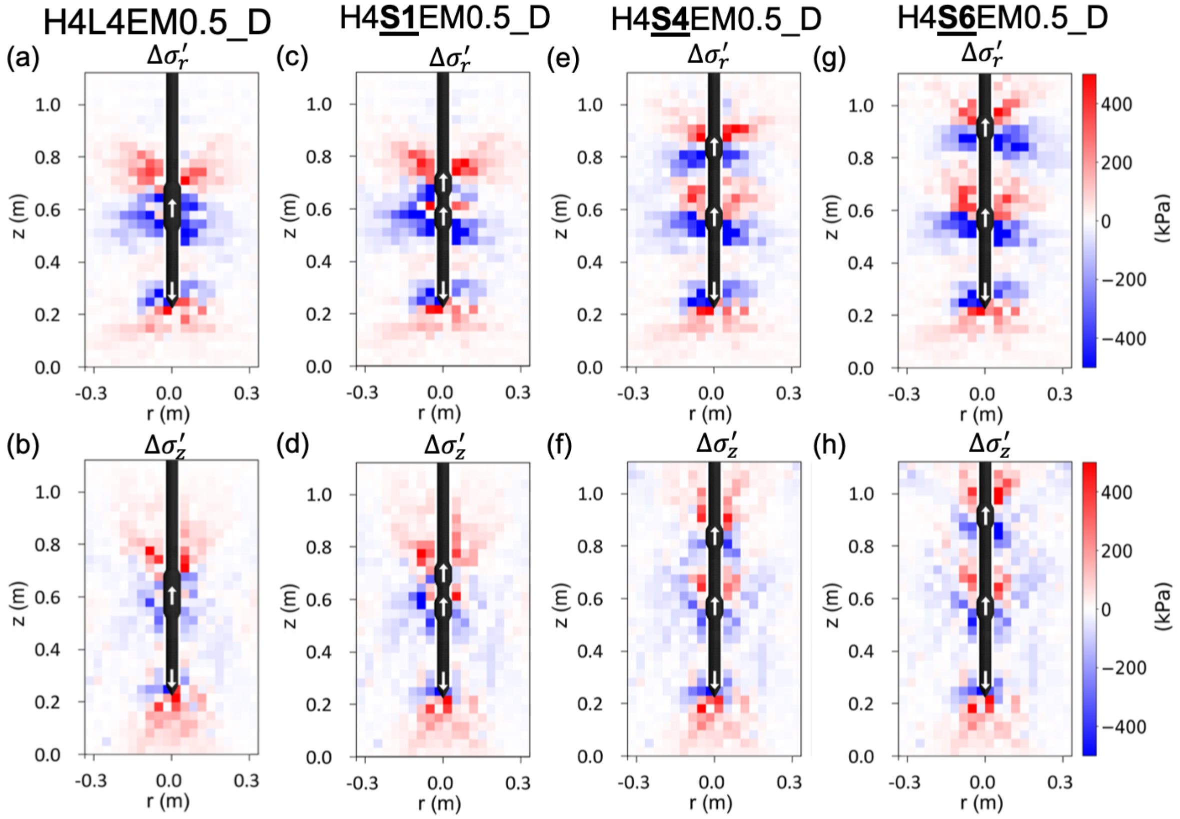

Figure 4.15: Change in soil stresses at the end of the tip advancement (TA) stage. (a–d) Radial stresses, and (e–h) vertical stresses for single–anchor probe H4L4EM0.5_D (simulation #2) and dual–anchor probes H4S1EM0.5_D (simulation #4), H4S4EM0.5_D (simulation #7), and H4S6EM0.5_D (simulation #9).

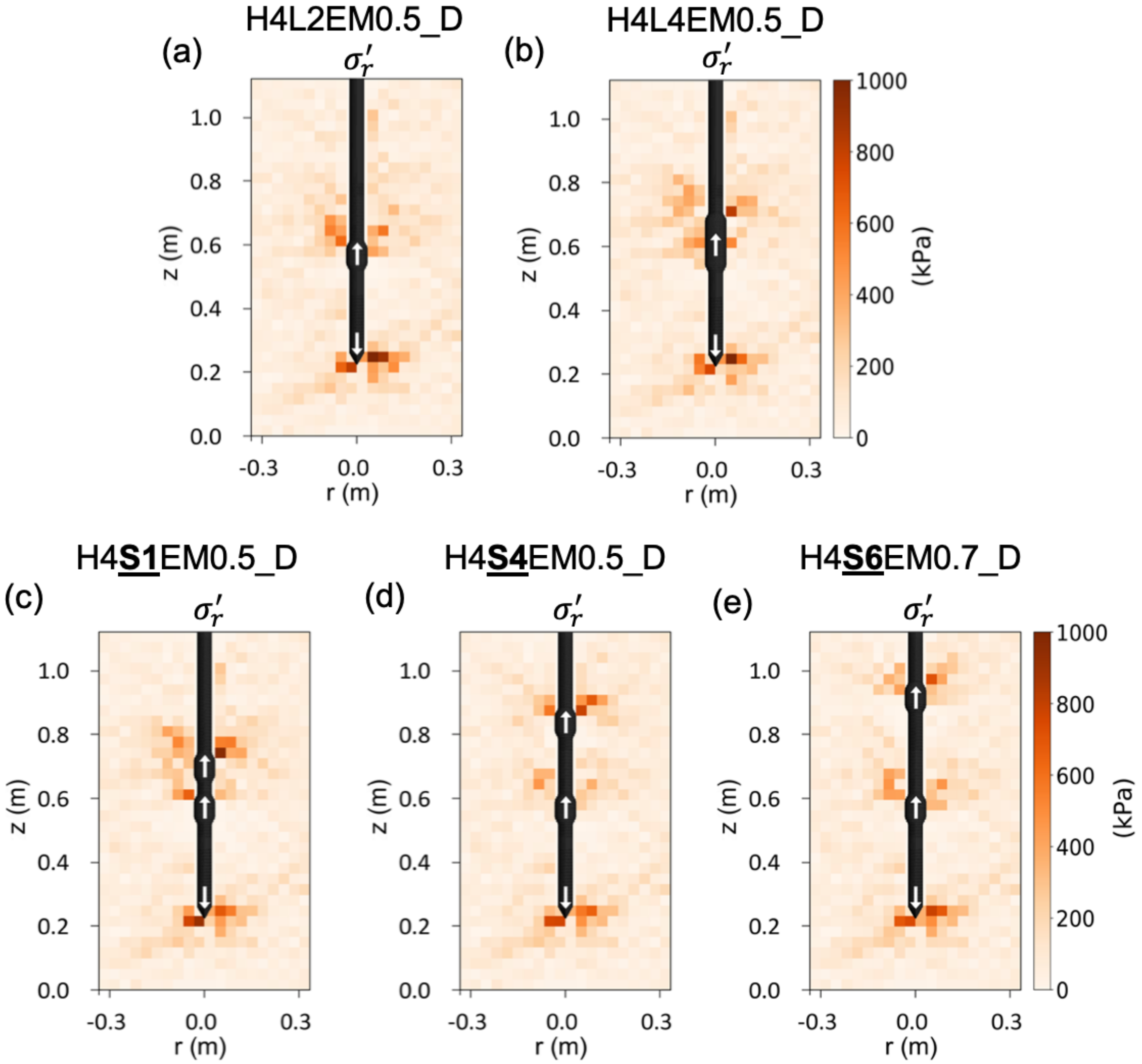

Figure 4.16: Radial stresses at the end of tip advancement (TA) stage for probes (a) H4L2EM0.5_D (simulation #1), (b) H4L4EM0.5_D (simulation #2), (c) H4S1EM0.5_D (simulation #4), (d) H4S4EM0.5_D (simulation #7), and (e) H4S6EM0.5_D (simulation #9).

The results of 19 simulations on probes with two anchors (simulations #3–#21) that have varying S, H, and EM are used to further investigate the interaction effects during the TA stages. During the displacement–controlled TA stage, the forces on the anchors and tip change due to either stress relaxation or remobilization, as previously described. Namely, F_a decreases and F_b increases as the anchors are displaced upward and Q_c increases as the tip is displaced downward. Figure 4.17 presents the forces on the bottom anchor (F_{a2} and F_{b2}) and Q_c with increasing S/D_{probe} at the end of TA for different anchor configuration conditions. Only values for the bottom anchor are presented here because the forces on the top anchor were approximately independent of S/D_{probe}; a similar independence of top anchor capacity on spacing has been reported by Misir [2018] in the finite element modeling of a shaft with two–plate anchors moving upward.

At the end of TA, F_{a2} increases as S$/D_{probe}$ is increased. However, the results suggest that F_{a2} is independent of the H and EM values (Figure 4.17a, b). F_{b2} also increases with increasing spacing (Figure 4.17c, d) due to the decrease in the inter–anchor interactions. This observation is consistent with results from previous numerical and experimental pullout tests on multi–plate and multi–helix anchors [Hao et al., 2019; Misir, 2018], which showed an increase in bottom anchor capacity and capacity per anchor with the increasing spacing. In the DEM simulations, the anchors with H of $4D_{probe}$ mobilize slightly greater F_{b2} than those with H of $1D_{probe}$, suggesting a small effect of the proximity to the probe tip. The anchors with EM of 0.5 and 0.7 mobilize greater F_{b2} than the anchors with EM of 0.3. However, F_{b2} values for the anchors with EM of 0.7 are slightly smaller than those for the anchor with EM of 0.5 (Figure 4.17d), likely due to the stronger inter–anchor interactions resulting from the greater expansion magnitude. In addition, the probes with EM of 0.5 mobilize similar F_{a2} and F_{b2} values as the probe with a single anchor case when S is $6D_{probe}$, suggesting that the anchor interactions diminish at this large spacing (Figure 4.17a, c). The Q_c forces at the end of TA appear to be independent of S/D_{probe}, although the values are smaller for simulations with a smaller H and greater EM (Figure 4.12e, f).

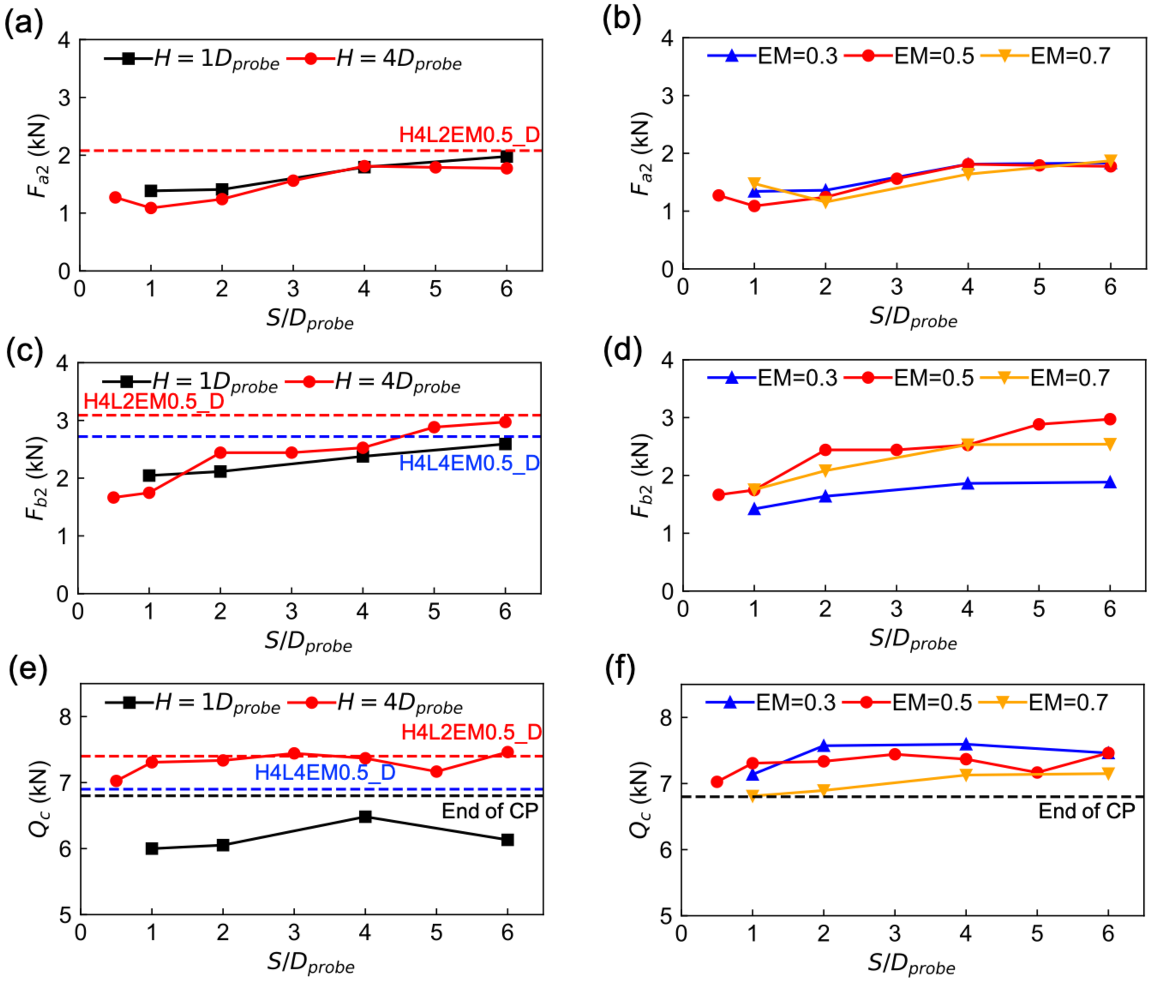

Figure 4.17: Change in forces at the end of the displacement–controlled tip advancement (TA) stage: (a–b) friction forces on the top anchor, (c–d) end bearing forces on the top anchor, and (e–f) tip resistance force with increasing spacing for probes with different anchor–tip distance (simulations #3–#21).

4.4.4 Probe Self-Penetration Potential

As previously discussed, probe self–penetration ability refers to the ability to mobilize greater total reaction forces than total resistance forces. For displacement–controlled simulations, the ratio of total reaction to total resistance forces (F_t/Q_t) can be used to evaluate the probe self–penetration ability, with F_t/Q_t values greater than 1.0 indicating successful self–penetration. Figure 4.18 shows the F_t/Q_t ratios for all the displacement–controlled simulations (#3–21) at the end of TA, which indicate that simulations with an H of $1D_{probe}$ and EM of 0.7 have F_t/Q_t greater than 1.0 (black squares and yellow triangles). Simulations with greater H and smaller EM can have F_t/Q_t smaller than 1.0. For example, at spacings of $0.5D_{probe}$ to $2D_{probe}$, the simulations with an H of $4D_{probe}$ and EM of 0.5 (red circles) have an F_t/Q_t slightly smaller than 1.0, but at larger spacings the ratios are greater than 1.0. Also, the simulations with an EM of 0.3 (blue triangles) all have F_t/Q_t smaller than 1.0.

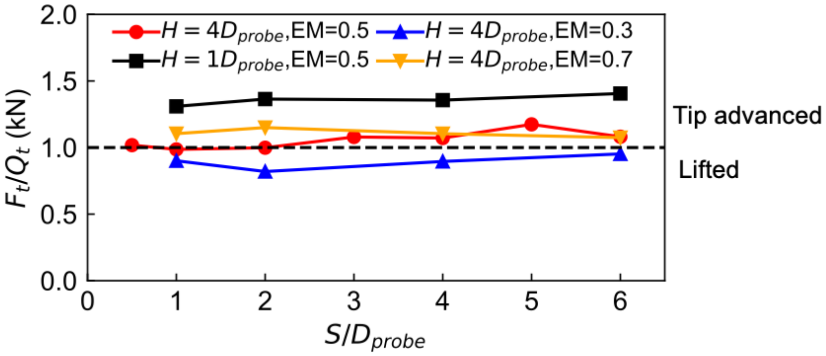

Figure 4.18: Ratios of total reaction force to total resistance force at the end of the tip advancement (TA) stage for displacement–controlled simulations on probes with dual anchors (simulations #3–#21).

The ability of the probe to advance its tip is further evaluated using force-limited motion (Figure 4.4c). An additional series of 12 simulations (#22–32, 36, 37) was performed with the goal of evaluating the effect of S, EM, and H on the self–penetration ability of the dual–anchor probes. The force-limited algorithm allows for the probe section that mobilizes a total force smaller than F_{target} to be displaced at a constant velocity. Therefore, the tip advancement ability can be evaluated in terms of the self–penetration displacement ΔD:

$$\Delta D = |\delta_{tip}| - |\delta_{anchor}| \tag{4.11}$$

where δ_{tip} and δ_{anchor} are the displacement vectors of the tip and the anchor, and a positive ΔD indicates the achievement of self–penetration where the net tip displacement is towards greater depths. Figures 4.19a–c show time histories of ΔD for probes with different anchor configurations. Tip advancement is achieved by the probes with combinations involving EM greater than or equal to 0.5 and S greater than or equal to $4D_{probe}$. It is noted that the simulation '$S = 0D_{probe}$' corresponds to H4L4EM0.5_F (simulation #35), which can be considered as a dual–anchor probe with zero inter–anchor spacing. The horizontal axis in the plot is normalized time ($\bar{t}$), which is defined as the time within the TA stage normalized by the total duration of the TA stage.

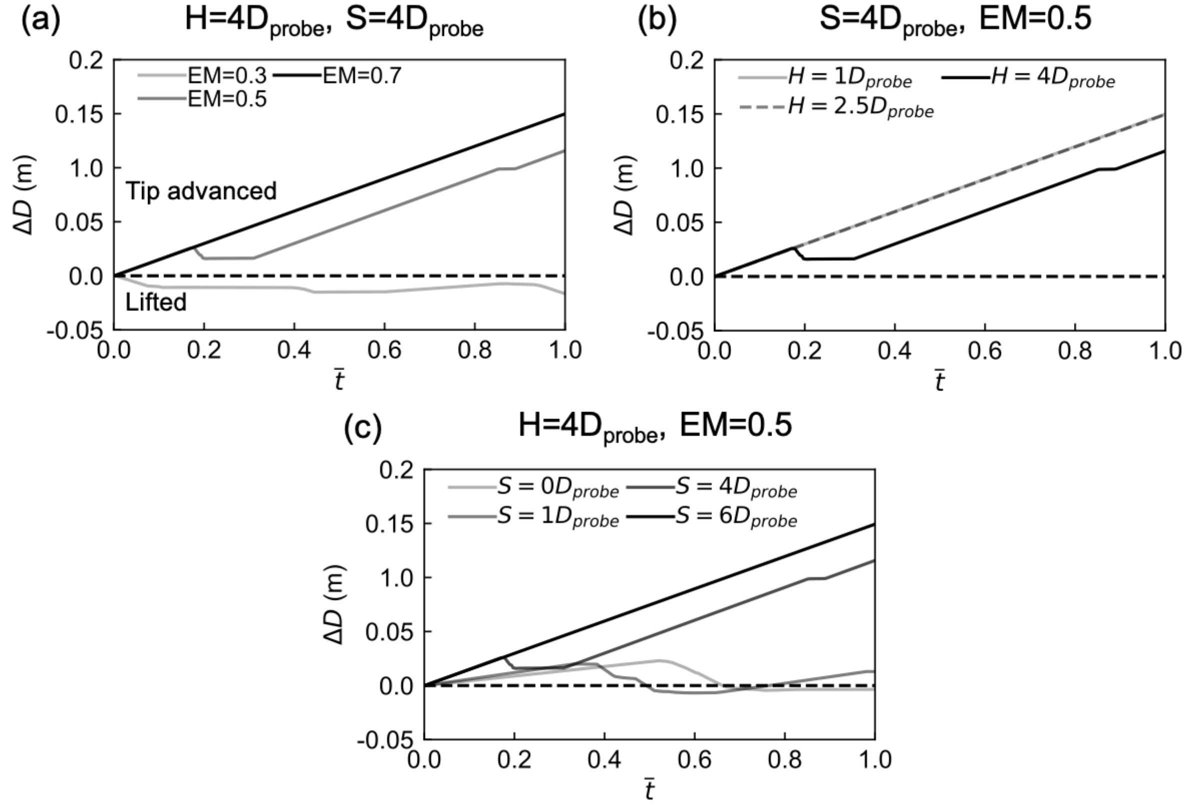

Figure 4.19: Tip advancement (TA) displacement ΔD for probes with different (a) expansion magnitudes (simulations #27, #29, #30), (b) anchor–tip distances (simulations #27, #28, #31), and (c) anchor spacings (simulations #23, #27, #35, #36) for force-limited simulations.

To explore the probe configurations that enable self-penetration, an additional series of 18 simulations (#33–50) were performed. In total, the results of 48 simulations using either displacement–controlled or force-limited motion are plotted in a dimensionless 3D space defined by EM, H/D_{probe}, and S/D_{probe} (Figure 4.20). In the figure, the black data points indicate the probe configurations that achieved self-penetration and the red datapoints represent the probe configurations that did not achieve self-penetration, as defined by the conditions described above (F_t/Q_t greater than 1.0 or a positive ΔD during TA). As shown, the result of the displacement-controlled and force-limited simulations are in agreement. The configurations that enable self–penetration include greater EM, smaller H/D_{probe}, and greater S/D_{probe}, as previously described. Using least square fitting, a plane that separates the configurations that achieved self–penetration from those that failed is identified, which is defined by $EM = -0.046 \times S/D_{probe} + 0.020 \times H/D_{probe} + 0.488$. In this equation, the negative –0.046 coefficient indicates that a smaller EM is required for probes with greater S to achieve self–penetration, while the positive 0.020 coefficient indicates that a greater EM is needed for probes with greater H to achieve self–penetration. Lastly, the 0.488 constant indicates the minimum EM value that would be required to achieve self–penetration if both H and S are zero. It is noted that it is likely that the plane that separates successful from unsuccessful self-penetration is dependent on the length of the anchors; particularly, the plane is expected to move downward as the anchor length is increased.

4.5 Implications and Limitations

The results presented in this study cover a limited number of conditions, including probes with one or two anchors, anchor lengths equivalent to 2 or $4D_{probe}$, and soil conditions that simulate a medium–dense coarse–grained soil under an overburden stress of 100 kPa, equivalent to a depth of about 10 m of saturated soil or 5 m of dry soil. The trends reported here should be verified using physical experiments across a range of overburden stresses as well as for coarse–grained soils with smaller particles, well–graded coarse soils, and fine–grained soils.

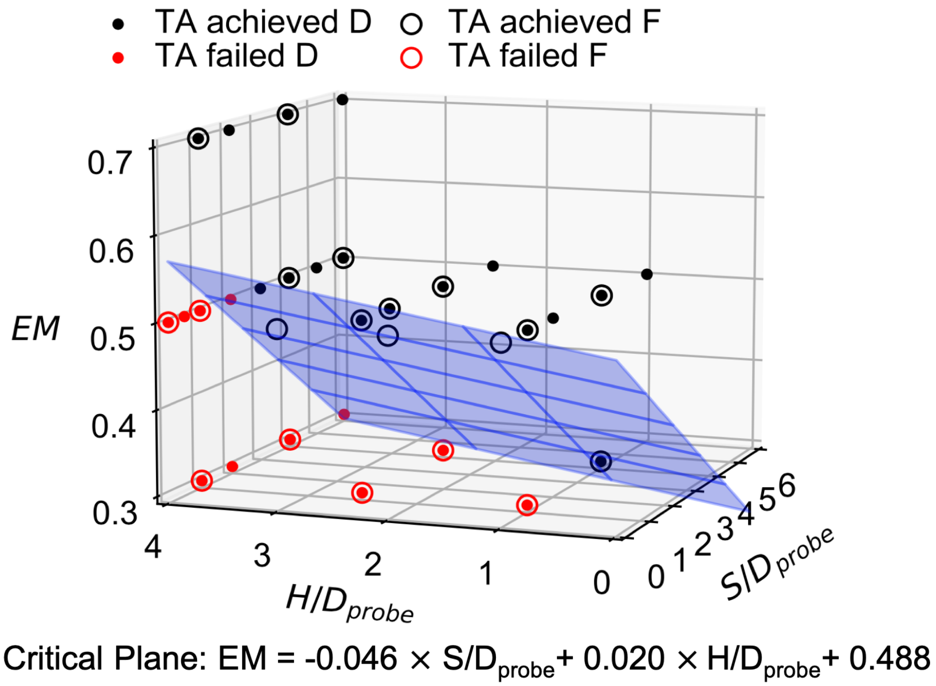

Figure 4.20: Tip advancement ability as a function of probe configuration (simulations #2–#49) for probes with anchor length (L) of $2D_{probe}$. Note: D refers to displacement-control motion and F refers to the force-limited motion.

Another aspect that needs to be examined is the possible effect of the particle size on the simulation results, in particular with regard to the interaction between the particles and the anchor's bearing area. In the simulations presented in this study, a D_{probe}/D_{50} of 3.1 was employed,and the ratio of the length of the anchor bearing area to the median particle size $(D_{anchor} - D_{probe})/(2D_{50})$ was 0.8. To explore possible particle size effects, a specimen with the same model parameters (Table 4.1) that employs the particle refinement method [McDowell et al., 2012] was generated to decrease the size of the particles contacting the probe. Specifically, these particles had a D_{50} of 6.3 mm, which produces a D_{probe}/D_{50} of 7.0 and $(D_{anchor} - D_{probe})/(2D_{50})$ of 1.7. This specimen contains five different zones, as shown in the model illustration and particle size distributions in Figure 4.21. An additional displacement-controlled simulation with a single-anchor probe with $H = 4D_{probe}$ and $L = 2D_{probe}$ was performed on this specimen. A comparison of the results with those from the original specimen is provided in Table 4.4 and Figure 4.22. In summary, the difference in the average q_c and f_s in the CP stage are 8.3% and 13.7%, respectively. At the end of the AE stage, there is a difference of 14.5% and 8.2% in the F_n and Q_c values, and at the end of the TA stage there is a difference of 11.0% and 11.8% in the F_t and Q_t values. While in general the forces are greater for the specimen with smaller particles, the differences are smaller than 15% and the final result was the same in both simulations, with tip advancement failing. Therefore, it can be concluded that while there may be a small dependency of the magnitude mobilized forces on the particle size, the conclusions of the simulations are unaffected. Despite the aforementioned potential

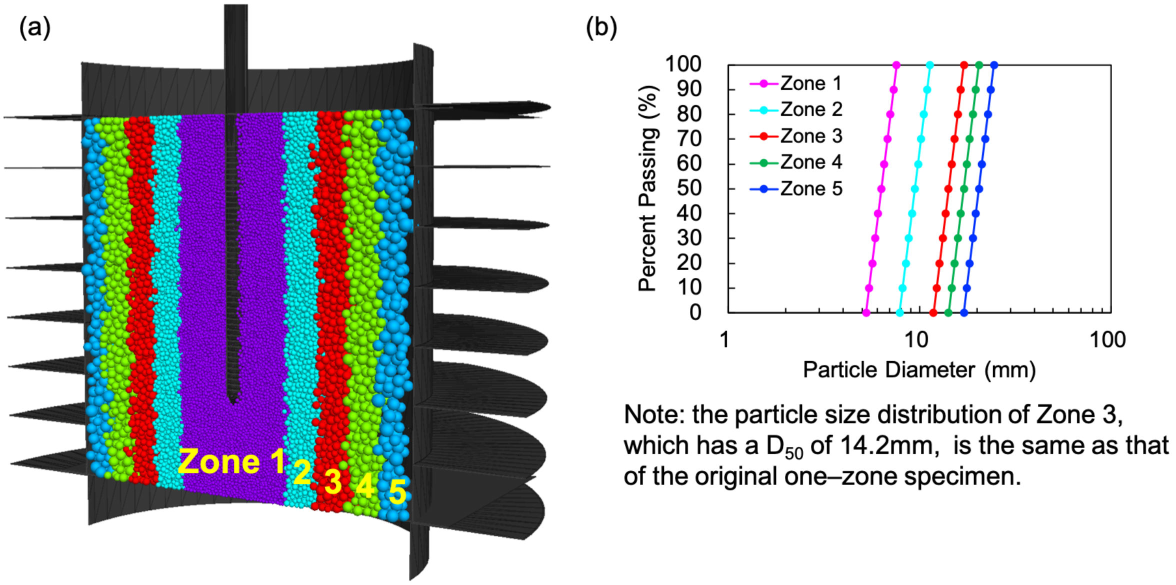

Note: the particle size distribution of Zone 3, which has a D_{50} of 14.2mm, is the same as that of the original one–zone specimen.

Figure 4.21: Refined soil specimen. (a) Virtual calibration chamber, probe and soil particles; (b) particle size distributions in the 5 zones of the soil sample (with the particle size upscaled by 1.5 and 1.2 for inner three zones and outer three zones, respectively).

Table 4.4: DEM simulation parameters.

Specimen	D_{50}	CP stage		AE stage		TA stage	
	(mm)	q_c (MPa)	f_s (kPa)	F_n (kN)	Q_c (kN)	F_t (kN)	Q_t (kN)
Original	14.2	4.8	30.0	16.5	6.1	5.5	7.6
Refined	6.3	5.2	34.1	18.9	6.6	6.1	8.5

*Note: the CP measurements (q_c and f_s) are averaged from 0.2 to 0.55 m soil depth; the AE and TA measurements (F_n, Q_c, F_t, Q_t) are the end values of each stage; the TA stage is displacement controlled (DC).

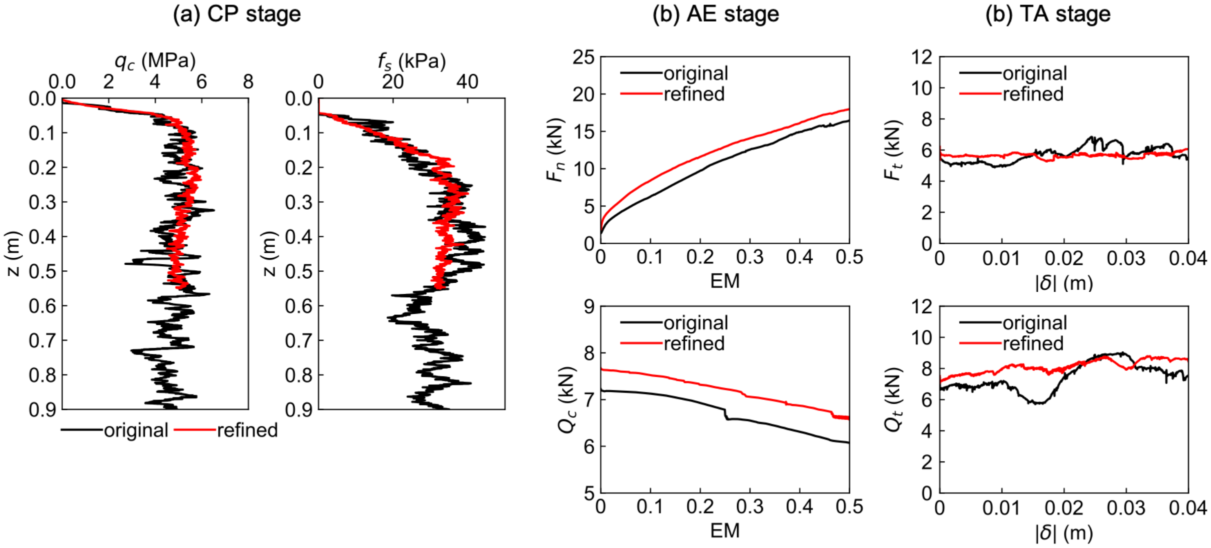

Figure 4.22: Comparisons between results of original one-zone specimen and those of refined five-zone specimen for single-anchor probe H4L2. (a) tip resistance and sleeve friction during the CP stage; (b) radial anchor force and tip resistance force during the AE stage; (b) total reaction force and resistance force during the TA stage. Note that while the CP stage of the refined specimen ends at 0.55 m depth, the comparisons is valid because the anchor and tip are both located in the region that q_c measurement is stable.

limitations, the results presented in this study can help in understanding the processes that produce the interactions between the anchors and the tip, and the identification of the plane that separates probe configurations leading to successful and unsuccessful tip advancement can guide the design of future bio–inspired self–penetration probe prototypes. Previous studies have also explored the effects of other parameters. For example, Chen et al. [2021] showed that the tip advancement ability of the probe increases with increasing anchor length. They also showed that the anchor reaction forces increase at a greater rate with increasing overburden stress than the penetration resistance forces, suggesting that tip advancement reaction becomes more feasible at greater depths. Finally, it can be expected that the reaction mobilized by a probe will increase as more anchors are deployed; however, it is likely that the capacity per anchor will decrease as more anchors are deployed.

4.6 Conclusions

3D DEM simulations of single and dual anchor bio–inspired probes were performed to evaluate the effects of the inter–anchor spacing, anchor–tip distance, and anchor expansion magnitude on the interactions between the anchors and the probe tip and on the probe's self–penetration ability. The simulations were performed in a virtual calibration chamber that applies constant vertical and radial stresses to the contained specimen to simulate the soil penetration process at an overburden stress representative of 10 m in saturated soil. Simulations were either performed with a displacement-controlled or a force-limited probe motion algorithm, and the final result of the simulation (i.e. self–penetration versus anchor lifting) was unaffected by the choice of motion control.

The simulation results indicate that the dual–anchor probes outperformed the single–anchor probes due to the mobilization of two bearing resistance components. It is shown that the anchorage capacity increases with increasing inter–anchor spacing due to a reduction in detrimental interactions between the anchors. At an inter–anchor spacing equivalent to five or six times the probe diameter, the forces mobilized during anchor expansion and tip advancement converged to those mobilized by individual anchors. This takes place when near–isolated failure modes are developed around each anchor, where particle displacements and changes in stresses at locations between the anchors are small. The results indicate that the reaction forces mobilized by the top anchor are approximately independent of inter–anchor spacing. In contrast, the forces mobilized by the bottom anchor decreased as the inter–anchor spacing was decreased due to the formation of an active wedge below the top anchor, which caused a reduction in effective stresses around the bottom anchor. In agreement with previous simulations, expansion of the anchors resulted in a decrease in the penetration resistance. This reduction was also influenced by the probe configuration, where smaller inter–anchor spacings, smaller anchor–tip distances, and greater anchor expansion magnitudes led to greater reductions.

Simulations using the two probe motion algorithms indicate that the self–penetration ability of the probe is increased for the following conditions: (i) increasing the inter–anchor spacing due to the reduction of the detrimental anchor interactions, (ii) decreasing the anchor–tip distance due to the greater reduction in penetration resistance, and (iii) increasing expansion magnitude due to the greater anchorage capacity and greater reduction in penetration resistance. The simulation results were used to define a plane in 3 unitless dimensions (EM versus S/D_{probe} versus H/D_{probe}) that separates the anchor configurations that enable self–penetration from those that result in anchor lifting. This plane could be used to guide the design of future probe prototypes to be deployed in the laboratory and field.

4.7 Data Availability Statement

The datasets generated and/or analyzed during the current study are available from the author on reasonable request.

4.8 Acknowledgements

This material is based upon work supported in part by the Engineering Research Center Program of the National Science Foundation under NSF Cooperative Agreement No. EEC–1449501. The first and second authors were supported by the National Science Foundation (NSF) under Award No. 1942369. Any opinions, findings, and conclusions or recommendations expressed in this material are those of the author(s) and do not necessarily reflect those of the National Science Foundation.

Chapter 5

DEM Simulations of a Self-Burrowing Bio-Inspired Probe in Assemblies of Varying Density

---

This chapter constitutes work in progress for a journal paper that will be submitted in the Fall of 2022. Chen, Y., Zhang, N., Fuentes, R., and Martinez, A. DEM Simulations of a Self-Burrowing Bio-Inspired Probe in Assemblies of Varying Density. To be submitted for possible publication.

5.1 Abstract

There has been a growing level of interest in the development of bio-inspired self-burrowing probes capable of penetrating soils without the aid of external reaction force provided by drill rigs and trucks. Such probes would facilitate site characterization activities and distribution of sensors underneath existing structures and in locations with limited access. For successful deployment in the field, a probe will be required to perform several self-burrowing cycles due to geometrical and geomechanical considerations. This study explores the performance of a dual-anchor self-burrowing probe in granular assemblies of varying density using Discrete Element Modeling (DEM) simulations. The simulated dual-anchor probe consists of an expandable top shaft (i.e. top anchor), expandable bottom shaft (i.e. bottom anchor), and a conical tip. The probe also employs horizontal oscillation of the conical tip as a strategy to reduce the soil penetration resistance to further penetrate the soil. The motions during the self-burrowing cycles, which consist of expansion and contraction of the anchors and advancement of the tip, are controlled using a balance of the reaction and resistance forces. Self-burrowing cycles are simulated in DEM to evaluate the probe's self-penetration performance as a function of soil density. The results show that anchor expansion and tip oscillation facilitate self-burrowing due to the reduction of tip resistance through the alteration of soil contact force forces around the anchor and tip. The performance of the self-burrowing probe in terms of self-burrowing distance is greater in the medium dense specimen than in the dense and loose specimens. A comparison of the total mechanical work done during the self-burrowing process indicates that a smaller tip penetration distance per unit of work is achieved in the denser specimen. Additionally, while tip oscillation aids in self-burrowing to greater depths, it also requires greater work. Overall, numerical simulations that explore the effect of different motion control parameters and soil properties can be helpful for the future design of probe prototypes that can be deployed in the field.

5.2 Introduction

With the growing need for developing efficient solutions for geotechnical engineering problems, the field of bio-geotechnics has received increasing attention in recent years [Martinez et al., 2021]. Conventional soil penetration activities in geotechnical engineering usually require energy-intensive equipment with large reaction masses (e.g. Mayne [2007]). Use of this conventional equipment can cause accessibility challenges for certain sites, such as urban and forested areas and outer space bodies, and have negative environmental and economic impacts (e.g. Purdy et al. [2020]). To address these disadvantages, self-burrowing probes inspired by earthworms, caecilians and bivalves have been the focus of investigations during the past five years.

Two common burrowing strategies used by animals are peristalsis locomotion and the 'dual anchor mechanism'. Soft-bodied animals that use peristalsis locomotion have circular and longitudinal muscles that allow them to form alternating waves of elongation and shortening that propagate along their body to mobilize reaction anchorage forces and push their bodies forward [Gans, 1973; Elder, 1980; Dorgan, 2018]. Bivalves, such as razor clams, use a 'dual anchor mechanism consisting of alternating penetrating (bivalve shell) and terminal (pedal or foot) anchors [Trueman, 1968a,b,d]. During penetration, the shell is expanded to form an anchor to provide reaction for penetration with the foot. During retraction, the foot is expanded and the shell is contracted. In this stage, the foot acts as a second anchor to drag the shell down into the soil.

Researchers have performed experimental and numerical investigations on bio-inspired self-burrowing probes. Overall, these investigations have demonstrated the feasibility of implementing bio-inspired strategies to enable self-burrowing. For instance, Winter et al. [2014] analyzed and developed a razor clam-inspired probe capable of burrowing in sands by local fluidization. [Tao et al., 2020] developed a razor clam-inspired probe which exhibited the ability of burrowing out of sands. Cortes and John [2018] and Naclerio et al. [2021] performed penetration tests of earthworm inspired probes that reduce the penetration resistance in sands and lunar regolith simulants. Ortiz et al. [2019] performed experimental penetration tests on a polychaete-inspired soft robot which reduced the resistance force by radial expansion and bi-directional bending.

Numerical methods, such as discrete element modeling (DEM), have also used for to perform bio-inspired studies since DEM can provide multi-scale data of soil responses and interactions between soils and probes. For example, Huang and Tao [2020] presented DEM results of a razor clam-inspired probe, showing that the radial anchor expansion led to a reduction in tip penetration force. Khosravi et al. [2018] employed DEM simulations to investigate the forces involved in a bioinspired self-burrowing probe in granular materials of varying density. The results indicated that a greater ratio between penetration and reaction forces was mobilized in the dense specimen than in the loose specimen during displacement-controlled probe motions. Martinez et al. [2020] used cavity expansion to assess self-penetration potential in clayey, silty and sandy soils. The results show that the most challenging conditions for self-penetration are in dense sandy soils. Chen et al. [2021, 2022] investigated the forces, soil stress states and deformations during the self-penetration process of a bio-inspired probe that uses a ‘anchor-tip’ strategy in DEM simulations. The results show that the tip penetration distance was increased as the anchor length and distance between the anchor was increased due to the greater relaxation of stresses ahead of the tip during anchor expansion. Chen et al. [2022] simulated a bio-inspired probe with two anchors, showing that deploying two anchors results in mobilization of greater total anchor capacity than the single-anchor probe. However, the probe with two anchors mobilized a smaller capacity per anchor.

There are two main simplifications in the aforementioned numerical studies, which may bring inaccurate or unrealistic estimation on the probe’s self-penetration ability. One simplification is that the motions of the simulated probe are usually displacement-controlled (e.g. Khosravi et al. [2018], Huang and Tao [2020], Chen et al. [2020]) or velocity-controlled with force limits (e.g. Chen et al. [2021]), which do not explicitly consider the acceleration of the probes as a result of the unbalanced forces. In particular, with displacement-controlled motion, the tip penetration displacement is assigned in the simulation and does not rely on the balance between the mobilized reaction and penetration resistance forces. Another simplification is that typically only one self-burrowing cycle is simulated, while probes deployed in the field will be required to perform multiple cycles of expansion and contraction of anchors and tip advancement to reach depths relevant for geotechnical engineering activities. Additionally, while other studies have considered the effect of soil density on the self-burrowing process, these have either ignored or simplified the interactions between different parts of the probe (i.e. anchor and tip) (e.g. Martinez et al. [2020])

The DEM study presented herein aims to perform more accurate simulations on the self-burrowing probes as well as to investigate the effects of density on the self-burrowing process. Therefore, force-controlled motions are used to simulate the dynamic interactions between the probe and soil during the self-burrowing process. Using this motion control, the achieved tip advancement depends on the balance between the reaction and resistance forces. The effects of specimen density on the self-penetration process are investigated via simulations on dense, medium dense and loose specimens. The mechanical work done during the entire self-burrowing process is also recorded and analyzed. Multiple cycles of the probe's self-burrowing motions in the dense specimen are simulated to further evaluate the probe's self-penetration ability.

5.3 Model Parameters

The DEM simulations were performed on an Intel(R) Xeon(R) CPU E5-2660 v4 computer server. The DEM model was developed in the PFC 3D software (Version 5.0, Itasca), consisting of a cylindrical chamber, bottom wall, bio-inspired probe and particles (Figure 5.1a). The chamber diameter (D_c) and height (H_c) both equal to 0.7 m. The chamber walls maintain constant locations throughout the simulations.

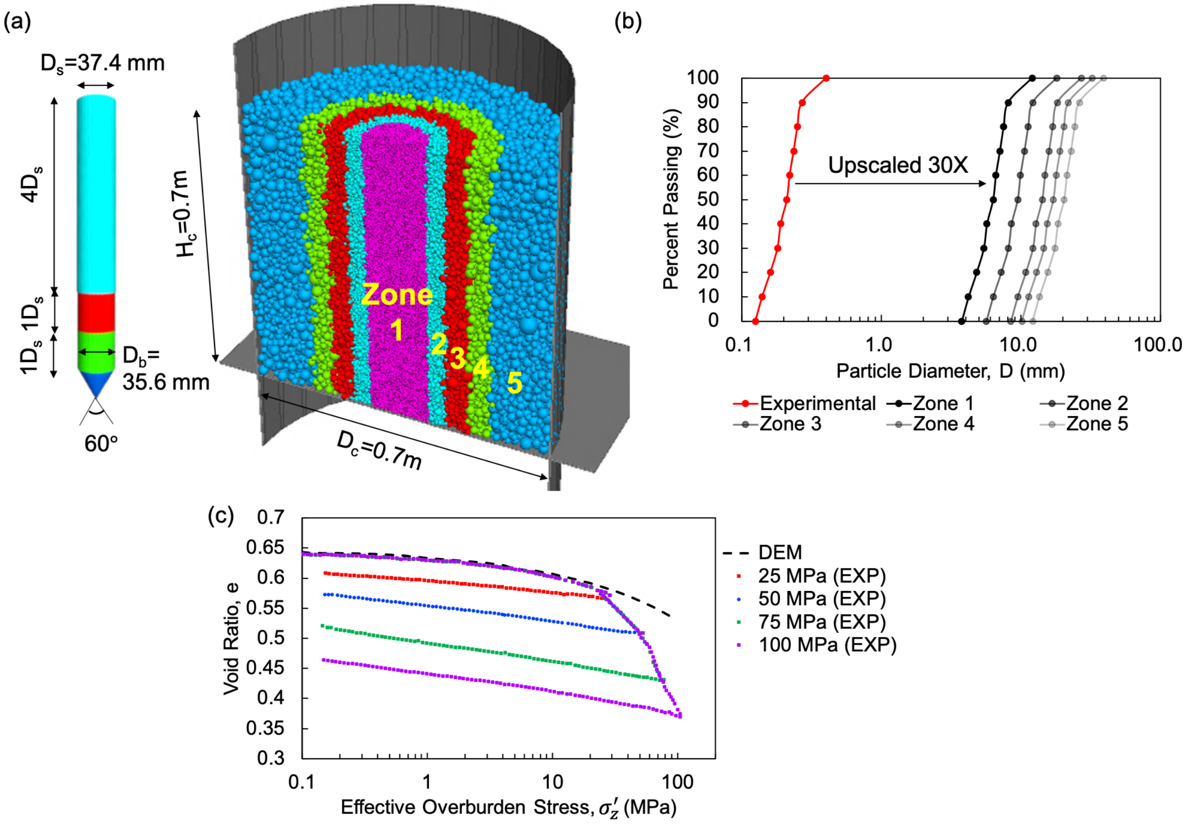

Figure 5.1: DEM simulation configuration. (a) bio-inspired probe, virtual calibration chamber and particles; (b) experimental particle size distribution of Fontainebleau sand [Yang et al., 2010] and 5 simulated zones; (c) validation of the DEM contact model for Fontainebleau sand via the DEM simulation of high pressure oedometric compression tests (after Zhang et al. [2021]).

There are about 152,000 particles in the chamber, which are upscaled from the experimentally measured sizes of Fontainebleau sand and are modeled using spheres. The particle refinement method [McDowell et al., 2012], which simulates particles in a number of zones that have different particle size upscaling factors, was employed to increase the number of particle-probe contacts while maintaining a reasonable computational time. The mean particle size (D_{50}) in the center zone is 6.3 mm and the particle sizes gradually increase from the inner zones to the outer zones with factor of 1.5 or 1.2, as shown in Figure 5.1b. The study presented in Chapter 6 indicates that while the PRM does not influence the penetration resistance magnitudes, it helps smoothen the trends due to the greater amount of probe-particle contacts (see Figure 6.5 in Chapter 6). The soil within each zone has a coefficient of uniformity (C_U) of 1.7 and a coefficient of curvature (C_C) of 1.2. The soil density is 2.65 g/cm^3.

The probe consists of three shafts and one conical tip, which are modeled using wall elements. The bottom and middle shafts have a diameter (D_b) of 35.6 mm, while the top shaft has a slightly larger diameter (D_s) of 37.4 mm. This larger diameter is required to avoid repeated calculation of the probe force at the overlapping section between the top and the middle shafts (Figure 5.1a). The total length of the probe is six times of top shaft diameter ($6D_s$), with the length of the top, middle and bottom shafts being $4D_s$, $1D_s$ and $1D_s$, respectively. The middle shaft is embedded into the top shaft with a length of $4D_s$. The tip apex angle is 60° and the probe density is 8.05 g/cm^3.

The contact model developed by Zhang et al. [2021] is used to simulate the behavior of Fontainebleau sand. This model was developed based on the standard Hertzian model. The contacts between particles are assumed to be elasto-plastic, the slip behavior at contacts is controlled by a friction coefficient μ, and each contact has a non-linear stiffness determined by the elastic properties of the particles (i.e. shear modulus G and Poisson's ratio υ). The main simulation parameters are listed in Table 5.1. Specifically, the particles have a shear modulus (G) of 32 GPa and a Poisson's ratio of 0.19. The particle friction coefficient is 0.275 (μ) and the particle rotation is inhibited to simulate the effects of particle angularity. The chamber wall friction coefficient is 0.0, while the values of G and

μ are same as those for the particles. The simulated probe has a shear modulus of 74 GPa, a Poisson's ratio of 0.265 and a friction coefficient (μ_p) of 0.35. Figure 5.1c compares the DEM results of the oedometric compression of cubic specimen under a pressure about 100 MPa and the experimental test results with varying pressures from Ciantia et al. [2019b]. At stresses smaller than 30 MPa, the loading response in the DEM simulation matches well with the experimental response. More detailed calibration parameters can be found in Zhang et al. [2021].

Table 5.1: DEM simulation parameters.

Parameters	Symbols	Values
Shear modulus for walls and particles	G	32 GPa
Poisson's ratio for walls and particles	υ	0.19
Shear Modulus for probe	G_p	74 GPa
Poisson's ratio for probe	υ_p	0.265
Particle friction coefficient	μ	0.275
Probe friction coefficient	μ_p	0.35
Chamber wall friction coefficient	μ'	0.0
Particle density	ρ	2.65 g/cm^3
Probe density	ρ_p	8.05 g/cm^3

In DEM simulations of penetration processes, the chamber-to-probe diameter (D_c/D_s) and probe-to-particle diameter ratios (D_s/D_{50}) should have sufficiently large values to minimize boundary and particle scale effects. In this study, the D_c/D_s and D_s/D_{50} values are 18.7 and 5.9, respectively, which are greater than values commonly employed in previous DEM studies on the soil penetration problems. For example, the D_c/D_s values were from 12.0 to 16.6 and D_{probe}/D_{50} values were from 2.7 to 3.1 in the 3D simulations from Arroyo et al. [2011], Butlanska et al. [2014], Zeng and Chen [2016], Ciantia et al. [2016], Ciantia et al. [2019a], Zhang et al. [2019], Huang and Tao [2020].

The dynamic effects in DEM simulations can be characterized by the inertial number (I). Namely, if I reaches sufficiently large values then the inertial effects become important in the simulation results. The maximum I value during the initial penetration stage are calculated as 7.5×10^{-4}, which satisfy the criteria ($I < 10^{-3}$-10^{-2}) for maintaining quasi–static conditions [Combe and Roux, 2009; Radjai and Richefeu, 2009; O'Sullivan, 2011]. During the penetration stage with oscillations, the maximum I value is calculated to be 2.3×10^{-1}, indicating that inertial effects are reflected in the simulation results.

5.4 Simulation Process

5.4.1 Specimen Generation

First, the number of particles is calculated based on the desired specimen void ratio (e) and the chamber size. The particles are then generated within the chamber using the radius expansion method, where the particle radii are multiplied stepwise by a given factor to generate the desired particle size distribution and a uniform isotropic stress state [O'Sullivan, 2011]. At this stage, the shear stiffness and Poisson's ratio are assigned to the walls and particles. Then, the simulation is cycled until an initial stress of zero and system equilibrium are both achieved.

After the initial cycling, the particle friction coefficient is assigned to the particles and the gravity is activated. Then, the second round of cycling is initiated and run until the system equilibrium is reached. Different particle friction coefficients are used to generate specimens with different void ratios (Table 5.2). In this study, the friction coefficients of 0.05, 0.2 and 0.5 yielded e of 0.57, 0.69 and 0.77, respectively. Ciantia et al. [2019b] performed both experimental analysis and DEM calibration on Fontainebleau sand, which showed that the maximum and minimum void ratio (e_{max}, e_{min}) of Fontainebleau sand were 0.90 and 0.51, respectively. Considering these values as valid for the DEM simulations presented here yields relative densities of 85%, 54% and 33%, respectively, which are referred to as 'dense', 'medium dense' and 'loose' hereinafter.

Once the specimen is settled under gravity, the sample quality is evaluated by checking the distribution of contact forces and soil stresses (Figure 5.2). Contact force chains depict the normal interparticle contact forces, where the color proportional to the force magnitude. It is noted that, in PFC, while the color scale for the contact force magnitude can be made the same for the three specimens, the scaling of the line thickness cannot

Table 5.2: Summary of the simulations performed in this study.

#	Specimen	Void Ratio	Density	Self-Burrowing Cycles Simulated	EM_s at the end of SE stage
1	Dense	0.57	85%	2	0.16
2	Medium Dense	0.69	54%	1	0.10
3	Loose	0.77	33%	1	0.35
4	Loose	0.77	33%	1	0.08

be made consistent through the three cases. The soil stress maps present the average stresses at the center of each element, which are measured using 196 measurement spheres placed in a vertical plane. The results show that the contact force chains and soil stresses distribute uniformly in the horizontal direction and gradually increase in magnitude as the depth increases. The specimen shown in Figure 5.2b indicates that there was negligible migration of particles among the different zones using the particle refinement method.

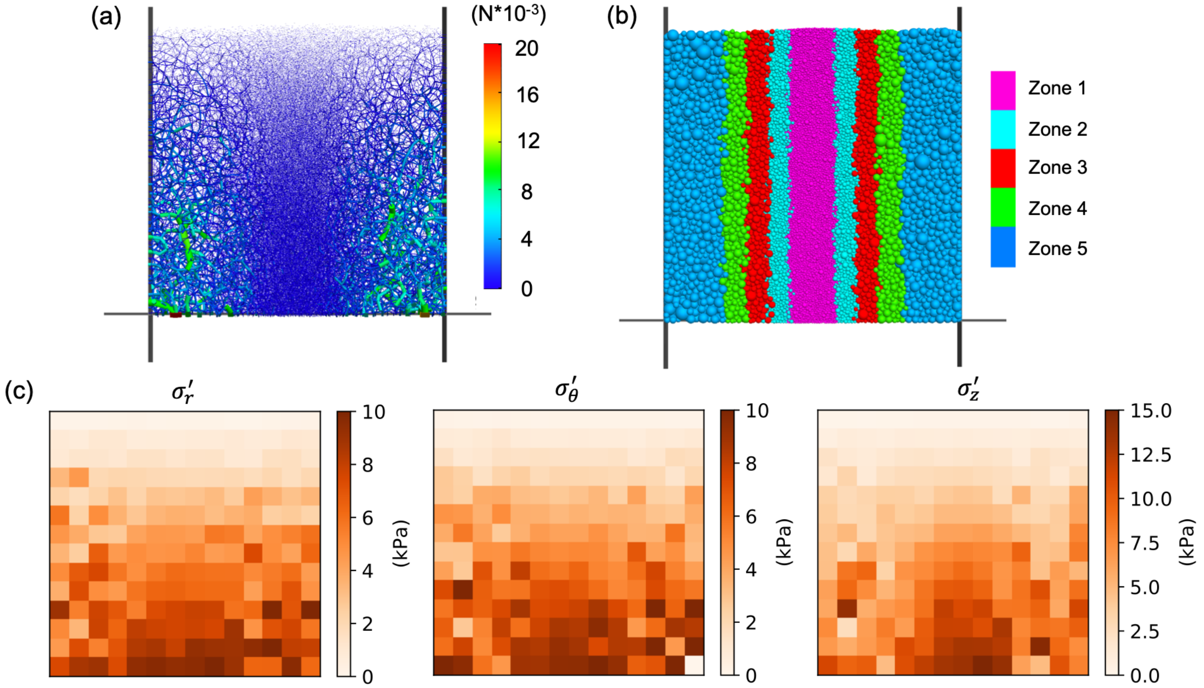

Figure 5.2: Dense specimen quality after gravity settlement. (a) contact force chains; (b) particle groups in the five zones; (c) radial, hoop and vertical soil stresses.

5.4.2 Bio-inspired self-burrowing Cycle

There are seven stages simulated in one self-burrowing cycle (Figure 5.3): initial penetration (IP), top shaft expansion (SE), tip penetration with oscillation (TPO), bottom shaft expansion (BE), top shaft contraction (SC), shaft retraction (SR), and bottom shaft contraction (BC). It is noted that the IP stage only exists before the first cycle of the self-burrowing process. In the schematic of these stages, the forces acting on the probe sections are marked with blue arrows. The symbol of each force is labeled only once for clarity. The probe motion control algorithms and the simulation termination criteria for each stage are also indicated and defined in the Figure 5.3. The termination criteria were chosen based on limitations stemming from the probe configuration and expectations of limitations during field testing. Table 5.3 provides more information regarding these termination criteria.

5.4.2.1 Initial Penetration Stage

The forces acting on each probe section are referred to as '$F_{m,n}$', with the first subscript m representing the direction of the force (i.e. r is radial and z is vertical) and the second subscript n representing the probe section that the force acts on (i.e. s is the top shaft, t is the tip, b is the bottom shaft and all is all three parts). This naming convention also applies to the displacements ($\delta_{m,n}$) and velocities ($v_{m,n}$). For example, '$F_{r,s}$' represents the radial force acting on the top shaft, '$\delta_{z,t}$' represents the vertical displacement of the tip, and '$v_{r,b}$' represents the radial velocity of the bottom shaft. One exception is '$F_{z,b}$', which represents the total vertical force acting on both the bottom and the middle shafts.

The initial penetration stage consists of quasi-static penetration and self-weight equilibrium of the bio-inspired probe. During quasi-static penetration, the entire probe is displaced downward from its initial position outside of the specimen to a tip depth of 0.34 m with a constant velocity of 0.4 m/s (D1 and C1 in Figure 5.3). As shown in Figure 5.4a for the three specimens with dense, medium dense, and loose densities, the probe mobilizes an average penetration resistance (q_c) of 6.21 MPa, 2.16 MPa and 0.78 MPa, respectively, at depths from 0.3 m to 0.34 m. The q_c increases by 2.88 times between the medium dense and dense specimens and it increases by 2.77 times between the loose and medium

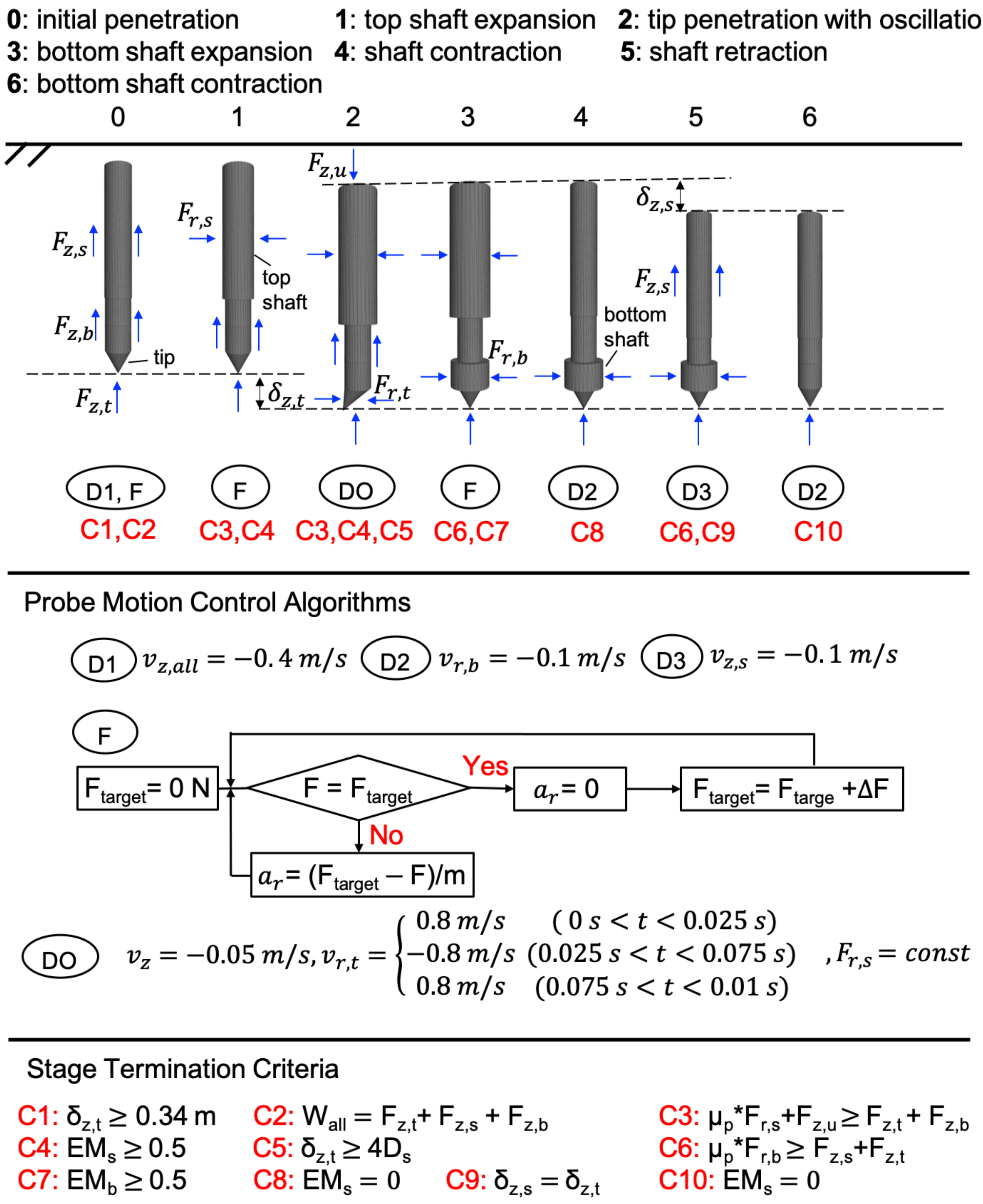

Figure 5.3: Schematic of the self-burrowing process (stages 0-6), control algorithms (displacement-controlled (D1-D3), force-controlled (F), displacement-controlled with oscillation (DO)) and terminal conditions (C1-C8) for each stage. Note that the initial penetration stage only occurs before the first cycle of self-penetration and the negative velocity represents either a downwards vertical or inwards radial velocity. Note that that the decision process for checking the termination criteria in the control algorithms aren't shown for clarity.

Table 5.3: Termination criteria for self-burrowing stages.

Name	Termination Criteria	Applied Stages	Logic
C1	$\delta_{z,t} \geq 0.34$ m	IP	Penetration depth that allows the entire probe to be embedded in the specimen
C2	$W_{all} = F_{z,t} + F_{z,s} + F_{z,b}$	IP	Force balance equation
C3	$\mu_p F_{r,s} + F_{z,u} \geq F_{z,t} + F_{z,b}$	SE, TPO	Force balance equation
C4	$EM_s \geq 0.5$	SE, TPO	Expected pyhsical limit of expansion of the top shaft
C5	$\delta_{z,t} \geq 4D_s$	TPO	$4D_s$ is the embedded middle shaft length inside the top shaft
C6	$\mu_p F_{r,b} \geq F_{z,s} + F_{z,t}$	BE, SR	Force balance equation
C7	$EM_b \geq 0.5$	BE	Expected pyhsical limit of expansion of the bottom shaft
C8	$EM_s = 0$	SC	Returns of the expanded top shaft to its original diameter
C9	$\delta_{z,s} = \delta_{z,t}$	SR	The top shaft retracts its original location relative to the tip
C10	$EM_b = 0$	BC	Returns of the expanded bottom shaft to its original diameter

dense. These increases in qc are consistent with the change of normalized tip resistance with sand density from Mayne [2007], which predicts an increase of about 2.5 times when the density increase from 33% to 54% and from 54% to 85%. The contact force chains have greater magnitudes at locations near the probe tip are shown in Figure 5.4b. The tip resistance is defined as:

$$q_c = \frac{4F_{z,t}}{\pi D_b^2} = \frac{4\sum_{i=1}^{N} F_{z,ti}}{\pi D_b^2} \tag{5.1}$$

Where the $F_{z,t}$ is the total vertical force acting on the conical tip, $F_{z,t}$ is the ith vertical component force on the cone, N is the number of contact forces on the cone and D_t is the diameter of the conical tip.

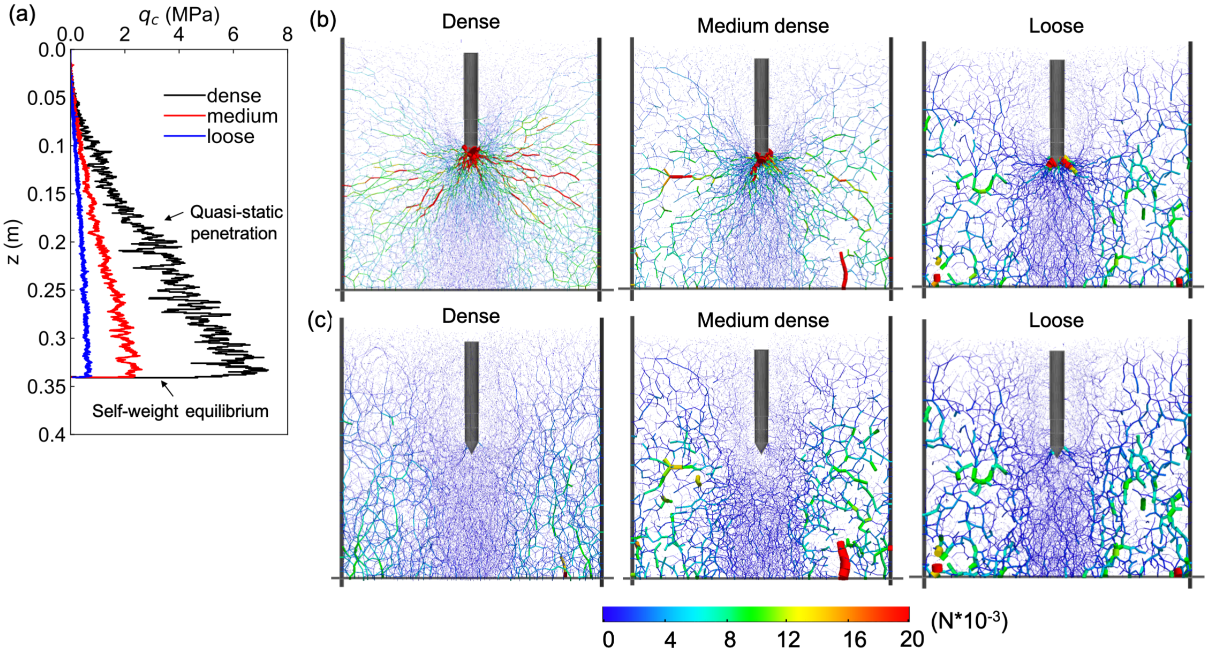

Figure 5.4: (a) Evolution of tip resistance with depth during the initial penetration stage; contact force chains at the end of the (b) quasi-static penetration and (c) self-weight equilibrium. Note that the color scale is same in all the figures but the thickness of force chains is not.

During the self-weight equilibrium of the probe, the balance of forces acting on the probe and Newton's second law are solved and the probe is displaced by a force-controlled loading algorithm (Figure 5.3). With this algorithm, the forces are balanced since the initial total resistance force ($Q_{z,all}$, Eq. 5.2) is greater than the probe's self-weight (W_{all}), resulting in an upward acceleration of the probe ($a_{z,all}$, Eq. 5.3). With the movement of the probe, the $Q_{z,all}$ is updated and compared to W_{all} again. This process repeats until the two forces (i.e. $Q_{z,all}$ and W_{all}) are equal to each other, resulting in an acceleration of zero (F in Figure 5.3). The upward movement of the probe leads to the relaxation of resistance forces near the tip, which is shown in the force chains at the end of self-weight equilibrium (Figure 5.4c). It should be noted that the purpose of the initial penetration stage (i.e. quasi-static penetration and self-weight equilibrium) is to achieve the initial embedment required for mobilization of the reaction forces during the remaining stages of the bio-inspired self-penetration process. Therefore, this first stage is only simulated during the first self-burrowing cycle of the simulation.

$$Q_{z,all} = F_{z,t} + F_{z,b} + F_{z,s} = \sum_{i=1}^{N_1} F_{z,ti} + \sum_{j=1}^{N_2} F_{z,bj} + \sum_{k=1}^{N_3} F_{z,sk} \tag{5.2}$$

$$a_{z,all} = \frac{Q_{z,all} - W_{all}}{m_{all}} \tag{5.3}$$

Where the $F_{z,t}$, $F_{z,b}$ and $F_{z,s}$ are the total vertical forces acting on the tip, bottom and middle shafts, and top shaft, with $F_{z,ti}$, $F_{z,bj}$ and $F_{z,sk}$ being the corresponding ith, jth and kth component forces and N_1, N_2 and N_3 being the corresponding numbers of contact forces. Finally, m_{all} is the probe mass.

5.4.2.2 Self-burrowing stages

During the SE stage, the top shaft is expanded using a stepwise force-controlled algorithm. The upscaling of particle diameter has been shown to have minor effects on the mobilized shaft forces in Chapter 4. As shown in Figure 5.3, the radial force on the top shaft ($F_{r,s}$, Eq. 5.4) is measured during the expansion process and the radial expansion acceleration is calculated based on the difference between the current $F_{r,s}$ and the target force (F_{target}) using the Newton's second law. Once $Ftarget$ is achieved, $Ftarget$ is increased by ΔF and then the next step of expansion is initiated. The ΔF value should be small enough to enable a stable $F_{r,s}$ at the end of each loading step. In this investigation, ΔF is 0.3 kN, 0.15 kN, and 0.05 kN for the dense, medium dense and loose specimens, respectively. It is noted that the $F_{r,s}$ during the SE stage is maintained at a smaller value than the $F_{r,s}$ that can be mobilized. Since there is no theoretical solution to the limit $F_{r,s}$ in shallow conditions, the maximum $Ftarget$ is determined by multiplying the maximum $F_{r,s}$ measured during the shaft expansion with a constant velocity of 0.02 m/s by a reduction factor of 0.85. The maximum $Ftarget$ values for the dense, medium dense and loose specimens are 1.50 kN, 0.76 and 0.49 kN, respectively. The top shaft expansion magnitude (EM_s) is calculated using Eq. 5.5. During the stepwise expansion, the SE stage is terminated once the mobilized reaction force is greater than the total resistance force (C3 in Figure 5.3) or once an EM_s of 0.5 is reached (C4 in Figure 5.3). In all simulated cases in this study, the C3 condition was not triggered.

$$F_{r,s} = \sum_{i=1}^{N} F_{z,si} \tag{5.4}$$

$$EM_s = \frac{D_{s,expanded} - D_s}{D_s} \tag{5.5}$$

Where the $F_{r,si}$ is the ith radial component force acting on the top shaft, N is the total number of forces on the top shaft, and D_s,expanded is the top shaft diameter after shaft expansion.

During the TPO stage, the bottom and middle shafts and conical tip are displaced downward at a velocity of 0.05m/s (DO in Figure 5.3). Meanwhile, the expansion algorithm of the top shaft is still active to maintain a constant $F_{r,s}$ value. An initial simulation on the dense specimen indicated that quasi-static advancement of the tip resulted in self-burrowing failure because the penetration resistance force was too large, resulting in a negligible penetration distance of 0.6 cm." Therefore, the tip oscillation strategy inspired by polychaetes [Ortiz et al., 2019; Dorgan, 2018] was employed to reduce the penetration resistance. Tip oscillation consisting of periodic right-left-right movements of the tip vertex with a period of 0.1 s, amplitude of 0.02m., and absolute velocity of 0.8 m/s (DO in Figure 5.3). The TPO stage stops when the total penetration resistance force (Q_z, Eq. 5.6) becomes greater than the maximum reaction force ($F_{z,max}$, Eq. 5.7) that can be mobilized , the EM_s reaches 0.5 or the penetration distance ($\delta_{z,t}$) reaches $4D_s$ (C3, C4 or C5 in Figure 5.3).

$$Q_z = F_{z,t} + F_{z,b} = \sum_{i=1}^{N_1} F_{z,ti} + \sum_{j=1}^{N_2} F_{z,bj} \tag{5.6}$$

$$F_{z,max} = \mu_p F_{r,s} + F_{z,u} \tag{5.7}$$

Where the $F_{z,t}$ and $F_{z,b}$ are the total vertical forces acting on the tip and on the bottom and middle shafts, respectively; μ_p is the probe friction coefficient; $F_{z,u}$ is the end bearing force acting on the top shaft (Figure 5.3).

During the BE stage, the bottom shaft is radially expanded using the same force-controlled algorithm described for the SE stage (F in Figure 5.3). This expanded bottom shaft serves as an anchor for retracting the top shaft at a later stage. The BE stage is terminated once the mobilized bottom shaft reaction force ($F_{z,b}$, Eq. 5.8) is greater than the penetration resistance or the bottom shaft expansion magnitude (EM_b, Eq. 5.9) reaches a limit of 0.5 (C6 or C7 in Figure 5.3).

$$F_{z,b} = \mu_p F_{r,b} \tag{5.8}$$

$$EM_b = \frac{D_{b,expanded} - D_b}{D_b} \tag{5.9}$$

Where the D_b,expand is the diameter of the bottom shaft after expansion.

The top shaft is contracted with a radial velocity of 0.1 m/s in the SC stage until the diameter returns back to its original value of 37.4 mm (D2 and C8 in Figure 5.3). Then, the top shaft is displaced downward at a velocity of 0.1 m/s in the SR stage (D3 in Figure 5.3). This downward movement is stopped once the reaction force on the bottom shaft is smaller than the sum of the shaft retraction resistance force and the tip resistance force or the shaft retraction distance ($\delta_{z,s}$) reaches the tip penetration distance mobilized in the TPO stage (C6 or C9 in Figure 5.3). Lastly, the tip is contracted with a radial velocity of 0.1 m/s in the BC stage until it returns to its original diameter of 35.6 mm (D2 and C10 in Figure 5.3). At this stage, one cycle of self-burrowing is completed, the probe shape has returned to the original condition and the entire probe has achieved a downward displacement of $\delta_{z,t}$.

Discrete element methods are usually computationally intensive, therefore the simulation time for this study is summarized here as a reference for future researchers. On the Intel(R) Xeon(R) CPU E5-2660 v4 computer server, the sample generation process with gravitational settlement takes about 14 days and the initial penetration of 0.34 m takes about 13 days. Achieving every 0.1 of expansion magnitude for the top and bottom shafts requires about 1 day. During the TPO stage, it takes about two days for 1 cm of tip advancement with oscillation. Contraction of shafts requires similar computational time as that for expansion. It takes about six hours for every 1 cm of shaft retraction. In total, the computational time is between 15 and 21 days for one self-burrowing cycle (the IP stage is not included) in this study.

5.5 Results

In this section, the probe forces and displacements, particle contact forces, particle displacements and mechanical work done during one cycle of self-penetration are presented. Simulation results for the dense, medium dense and loose specimens are compared to investigate the effects of specimen density on the self-penetration process. A second cycle of self-penetration in the dense specimen is also presented to further evaluate the probe self-burrowing ability. A summary of the simulations performed in this study is presented in Table 5.2.

5.5.1 One Self-Burrowing Cycle in the Dense Specimen

The evolution of probe forces and displacements during the six stages of self-burrowing process for the dense specimen are shown in Figure 5.5, excluding the initial penetration stage. The duration of each stage is indicated by the gray dashed lines. At the end of the SE stage, the top shaft achieves a radial force of about 1.5 kN with an expansion magnitude of 0.16, while the penetration resistance force increased from nearly zero, which is measured at the end of self-weight equilibrium, to a value of 0.22 kN (Figure 5.5a).

During the TPO stage, the middle and bottom shafts and the tip are displaced downward accompanied by simultaneous tip oscillation in the horizontal direction while the top shaft maintains its location and continues to expand to keep the $F_{r,s}$ value constant.

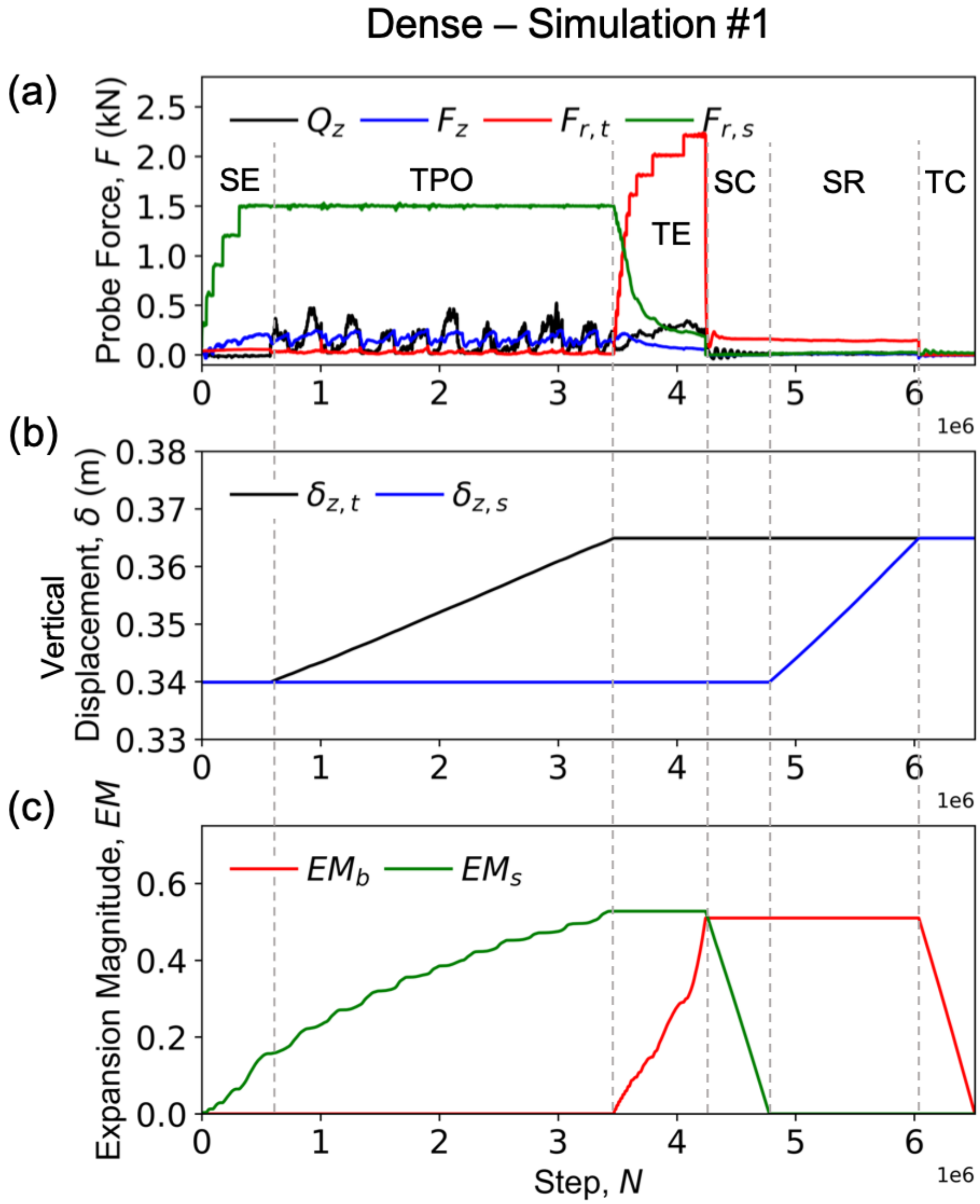

Figure 5.5: The evolution of probe forces and displacements with simulation steps during the self-penetration process in the dense specimen. (a) penetration resistance force, vertical top shaft force, radial top shaft force, and radial bottom shaft force; (b) penetration displacements of the tip and the top shaft; (c) expansion magnitude of the top and the bottom shafts.

The Q_z value oscillates with a maximum value of 0.51 kN and minimum values or around zero kN (Figure 5.5a). This trend indicates that the tip oscillation strategy can reduce the penetration resistance and prevent its remobilization of the penetration force to the value measured at the end of quasi-static penetration, as observed by Chen et al. [2021, 2022] in simulations without tip oscillation. At the end of TPO stage, the EM_s reaches 0.52, which exceeds the expansion limit of 0.5; therefore the TPO stage is terminated (Figure 5.5c). At this stage, the tip achieves an advancement of 2.5 cm with 5 cycles of tip oscillation (Figure 5.5b). It is noted that even though the mobilized shaft reaction force (F_z, Eq. 5.10) is smaller compared to the Q_z values, the total reaction force ($F_{z,max}$, Eq. 5.7) that can be mobilized is calculated to be 0.69 kN, which is greater than Q_z and thus enables tip advancement.

$$F_z = F_{z,s} + F_{z,u} \tag{5.10}$$

Where $F_{z,s}$ and $F_{z,u}$are the side friction force and end bearing force acting on the top shaft (Figure 5.3), respectively.

During the BE stage, the probe penetration is stopped and the bottom shaft is expanded radially using the force-controlled motion. At the end of the BE stage, the bottom shaft mobilizes a $F_{r,b}$ of 2.43 kN and a corresponding EM_b of 0.46. It is noted that, the $F_{r,s}$ on the top shaft decreases to 0.25 kN at the end of the BE stage due to arching that causes a relaxation of the contact forces around the top shaft. This reduction has the similar mechanism with the tip resistance relaxation induced by shaft expansion during the SE stage.

Once the bottom shaft has been expanded, the top shaft is contracted during the SC stage and then retracted during the SR stage. The bottom shaft reaction force is large enough for the retraction stage to be completed since the retraction resistance force (i.e. $F_{z,s}$) mobilized by the top shaft is smaller than 0.1 kN throughout the SR stage. After that, the bottom shaft is contracted and the first self-burrowing cycle is completed.

Effects of density on the self-penetration process The SE and TPO stages are the most influential stages for achieving self-penetration, therefore the discussion regarding effects of specimen density on the self-penetration process are focused on these two stages. The evolution of probe forces and displacements for the medium dense and loose specimens are presented in Figures 5.6 and 5.7, respectively.

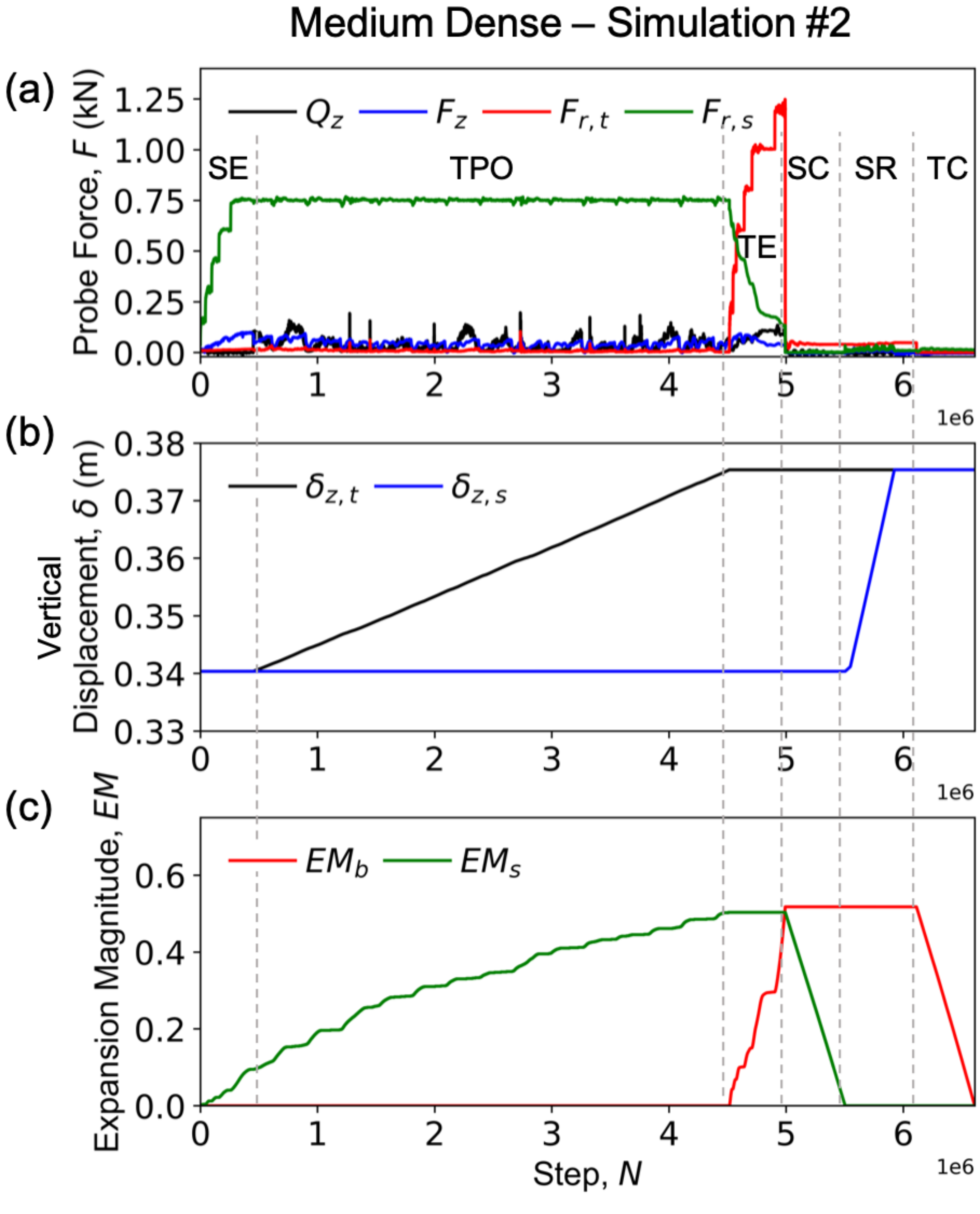

Figure 5.6: The evolution of probe forces and displacements with simulation steps during the self-penetration process in the medium dense specimen. (a) penetration resistance force, vertical top shaft force, radial top shaft force, and radial bottom shaft force; (b) penetration displacements of the tip and the top shaft; (c) expansion magnitude of the top and the bottom shafts.

The SE stage is terminated once a target $F_{r,s}$ of 0.76 kN is reached which corresponded

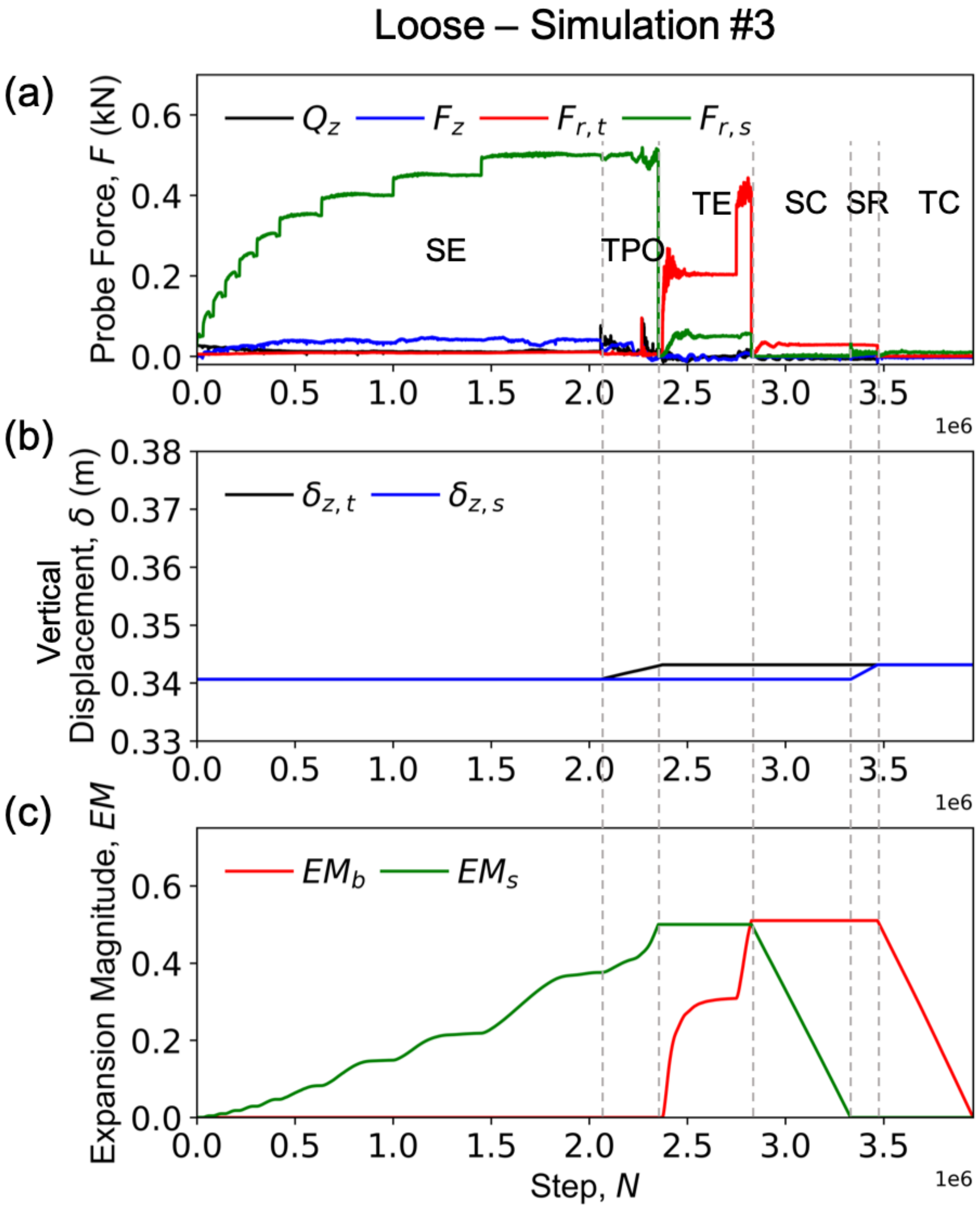

Figure 5.7: The evolution of probe forces and displacements with simulation steps during the self-penetration process in the loose specimen. (a) penetration resistance force, vertical top shaft force, radial top shaft force, and radial bottom shaft force; (b) penetration displacements of the tip and the top shaft; (c) expansion magnitude of the top and the bottom shafts. Note that the TPO stage started with a EMs of 0.35.

to an EM_s of 0.1 in the medium dense specimen (Figure 5.6). For the loose specimen, the SE stage is terminated once a target $F_{r,s}$ of 0.49 kN is generated which corresponded to an EM_s of 0.35 (Figure 5.7). In comparison to the dense and medium dense specimens, a greater expansion magnitude of 0.35 is required in the loose specimen to mobilize the target $F_{r,s}$.

During the TPO stage, the tip achieves a downward displacement of 3.5 cm and 0.25 cm in the medium dense and loose specimens, respectively, accompanied with 7 and 0.5 cycles of tip oscillation (Figures 5.6b and 5.7b). Both simulations are terminated when the EM_s reaches a value of 0.50 (Figures 5.6c and 5.7c). The results indicate that the probe's self-penetration ability is greater in the medium dense specimen than in the dense specimen. This is because the ratio of the radial shaft force to the average resistance force ($F_{r,s}/Q_z$) is 25.3 for the medium dense specimen, which is significantly greater compared to the $F_{r,s}/Q_z$ ratio of 10.7 for dense specimen. This finding is in agreement with the cavity expansion solutions presented in Martinez et al. [2020], which showed that the ratio of cavity limit pressure to tip resistance (P_L/q_c) increases as the soil density decreases. In this study, the authors conclude that the smaller P_L/q_c for the denser soils translates into a smaller self-burrowing ability. It is noted that, the analytical method in Martinez et al. [2020] does not take into account the interactions between the different probe sections that lead to changes in the tip resistance during SE and in radial anchor force during tip advancement, which have been shown to be important for the self-burrowing process by Chen et al. [2021, 2022].

The results in Figure 5.7 indicate that self-burrowing ability in the loose specimen is less than the other two specimens despite the fact that the $F_{r,s}/Q_z$ value is the highest (35.6) in this specimen, which does not agree with the findings from Martinez et al. [2020]. Therefore, two possible explanations are proposed for the low performance in the loose specimen. Firstly, it is possible that the high void ratio of the soil results a punching failure which makes the top shaft unable to maintain the required radial force during tip advancement. This mechanism is investigated later in the meso-scale results section. Secondly, it is possible that the EM_s at the end of the SE stage is too large (i.e.

0.35), which makes the EM_s reach the limit of 0.5 early in the TPO stage, causing its termination when the tip vertical displacement is small. This assumption is investigated in the following section by terminating the SE stage at a smaller EM_s.

At the end of the BE stage, $F_{r,b}$ of 1.25 kN and 0.45 kN are mobilized in the medium dense and loose specimens, respectively. In both specimens, the $F_{r,b}$ values are large enough compared to the mobilized vertical shaft force ($F_{z,s}$) values, thus enable the top shaft to complete contraction in the SC stage and complete retraction in the SR stage.

5.5.2 Effects of Initial Expansion Magnitude on the Self-Penetration Process

An additional simulation was performed with the loose specimen to explore the effect of the EM_s on the self-burrowing performance, where the SE stage was terminated when the EM_s reached a value of 0.08, with corresponded to an $F_{r,s}$ of 0.35 kN (Figure 5.8). As shown in Figure 5.8, the small EM_s of 0.08 at the beginning of TPO enables a tip advancement of 2.5 cm during 5 cycles of tip oscillation. This result indicates that the continued shaft expansion during the TPO stage is important for achieving a greater self-penetration displacement. Therefore, maintaining a small initial EM_s before the TPO stage is necessary for allowing the shaft to be further expanded. Due to the greater tip advancement in the simulation with the smaller EM_s, only the results of this simulation are presented and discussed in the following sections.

5.5.3 Meso-Scale Results during One Cycle Self-Burrowing Cycle

The contact force chain maps and particle displacement fields during the self-penetration process are presented in this section for the dense (Figures 5.9 and 5.10) and loose (Figures 11 and 12) specimens. The contact force chain maps depict the normal contact forces between particles and the particle displacement fields shows the displacement of each individual particle, where the magnitudes of the contact forces and particle displacements are proportional to their colors in the figures. It is noted that particle displacements as a result of the stages after the initial penetration are shown in the figures, meaning that

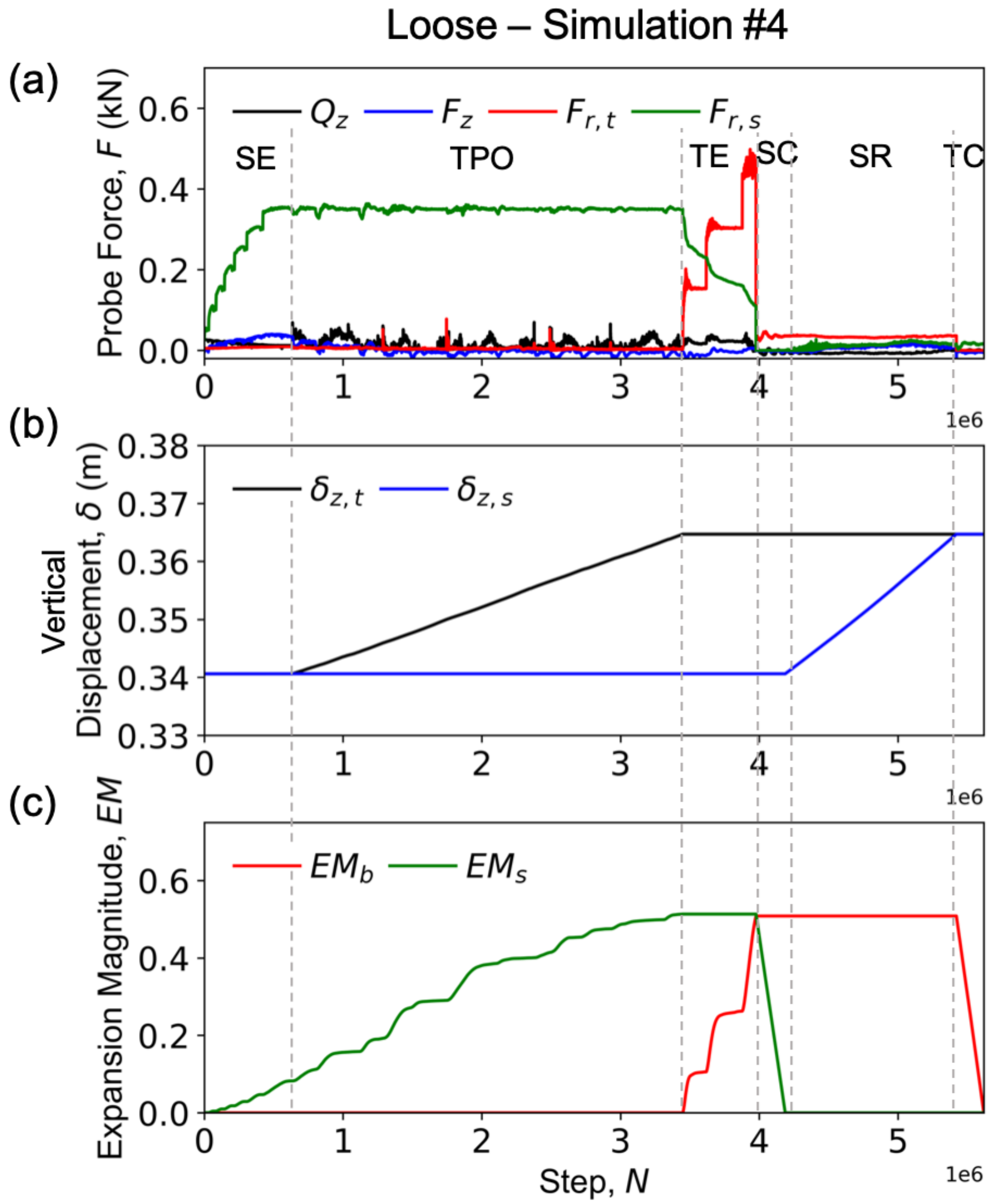

Figure 5.8: The evolution of probe forces and displacements with simulation steps during the self-penetration process in the loose specimen. (a) penetration resistance force, vertical top shaft force, radial top shaft force, and radial bottom shaft force; (b) penetration displacements of the tip and the top shaft; (c) expansion magnitude of the top and the bottom shafts. Note that the TPO stage started with a EMs of 0.08.

the displacements produced during initial penetration are not shown. The contact forces

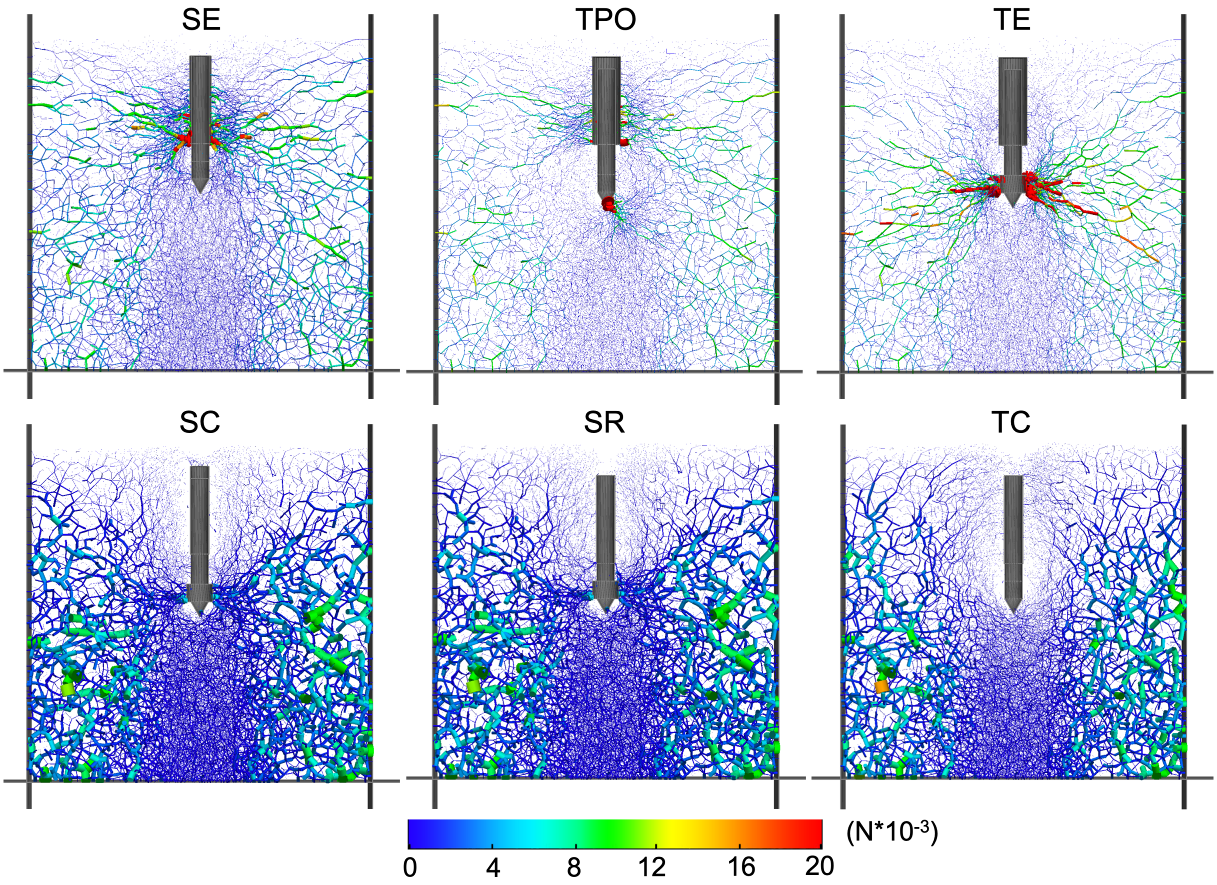

Figure 5.9: Contact force chains at the end of the six stages (SE, TPO, BE, SC, SR, BC) during the self-penetration process in the dense specimen. Note that the color scale is same in all the figures but the thickness of force chains is not.

reflect the probe-particle interaction during the self-burrowing process. The large contact forces aggregate near the probe sections that are being displaced and loaded. For example, concentration of contact forces occurs around the top shaft in the SE stage, below the tip in the TPO stage and around the bottom shaft in the BE stage (Figure 5.9). Similarly, the large contact forces vanish near the probe sections that are being unloaded; this can be seen around the top shaft in the SC stage and around the bottom shaft in the BC stage (Figure 5.9). Also, the contact forces around the middle and bottom shafts are very small in magnitude in the TPO stage due to the continued expansion of the top shaft and advancement of the tip that lead to relaxation of contact forces. The contact forces near

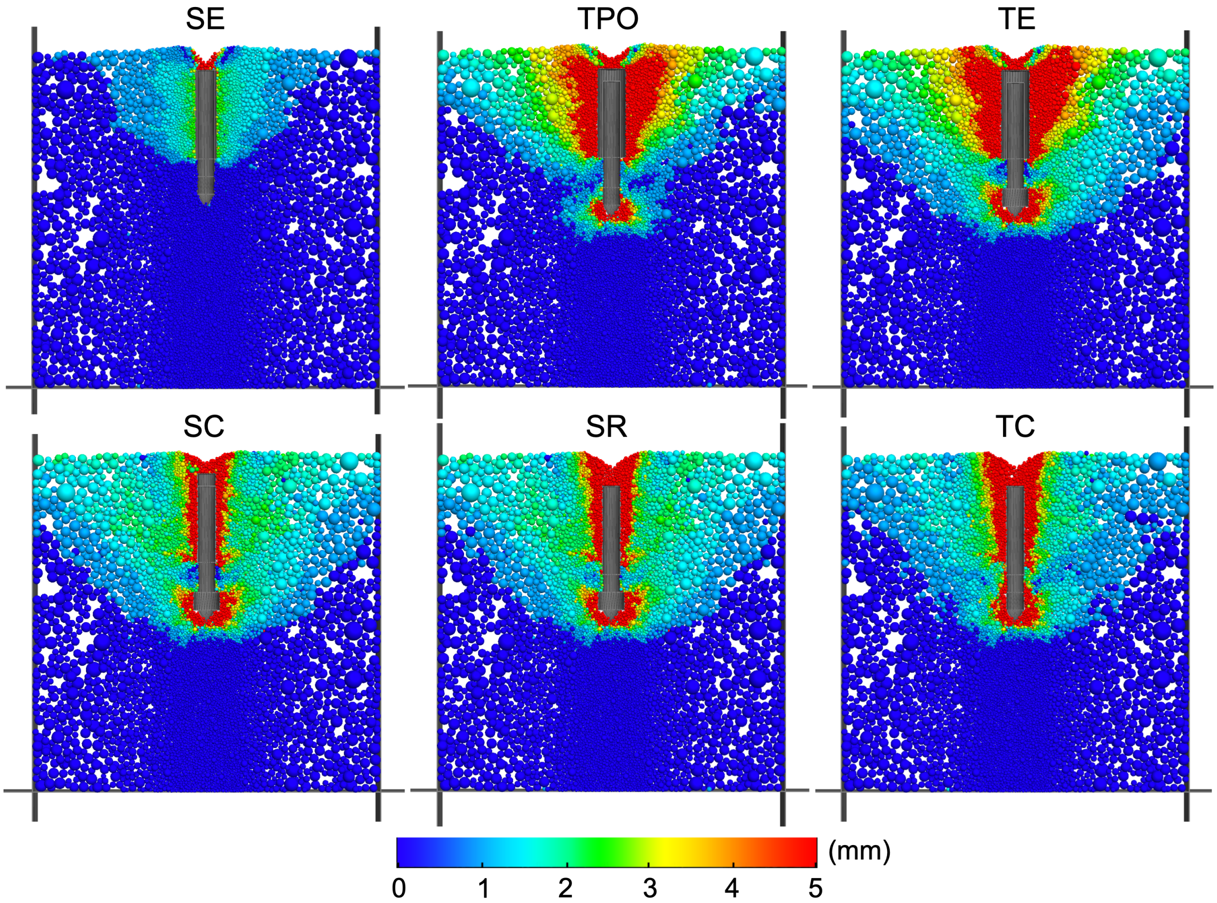

Figure 5.10: Particle displacements at the end of the six stages (SE, TPO, BE, SC, SR, BC) during the self-penetration process in the dense specimen. Note that the displacements are recorded from the beginning of the SE stage (i.e. the displacements during initial penetration are not included).

the tip become very small in the BE stage due to the expansion of the bottom shaft that leads to relaxation of the forces below the tip. A similar kind of interactions between the anchor and the tip has been discussed in Chen et al. [2022].

The particle displacement fields show the zones of high deformation that correspond to the soil failure zones. The particle displacements around the top shaft are characteristic of a shallow failure. Despite this, the displacements are relatively small at the end of the SE stage in the dense specimen due to the small EM_s. At the end of the TPO stage, the displacement magnitudes are greater, forming a more pronounced symmetric shallow failure zone that extends from the bottom of the top shaft up to the soil free surface (Figure 5.10). The particle displacements are also large near the tip due to the downward and oscillating tip movements. At the end of the BE stage, the bottom shaft expansion enlarges the failure zone around the bottom shaft and tip. After SC, the particle displacements around the top shaft decreases due to the shaft contraction, with magnitudes greater than 3.5 mm only remaining in a zone close to the probe. Finally, more modest changes in particle displacements occur during the SR and BC stages, with some changes around the tip due to the contraction of the tip.

The contact force chains and particle displacements at the end of SE, TPO, and BE stages in the loose specimen are presented in Figure 5.11 and 5.12. The contact forces in the loose specimen have similar distributions around the shaft and tip as those in the dense specimen but are smaller in magnitudes (Figure 5.11) with concentrations near the probe sections that are being loaded. In the SE, TPO, and BE stages, the failure zones with large particle displacements are located much closer to the probe shafts and tip than those in the dense specimen (Figure 5.12). This observation reflects the punching failure that occurs in the loose specimen which results in a large top shaft expansion required to maintain the target top anchor force. During the SC, SR, and BC stage, the size of the failure zone increases around the probe in the loose specimen. This is especially obvious after the SR stage, likely because the greater void space leads to greater particle displacements above and around the shaft after the shaft retraction.

5.5.4 Mechanical Work Done during One Cycle of Self-Penetration

The total mechanical work (W) done during the self-burrowing process is composed of the work for seven different probe motions: top shaft expansion (W_{SE}, Eq. 5.11), tip penetration (W_{TP}, Eq.11), tip oscillation (W_{TO}, Eq. 5.13), bottom shaft expansion (W_{BE}, Eq. 5.14), top shaft contraction (W_{SC}, 5.11), shaft retraction (W_{SR}, Eq. 5.15), and bottom shaft contraction (W_{BC}, Eq. 5.14). The work done during the initial penetration is also calculated for the purposes of comparison (Eq. 5.12).

$$W_{SE(orSC)} = \sum_{i=1}^{i_{max}} F_{r,s} v_{r,s} \Delta t_i \tag{5.11}$$

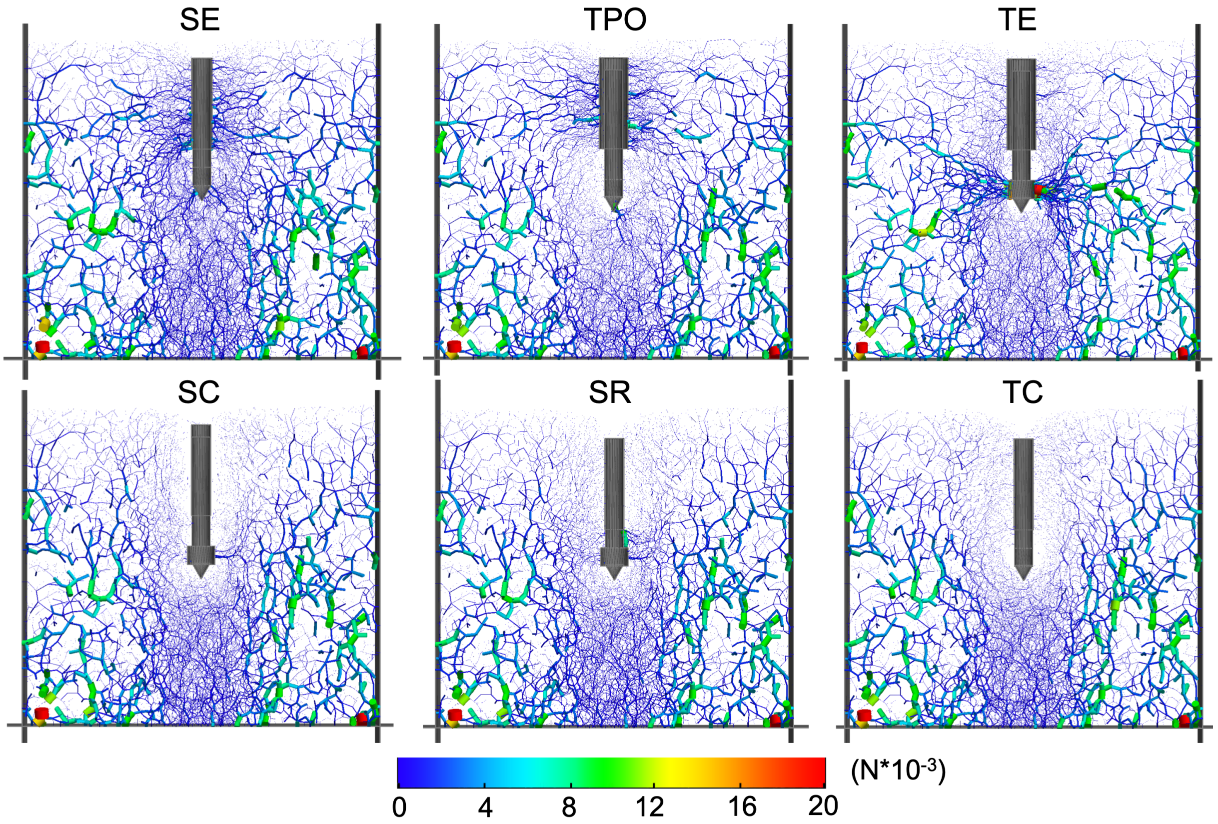

Figure 5.11: Contact force chains at the end of the six stages (SE, TPO, BE, SC, SR, BC) during the self-penetration process in the loose specimen. Note that the color scale is same in all the figures but the thickness of force chains is not.

$$W_{TP} = \sum_{i=1}^{i_{max}} Q_z v_{z,t} \Delta t_i \tag{5.12}$$

$$W_{TO} = \sum_{i=1}^{i_{max}} F_{r,t} \frac{v_{r,t}}{2} \Delta t_i \tag{5.13}$$

$$W_{BE(orBC)} = \sum_{i=1}^{i_{max}} F_{r,b} v_{r,b} \Delta t_i \tag{5.14}$$

$$W_{SR} = \sum_{i=1}^{i_{max}} F_{z,s} v_{z,s} \Delta t_i \tag{5.15}$$

Where the $F_{r,s}$ and $v_{r,s}$ are the radial force and the radial velocity of the top shaft, the Q_z and $v_{z,t}$ are the total penetration resistance force and the vertical velocity of the tip, $F_{r,t}$ and $v_{r,t}/2$ are the radial force and the average radial velocity of the tip, $F_{r,b}$ and $v_{r,b}$

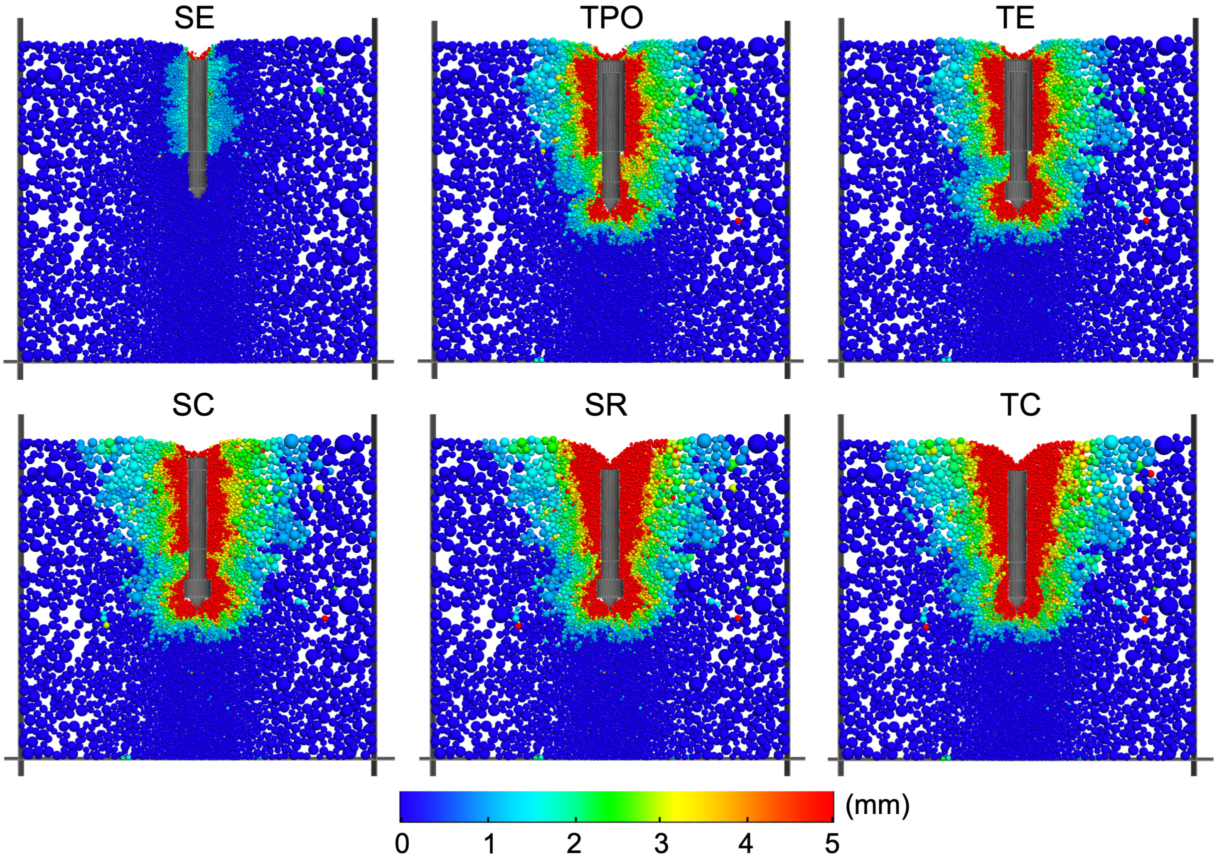

Figure 5.12: Particle displacements at the end of the six stages (SE, TPO, BE, SC, SR, BC) during the self-penetration process in the loose specimen. Note that the displacements are recorded from the beginning of the SE stage (i.e. the displacements during initial penetration are not included).

are the radial force and the radial velocity of the bottom shaft, Δt_i is the timestep of the ith simulation step and i_{max} is the maximum simulation step.

Penetrating and self-burrowing in denser soils requires a greater amount of total work. The history of mechanical work done during each stage of a single cycle of self-burrowing in the three specimens are presented in Figure 5.13. The total work during the initial tip penetration is greatest for the dense specimen (216.2 J), followed for the medium dense (82.9 J) and loose specimen (28.1 J) (Figure 5.13a). The results for the self-burrowing cycles indicate that most of the work is done during tip oscillation, which accounts for 45.7 J, 17.7 J, 3.2 J for the dense, medium dense and loose specimens, respectively, totaling 56.2%, 50.6%, 32.0% of the total self-burrowing work. Expansion of the top and bottom shafts also require a significant amount of work, accounting for 17.5 J and 21.0 J for the dense specimen, 19.6 J and 25.0 J for the medium dense specimen, and 3.3 J and 3.1 J for the loose specimen. The work done by shaft contraction, shaft retraction and bottom shaft contraction are negligible. Figure 5.14 shows the total work done in each simulation during a self-penetration cycle (i.e. exploding the initial penetration), with totals of 81.3 J, 34.9 J and 10.1 J for the dense, medium dense and loose specimens, respectively. The corresponding self-burrowing efficiencies are 0.03 cm/J, 0.10 cm/J, and 0.25 cm/J for the dense, medium dense and loose specimens, respectively. The self-burrowing without tip oscillation requires a total work of 4.5 J for the penetration distance of 0.06 cm in the dense specimen, with 0.14 J from penetration and 4.37 J from top shaft expansion. Therefore, the corresponding self-burrowing efficiency is 0.01 cm/J, which is one third of that with tip oscillation.

5.5.5 Multi-Cycle of Self-Penetration in Dense Specimen

A second self-burrowing cycle was simulated on the dense specimen to evaluate the continued performance of the bio-inspired probe. The evolution of the probe forces and displacements are presented in Figure 5.15. In the second cycle, the probe achieves a penetration displacement of 4 cm, which is greater than the displacement achieved in the first cycle (i.e. 2.5 cm). The TPO stage in the second cycle is also terminated due to the EM_s reaching the limit of 0.5. These results indicate that self-burrowing relies on maintaining of shaft reaction force during penetration, which may be easier to be realized at greater depths according to Chen et al. [2021]. Therefore, the results suggest that self-burrowing can be achieved as long as the initial embedment is enough and the first cycle of penetration is successful. However, this inference should be further examined by simulating more cycles of self-penetration in specimens with varying density.

5.6 Conclusions and Future Work

This study presents DEM simulations of the force-controlled self-burrowing process of a bio-inspired probe in granular assemblies of different densities. The simulated self-burrowing process consists of alternative expansion and contraction of two shafts and

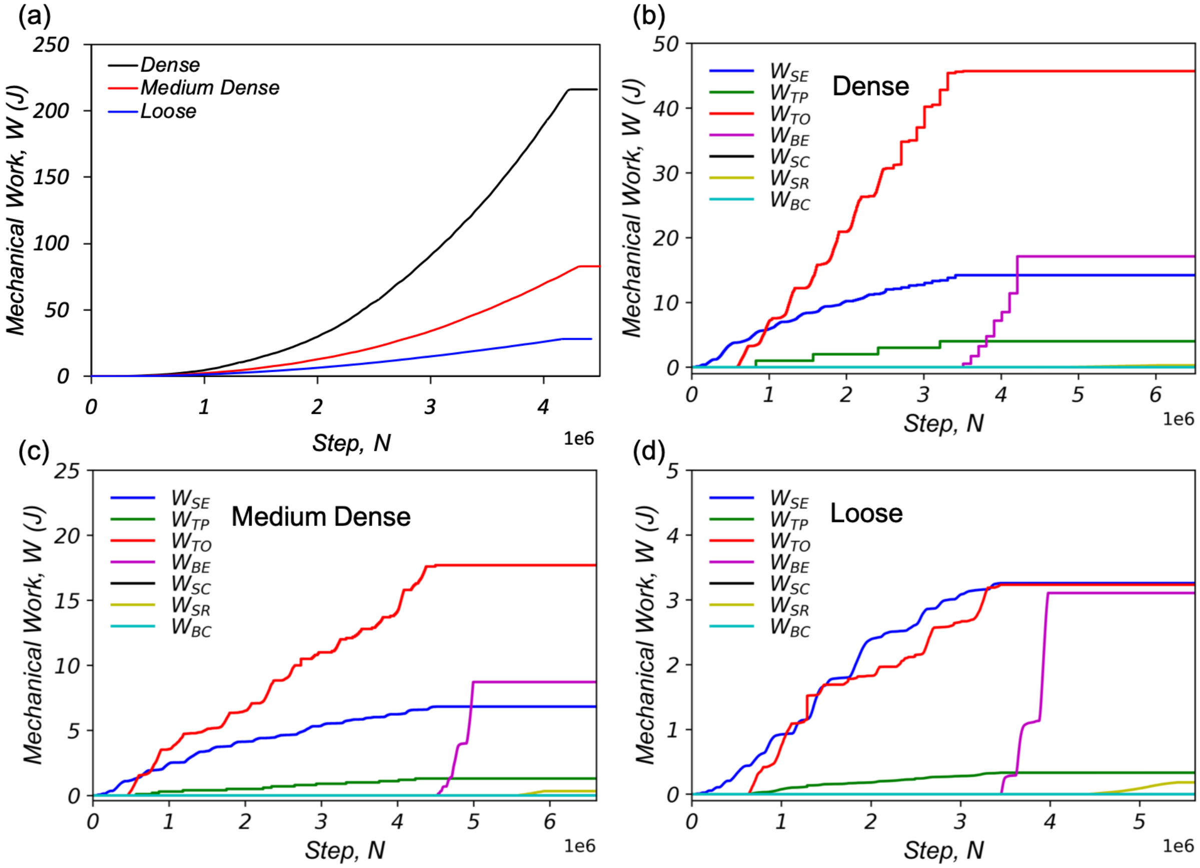

Figure 5.13: The mechanical work done during the (a) initial penetration stage and the six self-penetration stages in the (b) dense, (c)medium dense, and (d) loose specimens. Note that the simulation step was reset to zero after the initial penetration stage and the y-axis scales are different for the different simulations.

tip penetration. Horizontal tip oscillation is also employed to reduce the penetration resistance to facilitate tip advancement while maintaining a constant radial shaft force. The simulation results of this study show that self-penetration can be achieved in dense, medium dense and loose specimens.

Pre-embedment of the probe is needed to initiate the self-burrowing stage, which can be achieved by a conventional penetration strategy such as quasi-static penetration. This initial embedment allows the top shaft to mobilize the anchor force in the shaft expansion stage. The self-weight equilibrium and shaft expansion induce a reduction of tip penetration resistance, which facilitate subsequent tip advancement. The results also indicate that if a probe has a limiting expansion magnitude of the top anchor, a small

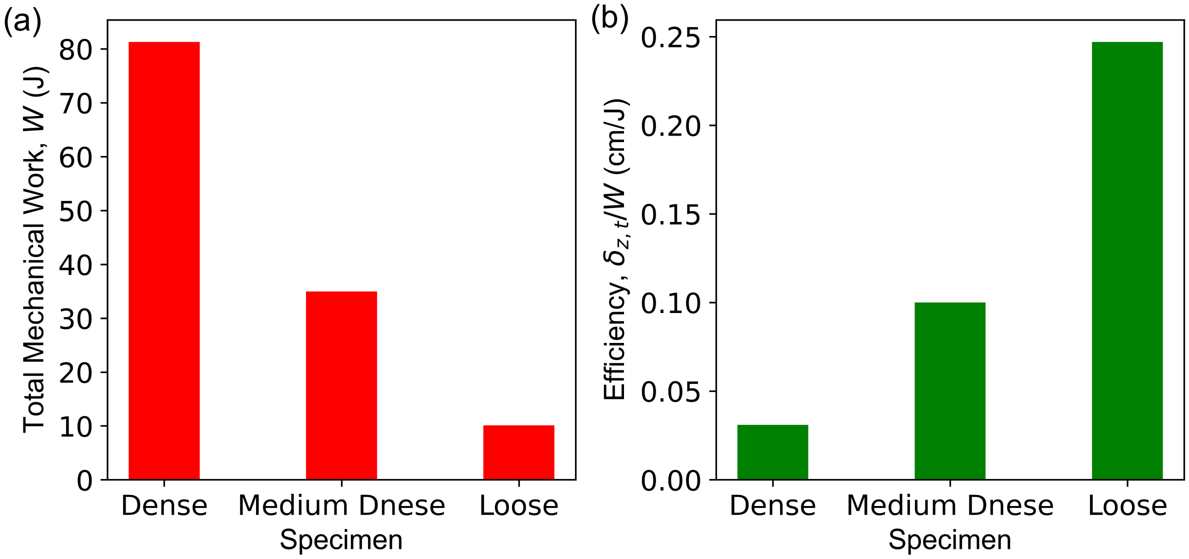

Figure 5.14: The total mechanical work consumed in one cycle of self-penetration and the efficiency regarding total work per penetration placement for the dense, medium dense and loose specimens.

expansion magnitude during the shaft expansion stage allows for continued expansion during the tip advancement stage. This continued expansion is necessary for mobilizing sufficient reaction forces during the tip penetration stage. Simultaneous tip oscillation during penetration can facilitate tip advancement by reducing the penetration resistance force.

The tip displacement after one cycle of self-penetration is greater in the medium dense specimen than in the dense and loose specimens. The loose specimen can mobilized the greatest anchor to penetration force ratio; however, the large void ratio led to a punching failure around the top anchor which created difficulties in maintaining a constant radial shaft force. This type of punching failure may not be observed at greater depths, which may make the loose improve its self-burrowing performance.

The force chain maps reflect the interaction between probe and particles and particle displacements show the failure zones within the specimens. Relaxation of contact forces around the middle and bottom shafts occurs when the top shaft is expanded, while force relaxation occurs below the tip when the bottom shaft is expanded. The contact forces in the loose specimen have distributions similar to those in the dense specimen but with

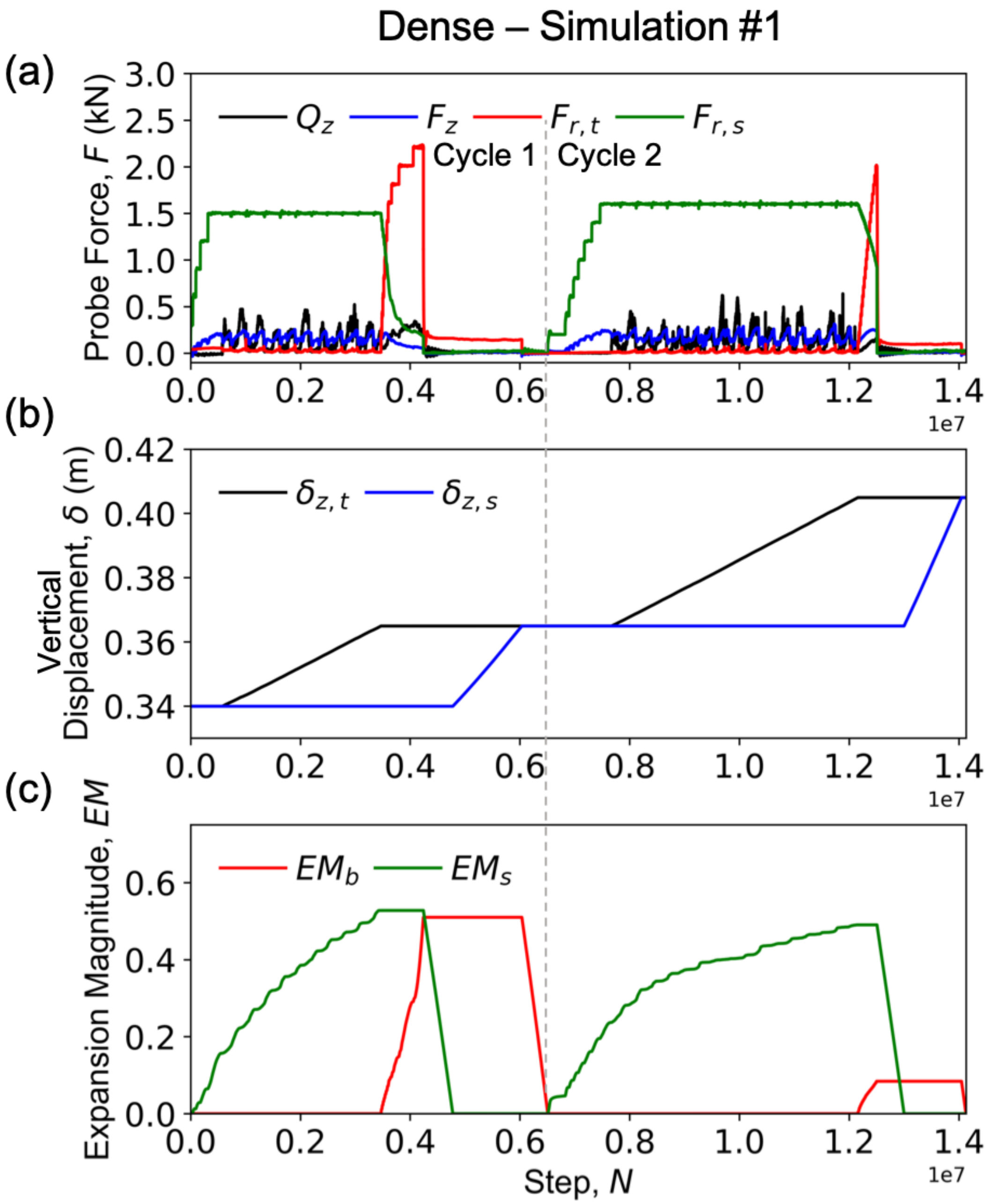

Figure 5.15: Two cycles of self-penetration in the dense specimen. (a) penetration resistance force, vertical top shaft force, radial top shaft force, and radial bottom shaft force; (b) penetration displacements of the tip and the top shaft; (c) expansion magnitude of the top and the bottom shafts.

smaller magnitudes. The particles with large displacements form a pronounced symmetric shallow failure zone that extends from the bottom of the top shaft up to the soil free surface in the dense specimen, whereas the a more localized punching failure zone forms around the probe in the loose specimen.

In one self-burrowing cycle, the total mechanical work done is greatest in the dense specimen, whereas the energetic efficiency regarding the penetration distance per unit work is highest in the loose specimen. Tip oscillation is shown to require most of the work among all self-burrowing stages and the expansion of the top and bottom shafts also require significant amount of work.

A second cycle of self-burrowing is simulated in the dense specimen to explore the continued performance of the probe. The results indicate that the self-penetration displacement is increased in the second cycle. In summary, the results presented here provide insight regarding the self-burrowing ability of the bio-inspired probe in specimens of varying density. Specifically, the function of each stage and the probe forces and displacements in one self-burrowing cycle have been analyzed. The effects of specimen density on the probe forces, displacements, and energetic efficiency are also investigated. Future work on more cycles of self-penetration in specimens with varying density are still needed. In addition, current studies on the self-penetration probe have been performed in uniform soils or specimens. Therefore, the self-penetration process in specimens with layered assemblies deserve further investigation.

5.7 Acknowledgements

This material is based upon work supported in part by the Engineering Research Center Program of the National Science Foundation under NSF Cooperative Agreement No. EEC–1449501. The first and third authors were supported by the National Science Foundation (NSF) under Award No. 1942369. Any opinions, findings, and conclusions or recommendations expressed in this material are those of the author(s) and do not necessarily reflect those of the National Science Foundation.

Chapter 6

DEM Modeling of Root Circumnutation-Inspired Penetration in Shallow Granular Materials

---

This chapter constitutes work in progress for a journal paper that will be submitted in the Fall of 2022. Chen, Y. and Martinez, A. DEM Modeling of Root Circumnutation-Inspired Penetration in Shallow Granular Materials. To be submitted for possible publication.

6.1 Abstract

Plant root growth is often accompanied by circumnutative motion which consists of downward helical movement of the root tip. Previous studies indicate that circumnutations allow plant roots to avoid obstacles that would impede root growth, while other studies have shown that the circumnutations can also reduce the penetration resistance mobilized during root growth. This study evaluates the reduction in penetration resistance to inform efficient soil penetration strategies for geotechnical applications. Discrete element modeling (DEM) simulations were performed on probes that employ circumnutation-inspired motion (CIM) to penetrate granular assemblies at shallow depths. These simulations investigate the effect of the ratio of tangential to vertical velocity (i.e. relative velocity) of the circumnutative motion as well as of the probe geometry (i.e. tip tilt angle and length). The results indicate that CIM penetration reduces the penetration force and work relative

to non-rotational penetration (NRP) by changing the soil fabric and diffusing the force chains around the probe tip. However, the circumnutative motion leads to an increase in the rotational torque and associated work. An optimal relative velocity and probe geometry exist for the simulated CIM probes resulting in a smaller total work than that required for non-rotational penetration. The CIM penetration is also shown to require smaller penetration forces and total work than the rotational penetration (RP) (i.e. with a straight tip), particularly at smaller relative velocity values.

6.2 Introduction

Plant roots are capable of penetrating different soil types, from soft clays to dense sands and overconsolidated clays. Implementing the strategies developed by plant roots into geotechnical practice may help improve the performance and efficiency of activities involving soil penetration, such as site investigation, tunneling and pile driving. Indeed, recently the field of bio-inspired geotechnics has focused on translating biological solutions for geotechnical engineering problems [Martinez et al., 2021], including self-burrowing probes and robots [Ortiz et al., 2019; Ma et al., 2020; Huang and Tao, 2020; Chen et al., 2021, 2022], tree-root inspired anchors and foundations [Mallett et al., 2018b; Burrall et al., 2020], and snakeskin-inspired surfaces and piles [Martinez et al., 2019; O'Hara and Martinez, 2020; Martinez and O'Hara, 2021].

When a root approaches a stiff soil layer, the soil can exert a stress on the root tip that exceeds the physiological limit on the plant cells, inhibiting axial root elongation (i.e. growth). To overcome this high penetration resistance, the root meristematic region grows radially, resulting in increased root diameter and enhanced root hair growth [Bengough and Mullins, 1990; Jacobsen et al., 2021]. The radial root growth reduces the soil effective stress ahead of the root tip and enables tip advancement in the weakened zone [Abdalla et al., 1969; Kirby and Bengough, 2002]. Savioli et al. [2014] performed finite element simulations of this plant growth process and showed the stress relaxation ahead of the root tip, ultimately causing soil failure in lateral extension conditions.

Another penetration strategy commonly used by plant roots is a pattern of helical movement of the root tip during root growth called root circumnutation (Figure 6.1(a)). Circumnutations can produce variable trajectories outlined by circular, elliptical, pendulum-like and irregular shapes [Stolarz, 2009; Tonazzini et al., 2012].Circumnutation has been observed in the roots of a range of plant species, including rice [Taylor et al., 2021], thale cress [Mullen et al., 1998; Simmons et al., 1995], pea [Kim et al., 2016] and maize [Del Dottore et al., 2016; Tonazzini et al., 2012]. Circular root circumnutation motions can be characterized by their vertical penetration velocity (v), period (T) and amplitude (R). In turn, the period (T) is related to the angular rotation velocity (ω) and the amplitude is related to the tilt angle (α) and the length (L_1) of the root tip (Figure 6.1(a)). The plant type and the soil conditions have been shown to affect the circumnutative motion characteristics. Table 6.1 summarizes the above mentioned characteristics of root circumnutation for selected species from the literature. The T, v and ω vary by orders of magnitude for different species, with T varying from 1 to 19.1 hours, v ranging from 1.8 to 36 mm/d, and ω varying from 9×10^{-5} to 1.7×10^{-3} rad/s. These quantities can be used to calculate the ratio of the tangential to vertical velocities, $\omega R/v$, referred to as relative velocity, which falls in a smaller range from 0.2π to 1.6π for the different species.

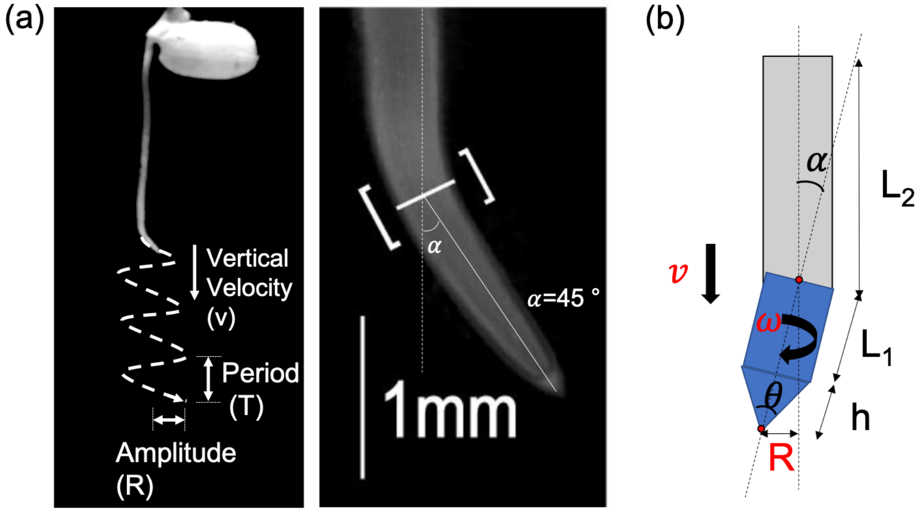

Figure 6.1: (a) Circumnutation motion of a rice root characterized by the period, vertical velocity, motion amplitude and tip geometry (after Taylor et al. [2021]); (b) schematic of probe that employs circumnutation-inspired motion simulated in DEM (note: the global z axis is the vertical direction and the global x and y axes are the two perpendicular horizontal directions).

Table 6.1: Parameters for root circumnutation motion.

Ref.	**Species**	**Period,** T	**Velocity,** v **(mm/d)**	**Tip angle,** α **(°)**	**Amplitude,** R **(mm)**	**Relative Tip Length,** L_1/D	$\omega R/v$	ω **(rad/s)**	ω/v **(rad/m)**
Taylor et al.2021	Rice (wildtype)	2 h	1.8	45.0	1.10	2.7-4.0	0.5pi	0.00087	41760
Mullen et al.1998	Thale cress (ecotype Columbia)	NA	NA	5.0-25.0	NA	6.0-6.5	NA	NA	NA
Simmons et al.1995	Thale cress	19.1 h	5.5	3.3	1.00	NA	0.5pi	0.00009	1413
Kim et al.2016	Pea	148 min	17	5.31	0.65	NA	0.74pi	0.00071	3608
Dottore et al.2016	Maize	1 h	36	1.4-11.3	0.15-1.25	3.2-6.4	0.2-1.6pi	0.00174	4176
Popova et al.2012	Maize	1 h	33.6	2.0-5.1	0.05-0.10	NA	0.29-0.70pi	0.00174	4474

The function of root circumnutation has been investigated by previous observational and experimental studies. Some studies proposed that root circumnutation facilitates root growth by avoiding obstacles [Darwin et al., 1883; Inoue et al., 1999]. Taylor et al. [2021] performed penetration experiments on soft root robots, showing that nutating robots can efficiently avoid obstacles whereas non-nutating robots cannot. A different function of the circumnutation motion has been proposed by Del Dottore et al. [2016] based on shallow penetration experiments on straight and circumnutating probes. The results showed that circumnutations reduce the penetration resistance and can decrease the amount of total work involved in soil penetration. This study also considered the effects of soil density, tip tilt angle and rotating period on the circumnutative penetration process. While this work shows the possible advantages of the circumnutation motion in soil penetration, there is still a lack of understanding of the mechanisms involved in the reduction of penetration resistance and total work required to optimize this penetration process.

Previous studies have developed plant-root inspired robots and probes. For example, Sadeghi et al. [2014] and Naclerio et al. [2021] showed that penetrating soil by developing additive structures near the tip (i.e. tip growth) overperforms direct penetration by reducing the penetration force and mechanical work. Other studies have investigated the process of rotational penetration (RP), consisting of simultaneous vertical and rotational motion with a straight tip. Sharif et al. [2019] and Cerfontaine et al. [2021] indicated that rotary-installed piles and screw piles require a smaller installation force than monotonically pushed piles, where a greater reduction of installation force was measured as the rotational speed was increased. Tang and Tao [2022] performed DEM simulations on rotational probes, which showed that an increase of rotational velocity led to reduction of tip resistance by more efficiently breaking the force chains around the probe tip. In addition, some rotational velocities enabled smaller energy consumptions compared to non-rotational penetration.

In this study, the penetration of a probe that employs the circumnutation-inspired motion at relatively shallow depths is simulated using the discrete element modeling (DEM) method. Here, the circumnutation trajectory is considered as circular. The effects of rotational velocity, vertical velocity, tip tilt angle and bottom shaft length on the forces and torques acting on the probe tip and the resulting mechanical work are investigated. To exemplify the effect of these parameters on CIM, Figure 6.2 shows the trajectories of the probe tips that employ vertical penetration and CIM penetration with relative velocities of 0.25π and 2π. The results of the DEM simulations are also analyzed in terms of particle displacements, force chains and fabric evolution to shed light on the effects of CIM on the interactions between the soil and the probes.

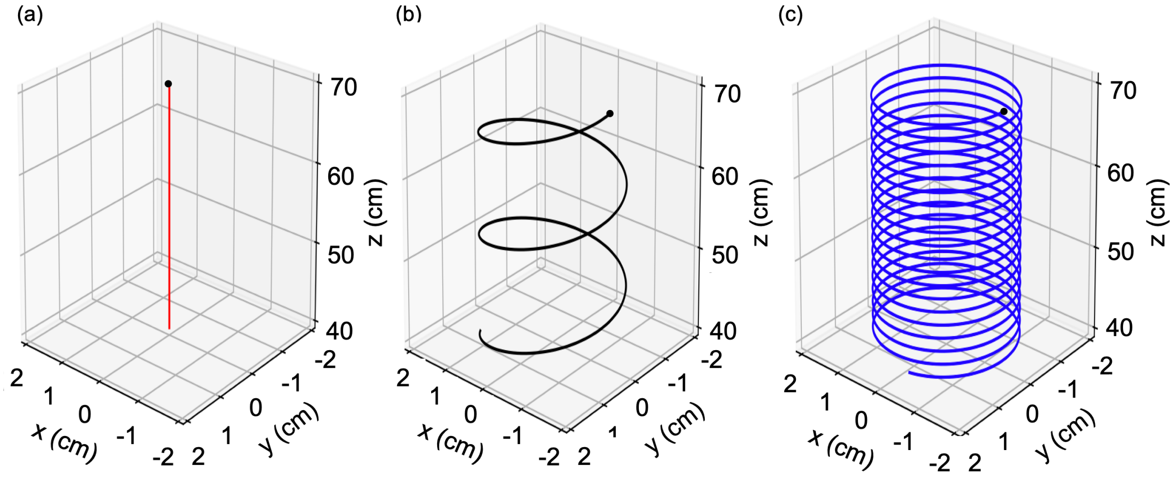

Figure 6.2: Trajectories of the probe tip that are displaced by (a) non-rotational motion and circumnutation-inspired motion with relative velocities of (b) 0.25π and (c) 2π. Note that the black point represents the initial location of the tip and the two CIM trajectories (b and c) are generated by probes that have a tip tilt angle $\alpha = 10°$ and bottom shaft length $L_1 = 1D$.

6.3 DEM Model

The DEM simulations are performed using the PFC 3D (version 5.0, Itasca) software. The DEM model consists of a virtual calibration chamber, a bio-inspired probe and soil particles. The chamber is 1.0 m in diameter ($D_{chamber}$) and 0.7 m in height ($H_{chamber}$), and consists of a cylindrical and a bottom wall (Figure 6.3). The friction coefficient of the wall is set to zero to minimize boundary effects. The boundary walls maintain a constant position during the simulations.

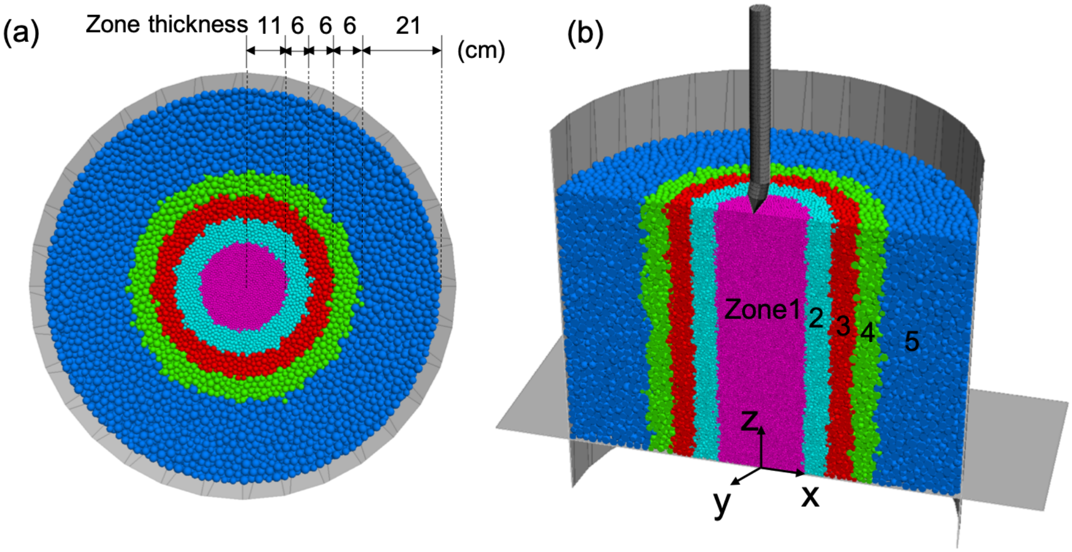

Figure 6.3: Virtual calibration chamber and soil specimen prepared using particle refinement method with 5 zones: (a) top view and (b) axial cross section.

The simulated bio-inspired probes have a diameter of 0.044 m (D) and an apex angle of 45°. The bio-inspired probe consists of an upright vertical top shaft, an inclined bottom shaft with length L1varying from 1D (0.044 m) to 3D (0.132 m) and an inclined conical tip with a tilt angle of α ranging between 10° and 30° (Figure 6.1(b)). During the penetration process, all three probe sections are displaced downward. Simultaneously, the two tilted probe sections (in dark gray, Figure 6.1(b)) rotate along the probe's longitudinal axis while the top shaft does not rotate (in light gray, Figure 6.1(b)).

Table 6.2 summarizes the simulation parameters. The specimens in the DEM simulations consists of about 278,200 particles. The soil particles are modeled as spheres with a density of 2650 kg/m^3. The particle contacts are modeled using a linear contact model with rolling resistance, which can provide resistance to particle rotation and simulate the interlocking effect of particle angularity [Ai et al., 2011; Wensrich and Katterfeld, 2012]. The sliding and rolling resistance coefficients (μ and μ_{rr}) are 0.4. The normal stiffness to particle diameter ratio (k_n/d) is 10^8 N/m^2 and the normal to shear stiffness ratio is 1.5. The normal stiffness and shear stiffness of the probe are 1.4×10^7 N/m and 9.5×10^6 N/m, respectively. The friction coefficient of the probe-particle contacts is 0.3.

Table 6.2: DEM simulation parameters.

Input Parameters	**Symbol**	**Value**
Normal Stiffness to Particle Diameter (N/m^2)	k_n/d	1.0E8
Normal to Shear Stiffness Ratio	k_n/k_s	1.5
Normal Stiffness of Probe (N/m)	k_{np}	1.4E7
Shear Stiffness of Probe (N/m)	k_{sp}	9.5E6
Sliding Friction Coefficient	μ	0.4
Rolling Friction Coefficient	μ_{rr}	0.4
Ball-probe Friction Coefficient	μ_{bp}	0.3
Ball-wall Friction Coefficient	μ'	0
Particle Density (kg/m^3)	G_s	2650

The particle sizes were upscaled to reduce the computational cost of the simulations. One important consideration in upscaling of particle sizes in penetration simulations is to maintain a sufficient number of contacts between the probe and the particles. This study employs the particle refinement method (PRM) to increase the number of probe-particle contacts while also reducing the computational cost of the simulations [McDowell et al., 2012]. Previous studies have shown the successful application and minimal effects of the PRM for penetration simulations [McDowell et al., 2012; Falagush et al., 2015; Sharif et al., 2019]. The PRM specimen developed for this study has particles with a median size (D_{50}) of 6.31 mm in the center zone, where the probe-particle contacts occur (zone 1 in Figure 6.3). The particle sizes increase gradually in the other four zones as shown in Figure 6.3(b) and Figure 6.4(a), with D_{50} of 9.47 mm, 14.20 mm, 17.04 mm and 20.45 mm

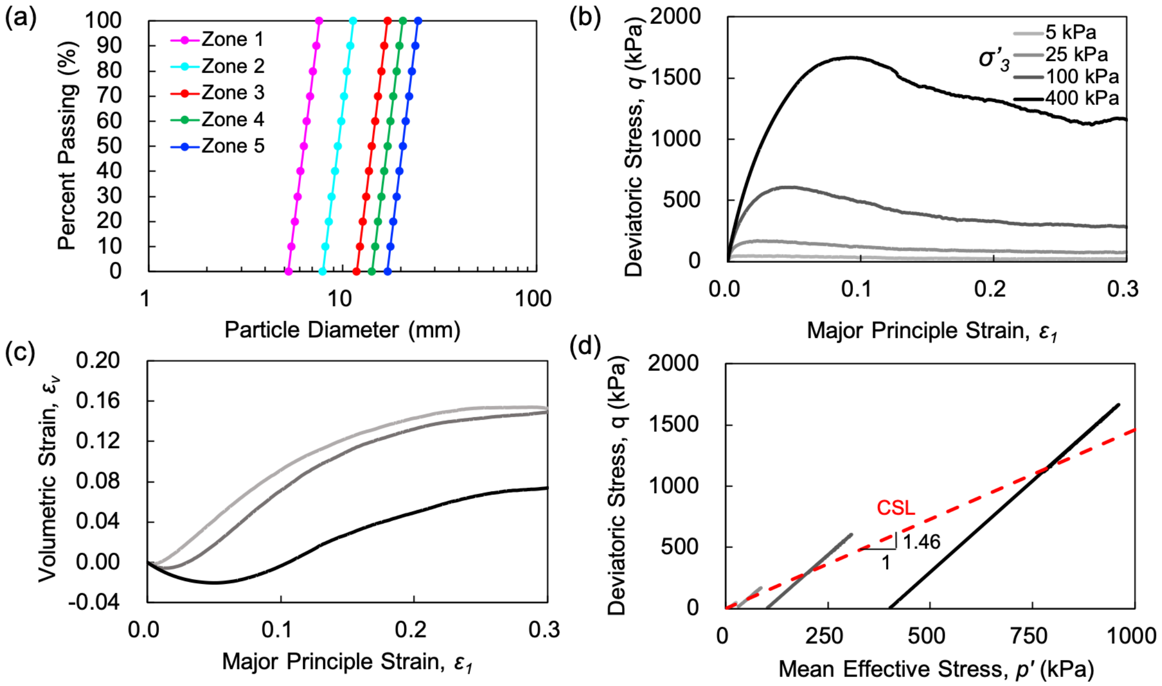

Figure 6.4: (a) Particle size distributions in the 5 zones of the soil sample; (b-d) evolution of deviatoric stress and volumetric strain with major principal strain and stress path in the drained triaxial compression simulations.

in zones 2, 3, 4 and 5, respectively. The particle upscaling factors between the adjacent zones are 1.2 or 1.5 to prevent particle migration between different zones [McDowell et al., 2012; Falagush et al., 2015; Sharif et al., 2019]. The soil in each zone is poorly graded with a coefficient of uniformity (C_u) of 1.2 and a coefficient of curvature (C_c) of 0.96 (Figure 6.4(a)).

The chamber-to-probe diameter ratio ($D_{chamber}/D$) and probe-to-particle diameter ratio (D/D_{50})are important parameters in penetration DEM simulations. In these simulations, $D_{chamber}/D$ is 15.9, which minimizes the chamber size effects [Khosravi et al., 2020]. The D/D_{50} in the center zone 1 is 7.0. Both ratios are within the range or larger than those used in previous 3D DEM studies. For example, in Arroyo et al. [2011], Zhang and Wang [2015], Zeng and Chen [2016], Ciantia et al. [2016, 2019b] and Zhang et al. [2019], the $D_{chamber}/D$ ratios vary from 12.0 to 16.6 and the D/D_{50} values range from 2.7 to 5.8.

The specimen preparation consists of a few steps. The soil particles are initially generated inside the cylindrical chamber using the radius expansion method, leading to a void ratio of 0.61. Then, the stiffness properties are assigned to the particles. The equation of motion and Newton's second law are then solved, allowing the particles to rearrange until the unbalanced force ratio becomes smaller than 10^{-4} (i.e. system equilibrium reached). Then, the frictional properties are assigned to the particles and walls and gravity is activated. The system cycles again until equilibrium is reached. The sample quality is verified by corroborating a linear increase in vertical and horizontal stresses with depth using 628 measurement spheres placed on a vertical x-z plane.

The simulated particle assembly exhibits the behaviors of typical coarse-grained soils, as presented in the results of triaxial compression simulations (Figure 6.4(b)-6.4(d)) and described in more detail by Chen et al. [2021, 2022]. The isotropically-consolidated triaxial compression simulations are performed on cubic specimens with a particle size distribution corresponding to zone 3. The triaxial simulations were performed with various confining stresses (σ'_r) from 5 kPa to 400 kPa and with an initial void ratio of 0.59. The results show that the simulated assemblies exhibit the expected behaviors of sandy soils, such as stress-dependency of the deviatoric stress (q), soil dilation and convergence towards the critical state at large strains. Specifically, greater deviatoric stresses were mobilized as σ'_r was increased (Figure 6.4(b)), more soil dilatation occurred at lower σ'_r (Figure 6.4(c)) and at large strains the soil state in q - mean effective stress (p') converged to the critical state line with a slope of 1.46, corresponding to a critical state friction angle of 36°.

To assess the possible effect of the PRM on the results, simulations of non-rotational penetration were performed on the PRM specimen (Figure 6.3) and on a uniform specimen with a unique particle size distribution with D_{50} of 14.2 mm,equivalent to that in zone 3. Figure 6.5(a) shows a comparison of tip resistance (q_c) with depth for both specimens. The profiles of q_c values with depth show similar trends and magnitudes. The q_c trace for the PRM specimen is significantly smoother than that for the uniform specimen. Specifically, a standard deviation of the q_c is of 0.04 MPa and 0.19 MPa for the PRM and uniform specimens, respectively (Figure 6.5(b)). The smaller oscillations in q_c for the PRM specimen are due to the greater number of probe tip-particle contacts, which is

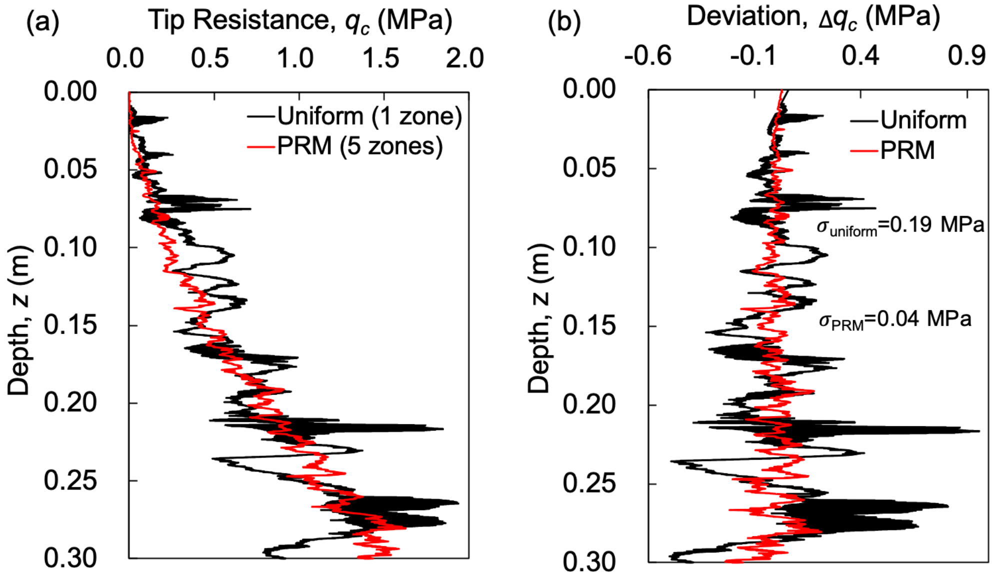

Figure 6.5: (a) Tip resistance and (b) deviation from mean values measured during cone penetration simulations on the PRM specimen and the single-zone specimen.

59 in comparison to 14 for the uniform specimen, in agreement with trends presented by Khosravi et al. [2020]. Overall, these results indicate that the PRM results in smoother and less variable q_c traces with depth but has no appreciable effect on the average q_c magnitudes.

6.4 Results

During CIM, the tilted bottom shaft and the conical tip are rotated around the probe's longitudinal axis at a given angular velocity while the entire probe is displaced downward at a given vertical velocity. The total vertical force(F_Z) during CIM is the sum of vertical forces acting on all probe sections as defined by Eq. 6.1:

$$F_Z = \sum_{i=1}^{N} F_{Ztip,i} + \sum_{j=1}^{N} F_{Zshaft1,j} + \sum_{k=1}^{N} F_{Zshaft2,k} \tag{6.1}$$

where $F_{Ztip,i}$ is the vertical component of contact force i acting on the probe tip, $F_{Zshaft1,j}$ and $F_{Zshaft2,k}$ are the vertical components of the contact force j and k acting on the bottom and top shafts, respectively, and N is the total number of vertical component forces.

The total torque is the sum of torque components acting on the tip and bottom shaft as defined in Eq. 6.2:

$$T_Z = \sum_{i=1}^{N}(F_{Xtip,i}d_{Xtip,i}+F_{Ytip,i}d_{Ytip,i})+\sum_{j=1}^{N}(F_{Xshaft1,j}d_{Xshaft1,j}+F_{Yshaft1,j}d_{Yshaft1,j}) \quad (6.2)$$

where $F_{Xtip,i}$ and $F_{Ytip,i}$ are the two i^{th} horizontal component forces acting on the tip, $d_{Xtip,i}$ and $d_{Ytip,i}$ are the distances at which the i^{th} horizontal component forces act with respect to the axis of rotation (i.e. probe centerline), $F_{Xshaft1,j}$ and $F_{Yshaft1,j}$ are the horizontal component forces acting on the bottom shaft, and $d_{Xshaft1,j}$ and $d_{Yshaft1,j}$ are the corresponding distances from the axis of rotation. The top shaft contribution to the T_Z is not considered because it was calculated to be negligible.

The total work (W_T) done doing CIM consists of the vertical (W_V) and rotational work (W_R). The work components are calculated as the sum of the products of force or torque with the corresponding vertical or rotational displacement, as follows:

$$W_T = W_V + W_R \quad (6.3)$$

$$W_V = \sum F_z v \Delta t \quad (6.4)$$

$$W_R = \sum T_z \omega \Delta t \quad (6.5)$$

In this study, 19 simulations were performed to investigate the probe and soil response during CIM (Table 6.3). The non-rotational simulation (#1) is a baseline for comparing with CIM. Simulations #2-10 explore the effects of the angular and vertical velocities, respectively, on the mobilized total vertical force, total torque and associated mechanical work. Simulations #11-15 are compared with simulations #1-6 to investigate the effects of penetration strategy on the probe's penetration performance. Simulations #16-17 and #18-19 are compared with simulation #2 to investigate the effects of probe geometry (tip tilt angle and bottom shaft length) on the CIM penetration process. The v and ω values in the simulations were chosen to yield a relative velocity range between 0.25π to 4.0π, which covers the circumnutation relative velocity measurements from the literature which range from 0.2π to 1.6π (Table 6.1). Here, it is assumed that the relative velocity, rather than the angular or vertical velocities, controls the CIM penetration process; this assumption is evaluated in a later section. To obtain the target relative velocity values, greater angular

Table 6.3: DEM simulations on circumnutation-inspired and rotational motions.

#	**Parameter**	$\boldsymbol{\alpha}$ (°)	$\boldsymbol{L_1/D}$	$\boldsymbol{R}$ **(mm)**	$\boldsymbol{v}$ **(m/s)**	$\boldsymbol{\omega}$ **(rad/s)**	$\boldsymbol{\omega R/v}$	$\boldsymbol{\omega/v}$ **(rad/m)**
1	(NR)	0	-	0	0.2	0	0	0
2						10.1	0.25π	50.3
3						20.1	0.5π	100.6
4	ω (CIM)	10	1	15	0.2	40.3	1π	201.25
5						80.5	2π	402.5
6						161.0	4π	805
7	ω, v (CIM)	10	1	15	0.1	10.1	0.5π	50.3
8						20.1	1π	100.6
9						40.3	2π	201.25
10						80.5	4π	402.5
11						10.1	-	50.3
12						20.1	-	100.6
13	ω (RP)	0	1	0	0.2	40.3	-	201.25
14						80.5	-	402.5
15						161.0	-	805
16	α (CIM)	20	1	30	0.2	10.1	0.48π	50.3
17		30		43			0.69π	
18	L_1 (CIM)	10	2	23	0.2	10.1	0.37π	50.3
19			3	31			0.49π	
20	(RCIM)	10	1	15	0.2	10.1	0.25π	50.3

and vertical velocities were considered than those from plant root measurements because these were deemed to be too small to be relevant for geotechnical applications.

6.4.1 Effect of the Angular and Penetration Velocities on Circumnutation-Inspired Penetration

The CIM simulations with different angular and penetration velocities (simulations #1-10) are examined to understand the effects on the total vertical force, total torque and work. During CIM penetration, the relative velocity depends on the angular and vertical velocities, the tip tilt angle and the length of the bottom shaft (i.e. relative velocity = $\omega R/v$).Since the tip tilt angle and bottom shaft length are kept at 10° and 0.044 m in these simulations, R remains unchanged.

The CIM relative velocity has an important effect on the vertical force, torque and work. CIM leads to a larger education in the tip resistance compared to that measured during NRP, with greater decreases of F_Z induced as the relative velocity is increased (Figure 6.6(a)). The torque during CIM is greater than during NRP, with small differences in T_Z between the simulations with varying CIM relative velocities (Figure 6.6(a)). These observations are consistent with the results of rotational penetration DEM simulations from Tang and Tao [2022], which showed that the tip resistance decreased while the torque did not increase significantly as the angular velocity was increased. Similarly, the DEM simulations on rotatory-installed piles by Sharif et al. [2021] also showed a decrease in total installation force with an increase in relative velocity, while the torque remained relatively unchanged at relative velocities greater than 0.24π. It is noted that in the simulation results shown in Figure 6.6(b), the T_Z for NRP oscillates around a value of zero. This is caused by unbalanced horizontal forces acting against the probe at any time that result in small but measurable torques.

Increasing the relative velocity leads to a decrease in the vertical work due to the decrease in the penetration resistance. In contrast, the rotational work increases with increasing relative velocity due to the increase in cumulative rotational displacement (Figure 6.6(c) and 6.6(d)). The cumulative vertical, rotational and total work at the end of penetration are presented in Figure 6.6(e), showing the decrease in W_V and increase in

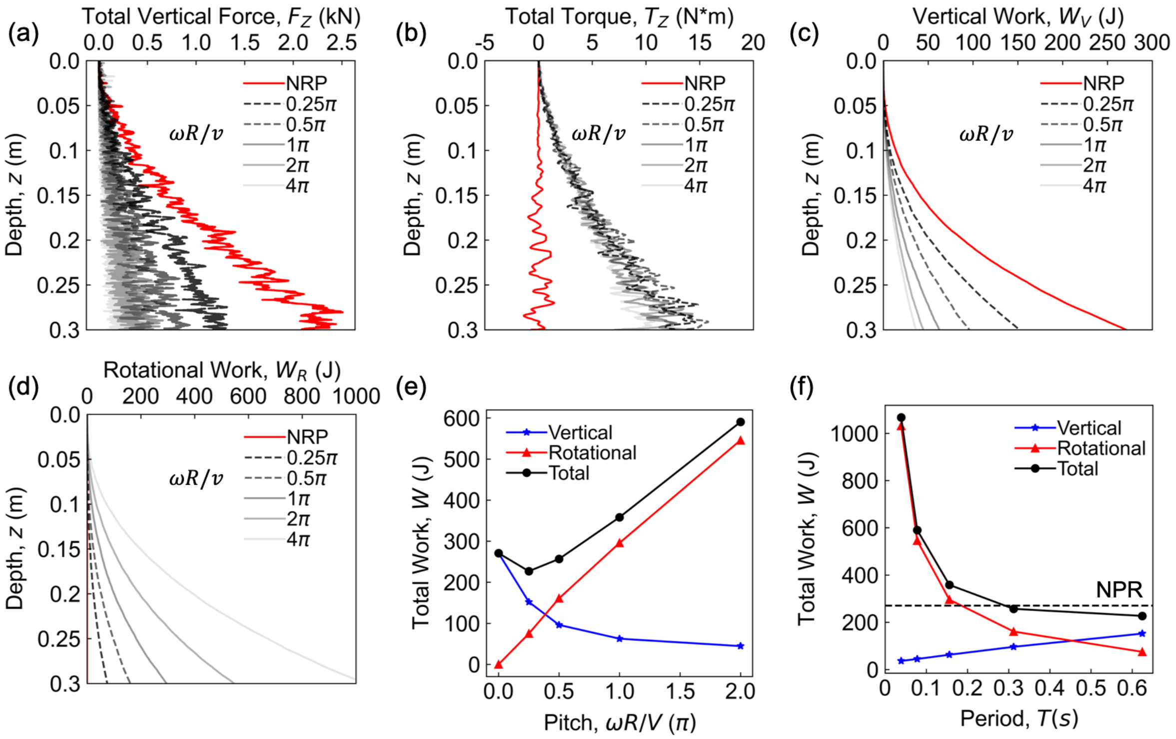

Figure 6.6: Effect of angular velocity. Profiles of (a) total vertical resistance force, (b) total torque, (c) vertical work and (d) rotational work with soil depth; change of total mechanical work as a function of (e) relative velocity and (f) period during CIM penetration. Note that the simulations (#1-6) presented herein have same geometry with tip tilt angle $\alpha = 10°$ and bottom shaft length $L_1 = 1D$.

W_R as the relative velocity is increased. The results show a decrease in the total work from relative velocities of 0π to 0.25π, with a minimum value of 226.8 J which is 16.2% smaller than the W_T for NRP (270.7 J). Based on interpolation of the data, relative velocities greater than 0π and smaller than 0.55π yield smaller W_T than NRP. Figure 6.6(f) shows the change in the W_V, W_R and W_T with circumnutation period, showing a decrease in W_T and W_V and an increase in W_R with increasing T. These trends are in agreement with the results presented by Del Dottore et al. [2017] based on experimental penetration tests of a root-inspired probe. By interpolating their results, the circumnutation relative velocities between 0.20π and 1.71π (with the optimal relative velocity of 0.78π) enable penetration a smaller W_T than NRP for probes a tilt angle of 10°.

The vertical penetration velocity also affects the forces and torques involved in CIM penetration. To explore these effects, five CIM simulations were performed with a v

of 0.2 m/s and ω varying from 10.1 rad/s to 161.0 rad/s (simulations #2-6), yielding relative velocities from 0.25π to 4π, and four simulations were performed with a v of 0.1 m/s and ω ranging from 10.1 rad/s to 80.5 rad/s (simulations #7-10), yielding relative velocities from 0.5π to 4π. The results indicate that W_V is relatively unaffected by the vertical velocity, yielding similar values for any given relative velocity (Figure 6.7(a)). The

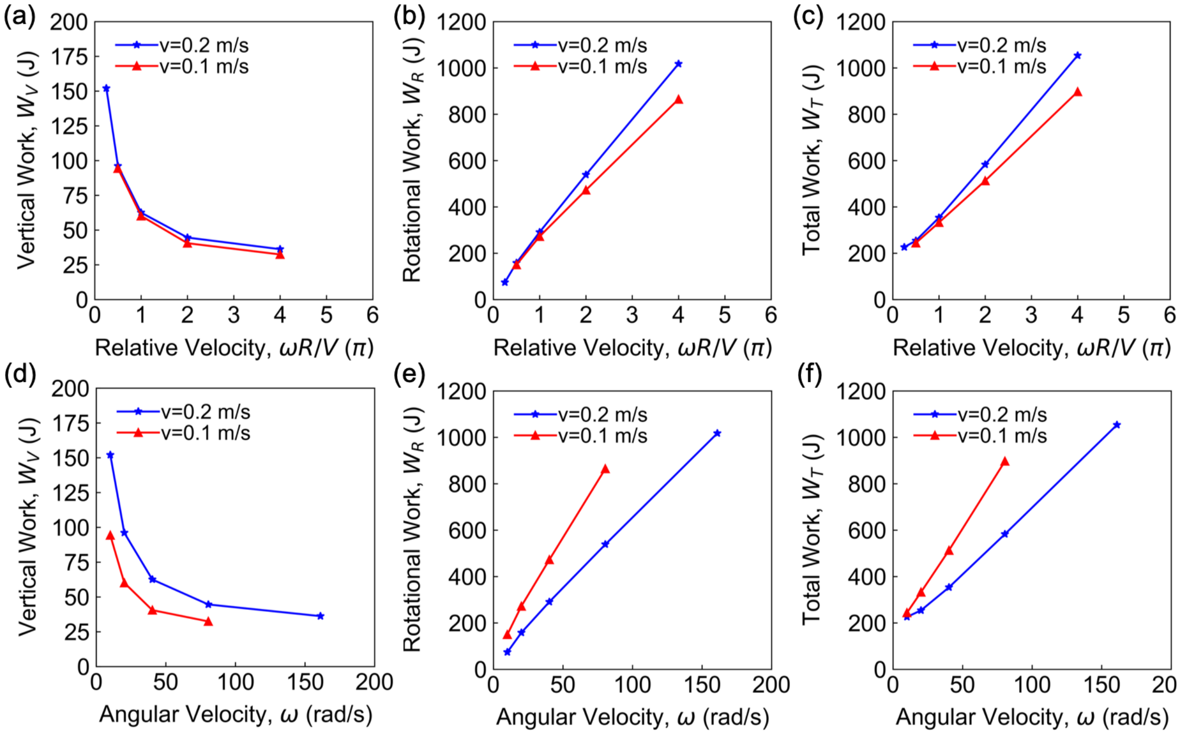

Figure 6.7: Effects of penetration velocity. Change of vertical, rotational and total mechanical work as a function of (a-c) relative velocity and (d-f) of angular velocity for CIM penetration (simulations #2-10).

W_R remains unaffected by v at relative velocities smaller than 1π; however, at greater relative velocities there is a measurable increase in W_R with v for any given relative velocity (Figure 6.7(b)). As a result of the changes in W_V and W_R, W_T shows a negligible difference with v at relative velocities smaller than 1π and an increase with v at greater relative velocities. Plotting the work values as a function of the angular velocity reveals that for a given ω, a greater penetration velocity results in an increase in W_V, a decrease in W_R and a decrease in W_T (Figure 6.7(d)-6.7(f)). The decrease in W_R and W_T is a result of the smaller rotational displacement for the greater penetration velocities. Overall, these results indicate that the relative velocity parameter has a controlling effect on the mechanical work at values smaller than 1π, corroborating the initial hypothesis. However, this hypothesis appears to be invalid at greater relative velocities.

6.4.2 Comparison of Circumnutation-Inspired Motion and Rotational Penetration

The vertical forces, torques and mechanical work are compared for CIM penetration and rotational penetration (RP), a penetration process usually involved in rotary-installed piles and helical anchors, where the shaft and tip are simultaneously rotated at a constant angular velocity. A set of RP simulations were performed where ω was varied between 10.1 and 161.0 rad/s (simulations #11-15). Figure 6.8 provides a comparison of the penetration resistance, torque and work measured during RP (ω = 10.1 rad/s, v = 0.2 m/s), CIM (ω =10.1 rad/s, v =0.2 m/s) and NRP (ω =0.0 rad/s, v =0.2 m/s). The results show that

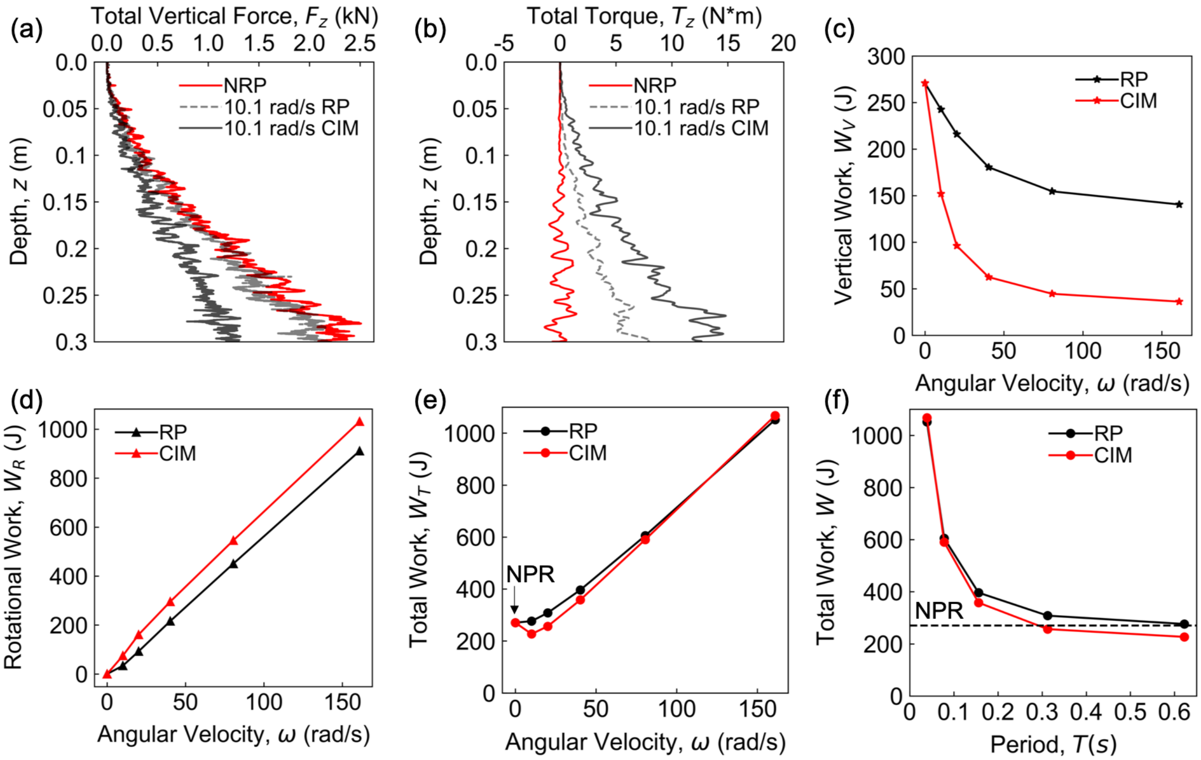

Figure 6.8: Comparisons between CIM and RP. Evolution of (a) total vertical force and (b) total torque with depth; change of (c) vertical, (d) rotational, and (e-f) total mechanical work as a function of angular velocity and circumnutation period.

CIM penetration yields a smaller F_Z (Figure 6.8(a)) but greater torque T_Z (Figure 6.8(b)) than RP. The greater T_Z values are driven by the greater horizontal distances between the probe centerline and the particle-probe contacts during CIM. These trends are reflected in the W_V and W_R values as a function of ω which show greater penetration work for RP and greater rotational work for CIM (Figure 6.8(c) and 6.8(d)). The W_T values at the end of penetration show smaller total work for CIM penetration, particularly for ω smaller than 80.1 rad/s or periods T greater than 0.078 s (Figure 6.8(e) and 6.8(f)). These results indicate that the greater reduction in vertical force during CIM penetration makes it a more energetically-efficient strategy than RP, particularly at smaller ω or greater T. Tang and Tao [2022] present analysis indicating that the RP reduces the vertical penetration forces due to the breakage of contact force chains around the penetrometer; this breakage of force chains was stronger at locations farther away from the tip's axis of rotation). This conclusion supports the greater reduction in F_Z during CIM penetration than during RP. Namely, the probe that employs CIM is more efficient at breaking force chains due to its tilted tip and bottom shaft. The evolution of force chains around the CIM probe is further investigated in the following sections.

6.4.3 Effects of the Probe Shape

The CIM penetration process is influenced by the amplitude of the motion, which is determined by the probe geometry, specifically the tip tilt angle and the bottom shaft length. To explore the effect of the tip tilt angle, a series of simulations was performed with constant vertical and an angular velocity of 0.2 m/s and 10.1 rad/s, respectively, a bottom shaft length of $1D$ and with tilt angles varying from 0° to 30° (simulations #2, 16 and 17). An angular velocity of 10.1 rad/s was chosen because it yielded the smallest total work for the reference probe configuration (i.e. $\alpha = 10°$, $L_1 = 0.044$ m). Comparisons are made with respect to NRP (simulation #1) and to RP (simulation #11), where the latter was also rotated at 10.1 rad/s. As shown in Figure 6.9(a), CIM penetration mobilizes F_Z magnitudes that are nearly half of those mobilized by NRP and RP. However, the effect of α on F_Z was small. The mobilized T_Z is greater for CIM penetration than for the NRP and RP cases, with T_Z increasing as α is increased (Figure 6.9(b)). These changes

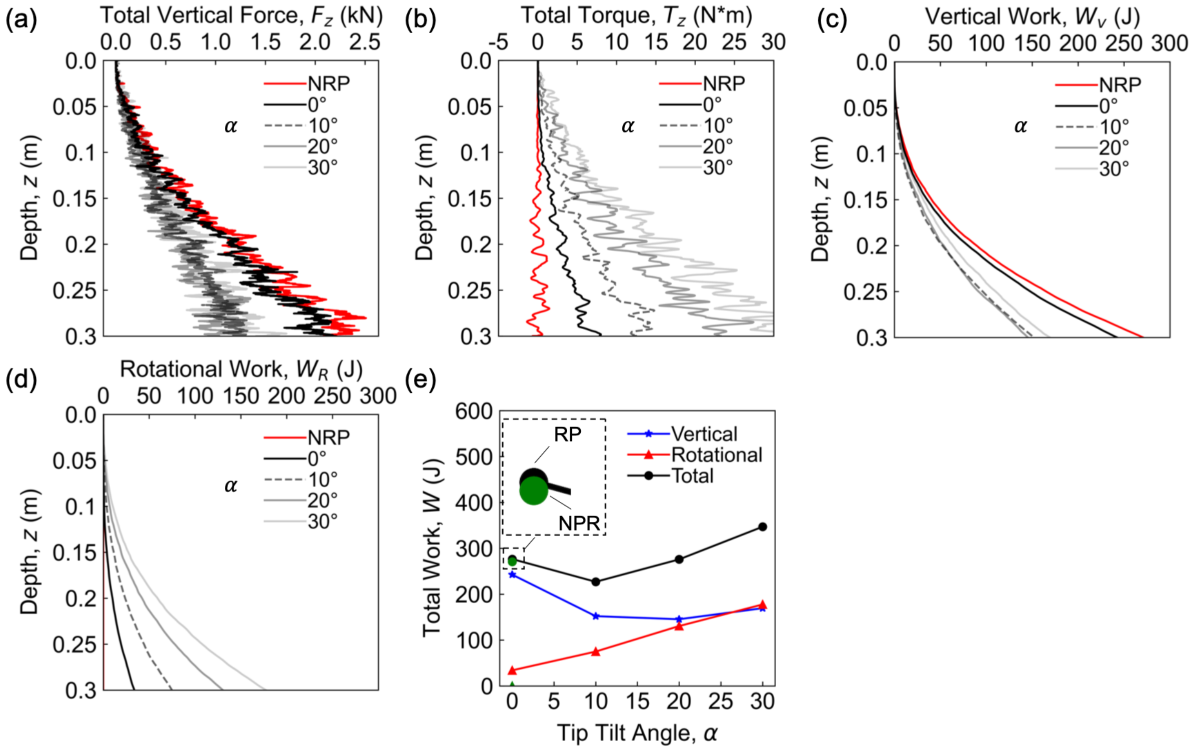

Figure 6.9: Effect of the tip tilt angle. Profile of (a) total vertical force, (b) total torque, (c) vertical work and (d) rotational work with soil depth for probes with different tip angles (simulations #1, 2, 16, 17); (e) change of total mechanical work as a function of tip tilt angle. Note that the simulations presented herein have the same angular velocity of 10.1 rad/s and the same bottom shaft length $L_1 = 1D$.

in F_Z and T_Z lead to concomitant decreases in the penetration work and increases in the rotational work for CIM penetration in comparison to NRP and RP (Figure 6.9(c) and 6.9(d)). The results show that for probes with the same vertical and angular velocities and a bottom shaft length L_1 of 0.044 m (equivalent to one probe diameter), a tip tilt angle of 10° results in the smallest amount of total work required (Figure 6.9(e)).

To explore the effect of bottom shaft length, Figure 6.10 presents the results of CIM simulations with a v of 0.2 m/s, ω of 10.1 rad/s, α of 10°, and L_1 ranging from $1D$ to $3D$ (simulations #2, 18 and 19). In this case, CIM penetration also mobilizes F_Z magnitudes that are nearly those of that mobilized by NRP and RP, with F_Z decreasing as L_1 is increased (Figure 6.10(a)). Conversely, the mobilized T_Z increases as L_1 is increased (Figure 6.10(b)). These trends are reflected in the decrease in W_V and increase in W_R with increasing L_1 (Figure 6.10(c) and 6.10(d)). Overall, the results show that for probes

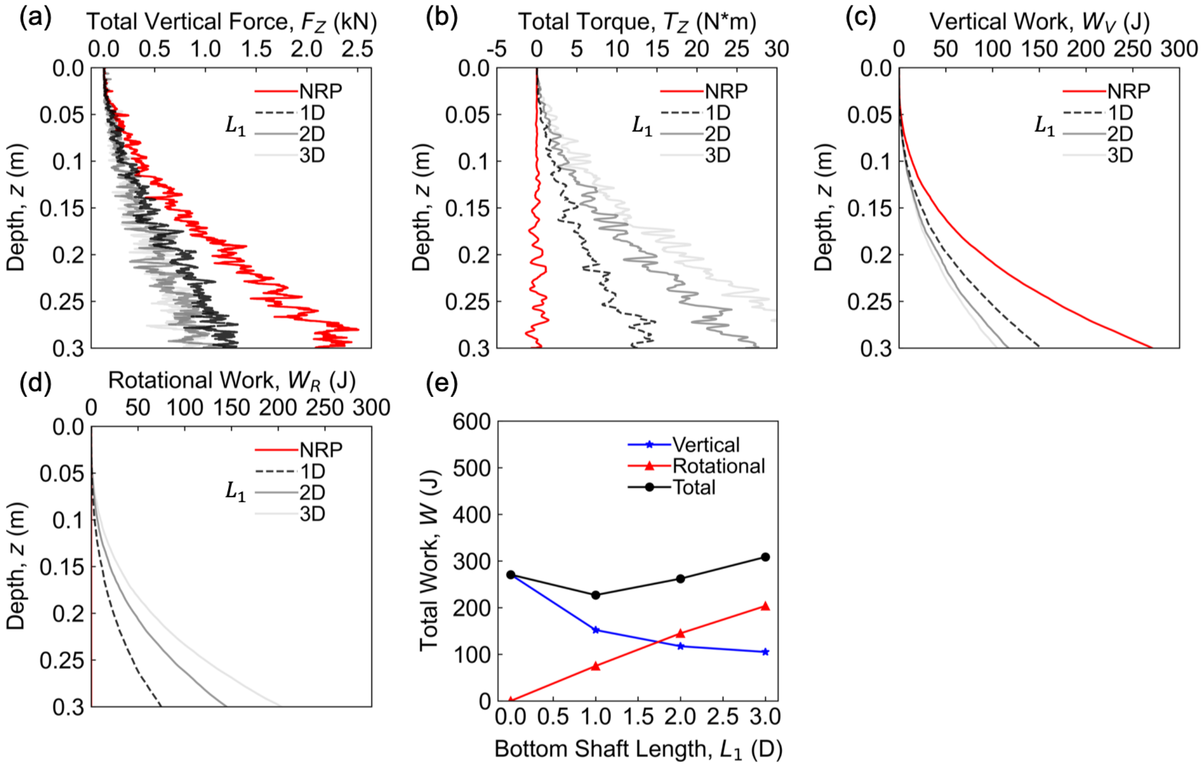

Figure 6.10: Effects of the bottom shaft length. Profiles of (a) total vertical force, (b) total torque, (c) vertical work and (d) rotational mechanical work with soil depth during CIM for probes with different bottom shaft lengths (simulations #1, 2, 18, 19); (e) change of total mechanical work as a function of bottom shaft length. Note that the simulations presented herein have the same angular velocity 10.1 rad/s and the same tip tilt angle α = 10°.

with the same vertical and angular velocities and a tilt angle of 10°, a bottom shaft length of 0.044 m (equivalent to one probe diameter) requires the smallest total mechanical work (Figure 6.10(e)).

6.4.4 Particle-Probe Interactions

This section examines the interactions between the probe and particles in more detail considering the effects of relative velocity, angular velocity and probe geometry. The particle-scale response is analyzed in terms of particle displacements, force chains and fabric evolution to shed light on the mechanisms controlling the CIM penetration and how they compare to those involved in NRP and RP.

6.4.4.1 Particle Displacements and Force Chains

The results of the NRP simulation (#1) and two CIM simulations with relative velocities of 0.25π (#2) and 2π (#9) for probes with $\alpha = 10°$ and $L_1 = 0.044$ m (i.e. geometry for reference simulation #2) are analyzed in detail in this section. Figure 6.11 presents spatial maps of total particle displacements at the end of penetration (i.e. probe depth of 0.3 m) along a vertical cross-section, where the color of the particles is proportional to their magnitude. The inferred failure zones for the three simulations, defined as the locations where the particle displacements are greater than 10 mm, are marked with dash lines. The failure zone for the NRP case has a conical shape which appears as a triangle in the cross-sectional view. In contrast, the failure zones in the CIM simulations have a truncated cone shape which appear as trapezoids in the cross-sectional view. This truncated conical shape is a result of the CIM process disturbing particles at greater radial distances from the probe tip as a result of the tilted tip. In fact, the width at the bottom of the truncated cone appears to increase from nominally zero for the NRP case to 3.1 cm and 5.2 cm for the CIM simulations with relative velocities 0.25π and 2π, respectively.

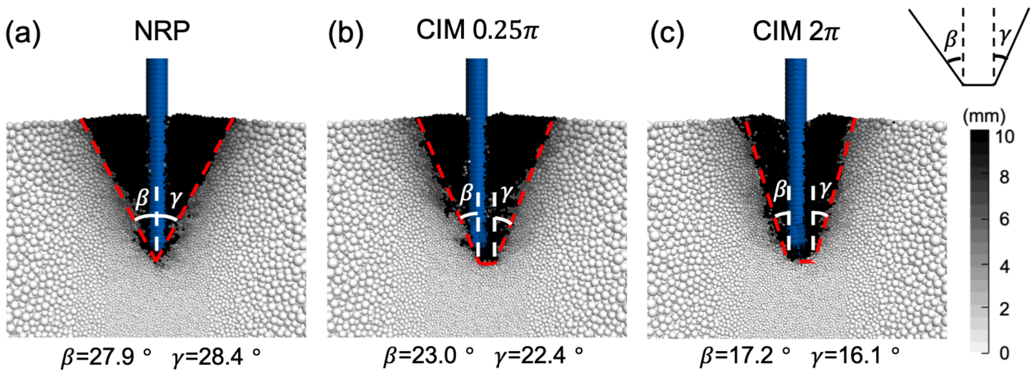

Figure 6.11: Total particle displacement magnitudes at the end of (a) NRP (simulation #1) and (b-c) CIM penetration with relative velocities of 0.25π (simulation #2) and 2π (simulation #5). Note that the simulations presented herein have the same bottom shaft length $L_1 = 1D$ and the same tip tilt angle $\alpha = 10°$.

The failure zone for NRP is approximately symmetric while the zone for CIM penetration is slightly shifted towards the right side, where the probe tip is located at the end of the simulation. The angles of the left and right sides of the failure zone are defined as β and γ, respectively, as shown in Figure 6.11. The angles are greatest for NRP, with a β

of 27.9° and γ of 28.4°. In contrast, the 2π CIM case has the smallest angles, with β and γ values of 17.2° and 16.1° , respectively. The smaller β and γ angles result in smaller volumes of the failure zones. Specifically, the failure zone volumes for NRP, and 0.25π and 2π CIM simulations are 7992 cm^3, 7054 cm^3 and 5036 cm^3, respectively, indicating that the volume of disturbed soil decreases as the relative velocity is increased.

The component displacements in the horizontal and vertical directions are shown in Figure 6.12, with rightwards and upwards displacements being defined as positive. The horizontal displacements in the NRP and 2π CIM simulations are nearly symmetric; however, the 0.25π simulation shows zones of large horizontal displacements at alternating locations along the probe length as a result of the probe tip trajectory (Figure 6.12(a)-6.12(c)). The particles close to the probe are displaced downward while the particles farther away from the probe are displaced upward, forming a shallow failure zone that propagates to the surface (Figure 6.12(d)-6.12(f)). In agreement with Figure 6.11, the

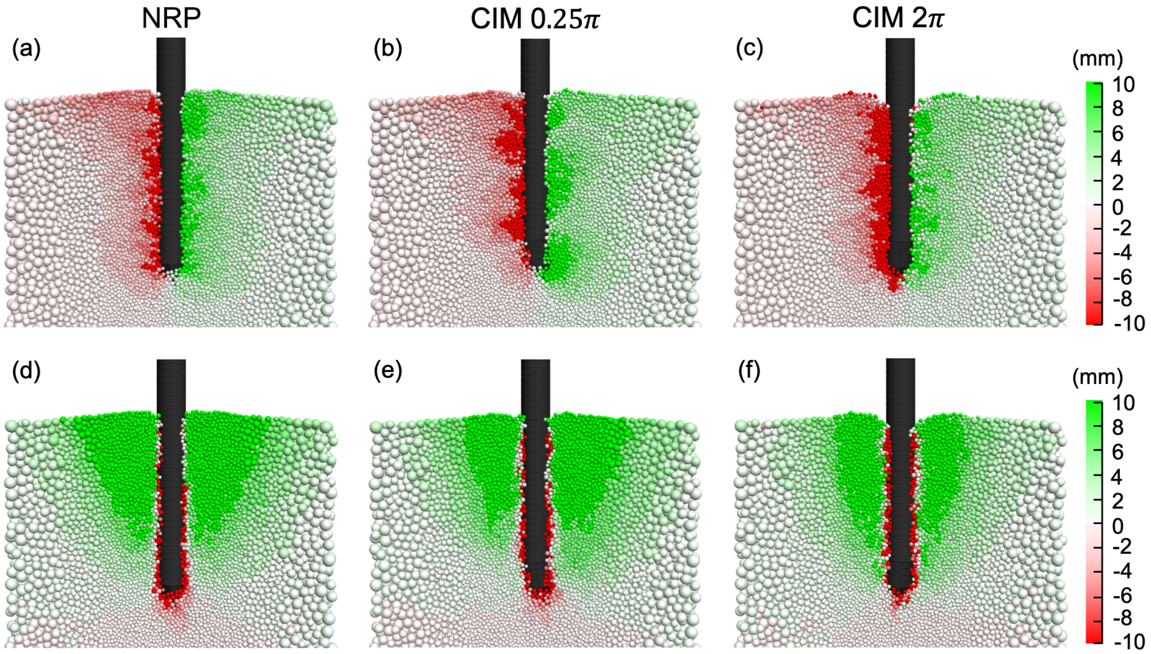

Figure 6.12: Soil particle (a-c) horizontal and (d-f) vertical displacements at the end of NRP (simulation #1) and CIM penetration with relative velocities of 0.25π (simulation #2) and 2π (simulation #5). Note that positive component displacements represent rightward and upward displacements; the simulations presented herein have the same bottom shaft length $L_1 = 1D$ and the same tip tilt angle $\alpha = 10°$.

size of the shallow failure zone is smaller for the simulations with 2π CIM than for those with 0.25π CIM and NRP.

The differences in failure zones are related to how the forces are transferred between the probe and the particles. Figure 6.13 depicts the normal contact forces greater than 5 N in force chain maps, where the thickness and color of the lines is proportional to the contact force magnitude. Greater contact forces are located around the tip for NRP than for CIM penetration, and the magnitude decreases between the 0.25π and 2π cases. These observations are consistent with the reduction in F_Z as the relative velocity is increased (i.e. Figure 6.6). The results indicate that the contact force magnitude and number of contacts around the tip decrease with increasing relative velocity, as described in more detail in the following section.

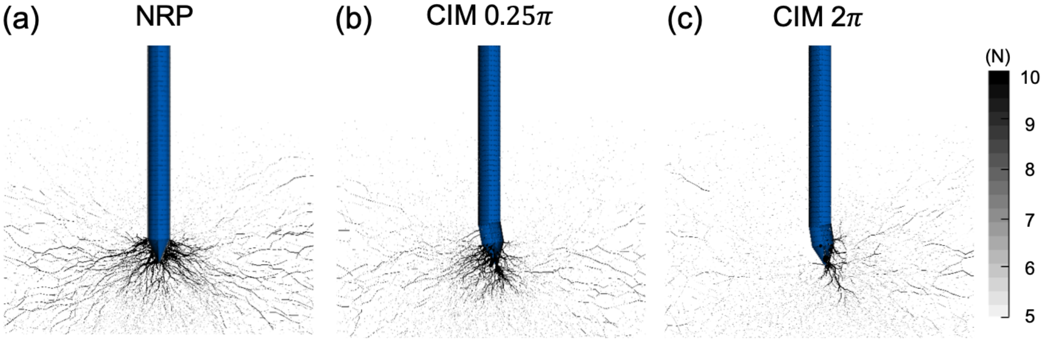

Figure 6.13: Particle normal contact forces at the end of (a) NRP (simulation #1) and (b-c) CIM with relative velocities of 0.25π (simulation #2), and 2π (simulation #5). Note that the simulations presented herein have the same bottom shaft length $L_1 = 1D$ and the same tip tilt angle $\alpha = 10°$.

6.4.4.2 Fabric Evolution

Aside from the magnitude and distribution of inter-particle forces, CIM penetration also alters soil fabric. The orientation of the contacts normal (CN) orientations and normal contact forces (NCF) can be characterized using angular distributions, which divides the contacts into bins with an angle interval of $\Delta\theta$ (i.e. Rothenburg and Bathurst [1989]). The angular distribution of CN and NCF can be approximately contoured by Fourier series, as defined in Eqs. 6.6 and 6.7:

$$E(\theta)_{CN} = \frac{1}{2\pi}[1 + a \times cos2(\theta - \theta_a)] \tag{6.6}$$

$$E(\theta)_{NCF} = f_0[1 + a_n \times cos2(\theta - \theta_n)] \tag{6.7}$$

where the a and a_n are the respective anisotropies for the CN and NCF distributions, θ_a and θ_n are the corresponding preferential orientations and f_0 is the average normal contact force.

The distribution of contact orientations and contact forces varies for different locations with respect to the probe tip. In addition, the location of the probe tip at a point in time depends on the depth, tip tilt angle, bottom shaft length and angular velocity (i.e. Figure 6.2). Therefore, it is required to define a local coordinate system to ensure that the location of the measurement zone with respect to the location of the probe tip remains consistent between different simulations. The global x and y axes represent the two perpendicular horizontal directions while the global z axis represents vertical direction (as previously defined in Figure 6.2 and 6.3). The local x' and y' axes are obtained by rotating the global x and y axes by an angle of θ, where θ is the difference between the global x axis and the horizontal axis normal to the probe tip (i.e. x'). The local coordinate system is defined such that the x' axis is colinear with the tip's horizontal orientation, as shown in Figure 6.14. The local y' axis is defined as the horizontal direction perpendicular to x' and the local z' axis is aligned in the vertical direction. Based on the definition of the local coordinate systems, the translation from global to local coordinate system can

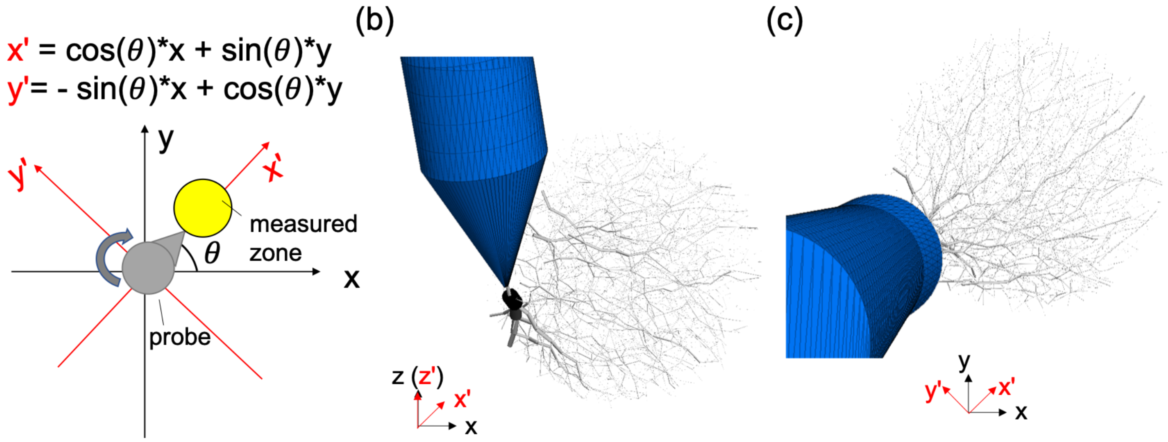

Figure 6.14: Coordinate systems and measurement zone for describing contact orientations: (a) global and local coordinates; (b) side and (c) top views of contact force chains in the measurement zone located close to the tip.

be achieved using Eqs. 6.8 and 6.9:

$$x' = cos(\theta)x + sin(\theta)y \tag{6.8}$$

$$y' = -sin(\theta)x + cos(\theta)y \tag{6.9}$$

To analyze the CN and NCF in different locations with respect to the probe tip, a measurement sphere with a diameter of 0.05 m and containing about 2,500 particles is placed at the location shown in the schematics in Figure 6.15(a)-6.15(d), which is at the same elevation as the probe tip. A second measurement sphere is placed directly below the probe's centerline, as shown in the schematics in Figure 6.15(e)-6.15(h).

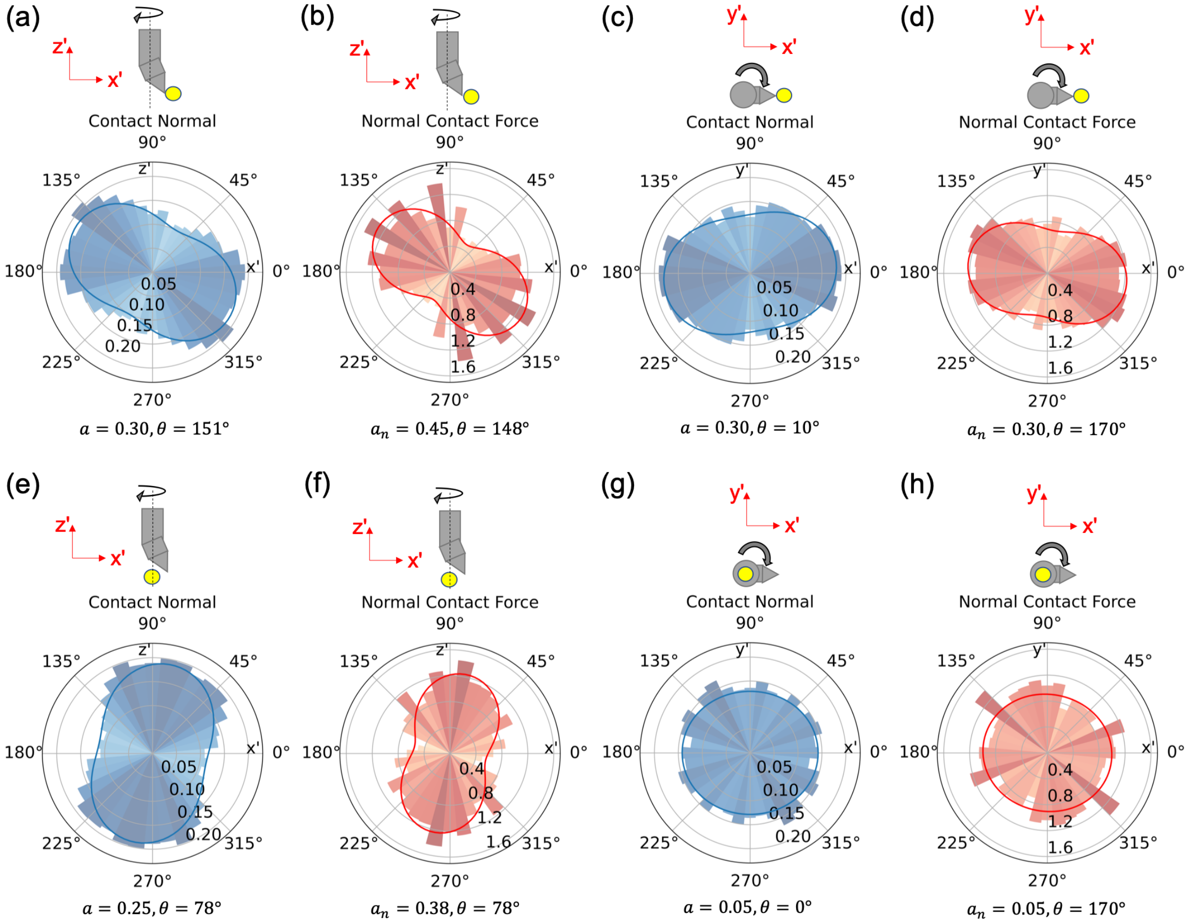

Figure 6.15: Contact orientations and magnitudes in local coordinate system for the optimal CIM with relative velocity of 0.25π (simulation #2). Polar plots of contact normal and normal contact forces in measure zones that are (a-d) close to the tip and (e-h) below the tip.

The CN and NCF angular distributions for the CIM simulation with a relative velocity of 0.25π (simulation #2) are presented in Figure 6.15(a)-6.15(h). Close to the probe tip, the CN and CNF distributions exhibit some anisotropy in the vertical x'-z' plane, with anisotropy values a and an of 0.30 and 0.45, respectively (Figure 6.15(a) and 6.15(b)). The preferential orientations θ_a and θ_n are 151° and 148°, respectively, which reflect the normal direction of particle-probe contacts. In the horizontal x'-y' plane, the CN and NCF distributions are also anisotropic, with both a and a_n values of 0.30 (Figure 6.15(c)). However, the distributions have preferential orientations close to the x' direction, with θ_a and θ_n of 10° and 170°, respectively (Figure 6.15(d)).This indicates that the rotational action of the probe does not significantly rotate the preferential orientation of the CN and NCF with respect to the pre-penetration distribution with a preferential orientation close to 0°. For the particles directly beneath the probe, the CN in the x'-z' plane have an anisotropic distribution with a preferential orientation at 78° (Figure 6.15(e) and 6.15(f)), which is due to the compression induced by the vertical penetration of the probe. In the x'-y' plane, both CN and NCF distributions are close to isotropic (Figure 6.15(g) and 6.15(h)).

The CN and CNF angular distributions for the NRP (simulation #1), CIM with relative velocity of 0.25π (simulation #2) and CIM with relative velocity of 2π (simulation #5) are compared to describe the effects of the circumnutation motion on the fabric changes. To do so, the CIM, CN and NCF distributions are normalized by the maximum number of contacts and the average contact force measured in the NRP simulation, respectively. Results are presented for locations close to the probe tip and below the tip in the vertical x'-z' plane as shown in Figure 6.16, where the schematics at the top of the subplots indicate the locations of the measured zones.

Close to the tip, the number of contacts and the contact force magnitude decreases as the relative velocity is increased (Figure 6.16(a) and 6.16(b)). Specifically, the coordination number decreases from 3.20 to 2.51, the void ratio increases from 0.63 to 0.69, and the average contact force decreases from 7.00 N to 1.24 N when the relative velocity is increased from 0π (i.e. NRP) to 2π (Table 6.4). These explain the reduction in total

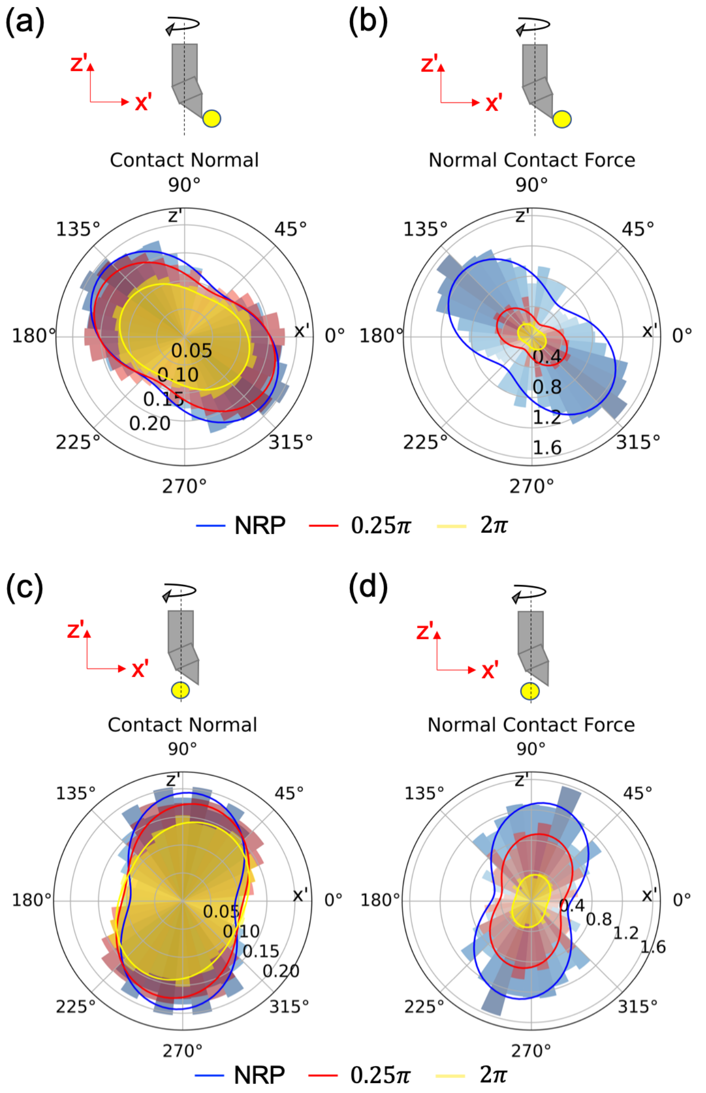

Figure 6.16: Orientations and magnitudes of contact normal (CN) and normal contact forces (NCF) for CPT and CIMs with the relative velocity of 0.25π (simulation #2), and 2π (simulation #5) in measure zones that are (a-b) close to the tip and (c-d) below the tip. Note that all CN values are normalized by the maximum CN and the average NCF of the NRP simulation.

Table 6.4: Orientations and magnitudes of contacts near the probe tip.

Measurement Zone Location	$\boldsymbol{\omega R/v}$	**CN**		**NCF**		**Average Coordination Number**	**Average Contact Force (N)**	**Void Ratio**
		$\boldsymbol{\alpha}$	$\boldsymbol{\theta}$	$\boldsymbol{a_n}$	$\boldsymbol{\theta_n}$			
Close to	NRP	0.30	142°	0.40	140°	3.20	7.00	0.63
the tip	0.25π	0.30	151°	0.45	148°	2.91	2.71	0.64
(Fig 16 a,b)	2π	0.20	155°	0.30	142°	2.51	1.24	0.69
Below	NRP	0.35	85°	0.45	79°	3.26	3.27	0.59
the tip	0.25π	0.25	78°	0.38	78°	3.22	2.35	0.59
(Fig 16 c,d)	2π	0.15	65°	0.25	72°	3.12	0.97	0.61

penetration force with increasing relative velocity observed in Figure 6.6(a). The angular distributions become less anisotropic as the relative velocity is increased, with a changing from 0.3 to 0.2 and a_n changing from 0.4 to 0.3 (Table 6.4). The contact orientations changes lightly towards the horizontal x' direction,from 142° for NRP to 155° for a relative velocity of 2π. This change in orientation is a result of the rotation action of the tip. Similar trends were found by Tang and Tao [2022] for rotational penetration, where the average contact normal angle between the conical tip and soil rotated towards the horizontal as the rotational speed was increased.

At the location below the probe tip, the coordination number and average contact force magnitude also decrease as the relative velocity is increased (Table 6.4). Specifically, the coordination number decreases slightly from 3.26 to 3.12, the void ratio increases slightly from 0.59 to 0.61, and the average contact force decreases from 3.27 N to 0.97 N as the relative velocity is increased from 0π to 2π. The CN distributions show a decrease in anisotropy with increasing relative velocity, with a decreasing from 0.35 to 0.15, while the CNF distribution shows a decrease in a_n from 0.45 to 0.25. These measurements also explain the reduction in F_Z with increasing relative velocity.

6.5 Implications for Penetration Processes in Geotechnics Practice

Circumnutation-inspired motion (CIM) can be applied as a new penetration technique in geotechnical engineering, which may help improve the performance and efficiency of soil penetration processes. While the results presented herein demonstrate the reduction in the vertical penetration force with increasing relative velocity and the reduction in total mechanical work for certain conditions, future investigations should address the effect of increasing depth and overburden stress on these trends.

As shown in this study, CIM penetration reduces the vertical penetration force. For example, for the CIM simulations with relative velocities of 0.25π and 2π, the vertical force was reduced by 41.6% and 90.5%, respectively, compared to that of non-rotational penetration Table 6.5. As a trade-off, the mobilized torque increases as the relative velocity is increased. This trade-off may benefit certain geotechnical applications such as drill rigs that are limited in their pushing force by the weight of the equipment but are less limited in the torque that can be applied. The environmental impacts from site investigation activities reported by Purdy et al. [2020] based on a life-cycle sustainability assessment (LCSA) can be used to exemplify the possible benefits of CIM penetration. The environmental impacts are a result of equipment mobilization (i.e. transport to the testing site), advancement (i.e. penetration, drilling), testing and sampling, and grouting. For a typical 30-m-deep exploration with a mobilization distance of 160 km considered in their study, equipment mobilization costs about 2.3, 2.3 and 10.2 GJ for CPT testing,

Table 6.5: Summary of penetration force, torque, total mechanical work.

Penetration Method	$\omega R/v$	**Penetration Force (N)**	**Torque (N×m)**	**Total Mechanical Work (J)**
NRP	0	2181	0	270.7
CIM	0.25π	1273	12.3	226.8
	2π	207	10.2	590.2
RP	0.25π	2139	7.3	276.4
	2π	1340	10.4	605.2

standard penetration testing (SPT) and Shelby tube sampling, respectively, accounting for 54.8%, 50.9% and 53.1% of the total energy spent. If CIM produces a significant reduction of the vertical penetration force, it may allow for using smaller equipment and thereby reduce the energetic cost of equipment mobilization; this reduction would be proportional to the weight and size of the required equipment.

6.6 Reversed circumnutation inspired motion

In this section, a reversed pattern of circumnutation inspired motion (RCIM) is explored and compared with CIM and NRP. The only difference between RCIM and CIM is the direction of rotation. During RCIM penetration, the titled tip and bottom shaft first rotate 360° clockwise and then rotate 360° counterclockwise. This reversed rotation pattern repeats during vertical penetration of the entire probe.

The penetration force, torque, mechanical work, and tip trajectory during the RCIM penetration are presented in Figure 6.17. The results of CIM and NRP penetration are also included for comparison. The presented RCIM and CIM simulations have the same tip tilt angle of 10°, bottom shaft length of $1D$, and relative velocity of 0.25π. The penetration forces mobilized during CIM and RCIM penetration are similar in magnitude, which are both smaller than that of NRP penetration. The torque exhibit reversed signs for RCIM but with a similar magnitude to that of CIM torque. Therefore, the vertical, rotational, and total work required during RCIM penetration are similar to CIM penetration. The difference between forces, torque and work of RCIM and CIM penetration may increase with an increasing relative velocity, however this assumption requires further exploration on RCIM with different relative velocities and probe geometry.

6.7 Conclusions

Circumnutations are helical movements involved in the soil penetration process of certain plant roots. In this study, probes that employ circumnutation-inspired motion are simulated using DEM in shallow, unconfined soil specimens to explore the forces, torques and energetic requirements, along with the particle-level mechanisms, involved in this bio-inspired soil penetration strategy. CIM penetration was simulated as circular movements

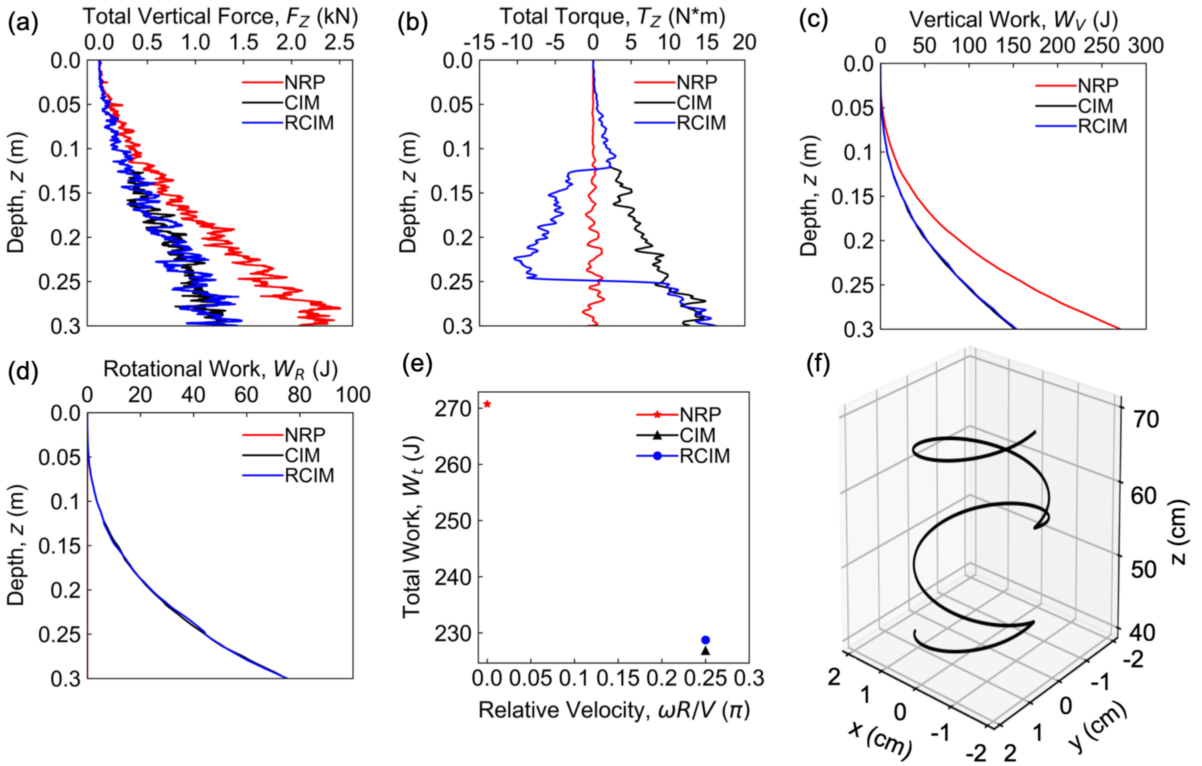

Figure 6.17: The (a) vertical penetration force, (b) torque, (c) vertical work, (c) rotational work, and (e) total work for the non-rotational penetration (NRP), circumnutation inspired motion (CIM), and reversed circumnutation inspired motion (RCIM); (f) is the tip trajectory for the reversed CIM. Note that the CIM and RCIM simulations (#2 and #20) presented herein have same geometry with tip tilt angle $\alpha = 10°$ and bottom shaft length $L_1 = 1D$ and same relative velocity $\omega R/v = 0.25\pi$.

of the probe's tilted tip on the horizontal plane accompanied by simultaneous vertical penetration of the entire probe.

The simulation results show that CIM penetration can mobilize vertical penetration forces that are as small as 10% of those mobilized during non-rotational penetration. The vertical penetration force, torque and mechanical work during CIM are controlled by relative velocity (i.e. the ratio of tangential to vertical velocities). An increase in the relative velocity leads to reductions of the vertical penetration force and vertical mechanical work at the cost of increases in the mobilized torque and rotational work. Out of all the probe motions and geometries considered in this investigation, a relative velocity of 0.25π, a tip tilt angle of 10° and a bottom shaft length equivalent to one probe diameter (i.e. 0.044 m) yields the minimum value in total work, which is 16.2% smaller than that involved in non-rotational penetration. The total mechanical work increases as the relative velocity, tip tilt angle and bottom shaft length are increased. Additionally, even when compared to rotational penetration, CIM penetration can mobilize smaller vertical penetration forces and total mechanical work.

Particle-level analysis shows that the reduction in penetration force with increasing relative velocity during CIM is due to the reduction in the volume of disturbed particles, coordination number and normal contact forces, as well as the increase in the soil void ratio in the vicinity of the probe tip. Analysis of the angular distributions of contact normal orientations and normal contact forces shows consistent changes as the relative velocity is increased, with reductions in the anisotropy of the angular distributions and reductions in contact numbers and contact force magnitudes.

6.8 Acknowledgements

This material is based upon work supported in part by the Engineering Research Center Program of the National Science Foundation under NSF Cooperative Agreement No. EEC–1449501. The authors were supported by the National Science Foundation (NSF) under Award No. 1942369. Any opinions, findings, and conclusions or recommendations expressed in this material are those of the author(s) and do not necessarily reflect those of the National Science Foundation.

Chapter 7

Conclusions and Future Work Recommendations

The research presented in this dissertation investigated different bio-inspired soil penetration processes for implementation in probes for geotechnical applications such as site characterization. The methodology employed throughout this dissertation is discrete element modeling (DEM), which explicitly simulates each individual particle and contact within a granular assemblies. The DEM simulation results presented in this dissertation expand the understanding of the soil behavior mechanisms relevant in different bio-inspired soil penetration strategies. Specifically, the probe-particle interactions, interparticle contact force distributions, soil deformation distributions, soil failure mechanisms, and mechanical work were explored during the bio-inspired soil penetration process. The effects of the probe configuration, probe motion, overburden stress, and soil density on the self-penetration process were investigated. The conclusions drawn during this investigation, as summarized in this chapter, will help guide the design of bio-inspired and field-deployable self-penetration probes for in-situ testing. These probes are intended to allow using smaller equipment to reduce testing challenges such as reaching sites with limited access and decrease the environmental and economic impacts of site characterization activities.

A schematic of different bio-inspired soil penetration methods is presented in Figure 7.1. According to existing numerical and experimental research on bio-geotechnics, soil penetration can be achieved by radial expansion of an anchor accompanied by vertical penetration of a tip (i.e. anchor-tip strategy) (e.g. Chen et al. [2021], Huang and Tao [2020]), modifying the tip shape (e.g. Hunt et al. and Martinez [2022], Mishra et al. [2018]), injection of a fluid into the soil to liquify it (Naclerio et al. [2021]), rotating the probe with a straight tip or a tilted tip (i.e. circumnutation inspired motion) (e.g. Del Dottore et al. [2017], Chen et al.), or performing cycles of axial extension and contraction (Tao et al. [2020]). This dissertation investigated the anchor-tip and circumnutation motion strategies. The following sections present conclusions for these two bio-inspired soil penetration strategies.

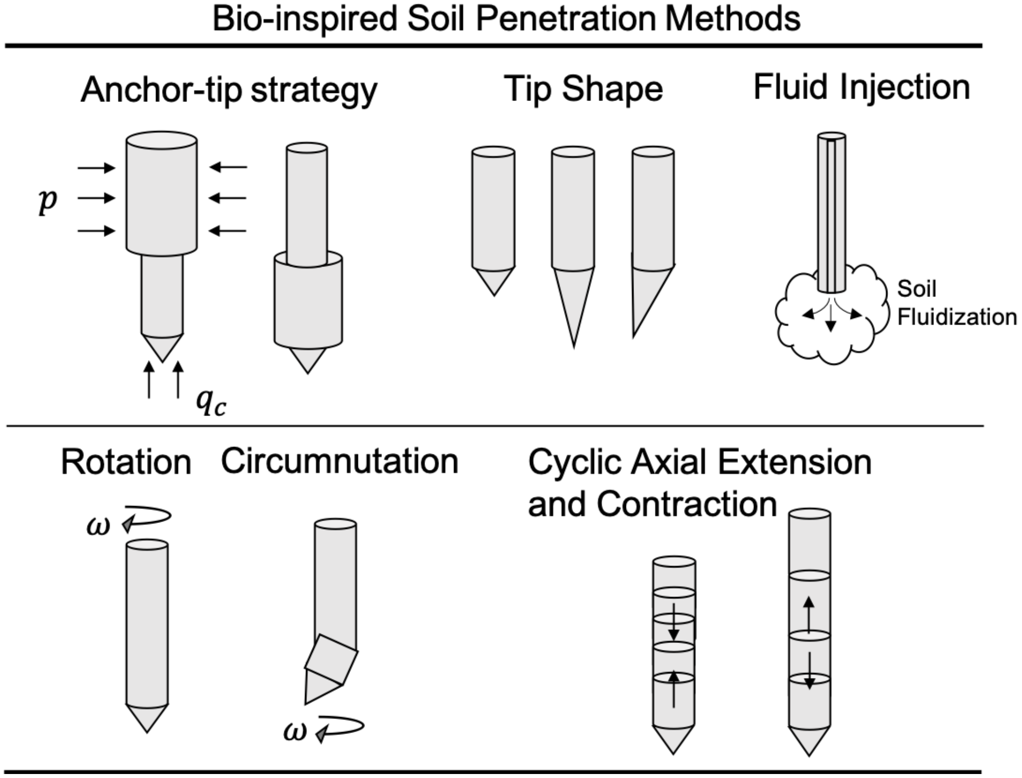

Figure 7.1: Schematic of bio-inspired soil penetration methods.

7.1 Conclusions: the Self-Penetration Process with the Anchor-Tip Strategy

The results presented in this dissertation show that the self-penetration performance of a bio-inspired probe that uses an 'anchor-tip' strategy can be significantly influenced by the probe configuration, number of anchors, and soil density and overburden stress. The geomechanical processes behind the self-penetration process have been explored using meso-scale interpretation of the DEM simulation results. The following bullets summarize the main findings of the soil penetration anchor-tip strategy:

- Assessment of the anchor-tip strategy using global quantities, such as probe forces, stresses and displacements indicates that expansion of the anchor leads to a reduction of the penetration resistance, which facilitates subsequent tip penetration. However, this reduction is temporary and the tip resistance is remobilized after the tip is advanced by a few centimeters. This remobilization of the tip resistance is accompanied by a decrease in the anchorage force if the anchor maintains a constant diameter. These trends indicate an interaction between the tip and the anchor of the probe which are a result of soil arching. The probe's self-penetration ability, defined as the ability of the probe to generate anchorage forces that are greater than the soil penetration forces, increases as the distance between the anchor and the tip is decreased, anchor length and expansion magnitude are increased, anchor friction coefficient is increased and the overburden stress is increased. Of particular note is that the anchorage reaction force increased at a great rate than the penetration force when the overburden stress is increased, indicating that self-penetrating the soil at greater depths than the biological analogues investigated in this dissertation is not only feasible but beneficial. These findings are presented in detail in Chapter 2.

- The self-penetration ability of a probe that uses the anchor-tip strategy is closely related to the interaction between the probe's anchor and the tip. The geomechanical processes involved in these interactions are explored using meso-scale simulation results, such as soil stress state and strain, stress path, contact force chains, and particle displacements. For example, when the anchor-tip distance is decreased and the anchor length is increased, there is a more significant relaxation of effective stresses ahead of the tip during anchor expansion, leading to a greater reduction in the penetration resistance and a greater tip advancement displacement (i.e. self-penetration displacement). Anchor expansion leads to a rotation of the effective principal stresses, soil dilation, and concentration of strong contact forces around the anchor, while simultaneously leading to tensile strains and a decrease in effective stresses at locations near the probe's tip. After advancement of the tip following anchor expansion, the contact force distribution around the tip is similar to that in the initial direct penetration stage, highlighting the remobilization of the penetration resistance. These findings are presented in detail in Chapter 3.

- Increasing the number of anchors from one to two in a probe that uses the anchor-tip strategy leads to an increase in the total anchorage force but it results in a decrease of the anchorage force mobilized per anchor. The bottom anchor capacity is shown to be highly related to the spacing between the two anchors. Namely, a greater bottom anchor force is mobilized when the spacing is increased because the detrimental interactions between the anchors are reduced. When the inter-anchor spacing is sufficiently large, the soil fails surrounding each anchor fails in a near-isolated manner. In a similar fashion as the probe with single anchor, expansion of the anchors leads to a reduction in tip penetration resistance. This reduction is greater when the anchor spacing is decreased, the anchor-tip distance is decreased, and the anchor expansion magnitude is increased. A critical plane is defined in three unitless dimensions (i.e. normalized anchor spacing, normalized anchor-tip distance, and anchor expansion magnitude) that can discern between the probe configurations that enable self-penetration from those that do not. These findings are presented in detail in Chapter 4.
- Complete cycles of self-penetration, consisting of alternating expansion and contraction of top and the bottom shafts that allow the probe to continue moving to deeper locations, are performed on specimens of varying density. The probe achieves a greater penetration displacement in the medium dense specimen than in the dense specimen because it mobilizes a greater shaft-to-tip force ratio in the former. The loose specimen mobilizes the greatest shaft-to-tip force ratio among three specimens; however, successful self-penetration requires limiting the expansion magnitude dur-

ing the initial top shaft expansion stage. The results also indicate that continued expansion of the top shaft during the tip penetration stage is essential for achieving a greater self-penetration displacement. Tip oscillation during the tip penetration stage is shown to successfully prevent remobilization of the penetration resistance, maintaining it at small magnitudes. The self-burrowing probe in the loose specimen has the greatest energetic efficiency because it achieves largest penetration distance per unit work. Two cycles of self-penetration process are simulated in the dense specimen, showing that the probe achieved a greater tip displacement in the second cycle. These findings are presented in detail in Chapter 5.

7.2 Conclusions: the Soil Penetration Process with Circumnutation Inspired Motion

The soil penetration process of a probe that uses circumnutation inspired motion was also investigated in this dissertation. The circumnutation inspired motion consists of helical movements in the horizontal plane of a tilted tip accompanied by simultaneous vertical displacement of the entire probe. The evolution of probe forces, torques, displacements, mechanical work, particle contact orientations, particle contact forces and particle displacements were discussed in this dissertation. The penetration ability and efficiency of the circumnutating probes was compared to that of probes that implement non-rotational penetration and rotational penetration with a straight tip. The following bullets summarize the main findings of the penetration that uses circumnutation inspired motion:

- The circumnutation inspired penetration can mobilize penetration forces as small as 10% of those mobilized during non-rotational penetration. The penetration forces during circumnutative penetration are also as small as 60% of those mobilized during rotational penetration with a straight tip. Consequently, the vertical penetration work required for the circumnutative penetration is also much smaller than that for non-rotational penetration and rotational penetration with a straight tip. This reduction in penetration force and vertical work could be used for developing future light weight penetrating devices. It is noted that the reduction in penetration force comes with a cost of increased torque, which leads to an increase in the rotational work. However, the total work for the penetration and rotation is smaller than the total work for non-rotational penetration when the ratio of tangential to vertical velocity (i.e. relative velocity) is smaller than 0.25π.

- The relative velocity, tip tilt angle, and the titled shaft length have an important influence for the circumnutation penetration process. Greater decrease of the penetration force occurs with increased relative velocity, tip tilt angle and bottom shaft length. Among all simulated probe configurations, the probe with a relative velocity of 0.25π, tip tilt angle of 10° and bottom shaft length equivalent to one probe diameter requires the minimum total work, which was 84% smaller than the work required for non-rotational penetration.
- During circumnutation inspired penetration, the coordination number and contact forces near the tip are reduced, while the void ratio in the same location is increased. Smaller volume of soil is disturbed by circumnutative penetration than by non-rotational penetration. The anisotropy of the angular distributions of contact normal orientations and the contact numbers decreases with an increase in the relative velocity.

7.3 Recommendations for Future Work

Beyond the scope of this dissertation, there are important topics that should be addressed in the future to further advance this research. They following bullets present several recommendations for future work:

- Expand the multicycle self-burrowing study on specimens with varying density. Specifically, more than three cycles of self-penetration in dense, medium dense and loose specimen could provide a complete understanding of the change of probe's penetration ability and energetic efficiency in shallow penetration condition. In the same vein, simulations in layered specimens (i.e. loose over dense sand, dense over loose sand) would be beneficial for understanding challenges that bio-inspired probes may encounter in heterogenous deposits which are more representative of field conditions.

- A numerical study on the effects of probe motion velocities on the self-penetration probe that uses the anchor-tip strategy, such as tip penetration velocity, anchor expansion rate, and tip oscillation velocity and period, would assist the development of a prototype of self-burrowing probe and the experimental testing configuration.
- Experimental and numerical studies on the bio-inspired soil penetration process in clayey specimens would facilitate the future application in different soil types other than granular materials. The numerical investigation in clay can be implemented using continuum methods, such as finite element modeling and material point method.
- Experimental and field testing bio-inspired probe prototypes that use the anchor-tip and circumnutation strategies in sands and clays is necessary to verify the trends reported in this dissertation.
- Experimental and numerical studies on the effects of probe's size on the soil penetration process would help expand the use of the bio-inspired strategies investigated herein from penetration with smaller probes, such as in in-situ testing, to penetration with larger objects, such as in driving of deep foundations.
- Studies on bio-inspired penetration process in varying directions, such as horizontal and inclined penetration, would be beneficial for the development of a future underground autonomous sensors network.
- Numerical studies on the circumnutation inspired penetration in deep conditions are needed. This study could complete the understanding of the mechanisms behind this penetration strategy and its performance at greater depth that is relevant to the scale in geotechnical engineering projects.
- The effects of particle size, gradation, particle angularity and particle crushing on the soil penetration processes deserve further investigation. The experimental or

numerical studies on these effects could guide the design and application of the future bio-inspired probe in different site conditions, such as in crushable soils.

- There are diverse organisms in the nature that can penetrate soil and deserve further studies to develop bio-inspired soil penetration strategies. For example, a bio-inspired probe with a soft outer layer like turtles may facilitate soil penetration because the soft skin of turtles has been shown to prevent penetration injury by dispersion force.

References

Kelly M Dorgan, Sanjay R Arwade, and Peter A Jumars. Burrowing in marine muds by crack propagation: kinematics and forces. *Journal of Experimental Biology*, 210(23): 4198–4212, 2007.

A Savioli, C Viggiani, and JC Santamarina. Root-soil mechanical interaction. In *Geo-Congress 2014: Geo-characterization and Modeling for Sustainability*, pages 3977–3984, 2014.

ER Trueman. The burrowing activities of bivalves. *Synp. zool. soc. Lond.*, 22:167–186, 1968a.

Kelly M Dorgan. The biomechanics of burrowing and boring. *Journal of Experimental Biology*, 218(2):176–183, 2015.

H Shin and Juan Carlos Santamarina. Open-mode discontinuities in soils. *Géotechnique Letters*, 1(4):95–99, 2011.

ZX Yang, RJ Jardine, BT Zhu, P Foray, and CDHC Tsuha. Sand grain crushing and interface shearing during displacement pile installation in sand. *Géotechnique*, 60(6): 469–482, 2010.

Ningning Zhang, Matteo O Ciantia, Marcos Arroyo, and Antonio Gens. A contact model for rough crushable sand. *Soils and Foundations*, 61(3):798–814, 2021.

Isaiah Taylor, Kevin Lehner, Erin McCaskey, Niba Nirmal, Yasemin Ozkan-Aydin, Mason Murray-Cooper, Rashmi Jain, Elliot W Hawkes, Pamela C Ronald, Daniel I Goldman, et al. Mechanism and function of root circumnutation. *Proceedings of the National Academy of Sciences*, 118(8), 2021.

Paul W Mayne. *Cone penetration testing*, volume 368. Transportation Research Board, 2007.

Alena J Raymond, James R Tipton, Alissa Kendall, and Jason T DeJong. Review of impact categories and environmental indicators for life cycle assessment of geotechnical systems. *Journal of Industrial Ecology*, 24(3):485–499, 2020.

Chris Purdy, Alena J Raymond, Jason T DeJong, and Alissa Kendall. Life cycle assessment of site characterization methods. In *Geo-Congress 2020: Geo-Systems, Sustainability, Geoenvironmental Engineering, and Unsaturated Soil Mechanics*, pages 80–89. American Society of Civil Engineers Reston, VA, 2020.

Alejandro Martinez, Jason DeJong, Idil Akin, Ali Aleali, Chloe Arson, Jared Atkinson, Paola Bandini, Tugce Baser, Rodrigo Borela, Ross Boulanger, et al. Bio-inspired geotechnical engineering: Principles, current work, opportunities and challenges. *Géotechnique*, pages 1–19, 2021.

DD Cortes and S John. Earthworm-inspired soil penetration. In *Proceedings of biomediated and bioinspired geotechnics (B2G) conference*, 2018.

A Khosravi, A Martinez, J DeJong, and D Wilson. Discrete element simulations of bio-inspired self-burrowing probes in sands of varying density. In *Proceedings of biomediated and bioinspired geotechnics conference*, 2018.

Alejandro Martinez, Jason T DeJong, Robert A Jaeger, and Ali Khosravi. Evaluation of self-penetration potential of a bio-inspired site characterization probe by cavity expansion analysis. *Canadian Geotechnical Journal*, 57(5):706–716, 2020.

Junliang Julian Tao, Sichuan Huang, and Yong Tang. Sbor: a minimalistic soft self-burrowing-out robot inspired by razor clams. *Bioinspiration & Biomimetics*, 15(5): 055003, 2020.

Sichuan Huang and Junliang Tao. Modeling clam-inspired burrowing in dry sand using cavity expansion theory and dem. *Acta Geotechnica*, 15(8):2305–2326, 2020.

Yuyan Chen, Ali Khosravi, Alejandro Martinez, and Jason DeJong. Modeling the self-penetration process of a bio-inspired probe in granular soils. *Bioinspiration & Biomimetics*, 16(4):046012, 2021.

R Borela, JD Frost, G Viggiani, and F Anselmucci. Earthworm-inspired robotic locomotion in sand: An experimental study with x-ray tomography. *Géotechnique Letters*, 11 (1):66–73, 2021.

Alejandro Martinez, Sophia Palumbo, and Brian D Todd. Bioinspiration for anisotropic load transfer at soil–structure interfaces. *Journal of Geotechnical and Geoenvironmental Engineering*, 145(10):04019074, 2019.

Alejandro Martinez and KB O'Hara. Skin friction directionality in monotonically-and cyclically-loaded bio-inspired piles in sand. *Deep Found. Inst. J*, 2021.

Kyle B O'Hara and Alejandro Martinez. Monotonic and cyclic frictional resistance directionality in snakeskin-inspired surfaces and piles. *Journal of Geotechnical and Geoenvironmental Engineering*, 146(11):04020116, 2020.

Hans Henning Stutz and Alejandro Martinez. Directionally dependent strength and dilatancy behavior of soil–structure interfaces. *Acta Geotechnica*, 16(9):2805–2820, 2021.

SD Mallett, S Matsumura, and J David Frost. Additive manufacturing and computed tomography of bio-inspired anchorage systems. *Géotechnique Letters*, 8(3):219–225, 2018a.

Gerrit J Meijer, David Muir Wood, Jonathan A Knappett, A Glyn Bengough, and Teng Liang. Root branching affects the mobilisation of root-reinforcement in direct shear. In *E3S Web of Conferences*, volume 92, page 12010. EDP Sciences, 2019.

Matthew Burrall, Jason T DeJong, Alejandro Martinez, and Daniel W Wilson. Vertical pullout tests of orchard trees for bio-inspired engineering of anchorage and foundation systems. *Bioinspiration & Biomimetics*, 16(1):016009, 2020.

Emanuela Del Dottore, Alessio Mondini, Ali Sadeghi, Virgilio Mattoli, and Barbara Mazzolai. An efficient soil penetration strategy for explorative robots inspired by plant root circumnutation movements. *Bioinspiration & biomimetics*, 13(1):015003, 2017.

Carl Gans. Locomotion and burrowing in limbless vertebrates. *Nature*, 242(5397):414–415, 1973.

HY Elder. Peristaltic mechanisms. *Aspects of animal movement*, 5:71–92, 1980.

Kelly M Dorgan. Kinematics of burrowing by peristalsis in granular sands. *Journal of Experimental Biology*, 221(10):jeb167759, 2018.

ER Trueman. A comparative account of the burrowing process of species of mactra and of other bivalves. *Journal of Molluscan Studies*, 38(2):139–151, 1968b.

Anthony G Bengough and Chris E Mullins. Mechanical impedance to root growth: a review of experimental techniques and root growth responses. *Journal of soil science*, 41(3):341–358, 1990.

Amy GR Jacobsen, George Jervis, Jian Xu, Jennifer F Topping, and Keith Lindsey. Root growth responses to mechanical impedance are regulated by a network of ros, ethylene and auxin signalling in arabidopsis. *New Phytologist*, 231(1):225–242, 2021.

AM Abdalla, DRP Hettiaratchi, and AR Reece. The mechanics of root growth in granular media. *Journal of Agricultural Engineering Research*, 14(3):236–248, 1969.

JM Kirby and AG Bengough. Influence of soil strength on root growth: experiments and analysis using a critical-state model. *European Journal of Soil Science*, 53(1):119–127, 2002.

Charles Darwin, Francis Darwin, et al. The power of movement in plants. 1883.

Naoto Inoue, Teruo Arase, Motoyuki Hagiwara, Takahisa Amano, Taiichi Hayashi, and Ryoichi Ikeda. Ecological significance of root tip rotation for seedling establishment of oryza sativa l. *Ecological Research*, 14(1):31–38, 1999.

Emanuela Del Dottore, Alessio Mondini, Ali Sadeghi, Virgilio Mattoli, and Barbara Mazzolai. Circumnutations as a penetration strategy in a plant-root-inspired robot. In *2016 IEEE international conference on robotics and automation (ICRA)*, pages 4722–4728. IEEE, 2016.

Jun Ai, Jian-Fei Chen, J Michael Rotter, and Jin Y Ooi. Assessment of rolling resistance models in discrete element simulations. *Powder Technology*, 206(3):269–282, 2011.

CM Wensrich and A Katterfeld. Rolling friction as a technique for modelling particle shape in dem. *Powder Technology*, 217:409–417, 2012.

Kelly M Dorgan, Chris J Law, and Greg W Rouse. Meandering worms: mechanics of undulatory burrowing in muds. *Proceedings of the Royal Society B: Biological Sciences*, 280(1757):20122948, 2013.

Arshad Kudrolli and Bernny Ramirez. Burrowing dynamics of aquatic worms in soft sediments. *Proceedings of the National Academy of Sciences*, 116(51):25569–25574, 2019.

Ryan D Maladen, Yang Ding, Chen Li, and Daniel I Goldman. Undulatory swimming in sand: subsurface locomotion of the sandfish lizard. *science*, 325(5938):314–318, 2009.

Nicholas J Gidmark, James A Strother, Jaquan M Horton, Adam P Summers, and Elizabeth L Brainerd. Locomotory transition from water to sand and its effects on undulatory kinematics in sand lances (ammodytidae). *Journal of Experimental Biology*, 214 (4):657–664, 2011.

ER Trueman. Burrowing habit and the early evolution of body cavities. *Nature*, 218 (5136):96–98, 1968c.

ER Trueman. The locomotion of the freshwater clam margaritifera margaritifera (unionacea: Margaritanidae). *Malacologia*, 6:401–410, 1968d.

Emmet Lewis Greacen and JS Oh. Physics of root growth. *Nature New Biology*, 235(53): 24–25, 1972.

Kelly M Dorgan, Peter A Jumars, Bruce Johnson, BP Boudreau, and Eric Landis. Burrow extension by crack propagation. *Nature*, 433(7025):475–475, 2005.

Elizabeth AK Murphy and Kelly M Dorgan. Burrow extension with a proboscis: mechanics of burrowing by the glycerid hemipodus simplex. *Journal of Experimental Biology*, 214(6):1017–1027, 2011.

Ali Sadeghi, Alice Tonazzini, Liyana Popova, and Barbara Mazzolai. A novel growing device inspired by plant root soil penetration behaviors. *PloS one*, 9(2):e90139, 2014.

Nicholas D Naclerio, Christian M Hubicki, Yasemin Ozkan Aydin, Daniel I Goldman, and Elliot W Hawkes. Soft robotic burrowing device with tip-extension and granular fluidization. In *2018 IEEE/RSJ International Conference on Intelligent Robots and Systems (IROS)*, pages 5918–5923. IEEE, 2018.

Daniel Ortiz, Nick Gravish, and Michael T Tolley. Soft robot actuation strategies for locomotion in granular substrates. *IEEE Robotics and Automation Letters*, 4(3):2630–2636, 2019.

Yifei Ma, T Matthew Evans, and Douglas D Cortes. 2d dem analysis of the interactions between bio-inspired geo-probe and soil during inflation–deflation cycles. *Granular Matter*, 22(1):1–14, 2020.

Peter A Cundall and Otto DL Strack. A discrete numerical model for granular assemblies. *geotechnique*, 29(1):47–65, 1979.

J Carlos Santamarina, Katherine A Klein, and Moheb A Fam. *Soils and waves.* J. Wiley & Sons New York, 2001.

Catherine O'Sullivan. *Particulate discrete element modelling: a geomechanics perspective.* CRC Press, 2011.

National Academies of Sciences Engineering, Medicine, et al. Nchrp 2018 annual report. 2019.

N Belheine, J-P Plassiard, F-V Donzé, F Darve, and A Seridi. Numerical simulation of drained triaxial test using 3d discrete element modeling. *Computers and Geotechnics*, 36(1-2):320–331, 2009.

Xueliang Zhao and T Matthew Evans. Discrete simulations of laboratory loading conditions. *International journal of geomechanics*, 9(4):169–178, 2009.

Yuyan Chen, Ali Khosravi, Alejandro Martinez, Jason DeJong, and Dan Wilson. Analysis of the self-penetration process of a bio-inspired in situ testing probe. In *Geo-congress 2020: biogeotechnics*, pages 224–232. American Society of Civil Engineers Reston, VA, 2020.

Kevin C Kuei, Jason T DeJong, and Alejandro Martinez. Particle size effects on the strength and fabric of granular media. In *Geo-Congress 2020: Modeling, Geomaterials, and Site Characterization*, pages 349–358. American Society of Civil Engineers Reston, VA, 2020.

Tom Lunne, John JM Powell, and Peter K Robertson. *Cone penetration testing in geotechnical practice.* CRC Press, 2002.

ASTM. *Standard test method for electronic friction cone and piezocone penetration testing of soils.* ASTM International, 2012.

A Khosravi, A Martinez, and JT DeJong. Discrete element model (dem) simulations of cone penetration test (cpt) measurements and soil classification. *Canadian Geotechnical Journal*, 57(9):1369–1387, 2020.

Matteo Oryem Ciantia, Marcos Arroyo, Joanna Butlanska, and Antonio Gens. Dem modelling of cone penetration tests in a double-porosity crushable granular material. *Computers and Geotechnics*, 73:109–127, 2016.

Ningning Zhang, Marcos Arroyo, Matteo Oryem Ciantia, Antonio Gens, and Joanna Butlanska. Standard penetration testing in a virtual calibration chamber. *Computers and Geotechnics*, 111:277–289, 2019.

Marcos Arroyo, Joanna Butlanska, Antonio Gens, Francesco Calvetti, and Michael Jamiolkowski. Cone penetration tests in a virtual calibration chamber. *Géotechnique*, 61(6): 525–531, 2011.

An-Bin Huang and Max Y Ma. An analytical study of cone penetration tests in granular material. *Canadian Geotechnical Journal*, 31(1):91–103, 1994.

Francesco Calvetti and Roberto Nova. Micro-macro relationships from dem simulated element and in-situ tests. In *Proc. 5th Int. Conf. Micromech. Granular Media: Powders and Grains*, pages 245–250, 2005.

Jia Lin and Wei Wu. Numerical study of miniature penetrometer in granular material by discrete element method. *Philosophical Magazine*, 92(28-30):3474–3482, 2012.

GR McDowell, O Falagush, and H-S Yu. A particle refinement method for simulating dem of cone penetration testing in granular materials. *Géotechnique Letters*, 2(3):141–147, 2012.

Joanna Butlanska, Marcos Arroyo, Antonio Gens, and Catherine O'Sullivan. Multi-scale analysis of cone penetration test (cpt) in a virtual calibration chamber. *Canadian geotechnical journal*, 51(1):51–66, 2014.

MJ Jiang, H-S Yu, and D Harris. Discrete element modelling of deep penetration in granular soils. *International journal for numerical and analytical methods in geomechanics*, 30(4):335–361, 2006.

Nan Zhang and T Matthew Evans. Three dimensional discrete element method simulations of interface shear. *Soils and foundations*, 58(4):941–956, 2018.

Zhiwei Zeng and Ying Chen. Simulation of soil-micropenetrometer interaction using the discrete element method (dem). *Transactions of the ASABE*, 59(5):1157–1163, 2016.

Mohammad A Sadek, Mehari Tekeste, and Mojtaba Naderi. Calibration of soil compaction behavior using discrete element method (dem). In *2017 ASABE Annual International Meeting*, page 1. American Society of Agricultural and Biological Engineers, 2017.

Matteo Ciantia, C O'Sullivan, and Richard J Jardine. Pile penetration in crushable soils: Insights from micromechanical modelling. In *17th European Conference on soil Mechanics and Geotechnical Engineering (ECSMGE 2019)*. International Society for Soil Mechanics and Geotechnical Engineering, 2019a.

GM Whiteley, WH Utomo, and AR Dexter. A comparison of penetrometer pressures and the pressures exerted by roots. *Plant and Soil*, 61(3):351–364, 1981.

BM McKenzie and AR Dexter. Radial pressures generated by the earthworm aporrectodea rosea. *Biology and fertility of soils*, 5(4):328–332, 1988.

Siul Ruiz, Dani Or, and Stanislaus J Schymanski. Soil penetration by earthworms and plant roots—mechanical energetics of bioturbation of compacted soils. *PloS one*, 10(6): e0128914, 2015.

Kenneth L Lee and H Bolton Seed. Dynamic strength of anisotropically consolidated sand. *Journal of the Soil Mechanics and Foundations Division*, 93(5):169–190, 1967.

Robert D Holtz, William D Kovacs, and Thomas C Sheahan. *An introduction to geotechnical engineering*, volume 733. Prentice-Hall Englewood Cliffs, 1981.

Michele Jamiolkowski, DCF Lo Presti, and Mario Manassero. Evaluation of relative density and shear strength of sands from cpt and dmt. In *Soil behavior and soft ground construction*, pages 201–238. 2003.

Peter K Robertson. Cone penetration test (cpt)-based soil behaviour type (sbt) classification system—an update. *Canadian Geotechnical Journal*, 53(12):1910–1927, 2016.

Andrew Noel Schofield and Peter Wroth. *Critical state soil mechanics*, volume 310. McGraw-hill London, 1968.

David Muir Wood. *Soil behaviour and critical state soil mechanics.* Cambridge university press, 1990.

John H Schmertmann. Guidelines for cone penetration test: performance and design. Technical report, United States. Federal Highway Administration, 1978.

G Baldi. Interpretation of cpt's and cptu's. 2nd part: Drained penetration of sands. *Proc. IV Int. Geotech. Sem., Singapore*, 1986.

D Potyondy. Stiffness matrix at a contact between two clumps, 2009.

HS Yu and GT Houlsby. Finite cavity expansion in dilatant soils: loading analysis. *Geotechnique*, 41(2):173–183, 1991.

R Salgado and M Prezzi. Computation of cavity expansion pressure and penetration resistance in sands. *International Journal of Geomechanics*, 7(4):251–265, 2007.

Fernando Schnaid. A study of the cone-pressuremeter test in sand. 1990.

R Ajalloeian and HS Yu. Chamber studies of the effects of pressuremeter geometry on test results in sand. *Geotechnique*, 48(5):621–636, 1998.

IF Collins, MJ Pender, and Wang Yan. Cavity expansion in sands under drained loading conditions. *International journal for numerical and analytical methods in geomechanics*, 16(1):3–23, 1992.

James Che and Kelly M Dorgan. It's tough to be small: dependence of burrowing kinematics on body size. *Journal of Experimental Biology*, 213(8):1241–1250, 2010.

Siul A Ruiz and Dani Or. Biomechanical limits to soil penetration by earthworms: direct measurements of hydroskeletal pressures and peristaltic motions. *Journal of The Royal Society Interface*, 15(144):20180127, 2018.

David E Sadava, David M Hillis, and H Craig Heller. *Life: the science of biology*, volume 2. Macmillan, 2009.

Christina M Barnett, Anthony G Bengough, and Blair M McKenzie. Quantitative image analysis of earthworm-mediated soil displacement. *Biology and fertility of soils*, 45(8): 821–828, 2009.

Jessica A Kurth and William M Kier. Scaling of the hydrostatic skeleton in the earthworm lumbricus terrestris. *Journal of Experimental Biology*, 217(11):1860–1867, 2014.

Seyed Ali Aleali, Paola Bandini, and Craig Michael Newtson. Multifaceted bioinspiration for improving the shaft resistance of deep foundations. *Journal of Bionic Engineering*, 17(5):1059–1074, 2020.

Sichuan Huang, Yong Tang, Hosain Bagheri, Dongting Li, Alexandria Ardente, Daniel Aukes, Hamidreza Marvi, and Junliang Tao. Effects of friction anisotropy on upward burrowing behavior of soft robots in granular materials. *Advanced Intelligent Systems*, 2(6):1900183, 2020.

Alejandro Martinez and JD Frost. The influence of surface roughness form on the strength of sand–structure interfaces. *Géotechnique Letters*, 7(1):104–111, 2017.

Alessandro Simoni and Guy T Houlsby. The direct shear strength and dilatancy of sand–gravel mixtures. *Geotechnical & Geological Engineering*, 24(3):523–549, 2006.

Yang Xiao, Yifei Sun, Hong Liu, and Feng Yin. Critical state behaviors of a coarse granular soil under generalized stress conditions. *Granular Matter*, 18(2):1–13, 2016.

Yadan Luo, Ziwei Wang, Zi Huang, Yang Yang, and Cong Zhao. Coarse-to-fine annotation enrichment for semantic segmentation learning. In *Proceedings of the 27th ACM International Conference on Information and Knowledge Management*, pages 237–246, 2018.

RJ Mair and David Muir Wood. *Pressuremeter testing: methods and interpretation.* Elsevier, 2013.

Gaël Combe and Jean-Noël Roux. Discrete numerical simulation, quasistatic deformation and the origins of strain in granular materials. *arXiv preprint arXiv:0901.3842*, 2009.

Farhang Radjai and Vincent Richefeu. Contact dynamics as a nonsmooth discrete element method. *Mechanics of Materials*, 41(6):715–728, 2009.

Jes Christoffersen, Morteza Monte Mehrabadi, and Sia Nemat-Nasser. A micromechanical description of granular material behavior. 1981.

Jérôme Fortin, Olivier Millet, and Géry de Saxcé. Construction of an averaged stress tensor for a granular medium. *European Journal of Mechanics-A/Solids*, 22(4):567–582, 2003.

RJ Jardine, BT Zhu, P Foray, and ZX Yang. Measurement of stresses around closed-ended displacement piles in sand. *Géotechnique*, 63(1):1–17, 2013.

Daichao Sheng, K Dieter Eigenbrod, and Peter Wriggers. Finite element analysis of pile installation using large-slip frictional contact. *Computers and Geotechnics*, 32(1):17–26, 2005.

Harry M Jol. *Ground penetrating radar theory and applications*. elsevier, 2008.

Miguel Angel Benz Navarrete, Pierre Breul, and Roland Gourvès. Application of wave equation theory to improve dynamic cone penetration test for shallow soil characterisation. *Journal of Rock Mechanics and Geotechnical Engineering*, 2021.

Wenhan Zhong, Hanlong Liu, Qi Wang, Wengang Zhang, Yongqin Li, Xuanming Ding, and Longlong Chen. Investigation of the penetration characteristics of snake skin-inspired pile using dem. *Acta Geotechnica*, 16(6):1849–1865, 2021.

SD Mallett, A Siegel, I Vego, and JD Frost. Uplift behavior of root-inspired anchorage models. In *Proceedings of International Symposium on Bio-mediated and Bio-inspired Geotechnics, Atlanta*, 2018b.

Floriana Anselmucci, Edward Andò, Gioacchino Viggiani, Nicolas Lenoir, Chloé Arson, and Luc Sibille. Imaging local soil kinematics during the first days of maize root growth in sand. *Scientific reports*, 11(1):1–13, 2021a.

F Anselmucci, E Andó, G Viggiani, N Lenoir, R Peyroux, C Arson, and L Sibille. Use of x-ray tomography to investigate soil deformation around growing roots. *Géotechnique Letters*, 11(1):96–102, 2021b.

Yuyan Chen, Alejandro Martinez, and Jason T DeJong. Dem study of the alteration of the stress state in granular media around a bio-inspired probe. *Canadian Geotechnical Journal*, (ja), 2022.

Nicholas D Naclerio, Andras Karsai, Mason Murray-Cooper, Yasemin Ozkan-Aydin, Enes Aydin, Daniel I Goldman, and Elliot W Hawkes. Controlling subterranean forces enables a fast, steerable, burrowing soft robot. *Science Robotics*, 6(55):eabe2922, 2021.

Peter K Robertson. Soil behaviour type from the cpt: an update. In *2nd International symposium on cone penetration testing*, volume 2, page 8. Cone Penetration Testing Organizing Committee, 2010.

HS Yu, F Schnaid, and IF Collins. Analysis of cone pressuremeter tests in sands. *Journal of geotechnical engineering*, 122(8):623–632, 1996.

Dongxue Hao, Dong Wang, Conleth D O'Loughlin, and Christophe Gaudin. Tensile monotonic capacity of helical anchors in sand: interaction between helices. *Canadian Geotechnical Journal*, 56(10):1534–1543, 2019.

Gizem Misir. Predicting the uplift capacity of vertically located two-plate anchors. *Acta Geotechnica Slovenica*, 15(2):47–57, 2018.

Anastasia Nally and James P Hambleton. Assessment of analysis techniques for multi-plate anchors in sand. In *Proceedings of the 44th Annual Conference on Deep Foundations*, 2019.

Dong Wang, RS Merifield, and Christophe Gaudin. Uplift behaviour of helical anchors in clay. *Canadian Geotechnical Journal*, 50(6):575–584, 2013.

AG Winter, RLH Deits, DS Dorsch, AH Slocum, AE Hosoi, et al. Razor clam to roboclam: burrowing drag reduction mechanisms and their robotic adaptation. *Bioinspiration & biomimetics*, 9(3):036009, 2014.

Jason DeJong Chen et al., Alejandro Martinez. Dem simulations of a bio–inspired site characterization probe with two anchors. *Acta Geotechnica*, in review, 2022.

Matteo Oryem Ciantia, Marcos Arroyo, Catherine O'Sullivan, Antonio Gens, and Tingfa Liu. Grading evolution and critical state in a discrete numerical model of fontainebleau sand. *Géotechnique*, 69(1):1–15, 2019b.

Maria Stolarz. Circumnutation as a visible plant action and reaction: physiological, cellular and molecular basis for circumnutations. *Plant signaling & behavior*, 4(5): 380–387, 2009.

A Tonazzini, L Popova, F Mattioli, and B Mazzolai. Analysis and characterization of a robotic probe inspired by the plant root apex. In *2012 4th IEEE RAS & EMBS International Conference on Biomedical Robotics and Biomechatronics (BioRob)*, pages 1134–1139. IEEE, 2012.

Jack L Mullen, Hideo Ishikawa, and Michael L Evans. Analysis of changes in relative elemental growth rate patterns in the elongation zone of arabidopsis roots upon gravistimulation. *Planta*, 206(4):598–603, 1998.

Carl Simmons, Dieter Söll, and Fernando Migliaccio. Circumnutation and gravitropism cause root waving in arabidopsis thaliana. *Journal of Experimental Botany*, 46(1): 143–150, 1995.

Hye-jeong Kim, Akie Kobayashi, Nobuharu Fujii, Yutaka Miyazawa, and Hideyuki Takahashi. Gravitropic response and circumnutation in pea (pisum sativum) seedling roots. *Physiologia plantarum*, 157(1):108–118, 2016.

Y Sharif, M Ciantia, Michael J Brown, Jonathan A Knappett, and JD Ball. Numerical techniques for the fast generation of samples using the particle refinement method. In *Proceedings of Proceedings of the 8th International Conference on Discrete Element Methods*, 2019.

Benjamin Cerfontaine, Matteo Ciantia, MJ Brown, and YU Sharif. Dem study of particle scale and penetration rate on the installation mechanisms of screw piles in sand. *Computers and Geotechnics*, 139:104380, 2021.

Yong Tang and Junliang Tao. Multiscale analysis of rotational penetration in shallow dry sand and implications for self-burrowing robot design. *Acta Geotechnica*, pages 1–20, 2022.

Omar Falagush, Glenn R McDowell, Hai-Sui Yu, and John P de Bono. Discrete element modelling and cavity expansion analysis of cone penetration testing. *Granular Matter*, 17(4):483–495, 2015.

Zitao Zhang and Yu-Hsing Wang. Three-dimensional dem simulations of monotonic jacking in sand. *Granular Matter*, 17(3):359–376, 2015.

Yaseen Umar Sharif, Michael John Brown, Matteo Oryem Ciantia, Benjamin Cerfontaine, Craig Davidson, Jonathan Knappett, Gerrit Johannes Meijer, and Jonathan Ball. Using discrete element method (dem) to create a cone penetration test (cpt)-based method to estimate the installation requirements of rotary-installed piles in sand. *Canadian Geotechnical Journal*, 58(7):919–935, 2021.

Leo Rothenburg and RJ Bathurst. Analytical study of induced anisotropy in idealized granular materials. *Geotechnique*, 39(4):601–614, 1989.

K.B. Chen Y. Hunt et al., O'Hara and A. Martinez. Numerical and physical modeling of the effect of cone apex angle on the penetration resistance in coarse-grained soils. *International Journal of Geomechanics*, in review, 2022.

Anand Kumar Mishra, Francesca Tramacere, Roberto Guarino, Nicola Maria Pugno, and Barbara Mazzolai. A study on plant root apex morphology as a model for soft robots moving in soil. *PloS one*, 13(6):e0197411, 2018.

A. Chen et al., Martinez. Dem modeling of root circumnutation-inspired penetration in shallow granular materials. *To be submitted for possible publication.*